PhD-FSTM-2023-117

The Faculty of Science, Technology and Medicine

DISSERTATION

Defence held on 10/11/2023 in Esch-sur-Alzette

to obtain the degree of

DOCTEUR DE L'UNIVERSITÉ DU LUXEMBOURG

EN BIOLOGIE

by

Alise Zagare
Born on 10 July 1990 in Aizkraukle (Latvia)

CONTRIBUTION OF TYPE 2 DIABETES AND GENETIC VARIANTS IN LRRK2 AND GBA TO PARKINSON'S DISEASE

Dissertation defence committee

Dr Jens C Schwamborn, dissertation supervisor
Professor, Université du Luxembourg

Dr Carole Linster, Chairman
Professor, Université du Luxembourg

Dr Rudi Balling,
Professor, University of Bonn

Dr Egils Stalidzans
Senior researcher, University of Latvia

Dr Alexander Kleger
Professor, University of Ulm

UNIVERSITY OF LUXEMBOURG

DOCTORAL THESIS

CONTRIBUTION OF TYPE 2 DIABETES AND GENETIC VARIANTS IN LRRK2 AND GBA TO PARKINSON'S DISEASE

by

Alise Zagare

Developmental and Cellular Biology Group

Luxembourg Centre for Systems Biomedicine

Dissertation defence committee

Dr Jens C. Schwamborn, dissertation supervisor

Dr Carole Linster

Dr Rudi Balling

Dr Egils Stalidzans

Dr Alexander Kleger

November 10, 2023

Affidavit

I hereby confirm that the PhD thesis “Contribution of Type 2 Diabetes and genetic variants in LRRK2 and GBA to Parkinson's Disease” has been written independently and without any other sources than cited.

Luxembourg, 10/11/2023 Alise Zagare

Nothing in life is to be feared, it is only to be understood

Marie Curie

Acknowledgements

This work would not be possible without the constant support and help that I received from many people. I want to thank my supervisor, lab members, all collaborators, the CET committee, PhD thesis jury and my family for their support and encouragement throughout this time.

First and foremost, I would like to express my sincere gratitude to my supervisor Prof. Jens Schwamborn for giving me the opportunity to work in his group. He has been a great mentor and I have learned so much from him. I greatly appreciate his continuous support during this time, his enthusiasm, motivation and sharing of his immense knowledge. I am really grateful not only for his guidance but also for challenging and encouraging me to try and learn new approaches and new methods that significantly advanced my work.

I want to thank all my lab colleagues for the great and supportive environment at work. I appreciate everyone's shared advice and knowledge. We have a truly amazing group, where people volunteer to help with anything in the lab and we support each other through good and rough days. I must admit that I have learned so many things about various topics during our lunchtime conversations. Discussions about global problems or weird personal experiences can make each day better or at least funnier.

My sincere thanks go to my CET committee members Asst. Prof. Carole Linster and Dr Egils Stalidzans for their assistance and advice during these years of my PhD. I would also like to express my gratitude to Prof. Rudi Balling and Prof. Alexander Kleger for being part of my thesis committee and taking the time to evaluate my work.

Finally, I would like to express a tremendous thanks to my family, especially my husband and my parents for their understanding, patience, and encouragement. Without their support, this PhD journey would not be possible.

Dissemination

The work carried out during PhD has resulted in two first-author manuscripts, two joint first-author manuscripts and seven contributing author manuscripts. They explain in detail the results obtained to fulfil the aims of my PhD. Three of the manuscripts are included in the PhD thesis.

Published

Monzel AS, Hemmer K, Kaoma T, Smits LM, Bolognin S, Lucarelli P, Rosety I, **Zagare A**, Antony P, Nickels SL, Krueger R, Azuaje F, Schwamborn JC. 'Machine learning-assisted neurotoxicity prediction in human midbrain organoids.' Parkinsonism Relat Disord. 2020 Jun; 75:105-109. doi: 10.1016/j.parkreldis.2020.05.011. Epub 2020 May 8. PMID: 32534431.

Zagare A, Gobin M, Monzel AS, Schwamborn JC. 'A robust protocol for the generation of human midbrain organoids.' STAR Protoc. 2021 May 4;2(2):100524. doi: 10.1016/j.xpro.2021.100524. PMID: 34027482; PMCID: PMC8121770.

Zagare A, Barmpa K, Smajic S, Smits LM, Grzyb K, Grünewald A, Skupin A, Nickels SL, Schwamborn JC. 'Midbrain organoids mimic early embryonic neurodevelopment and recapitulate LRRK2-p.Gly2019Ser-associated gene expression.' Am J Hum Genet. 2022 Feb 3;109(2):311-327. doi: 10.1016/j.ajhg.2021.12.009. Epub 2022 Jan 24. PMID: 35077669; PMCID: PMC8874228.

Accepted

Isabel Rosety, **Alise Zagare**, Claudia Saraiva, Sarah Nickels, Paul Antony, Catarina Almeida, Enrico Glaab, Rashi Halder, Sergiy Velychko, Thomas Rauen, Hans R. Schöler, Silvia Bolognin, Thomas Sauter, Javier Jarazo, Rejko Krueger, Jens C. Schwamborn (Sept 2023). 'Impaired dopaminergic neuronal differentiation in GBA associated Parkinson's disease midbrain organoids is accompanied by an increased progenitor pool in cell cycle arrest.' *Accepted to Npj Parksinon's Disease*.

In revision

Alise Zagare, German Preciat, Sarah. L Nickels, Xi Luo, Anna S Monzel, Gemma Gomez-Giro, Graham Robertson, Christian Jaeger, Jafar Sharif, Haruhiko Koseki, Nico J Diederich, Enrico Glaab, Ronan MT Fleming, Jens C Schwamborn (Sept 2023). 'Omics data integration allows the identification of an idiopathic Parkinson's disease signature.' *Under revision in Communications Biology.*

Submitted

Kathleen Mommaerts, Anna S. Monzel, **Alise Zagare**, Sarah L. Nickels, Nico J. Diederich, Laura Longhino, William Mathieson, Paul M. A. Antony, Fay Betsou, Jens C. Schwamborn (Sept 2023). 'Cystatin C secretion in blood derivatives and cellular models of idiopathic Parkinson's disease'. *Submitted to Parkinson's Disease.*

Alise Zagare, Janis Kurlovics, Catarina Almeida, Daniele Ferrante, Daniela Frangenberg, Laura Neises, Ahmed Hemedan, Armelle Vitali, Gemma Gomez-Giro, Christian Jaeger, Paul Antony, Rashi Halder, Marek Ostaszewski, Rejko Krueger, Enrico Glaab, Johannes Meiser, Egils Stalidzans, Giuseppe Arena, Jens C Schwamborn (Sept 2023). 'Insulin resistance disrupts midbrain metabolic & functional homeostasis and aggravates dopaminergic neuron loss in GBA-PD.' *Submitted to PNAS.*

In preparation

Axel Chemla, Giuseppe Arena, Ginevra Sacripanti, Kyriaki Barmpa, **Alise Zagare**, Paul Antony, Jochen Ohnmacht, Pierre Garcia, Jaqueline Jung, Anne Marie Marzesko, Manuel Buttin, Thorsten Schmidt, Anne Grünewald, Jens C.Schwamborn, Rejko Krüger, Claudia Saraiva (2023). 'Parkinson's disease-related Miro1 mutation induces mitochondrial dysfunction and loss of dopaminergic neurons *in vitro* and *in vivo.'*

Gemma Gomez-Giro, Daniela Frangenberg, Daniela Vega, **Alise Zagare**, Kyriaki Barmpa, Paul M.A. Antony, Graham Robertson, Rahman Sabahi, Yagmur Demircan, Gülden Akçay, Kristian Haendler, Nathalie Kruse, Florentia Papastefanaki, Rebecca Matsas, Malte Spielman, Regina Luttge, and Jens C. Schwamborn (2023). 'Alpha-synuclein pathology transfer in a midbrain-hindbrain assembloid model.'

Sonia Sabate-Soler, Cláudia Saraiva, Anna-Sophie Zimmermann, **Alise Zagare**, Kyriaki Barmpa , Kristian Haendler, Susana Rosa, Evan Williams, Lino Ferreira, Malte Spielman, Jens Schwamborn (2023). 'Vascularization of human midbrain organoids leads to reduced hypoxia and increases the morphological complexity of microglia'.

Armin Rauschenberger, Alexandre Baron, **Alise Zagare**, Armelle Vitali, Li Zhang, Jochen Ohnmacht, Javier Jarazo, Philip Seibler, Christine Klein, Enza Maria Valente, Axel Methner, Jens Schwamborn, Enrico Glaab, Rejko Kruger, Giuseppe Arena (2023). 'Mutations in the PD-associated PINK1 gene induce dopaminergic loss by the mitochondrial-nuclear crosstalk.'

Abbreviations

αSyn	α-Synuclein (protein)
2D	Two-dimensional
3D	Three-dimensional
AA	Ascorbic acid
AD	Alzheimer's disease
AGEs	Advanced glycation end products
ASO	Antisense oligonucleotide
ATP	Adenosine triphosphate
BBB	Blood-brain-barrier
BCL2	B-cell lymphoma 2
BMI	Body mass index
BMP	Bone morphogenic protein
BSA	Bovine serum albumin
CBM	Constraint-based model
CHIR	CHIR-99021
cAMP	Cyclic adenosine monophosphate
CNS	Central nervous system
CSF	Cerebrospinal fluid
DEGs	Differentially expressed genes
DMEM	Modified Dulbecco's Eagle medium
DMSO	Dimethylsulfoxide
DW	Dry weight
ETC	Electron transport chain
ER	Endoplasmic reticulum
FACS	Fluorescence-activated cell sorting
FDR	False-discovery rate

FGF	Fibroblast growth factor
FOXO	Forkhead Box O1
FVA	Flux variability analysis
GBA	Glucosylceramidase beta
GCase	Glucocerebrosidase
GC-MS	Gas chromatography-mass spectrometry
GSK3β	Glycogen synthase kinase 3 beta
GSM	Genome-scale model
hBDNF	Human brain-derived neurotrophic factor
hGDNF	Human glial cell-derived neurotrophic factor
IAPP	Islet amyloid polypeptide
IGF2	Insulin-like growth factor 2
INS	Insulin (gene)
IPD	Idiopathic Parkinson's disease
iPSC	Induced pluripotent stem cell
IR	Insulin resistant
IRS	Insulin receptor substrate
IS	Insulin sensitive
LC-MS	Liquid chromatography-mass spectrometry
LFP	Local field potential
LPC	Lysophosphatidylcholine
LPE	Lysophosphatidylethanolamine
LRRK2	Leucine-rich repeat kinase 2
MAO	Monoamine oxidase
MAP2	Microtubule-associated protein 2
MGO	Methylglyoxal
MPTP	1-methyl-4-phenyl-1,2,3,4-tetrahydropyridine

MCI	Mitochondrial Complex I
MEA	Multi-electrode array
MRI	Magnetic resonance imaging
mTOR	Mammalian target of rapamycin
NAD	Nicotinamide adenine dinucleotide
NC	Negative control
NESC	Neuroepithelial stem cell
OXPHOS	Oxidative phosphorylation
PBM	Probabilistic Boolean modeling
PBS	Phosphate-buffered saline
PC	Phosphatidylcholine
PCA	Principal component analysis
PC-P	1-alkenyl,2-acylphosphatidylethanolamines
PC-O	1-alkyl,2-acylphosphatidylethanolamines
PD	Parkinson's disease
PE	Phosphatidylethanolamine
PFA	Paraformaldehyde
PINK1	PTEN-induced kinase 1
PPAR-γ	Peroxisome proliferator-activated receptor gamma
PMA	Purmorphamine
ROS	Reactive oxygen species
RT	Room temperature
SHH	Sonic-hedgehog
SREBP	Sterol-regulatory-element-binding protein
SNCA	α-Synuclein (gene)
SNpc	Substantia nigra pars compacta
TCA	Tricarboxylic acid cycle

TG	Triglycerides
TGFβ	Transforming growth factor
TH	Tyrosine hydroxylase
T2D	Type 2 Diabetes
UPS	Ubiquitin-proteosome system
VPS35	Vacuolar protein sorting-associated protein 35
VTA	Ventral tegmental area
WNT	Wingless-related integration site
WT	Wild type

Abstract

Contribution of Type 2 Diabetes and genetic variants in LRRK2 and GBA to Parkinson's Disease

Population aging is a global demographic trend that presents a considerable threat of an increase in the incidence of age-related disorders, such as Parkinson's disease (PD). PD is currently the second most frequent neurodegenerative disease. It is characterized by selective and progressive midbrain dopaminergic neuron death leading to impairment of voluntary movement which clinically manifests as severe motor impairment. Although age is the strongest risk factor for PD, it has been suggested that PD-associated mutations contribute to the neurodevelopmental defects leading to incomplete dopaminergic neuron differentiation increasing their susceptibility to neurodegeneration with aging. To investigate this hypothesis, we analyzed PD neurodevelopmental aspects mediated by the two most common PD-associated mutations - LRRK2-G2019S and GBA-N370S using midbrain organoids for *in vitro* disease modeling. We demonstrate that both mutations compromise dopaminergic neuron differentiation resulting in an immature neural population. Furthermore, midbrain organoids harboring the LRRK2-G2019S mutation display the transcriptomic signature of LRRK2-associated PD and untimely glia differentiation, while GBA-N370S mutant organoids capture most relevant GBA-associated PD phenotypes, such as a decreased activity of glucocerebrosidase, lysosomal defects and altered lipid metabolism.

In addition to neurodevelopmental defects, lifestyle factors, such as Type 2 Diabetes (T2D) can further increase cellular vulnerability and predispose to neurodegeneration or aggravate existing PD phenotypes. An increasing amount of epidemiological evidence highlights T2D as a risk factor for PD development. Although both diseases are highly heterogeneous, they seem to share pathophysiological mechanisms that underly their comorbidity. We show that T2D-associated insulin resistance impairs neural activity and alters lipid and energy metabolism of non-PD midbrain organoids. Moreover, we demonstrate that insulin signaling is dysregulated in GBA-N370S midbrain organoids at the transcriptomic level, and insulin resistance effects on GBA-N370S mutation phenotypes are governed by FOXO1 activation downstream of insulin signaling. In addition, we show that antidiabetic treatment, particularly, Pioglitazone rescues PD-associated dopaminergic neuron loss, dopamine levels, and cell death in GBA-N370S-carrying midbrain organoids.

Taken together, in this thesis we demonstrate that LRRK2-G2019S and GBA-N370S mutations alter neurodevelopmental processes and provide evidence that T2D-associated insulin resistance is implicated in PD-related pathophysiology.

Motivation and Aims

Due to the general aging of the population, PD incidence is expected to increase along with its related socio-economic and healthcare challenges. Despite extensive research over the past decades devoted to understand the underlying molecular mechanisms of PD, the main causes of PD-associated selective loss of dopaminergic neurons remain rather elusive. For this reason, there is also still a lack of effective preventative or disease-modifying treatment. Improving early diagnosis of PD might be a key factor in effective treatment development. However, the multifactorial nature of PD complicates the identification of early molecular events that can also be highly variable between patients. Genetic and environmental/lifestyle risk factors contribute to PD molecular heterogeneity, therefore, it is crucial to understand each factor's specific input to PD pathogenesis to tailor patient clinical care and develop stratified treatment strategies. Moreover, PD is currently the fastest-growing neurodegenerative disease in the world. Since only about 10% of PD cases are inherited, it suggests that risk factors play an essential role in PD development.

The main aim of my thesis was to study the two most frequent PD-associated mutation LRRK2-G2019S and GBA-N370S as well as a lifestyle risk factor - T2D contribution to PD development using midbrain organoids as *in vitro* model. The genetic variants LRRK2-G2019S and GBA-N370S have been associated with altered neurodevelopment (elaborated in section 2.2.), suggesting that predisposition to PD for the carriers of these two mutations might be determined very early in life. Therefore, the main focus was to investigate LRRK2-G2019S and GBA-N370S associated early neurodevelopmental changes affecting dopaminergic neuron maturity and leading to their increased vulnerability and susceptibility to degeneration. On the other hand, modifiable risk factors, such as T2D, may arise later in life and intensify age-related or mutation-induced molecular changes promoting cellular damage and disease development. Growing evidence suggests that T2D is a considerable risk factor for PD development through shared disease mechanisms (elaborated in section 1.2.2). Nevertheless, common pathway dysfunction also implies shared therapeutic strategies. Thus, another objective of my thesis was to investigate T2D as a risk factor for PD and explore the potential beneficial effects of antidiabetic drugs in PD treatment.

The concrete aims of this work:

1. Validate the suitability of midbrain organoids for PD modeling by characterizing midbrain organoid cellular composition and developmental trajectories using single-cell RNA sequencing data.

2. Investigate LRRK2-G2019S mutation-caused neurodevelopmental alterations by comparing the single-cell transcriptome of healthy-individual-derived midbrain organoids with their isogenic LRRK2-G2019S counterparts.

3. Investigate GBA-N370S mutation-associated metabolic and neurodevelopmental phenotypes in PD-patient-derived midbrain organoids.

4. Investigate T2D-associated insulin resistance effects on healthy individual-derived midbrain organoids.

5. Model GBA-N370S associated PD and T2D comorbidity to investigate insulin resistance effect on PD phenotypes.

6. Explore antidiabetic drug potential in PD therapy.

Table of Contents

CHAPTER 1

Synopsis

1. Introduction

1.1. Parkinson's disease

The first medical description of Parkinson's disease (PD) was published in 1817 in 'An Essay on the Shaking Palsy' by English surgeon-apothecary James Parkinson (Parkinson 2002). Today we know PD as the most common movement disorder and the second most prevalent neurodegenerative disease. The progressive increase in global population aging, coincides with the rise in the number of individuals affected by neurodegenerative diseases, including PD. PD is the fastest-growing neurodegenerative disease in terms of prevalence, disability and mortality, with more than a doubling number of patients between 1990 and 2019, reaching an estimated 8.5 million global prevalence in 2019 (Collaborators 2018, Ou et al. 2021). It is also expected that the trend of patient number increase will continue over the next years between 5 to 35 new cases per 100,000 individuals yearly (Twelves, Perkins, and Counsell 2003). Although over the last decades there has been significant progress in comprehending the molecular basis for neurodegeneration occurring in PD, the available treatment is still only symptomatic. However, considering the escalating prevalence of PD, efforts to develop disease-modifying treatments are essential to suspend the growing socio-economic burden.

1.1.1. Clinical manifestation

The most characteristic clinical signs of PD are cardinal motor symptoms - bradykinesia, resting tremor, rigidity, and postural instability, which are factors used to diagnose PD (Varadi 2020, Sveinbjornsdottir 2016). However, motor deficits appear only when at least 50% of dopaminergic neurons are lost (Hustad and Aasly 2020). Before the onset of motor impairment or during the so-called prodromal phase of PD, patients experience diverse non-motor symptoms. There is growing evidence that non-motor symptoms precede motor impairment even by decades and therefore might be critical for PD's early diagnosis (Kalia and Lang 2016, Kouli, Torsney, and Kuan 2018). Early non-motor symptoms include olfactory impairment, pain, fatigue, depression, hallucinosis, memory retrieval deficits, anxiety, as well as constipation, and urinary incontinence (Poewe et al. 2017, Varadi 2020). Another frequent early non-motor symptom of PD is sleeping disorders. They

can include insomnia, rapid eye movement (REM) sleep behavior disorder and excessive daytime sleeping (Loddo et al. 2017). Non-motor symptoms can accompany motor dysfunction over the course of PD by significantly worsening the life quality of PD patients (Jankovic and Tan 2020). In general, symptom development and severity are strongly linked to the progression of neurodegeneration, which is highly variable among patients (Kouli, Torsney, and Kuan 2018). PD heterogeneity in terms of the diversity of motor and non-motor symptoms (Figure 1.1), and course of progression, presents a great clinical challenge for the early PD diagnosis and choice of treatment strategies.

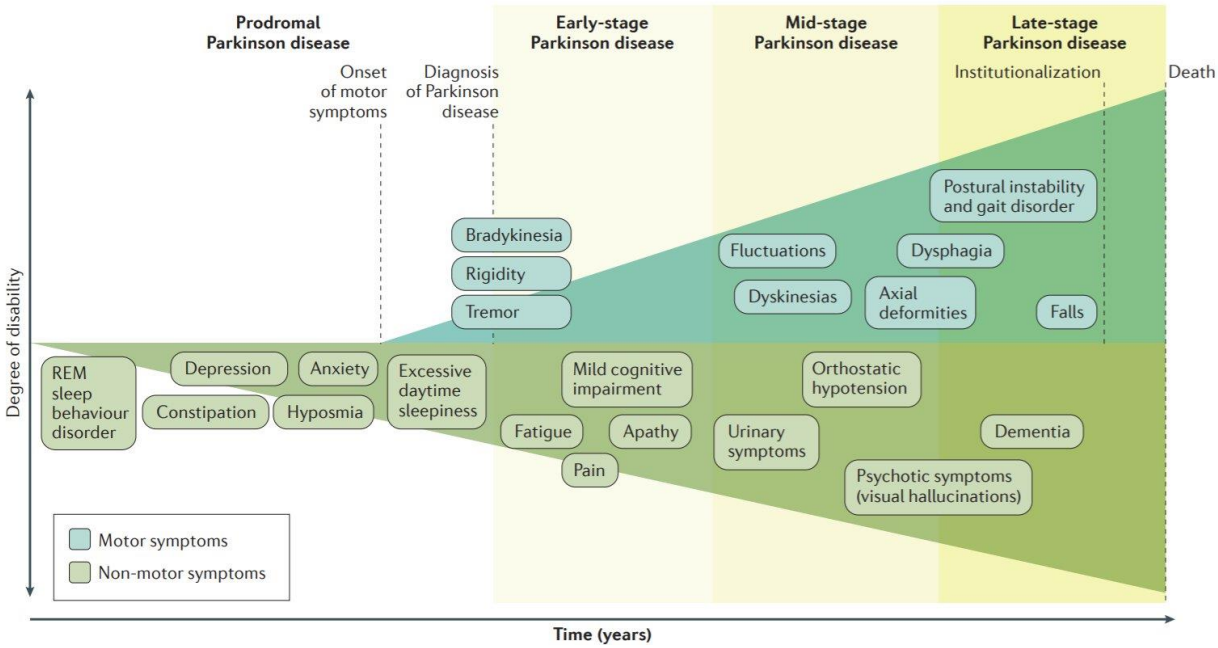

Figure 1.1. Clinical symptoms and course of PD progression. Non-motor symptoms precede motor symptoms but do not cause disability. Diagnosis of PD is based on the occurrence of motor-symptoms. Non-motor symptoms can be present throughout the entire course of PD. Increasing severity of motor symptoms over the PD course leads to progressive disability (Poewe et al. 2017).

1.1.2. Etiology and risk factors

PD is a multifactorial disease, and results from a complex interplay between aging, genetic and environmental factors. Only 5-10% of PD cases are monogenetic. Studies of familial PD have identified autosomal dominant (SNCA, LRRK2) and autosomal recessive (Parkin, PINK1, DJ1, ATP13A2, VPS35) forms of monogenetic hereditary PD (Klein and Westenberger 2012). These genes have provided great insight into potential molecular mechanisms of PD pathogenesis. However, monogenetic PD cases are rare and molecular causes of neurodegeneration cannot be generalized to all patients. The vast majority or about 90% of PD cases are sporadic and with unknown causes (idiopathic) (Klein and Westenberger 2012). Here age is the primary risk factor

(Kouli, Torsney, and Kuan 2018). According to epidemiological studies, the PD incidence rate sharply increases in the population above the age of 50 (Van Den Eeden et al. 2003, Pringsheim et al. 2014, Poewe et al. 2017). Genetic factors of sporadic PD have been identified through genome-wide association studies (GWAS) or exome sequencing (Figure 1.2.). The most frequent genetic risk factors identified that are associated with increased PD risk are the LRRK2-G2019S mutation (c.6055G>A transition) and several mutation variants in the GBA gene, namely p.E326K, p.T369M, p.N370S and p.L444P, whose frequency vary between different ethnicities (Blauwendraat et al. 2020, Day and Mullin 2021). Contrary to genetic variants causing hereditary PD, LRRK2 and GBA variants have incomplete penetrance, suggesting that other risk factors contribute to PD development.

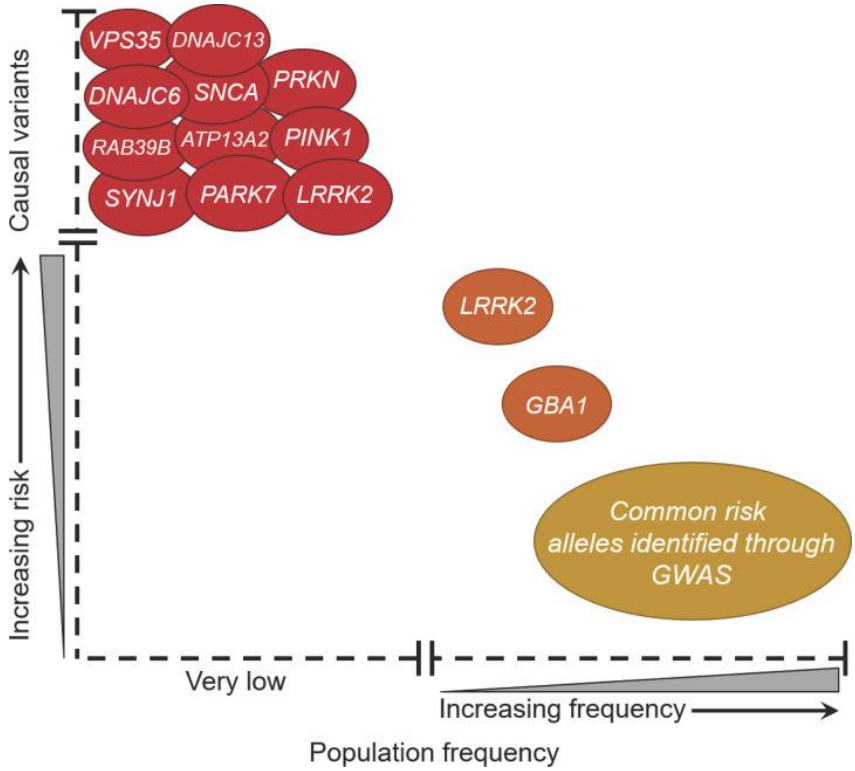

Figure 1.2. Genetics of PD. Mendelian genes identified by linkage analysis are in red. Mutations in these genes are rare but they are PD causative. Genes associated with moderate to high risk of PD are in orange. Most often identified by exome sequencing of PD patients or GWAS. High-frequency, but low-risk variants in more than 20 genes identified by GWAS of large cohorts are in yellow (Chandler et al. 2021).

Also, gender seems to have a role, since PD is more common in men than in women (Van Den Eeden et al. 2003, Baldereschi et al. 2000). In addition, through clinical association studies, multiple environmental and behavioral factors have been identified as contributors to PD

development (Jankovic and Tan 2020). Exposure to pesticides (diquat, paraquat, rotenone), heavy metals (iron, mercury, manganese, copper, lead) and industrial toxicants have been named as the main environmental risk factors (Zhao et al. 2023, Caudle et al. 2012, Pouchieu et al. 2018). Furthermore, head injury, inactive lifestyle and obesity are also suggested to increase the risk of acquiring PD (Delic et al. 2020, Muslimat Kehinde et al. 2019, Park et al. 2022, Vecchio et al. 2018). Although the last-mentioned lifestyle factors might not be the greatest contributors to PD development, these factors are modifiable and therefore present a preventative strategy to delay PD onset or attenuate its progression. Another modifiable risk factor for PD is T2D, where a growing amount of evidence suggests the link between both diseases and shared pathophysiology (Athauda et al. 2022). The relationship between PD and T2D will be further discussed in detail in section 1.2.

1.1.3. Neuropathology

The main pathological hallmarks of PD are the progressive loss of dopaminergic neurons particularly in the *substantia nigra pars compacta* (SNpc) region of the basal ganglia and the Lewy pathology that includes misfolded alpha-synuclein (αSyn) protein structures called Lewy bodies and Lewy neurites (Kouli, Torsney, and Kuan 2018).

Selective loss of dopaminergic neurons

Although the selective loss of SNpc dopaminergic neurons is a characteristic PD feature, also other types of neurons undergo neurodegeneration over the course of PD. Brain structural analysis from magnetic resonance imaging (MRI) scans comparing healthy control and PD patient brains has revealed a relatively mild, however, global atrophy of PD brains that occurs already at the early stages of the disease. The structures that are affected and show reduced volume, include the hippocampus, thalamus, brainstem, and subcortical areas (Zeighami et al. 2015, Oltra et al. 2022, Tremblay et al. 2021). However, the distinct feature of PD compared to other neurodegenerative diseases is the loss of neuromelanin-containing dopaminergic neurons in the ventrolateral part of SNpc region in the basal ganglia, which correlates with disease duration (Damier et al. 1999, Fearnley and Lees 1991). These dopaminergic neurons project to the putamen in the striatum, forming the nigrostriatal pathway which is critical in the regulation of voluntary movement (Menegas et al. 2015). The underlying mechanisms of regional selectivity and temporospatial loss of these dopaminergic neurons are not fully understood. However, it is known that SNpc dopaminergic neurons have long projections and complex arborization patterns (Braak et al. 2004). It is estimated that a single SNpc dopaminergic neuron in the human brain has between 1 and 25 million synaptic connections in the striatum (Bolam and Pissadaki 2012). In rat

brain, it was estimated that a single SNpc dopaminergic neuron has about 10 times more synapses in the striatum (100,000 to 250,000) than a single dopaminergic neuron from the ventral tegmental area (VTA) (12,000 to 30,000) and up to 50 times more than a single GABA interneuron, which has approximately 5,000 synapses in the striatum (Bolam and Pissadaki 2012). This unique SNpc dopaminergic neuron morphology and their pacemaking activity can be only sustained by high levels of energy which is generated in the form of adenosine triphosphate (ATP) (Ni and Ernst 2022, Pissadaki and Bolam 2013). It is proposed that the high energy demand of SNpc dopaminergic neurons underlies their selective vulnerability to degeneration. Therefore, any genetic or metabolic cause of energy generation pathway disruption may lead to SNpc dopaminergic neuron death (Ni and Ernst 2022).

Lewy pathology

Lewy pathology is the presence of intraneuronal inclusions that mainly consist of aggregated αSyn (Spillantini et al. 1998). Lewy bodies are found in neuron bodies and are spherical, intracytoplasmic inclusions with a dense core surrounded by irradiating filaments (Shahmoradian et al. 2019). Lewy neurites are abnormal neurites, containing αSyn filaments (Spillantini et al. 1998, Braak et al. 1999). Aggregation of αSyn and Lewy pathology formation has been considered one of the driving mechanisms of neurodegeneration. However, the molecular processes that trigger αSyn aggregation are poorly understood. (Mahul-Mellier et al. 2020). It is also known that besides misfolded αSyn, Lewy bodies contain lipids, membranous organelles and ubiquitin that suggest more complex molecular interactions mediating Lewy pathology, than simply αSyn aggregation (Gai et al. 2000, Mahul-Mellier et al. 2020).

1.1.4. Pathogenesis

Multiple mechanisms have been associated with PD onset and progression. These mechanisms mainly include the failure of cellular processes that are responsible for the maintenance of sufficient energy levels and clearance of misfolded proteins leading to the neuropathology of the PD. In addition, neuroinflammation, triggered by pathophysiological events is shown to contribute to PD progression. The proposed 'multiple hit hypothesis' suggests that it is rather a combination of numerous insults that converge leading to neural death (Sulzer 2007). Some of those hits such as particular mutations or prenatal exposure to toxins might already occur at the early neurodevelopment stage and contribute to PD development later in life (Schwamborn 2018, Thiruchelvam et al. 2002).

Mitochondrial dysfunction

Mitochondria are the so-called powerhouse of the cell. It is a double-membrane-bound organelle which generates most of the cellular energy in the form of ATP (Brand et al. 2013). Mitochondrial dysfunction can be a consequence of mitochondrial biogenesis impairment, increased levels of reactive oxidative species (ROS), deficient mitophagy, disrupted mitochondrial dynamics, calcium (Ca^{2+}) imbalance, compromised electron transport chain (ETC) functionality, or mitochondrial DNA alterations (Prasuhn, Davis, and Kumar 2020). The reason why mitochondrial dysfunction is one of the key mechanisms in PD is the immense ATP needs of the long, complex dopaminergic neurons of the SNpc. Moreover, several of the genes responsible for genetically inherited PD, are linked to mitochondrial homeostasis, providing strong evidence of mitochondrial dysfunction role in PD. For instance, PINK1 and Parkin are involved in mitochondria quality control and regulation of damaged mitochondria removal through mitophagy (Ge, Dawson, and Dawson 2020). DJ1 has a neuroprotective role by eliminating ROS, protecting mitochondria from damage and preventing cells from ROS-induced cell death (Taira et al. 2004). The main source of ROS is SNpc dopaminergic neuron accelerated metabolism. Moreover, in dopaminergic neurons, additional ROS is produced during the dopamine oxidation process catalyzed by the mitochondrial enzyme monoamine oxidase (MAO) (Mita et al. 2018). The excess of ROS leads to detrimental effects such as DNA damage, lipid peroxidation and protein oxidation with functional consequences (Sabari et al. 2023). Also, in the case of LRRK2 mutations, which is the most common cause of monogenic PD forms and one of the most common causes of sporadic PD, mitochondrial defects have been observed. It is proposed that mutations in LRRK2 (G2019S and R1441C) alter Ca^{2+} homeostasis and depolarization-induced mitophagy (Wauters et al. 2020). Moreover, PINK1, VPS35, Parkin and SNCA mutations affect mitochondrial complex I (MCI) functionality (Grunewald, Kumar, and Sue 2019). MCI is the first enzyme of the ETC and its inhibition is linked to reduced levels of ATP and elevated ROS production (Bose and Beal 2016). Furthermore, Parkin is known to affect mitochondrial DNA transcription (Grunewald, Kumar, and Sue 2019).

Apart from mutations in PD-associated genes, mitochondrial damage can result from toxin exposure. An increased interest in the mitochondria role in PD started with the observation of drug 1-methyl-4-phenyl-1,2,3,4-tetrahydropyridine (MPTP) triggered inhibitory effects on MCI leading to PD motor symptoms and selective loss of SNpc dopaminergic neurons. Other toxins, such as the pesticide rotenone, also inhibit MCI (Nonnekes et al. 2018). Importantly, reduced activity of MCI has been found in tissue isolated from idiopathic PD patients (Flones et al. 2018, Schapira et al. 1990). However, it is still under debate whether MCI dysfunction is a cause or consequence of PD-associated neurodegeneration (Subrahmanian and LaVoie 2021). In addition,

recent GWAS of sporadic PD has identified several genes linked to mitochondria function that are associated with increased PD risk, providing further evidence of mitochondrial dysfunction relevance in PD (Billingsley et al. 2019, Navarro et al. 2021).

Lipidome alterations

Lipids are heterogeneous molecules with a variety of important functions in the central nervous system (CNS). They act as bioactive signaling molecules, ensure cell membrane structural integrity and participate in energy metabolism as substrates for energy generation or energy storage sources (Tracey et al. 2018). The importance of lipids is reflected in the fact that brain lipid content is the second highest in the human body after adipose tissue, which constitutes about 50% of the brain's dry weight (Hamilton et al. 2007). Lipid classes such as cholesterol and sphingolipids are crucial in brain development, neurogenesis, and synaptogenesis. In addition, cholesterol plays a role in axon regeneration processes after nerve injury (Hussain et al. 2019). The role of lipids in the CNS extends to myelin formation ensuring efficient transmission of electrical impulses (Poitelon, Kopec, and Belin 2020). Although SNpc dopaminergic neurons are mostly unmyelinated, myelin is crucial to ensure neural plasticity and proper interactions throughout the brain (Braak and Del Tredici 2004). Multiple PD-associated mutations, such as GBA, VPS35 and PINK1 are involved in lipid metabolism, and mutations in these genes can alter cellular lipid composition (Franks et al. 2008, Navarro-Romero et al. 2022, Flores-Leon and Outeiro 2023). Furthermore, a recent study of serum and cerebrospinal fluid (CSF) lipid profiles from LRRK2-G2019S mutation-carrying PD patients revealed altered sphingolipid and glycerophospholipid metabolism, indicating changed lipid homeostasis as a potentially common PD-associated pathogenic mechanism (Galper et al. 2022). Disruption of lipid homeostasis is strongly associated with neurodegeneration mainly through mechanisms that involve endoplasmic reticulum (ER) stress, mitochondrial dysfunction, and pro-inflammatory responses (Flores-Leon and Outeiro 2023). Moreover, Lewy bodies are enriched with lipids suggesting lipid alterations might have role in aSyn aggregation and the formation of Lewy bodies (Shahmoradian et al. 2019).

aSyn aggregation

The protein aSyn is small, natively unfolded, abundantly found in presynaptic terminals, and involved in neurotransmitter release by regulating synaptic vesicle cycling (Wang et al. 2014, Sharma and Burre 2023). In the course of PD, aSyn changes its conformation, from a soluble monomer to insoluble amyloid fibrils that spread throughout the brain (Hijaz and Volpicelli-Daley 2020). Moreover, preformed fibrils recruit monomeric aSyn for further aggregate formation, thus

reducing overall levels of functional aSyn pools and reducing synaptic activity and neural functionality (Volpicelli-Daley et al. 2011). Duplication and triplication of the SNCA gene, encoding the aSyn protein is known to cause hereditary early-onset PD (Chartier-Harlin et al. 2004). In addition, GWAS have identified variations in the SNCA locus relevant for sporadic PD cases (Simon-Sanchez et al. 2009, Satake et al. 2009). As shown in animal and cellular models, genetic variants of SNCA result in increased levels of aSyn and reduced amount of dopaminergic neurons (Oliveira et al. 2015, Kilpelainen et al. 2019). It is also shown that aSyn modulates autophagy, which is one of the main mechanisms of aSyn inclusion clearance (Tang et al. 2021, Oliveira et al. 2015, Gao et al. 2019). Currently, there is uncertainty in the field regarding the toxicity of aSyn fibrils and transient oligomers. A common opinion is that oligomers are more toxic to the neurons than fibrils. It has been shown that oligomers exert cytotoxicity by binding to lipid bilayers and disrupting their integrity (Fusco et al. 2017, Cascella et al. 2021, Winner et al. 2011). However, higher toxicity of aSyn fibrils has been proposed in mice models, observing that fibrils alone can propagate aSyn pathology (Volpicelli-Daley et al. 2011).

Impairment of protein clearance

Protein misfolding and aggregation are common pathological mechanisms of multiple neurodegenerative diseases, including PD (Ebrahimi-Fakhari, Wahlster, and McLean 2012). In the case of PD, it is the aggregation of the aSn protein which is implicated in the disease pathology. In neurons, there are two major proteolytic systems – the ubiquitin-proteosome system (UPS) and autophagy, which are responsible for protein turnover and clearance of altered proteins (Ebrahimi-Fakhari, Wahlster, and McLean 2012). UPS first marks target proteins by ubiquitin covalent binding, which serves as a signal for proteosome for target protein degradation (Ebrahimi-Fakhari, Wahlster, and McLean 2012). One of the monogenic forms of PD, involving Parkin, which is an E3 ligase, is also linked to UPS dysfunction (Um et al. 2010). Moreover, it has been reported that gene expression levels and proteasomal enzymatic activity are changed in sporadic PD brains, with reduced levels of several proteasome components particularly in the SNpc region (McNaught et al. 2003, Grunblatt et al. 2004).

On the other hand, autophagy is responsible for protein and defective organelle degradation in lysosomes. Targets of degradation are first engulfed by autophagosomes and then transported to the lysosome (Ebrahimi-Fakhari, Wahlster, and McLean 2012). Mutation in the GBA gene which encodes the lysosomal enzyme glucocerebrosidase (GCase), is known to cause lysosome dysfunction (Do et al. 2019). Lysosome defects are shown to increase levels of aggregated aSyn (Navarro-Romero et al. 2022). It has also been reported that high levels of aSyn impair lysosomal function by changing lysosomal Ca^{2+} levels and pH (Nascimento et al. 2020). Another mutation

that has been linked to autophagy impairment is the LRRK2-G2019S, which particularly inhibits chaperone-mediated autophagy (Orenstein et al. 2013). Since the GBA and LRRK2 mutations are very common among PD patients, the impairment of protein clearance and therefore compromised aSyn aggregate degradation might have an important role in numerous PD cases.

Neuroinflammation

While acute inflammation usually is neuroprotective against injuries, toxins or infections, chronic inflammation is associated with the development of neurodegeneration (Kwon and Koh 2020). The causes of chronic inflammation include aging, protein aggregates, chronic infection, and genetic factors. The immune response is mediated by microglia and astrocytes by secretion of cytokine, chemokines, and trophic factors, however, a persistent response results in oxidative stress that can damage neurons (Isik et al. 2023). Microglia are the resident immune cells of the brain and higher levels of reactive microglia have been observed in PD patient brains (McGeer et al. 1988, Doorn et al. 2014). Several genes have been identified as causative of microglia dysfunction that could contribute to the pathology of PD (Lopes et al. 2022, Andersen et al. 2021). Furthermore, astrocytes, the brain's most prevalent cell type, and primary support cells for neurons, have also been associated with neuroinflammation. Some of the genes responsible for monogenic PD have been identified as highly expressed in astrocytes, and mutations in these genes, for instance, DJ1, and LRRK2, alter astrocyte inflammatory responses (Booth, Hirst, and Wade-Martins 2017, Streubel-Gallasch et al. 2021). Lately, there has been an increasing interest in glial cell senescence. Senescent microglia and astrocytes not only lose their immune competence but also, present a specific senescence-associated secretory phenotype. This secretome includes a variety of cytokines and chemokines, which can be toxic to the surrounding cells, including dopaminergic neurons (Russo and Riessland 2022, Preininger and Kaufer 2022).

1.1.5. Modeling Parkinson's disease

To better understand different aspects of PD, several models have been developed over the years to recapitulate disease pathology and develop potential therapeutic strategies.

Animal models

Rodent, non-human primate, or non-mammalian species models have been used to study the systemic effect of genetic mutations or toxin exposures. Neurotoxin-based approaches include animal exposure to 6-OHDA, MPTP, and agrochemicals such as rotenone, and paraquat. Genetic-based approaches include transgenic and viral vector-mediated models usually based on genes associated with monogenic PD. PD-associated aSyn pathology can be achieved by SNCA overexpression or an introduction of αSyn-preformed fibrils directly into the brain of an animal

(Konnova and Swanberg 2018). However, transcriptomic and metabolomic differences between species as well as specific brain characteristics do not allow full translation of results from animal models to humans (Pembroke, Hartl, and Geschwind 2021, Potashkin, Blume, and Runkle 2010). Additionally, ethical concerns limit animal model use in research.

Postmortem samples

Postmortem samples of the human brain have been irreplaceable for definitive PD diagnosis and characterization of the end-stage of the disease (Signaevsky et al. 2022). However, postmortem tissue does not allow us to explore disease progression and does not provide answers as to whether observed pathological changes are the cause or consequence of neuron death (Hartmann 2004). Donor recruitment and tissue collection as well as appropriate tissue preservation are essential limiting factors that still lack a standardized approach worldwide (Shepherd, Alvendia, and Halliday 2019).

Monolayer cellular models

There have been a variety of cellular models used for PD modeling. For instance, immortalized cell lines, such as the neuroblastoma cell line SH-SY5Y and the pheochromocytoma cell line PC12, develop neuron-like properties and can be relatively easily used for genetic manipulations or viral transduction (Xicoy, Wieringa, and Martens 2017). Primary neurons isolated from rodents are more physiologically relevant, however, also more difficult to maintain in the culture (Falkenburger, Saridaki, and Dinter 2016). Human primary cells such as skin fibroblasts are easily accessible and present a robust model. Fibroblasts can provide insights into patient-specific cellular dysfunctions, however, they fail to demonstrate neuron-specific pathogenic processes (Auburger et al. 2012).

The discovery of induced pluripotent cells (iPSCs) enabled human somatic cell reprogramming to stem cells which can be further differentiated towards any cell type (Takahashi and Yamanaka 2006). iPSC-derived dopaminergic neurons have been generated based on midbrain development principles during embryogenesis (Arenas, Denham, and Villaescusa 2015). Dopaminergic neuron generation first requires iPSC guidance to the neuroectoderm fate through the inhibition of SMAD signaling, which includes the bone morphogenetic protein (BMP), and members of the transforming growth factor β (TGFβ) protein family (Chambers et al. 2009). Midbrain dopaminergic lineage is then specified by activation of sonic hedgehog (SHH), wingless-related integration site (WNT) and fibroblast growth factor (FGF) 8 signaling (Arenas 2014). Further differentiation of dopaminergic neurons is achieved by the addition of neurotrophic factors, such as the brain-derived neurotrophic factor (BDNF) and glia-derived neurotrophic factor (GDNF)

(Galet, Cheval, and Ravassard 2020). iPSC-derived dopaminergic neurons enable the investigation of PD mechanisms on a patient-specific genetic background in the cell type that is particularly vulnerable in PD. Nevertheless, it is still a rather simple model system and does not reflect more systemic aspects of PD in terms of cellular interactions (Ferrari et al. 2020, Avazzadeh et al. 2021).

Midbrain organoids

A further recent advancement in iPSC technology are the so-called organoids. Organoids are self-organized three-dimensional (3D) cellular models that aim to recapitulate *in vivo* tissue complexity (Figure 1.3.) (Yin et al. 2016). Organoids usually contain multiple tissue-specific cell types that enable the investigation of cellular interactions during tissue development as well as in healthy and diseased states. The first protocol of cerebral organoid generation and their application in disease modeling of microcephaly was published in 2013 by Lancaster and colleagues (Lancaster et al. 2013). Lancaster's approach was based on unguided differentiation, which resulted in high variability and low reproducibility. Over recent years organoid technology has been advanced and more regional-specific brain organoid protocols have been developed using region-specific patterning factors to guide cell fate towards cellular identities of the the desired brain region (Lee et al. 2017). Guided protocols have been developed to generate, for instance, cortical tissue (Qian et al. 2020), midbrain (Jo et al. 2016), cerebellum (Muguruma et al. 2015), hippocampus and choroid plexus (Sakaguchi et al. 2015) organoids.

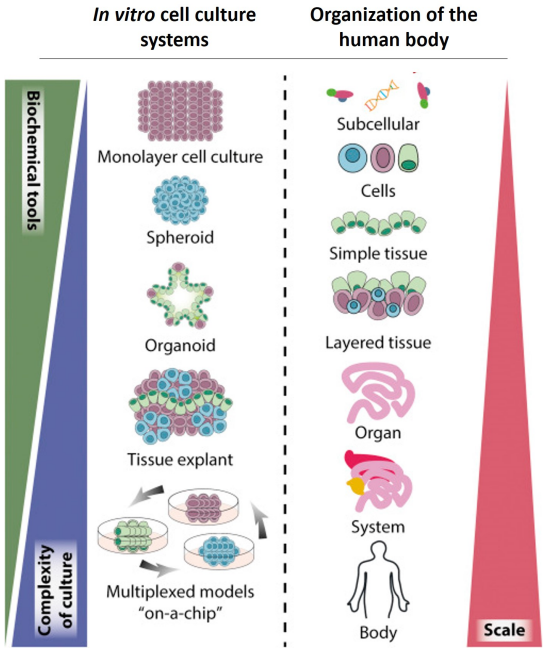

Figure 1.3. The complexity of *in vitro* model systems compared to the cellular organization in the human body. Organoids represent a good compromise between the complexity of the model and experimental limitations (Adapted from Yin et al., 2016).

In the context of PD, midbrain organoids are of high relevance since the main hallmark of PD is the loss of dopaminergic neurons in the midbrain region. To further increase the regional specificity, midbrain organoid generation can be initiated from fate-restricted neural progenitor cells that efficiently differentiate into neural tube lineage cells, including midbrain dopaminergic neurons (Reinhardt et al. 2013). Neuroepithelial stem cells (NESCs) described in Reinhardt et al., are generated from iPSCs through embryoid bodies. The neural induction is achieved by stimulation of WNT and SHH signaling pathways. The main advantages of NESCs are that they are easy to handle, easy to expand and they can robustly differentiate into dopaminergic neurons (Reinhardt et al. 2013). The efficiency in midbrain organoid generation from NESCs has been shown in protocols developed in our group (Monzel et al. 2017, Nickels et al. 2020, Smits et al. 2019). It has also been shown that midbrain organoids besides dopaminergic neurons include other neural cell types, as well as astrocytes and oligodendrocytes (Monzel et al. 2017, Smits et al. 2020, Zagare et al. 2022). Furthermore, midbrain organoids demonstrate electrophysiological activity, and the presence of functional synaptic connections (Monzel et al. 2017). These advantageous properties of midbrain organoids demonstrate their great potential in PD modeling, yet the lack of vasculature and immune cells urges further model development.

1.2. The link between Parkinson's disease and Type 2 Diabetes

Type 2 Diabetes is a chronic condition characterized by increased blood glucose and insulin resistance. T2D is classified as a lifestyle disease with a global prevalence above 10% (Sun et al. 2022, Kotwas et al. 2021). The incidence of T2D is increasing with aging, however, the number of younger patients (<40 years) is dramatically growing (Xie et al. 2022). T2D has been named one of the top public health priorities since it is linked to severe complications and disability and is one of the common causes of death in developed countries (Kotwas et al. 2021, Bergman et al. 2012). Since T2D is a complex and systemic disease it shares common dysregulated pathways with other pathologies. Hence, T2D is associated with an increased risk of developing cancer, cardiovascular diseases, as well as neurodegenerative diseases, including PD (Rahman, Athar, and Islam 2020, Ma et al. 2022, Athauda et al. 2022, Barbagallo and Dominguez 2014). Considering alarming epidemiological data, it is crucial to understand molecular mechanisms underlying the comorbidities of T2D. Here we focus on the shared pathophysiological mechanisms between T2D and PD, with an attempt to understand through which pathways T2D contributes to the development and progression of PD-associated neurodegeneration.

1.2.1. Epidemiological evidence

A growing number of epidemiological data support the link between T2D and PD. Comorbid T2D is associated with more drastic motor symptoms and cognitive decline in PD (Athauda et al. 2022). Multiple studies, analyzing patient data from large cohorts ranging from several thousand up to millions of participants, have reported significantly increased incidence of PD among T2D patients compared to the reference cohorts (Pezzoli et al. 2023, Han et al. 2023, De Pablo-Fernandez et al. 2018, Aune et al. 2023, Chohan et al. 2021). Hazard ratios in these studies ranged from 1.09 to 1.64, meaning that T2D patients on average have a 37% increased risk of developing PD. In the same studies, it was observed that T2D patients with more complications and earlier onset reach even a threefold higher risk of developing PD. Furthermore, it has been reported that also prediabetes increases the risk of PD development (Aune et al. 2023, Sanchez-Gomez et al. 2021). Both T2D and prediabetes, are associated with reduced cognitive function in PD (Park, Choi, and Kim 2023, Bohnen et al. 2014, Pagano et al. 2018). In addition, T2D has been shown to accelerate the progression of PD-related motor symptoms (Kotagal et al. 2013, Pagano et al. 2018, Athauda et al. 2022)

Additional evidence that both diseases are linked is proposed by the observed beneficial effect of antidiabetic drugs on PD symptoms and even PD delay. Pezzoli and colleagues report that antidiabetic treatment delays PD onset for about 6 years (Pezzoli et al. 2023). Another study showed a lower incidence of PD cases in the T2D patient group that received antidiabetic therapy compared to patients with untreated T2D (Brauer et al. 2020). Moreover, PD incidence among T2D patients as well as PD symptom severity significantly depends on the received antidiabetic treatment (Brauer et al. 2020, Wang et al. 2020).

Altogether, epidemiological evidence suggests shared pathophysiological mechanisms through which T2D contributes to the development and progression of PD. Moreover, antidiabetic therapy demonstrates preventative and PD-modifying potential.

1.2.2. Molecular links

There are several common pathophysiological mechanisms proposed between T2D and PD, including insulin signaling dysregulation, protein misfolding, oxidative stress linked to mitochondrial dysfunction, inflammation and altered lipid metabolism (Figure 1.4.) (Sabari et al. 2023, Zhang et al. 2020).

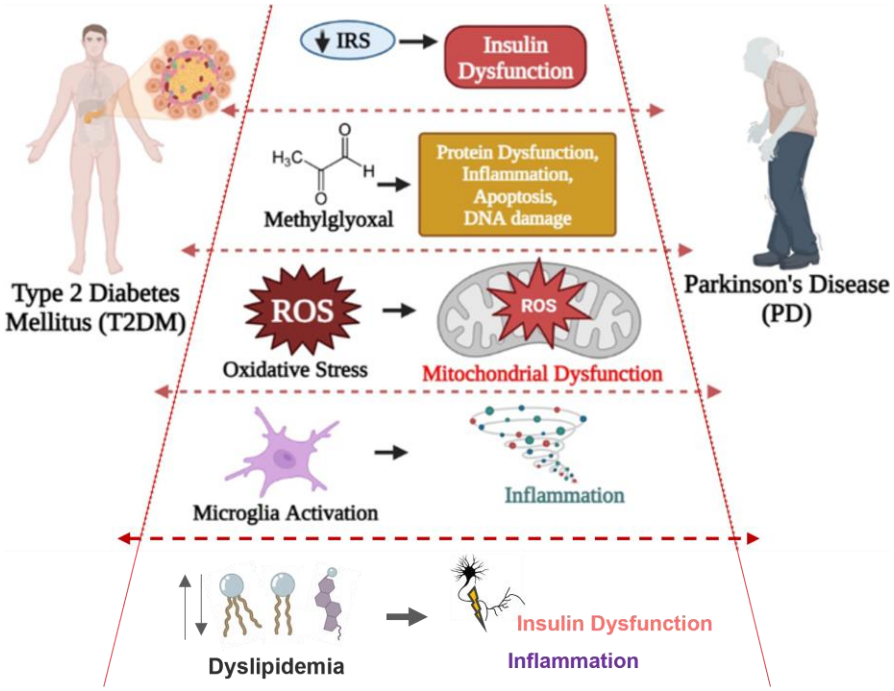

Figure 1.4. Proposed shared disease mechanisms that underly comorbidity of T2D and PD (Adapted from Sabari et al., 2020).

Insulin signaling function and dysfunction in the brain

Insulin is produced by the pancreatic β-cells in response to glucose increase in blood. Persistent hyperglycemia, results in a constantly high insulin concentration in blood and tissue overstimulation. As a result, tissue becomes irresponsive and develops insulin resistance. Insulin resistance is the main hallmark of prediabetes and T2D (Khan et al. 2019). In addition, constant insulin secretion promotes pancreatic β-cell dysfunction (Cerf 2013). Due to insulin resistance, cells are not able to uptake glucose, which is the main energy substrate of the cells. Glucose stays in the blood causing cardiovascular complications, retinopathy, renal failure, neuropathy, and impaired wound healing resulting in infections (Khan et al. 2019). However, insulin signaling is not restricted to the regulation of glucose uptake. It is a complex signaling pathway, which besides cellular metabolism, regulates other crucial cellular functions, such as protein synthesis via mammalian target of rapamycin (mTOR), protein phosphorylation via glycogen synthase kinase 3 (GSK3β), gene expression via forkhead box-containing protein O subfamily (FOXO) transcription factors and Ras/ERK branch as well as cell survival via B-cell lymphoma 2 (BCL-2) protein family members (Figure 1.5.) (De Meyts 2000, Batista, Haider, and Kahn 2022). Although insulin signaling has pleiotropic effects, not all downstream pathways are affected in all tissues. The biological outcomes of insulin signaling depend on tissue type and physiological context (Batista, Haider, and Kahn 2022).

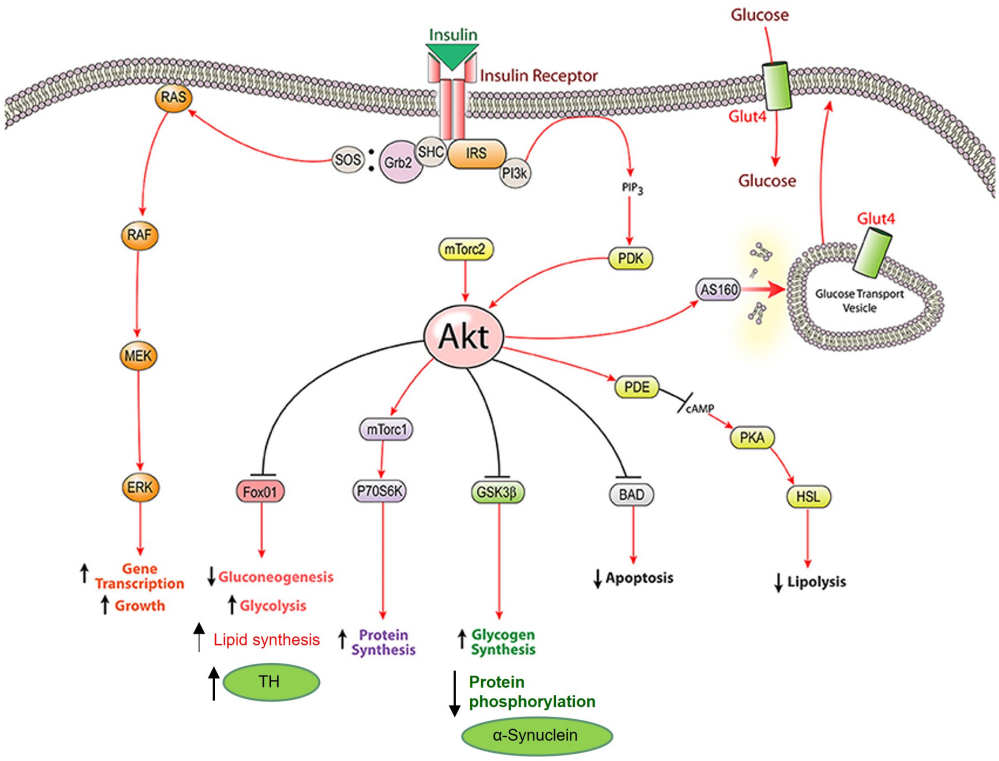

Figure 1.5. Simplified representation of insulin signaling pathway. Insulin binding to the insulin receptor triggers phosphorylation of insulin receptor substrate – IRS for activation of the PI3K/AKT signaling cascade and SHC for activation of Ras/ERK signaling cascade (Adapted from Grote and Wright, 2016).

Less is known about specific insulin functions in the brain. For many years the brain has been considered an insulin-independent organ. This assumption was mainly based on the glucose uptake pattern in the brain which in most of the brain areas occurs in an insulin-independent manner through the glucose transporters GLUT1, GLUT3, GLUT6 and the Na^+/glucose cotransporter SGLT1 (Milstein and Ferris 2021, Koepsell 2020). A crucial finding was the observation of insulin receptor ubiquitous expression throughout the brain (Hopkins and Williams 1997). Since then, the insulin-dependent GLUT4 and GLUT8 transporters have also been proven to be present in the brain (Doege et al. 2000, El Messari et al. 1998). It has been proposed that GLUT4 may enable rapid high-affinity glucose uptake for neurons with extremely high energy requirements. So far, this has been only studied in the context of hippocampal neurons and their cognitive activity (Emmanuel et al. 2013). However, SNpc dopaminergic neurons also have a complex architecture that determines their high energy needs. Moreover, based on animal studies, GLUT4 is expressed in multiple brain regions, including basal ganglia, which includes the nigrostriatal pathway and further suggests that SNpc dopaminergic neurons might be equipped with insulin-dependent GLUT4 (Leloup et al. 1996, El Messari et al. 1998). At the same time, this would mean that they are vulnerable to insulin signaling impairment and insulin resistance.

It has been shown that insulin plays an important role in the CNS. It regulates such crucial processes as neural development, neurotransmission, cognitive function, and nutrient homeostasis in the CNS as well as in the periphery by regulating appetite and energy storage (Gray, Meijer, and Barrett 2014). In addition, insulin has neurotrophic and neuroprotective properties (Duarte, Moreira, and Oliveira 2012). Nevertheless, insulin routes in the CNS are still unclear. In mice models, it has been demonstrated that insulin crosses the blood-brain barrier (BBB) by insulin receptor-mediated transport or even independently (Rhea, Rask-Madsen, and Banks 2018, Konishi et al. 2017). In humans, it has been shown that insulin concentration increases in CSF after peripheral insulin infusion, demonstrating that insulin can enter the CSF from the peripheral blood (Wallum et al. 1987). However, insulin concentration detected in the CSF compared to blood insulin concentration is about 80-90% lower, and might not be sufficient to significantly activate the signaling cascade (Gray and Barrett 2018). This suggests higher insulin receptor sensitivity in the brain compared to their counterparts in the periphery or a local insulin source. As reviewed by Dakic and colleagues, immunoreactive insulin has been found in neural cultures of mouse, rat and rabbit origin (Dakic et al. 2023). In human postmortem samples insulin and its cleaved C-peptide presence have been also observed (Dorn et al. 1983). Although at very low levels, the insulin gene (INS) is expressed in the human brain, further supporting local insulin synthesis in the CNS. Interestingly, the INS gene clusters together with dopamine rate limiting enzyme tyrosine hydroxylase (TH) and insulin-like growth factor2 (IGF2) genes on chromosome 11 with possible shared regulatory mechanisms. Although the expression of these genes is cell type-specific, they show some degree of coordinated expression upon glucose concentration increase as observed in human pancreatic islet cultures (Mutskov and Felsenfeld 2009). Interestingly, in PD patient postmortem samples, it has been observed that particularly TH expressing dopaminergic neurons of the SNpc are positive to insulin resistance markers, compared to other neurons, glia and microglia (Bassil et al. 2022). Overall, considering the importance of insulin in the CNS as well as its local and peripheral origin, both systemic or local insulin resistance or even defective insulin signaling would affect brain function and might predispose to neurodegenerative disease development.

Lipid metabolism

Insulin signaling plays a role in the regulation of lipid homeostasis by the activation of sterol-regulatory-element-binding protein (SREBP) (DeBose-Boyd and Ye 2018). SREBPs are transcription factors required for the synthesis of unsaturated fatty acids and cholesterol, which are both important components of cell membranes and precursors for numerous biologically active molecules. The brain contains about 25% of the total cholesterol found in the human body

(Bjorkhem and Meaney 2004). Importantly, brain cholesterol levels are independent of those in the periphery since cholesterol uptake from circulation is prevented by the BBB. Therefore, particularly in the brain appropriate insulin action is crucial to ensure cholesterol homeostasis, since cholesterol is involved in neurodevelopment, synapse formation and myelin synthesis (Suzuki et al. 2010). It is believed that hyperinsulinemia, which precedes insulin resistance, overstimulates SREBPs, resulting in accelerated lipogenesis and subsequential accumulation of lipids. Additionally, lipid level increase is caused by high-fat diet usually characteristic for T2D patients (Shetty and Kumari 2021). T2D-associated dyslipidemia includes increased fasting triglycerides (TG), decreased levels of high-density lipoprotein cholesterol and increased levels of low-density cholesterol (Yanai, Hirowatari, and Yoshida 2019). Free fatty acids released from TGs, can potentiate insulin resistance, and modulate inflammatory responses (Boden 2003, Shetty and Kumari 2021). Palmitic acid (C16:0), which is one of the most abundant dietary and plasma fatty acids, has been particularly associated with lipotoxicity. When palmitic acid levels exceed the mitochondrial β-oxidation capacity, it is used in the synthesis of deleterious complex lipids, such as diacylglycerides and ceramides (Palomer et al. 2018). Ceramides are known to dephosphorylate the central protein of insulin signaling – AKT, thus modulating AKT downstream effects (Schubert, Scheid, and Duronio 2000, Ghosh et al. 2007). This pathogenic mechanism can be aggravated in case of PD-associated mutations in the GBA gene, which leads to the accumulation of glucosylceramides, and are antagonists of insulin signaling (Chavez et al. 2014). Moreover, ceramides are associated with an increased pro-inflammatory response, which in case of PD would accelerate the existing immune response (Hammerschmidt and Bruning 2022).

Mitochondrial dysfunction/oxidative stress

Mitochondrial dysfunction and particularly impaired MCI functionality have been associated with PD pathophysiology (elaborated in section 1.1.4.) Similarly, altered mitochondrial morphology and decreased activity of MCI have been observed in T2D patient skeletal muscle depending on the degree of insulin resistance (Kelley et al. 2002). Interestingly, MCI exhibits hyperactivity in pancreatic cells as shown in the diabetic rat model (Wu et al. 2017). MCI is the major ROS generation site, therefore, any dysfunction of this enzyme is strongly linked to increased ROS production (Guo et al. 2013). Most of the ROS are byproducts of mitochondrial energy metabolism (Sergi et al. 2019). It has been suggested that ROS can phosphorylate insulin receptor substrate (IRS) at serine residues, which leads to IRS degradation and insulin signaling inhibition (Evans, Maddux, and Goldfine 2005). Increased ROS can also further damage the mitochondrial respiratory complex and induce mitochondrial DNA mutations amplifying mitochondrial damage and ROS production (Guo et al. 2013). Apart from mitochondria, another source of ROS is caused

by chronic hyperglycemia-induced glucose autoxidation, formation of advanced glycation products (AGEs) and glucose metabolism through glycolysis side pathways, such as polyol, protein kinase C and the hexosamine pathways, all resulting in additional ROS production (Sabari et al. 2023, Gonzalez et al. 2023). T2D-induced ROS contribute to the exhaustion of antioxidative mechanisms and ultimately results in oxidative damage. Due to the high abundance of polyunsaturated fatty acids, the brain is particularly susceptible to ROS-induced lipid peroxidation which leads to fatty acid intensified degradation and loss of cell membrane integrity, contributing to neural damage (Ayala, Munoz, and Arguelles 2014). Moreover, the decomposition of peroxidized lipids, results in the formation of reactive metabolites, such as aldehydes, which can further modify other molecules. Specifically, dopamine is prone to oxidation, and it has been shown that brain polyunsaturated fatty acid-derived dopamine adducts trigger apoptosis *in vivo* and *in vitro* (Liu et al. 2008), which might be a relevant mechanism in PD pathogenesis.

Protein misfolding

Both PD and T2D belong to protein misfolding diseases. Pancreatic islet amyloid polypeptide (IAPP) is the major component of amyloid deposits in pancreatic β-cells, while αSyn is prone to aggregation in PD. IAPP aggregation precedes dysfunction of β-cells and has been observed in more than 90% of T2D cases (Mukherjee et al. 2017). Interestingly, αSyn is highly abundant in pancreatic cells and has been found in β-cell amyloid deposits along with IAPP (Mucibabic et al. 2020). Similarly, IAPP co-deposits with αSyn have been identified in the brains of PD patients (Meng et al. 2023). The physiological function of IAPP is to regulate glucose homeostasis and blood pressure via the renin-angiotensin system (Raimundo et al. 2020). In addition, IAPP can cross BBB to activate noradrenergic neurons in the brainstem regulating the appetite (Schultz et al. 2019). IAPP is co-secreted with insulin in response to increased glucose concentration in the blood, meaning that IAPP levels are elevated in T2D, increasing the risk for aggregate formation. Studies show that IAPP promotes αSyn fibril formation and vice versa (Mucibabic et al. 2020, Galper et al. 2022). The cross-seeding and formation of heterologous fibrils can enhance the progression of both T2D and PD. Moreover, T2D-associated chronic hyperglycemia leads to the formation of AGEs, which are nonenzymatically glycated proteins and lipids (Prasad et al. 2019). Glucose itself has lower reactivity than byproducts of glucose metabolism. The most reactive glycating agent is methylglyoxal (MGO) (Vicente Miranda, El-Agnaf, and Outeiro 2016), which is responsible for structural and functional protein changes and impairment of protein clearance (Sirangelo and Iannuzzi 2021). In PD cellular models it has been shown that MGO potentiates αSyn aggregation (Miranda et al. 2021). Moreover, AGEs have been detected in Lewy bodies found in PD patient postmortem brains (Münch 2000), confirming the role of glycation in αSyn pathology.

Inflammation

Chronic inflammation is a common pathogenic mechanism of PD and T2D. T2D-mediated toxic lipid accumulation, protein aggregation and formation of AGEs accelerate microglia performance and exacerbate inflammatory responses (Sabari et al. 2023). In animal models, it has been shown that T2D trigger inflammation in the CNS by activation of astrocytes and microglia (Nagayach, Patro, and Patro 2014, Hwang et al. 2014). T2D's contribution to neuroinflammation can accelerate neural damage and thus worsen the course of PD.

1.2.3. Challenges of modeling Type 2 Diabetes *in vitro*

Most of the knowledge about the role of insulin in the CNS has been acquired from animal models. However, it is known that physiological insulin levels in rodent blood and CSF are greater than in humans, suggesting species-dependent differences in the development of insulin resistance and T2D (Rhee et al. 2013). Furthermore, many relevant results regarding insulin concentration in CSF and GLUT4 distribution in the brain have been described in studies that date back to the 80s and 90s. There is a lack of more recent studies on human samples or subjects addressing the role, transport, and functionality of insulin in the CNS.

Human iPSC-derived cellular models hold great potential in modeling some of these aspects, however, iPCS-derived neuronal cell culture media similar to any other *in vitro* base media is far from the *in vivo* cellular environment representation. The standard media for cell culture contain extremely high insulin (~400nM) and glucose (~21.25mM) concentrations. Moreover, most of the amino acid concentrations exceed the physiological levels to ensure cell viability and growth *in vitro.* Eventually, cells are cultured under conditions that are diabetic. The standard cell culture media was defined in the 1950s and has not been significantly modified since then (Eagle 1959, Golikov et al. 2022). The initial media contained 5.5mM glucose, however, the concentration was later increased to support the growth of cancer cells *in vitro* and was not much optimized for cell-type specific cultures (Golikov et al. 2022). Currently, neuronal cultures are maintained in media containing high levels of glucose (21.25mM) and supplemented with neurotrophic additives containing a high dosage of insulin to support neuronal growth and viability. A study on insulin concentration effects on human and rodent neural culture showed that human-origin neural stem cells are highly sensitive to insulin concentration changes. Significant cell death was observed in cultures maintained without insulin as well as in cultures maintained in high insulin concentration, where cells also displayed insulin resistance phenotypes. At the same time rodent origin neural stem cell cultures were not affected by high insulin concentration (Rhee et al. 2013). Also, glucose concentration in the current neural basal media can be optimized. The *BrainPhys* medium specifically developed to increase the neural activity of iPCS-derived neuron cultures, contains 2.5

mM glucose (physiological concentration in healthy brains) and optimized levels of amino acids and inorganic salts (Bardy et al. 2015). However, most of the T2D studies *in vitro* are based on short glucose concentration changes from already prediabetic or diabetic to even higher glucose concentration. For instance, studies of glucose concentration change *in vitro* neural cultures for up to 48h with a glucose concentration increase of up to 60 mM demonstrate that hyperglycemia-induced ROS alters neural functionality and increases apoptosis (Singh, Jain, and Sharma 2013, Kumar et al. 2017, Vincent et al. 2005). Although these studies recapitulate short-term, extreme consequences, they fail to represent the full T2D pathophysiology and long-term effects.

Overall, nonphysiological media can interfere with cell metabolic and signaling processes, complicating *in vitro* disease modeling whilst also reducing *in vitro* study reproducibility and clinical translation (Golikov et al. 2022). On the other hand, diabetic conditions might increase the aging-phenotype in cultured cells, which is relevant for age-related diseases, such as PD, but is missing in iPSC-derived models since cells are rejuvenated during the reprogramming process.

2. Summary and Discussion of the results

This section summarizes relevant results presented in the included manuscripts (see Chapter 3) with a focus on midbrain organoid validation for *in vitro* PD modeling, LRRK2-G2019S and GBA-N370S genetic risk variant contribution to neurodevelopmental impairment and insulin resistance role in PD.

2.1. Midbrain organoid similarity to the human midbrain

Midbrain organoids have successfully been used to study PD (Monzel et al. 2020, Smits et al. 2019). In this thesis, in **Manuscript I, Manuscript II, and Manuscript III,** midbrain organoids are also used to investigate PD-relevant phenotypes and risk factor roles in the development of PD. Particularly, in **Manuscript I**, to evaluate the physiological relevance of midbrain organoids, we compare single-cell RNA expression data from 35 and 70 days old midbrain organoids generated in our lab (Smits et al. 2020) to six - eleven weeks old human embryonic midbrain samples (La Manno et al. 2016). We demonstrate that the transcriptomic profile and cellular composition of 35 days old midbrain organoids highly resemble week 9, while 70 days old midbrain organoids resemble week 10 of the human embryonic midbrain (**Manuscript I Figure 1C**). Usually, experiments with midbrain organoids are performed around these time points – 35 and 70 days, expecting that a variety of cellular identities evolves over time. In total, we found eight different cellular populations present in midbrain organoids at both time points (35 and 70 days) (**Manuscript I Figure 2**). In comparison, the human embryonic midbrain contained 25 different

cellular identities (La Manno et al. 2016). Since midbrain organoids are derived from the neuroectoderm, they do not include mesodermal origin cells, such as vascular cells and microglia, hence it was expected that midbrain organoids do not fully represent *in vivo* midbrain cellular diversity. Nevertheless, shared cellular populations between midbrain organoids and embryonic midbrain demonstrated highly similar transcriptomic signature. This suggests that although midbrain organoids are less complex than the actual tissue, they include physiologically relevant cellular populations. Identified cell clusters in midbrain organoids included neuroblasts, progenitors, neurons, glia and pericytes. Although pericytes are part of the vasculature, pericytes in the CNS develop from the neuroectoderm (Cathery et al. 2018). Neuron clusters were further subdivided based on the expression of maturity and neuron-specific markers, introducing young neurons, mature dopaminergic neurons, and non-dopaminergic neuron clusters (**Manuscript I Figure 2**). Importantly, we observed that cell population proportions change over time. 70 days old midbrain organoids comprised fewer neuroblasts and young neurons, but an increased amount of glia cells compared to 35 days old organoids, confirming that midbrain organoid model maturity and complexity increase over time (**Manuscript I Figure 4B**). Other single-cell RNA sequencing studies of iPSC-derived midbrain organoids show very similar cellular populations to those found in midbrain organoids generated in our lab (Fiorenzano et al. 2022, Patikas, Ansari, and Metzakopian 2023). Particularly, Fiorenzano and colleagues identify and characterize different subtypes of dopaminergic neurons, which is a relevant next step in addressing midbrain organoid physiological relevance.

Overall, the high similarity between embryonic midbrain *in vivo* and midbrain organoids *in vitro* provides evidence of midbrain organoid brain region specificity and potential to model human midbrain development. At the same time, the high resemblance to embryonic stages of development is a considerable limitation of midbrain organoids. In the context of PD, midbrain organoids are suitable for modeling neurodevelopmental aspects of the disease, while capturing age-associated phenotypes might present some challenges and require model optimization.

2.2. Neurodevelopmental component of Parkinson's disease

As discussed in section 1.1.2, genetic variants LRRK2-G2019 and GBA-N370S are the most frequent genetic risk factors implicated in PD pathology. In this thesis, **Manuscript I** and **Manuscript II**, we demonstrate how these mutations affect neurodevelopmental processes that might underly dopaminergic neuron increased susceptibility to degenerate.

LRRK2-G2019S

The G2019S mutation in the LRRK2 gene stands out as the most frequent pathogenic variant associated with both familial and sporadic cases of PD (Day and Mullin 2021). However, the LRRK2-G2019S variant has incomplete penetrance, meaning that not all carriers will have PD and other factors play an important role in PD development (Day and Mullin 2021). It also suggests that the LRRK2-G2019S mutation might affect crucial developmental or functional aspects of dopaminergic neurons, increasing their vulnerability, and allowing the second hit to determine PD manifestation. Interestingly, LRRK2 expression is increased in early tissue development including developing neurons, suggesting that G2019S pathogenesis would be more detrimental at developmental stages than in fully differentiated tissue when LRRK2 expression is comparingly lower (Zechel et al. 2010, Milosevic et al. 2009). For example, the deletion of the LRRK2 gene in the zebrafish model results in neurodevelopmental perturbations of MAO activity and a subsequential increase in dopamine degradation (Suzzi et al. 2021), while in mice the LRRK2-G2019S mutation mediates alterations in striatal neural circuit formation and defective synaptogenesis (Matikainen-Ankney et al. 2016). In **Manuscript I,** we used midbrain organoids to model early developmental stages to investigate how the LRRK2-G2019S mutation influences cellular development and whether LRRK2-G2019S introduces a PD-specific molecular signature already in early neurodevelopment. We used single RNA sequencing data of 35 and 70 days old midbrain organoids derived from a healthy individual and its isogenic LRRK2-G2019S carrying counterparts. This experimental setup allowed us to specifically investigate mutation-associated changes on the genetic background of a healthy individual. We found that mutant organoids have a distinct transcriptomic signature compared to the wild-type (WT) midbrain organoids, and the differentially expressed genes (DEGs) were enriched in LRRK2-associated PD pathways and developmental processes (**Manuscript I Figure 3A-B**). Moreover, there were five times more DEGs between 70 days old LRRK2 mutant and WT midbrain organoids than between 35 days old ones, suggesting that the LRRK2-G2019S mutation induces time/age-dependent molecular changes in a progressive manner (**Manuscript I Figure 3C**). In the dopaminergic neuron cluster, DEGs revealed that the most LRRK2-G2019S-affected cellular processes were linked to cytoskeleton and synapse maintenance, neurodevelopment and γ-secretase regulation, involved in protein cleavage (**Manuscript I Figure 3E-F**). Furthermore, we observed several differences in cellular population abundance between LRRK2 mutant and WT midbrain organoids. We found that the less mature neuroblast cluster increased within the LRRK2-G2019S mutation carrying midbrain organoids from day 35 to day 70. Concurrently, a reduction in the number of non-dopaminergic neurons was noted in the corresponding timeframe (**Manuscript I Figure 3B**), suggesting that the maturity of

mutant organoids decreases over time, contrary to the WT midbrain organoids. In addition, there was an absence of a pericyte cluster in LRRK2-G2019S midbrain organoids (**Manuscript I Figure 4A-B)**. Pericytes wrap around endothelial cells and are essential for blood vessel and BBB maintenance. Moreover, it has been reported that the LRRK2-G2019S mutation alters angiogenesis-related genes and reduces BBB integrity facilitating toxic factor transport to the brain (de Rus Jacquet et al. 2023).

We applied trajectory-based differential expression analysis to further investigate developmental deviation induced by the LRRK2-G2019S mutation. Trajectory-based differential expression analysis allows the exploration of dynamic changes in gene expression occurring during cellular differentiation or response to stimuli by organizing cells along a pseudotime trajectory based on cell progress through the determined transition (Van den Berge et al. 2020). Neuroblasts in 35-day-old midbrain organoids were determined as the starting point of the developmental trajectory. We observed that dopaminergic neurons within WT midbrain organoids follow a developmental trajectory, demonstrating increasing maturity over time (**Manuscript I Figure 5A**). Contrary, dopaminergic neurons within mutant organoids from both time points were clustered together on the developmental trajectory, indicating their impaired differentiation capability (**Manuscript I Figure 5A**). Moreover, temporal expression of TH, showed that mutant organoids have lower levels of TH compared to WT organoids at both time points (**Manuscript I Figure 5C**). Although we did not find a reduction of dopaminergic neurons in mutant organoids compared to WT organoids (**Manuscript I Figure 4B**), hampered neural differentiation and lower levels of TH strongly suggest that the LRRK2-G2019S mutation affects dopaminergic neuron maturation. Consistent with our results, a study in iPSC-derived dopaminergic neurons carrying the LRRK2-G2019S mutation showed altered differentiation of dopaminergic neurons leading to their death (Walter et al. 2021). Furthermore, we observed an accelerated glia differentiation, that could be a potential attempt to support immature dopaminergic neuron functions. The glial population within mutant organoids exhibited an initial augmentation at day 35, followed by a subsequent twofold reduction at day 70 (**Manuscript I Figure 4A-B**). Additionally, when examining the pseudotime trajectory, glial cells within day 35 mutant organoids had already progressed near the terminal point of the trajectory, signifying an accelerated differentiation process (**Manuscript I Figure 5A**).

Furthermore, we found that multiple genes associated with PD – namely DNAJC12, GATA3, PTN and APP display temporal expression patterns in the human embryonic midbrain, suggesting their role in the regulation of neurodevelopmental processes (**Manuscript I Figure 6A**). We also observed that the expression of these genes is significantly different between mutant and WT

midbrain organoids (**Manuscript I Figure 6B-E**). This finding not only implies that LRRK2 plays a regulatory role in governing the expression of these genes but also provides additional evidence for the involvement of LRRK2 in the modulation of neurodevelopmental processes.

Altogether, these results demonstrate that the LRRK2-G2019S mutation is implicated in defective dopaminergic neuron development and maturation that trigger adaptive events, such as untimely glia differentiation. These initial neurodevelopmental disruptions could be the major contributors to the increased dopaminergic neuron vulnerability to degeneration.

GBA-N370S

Currently, it is known that heterozygous genetic variants of the GBA gene are one of the most common causes and major genetic risk factors for PD development, affecting 5-15% of all PD patients. One of the most frequent variants of GBA found in PD patients is a missense mutation c1226A>G (N370S), particularly prevalent in the Ashkenazi Jewish population (Smith and Schapira 2022). Since the GBA-N370S mutation is rather a risk factor than a PD determinant, similar to the LRRK2-G2019S case, we were interested in the neurodevelopmental contribution of the GBA-N370S variant underlying dopaminergic neuron vulnerability to neurodegeneration. In **Manuscript II,** we investigated phenotypic differences between GBA-N370S mutation carrying PD patient-specific and healthy individual-derived midbrain organoids. A characteristic feature of GBA-PD is the decreased activity of GCase (Gegg et al. 2012). Accordingly, mutant organoids demonstrated decreased GCase activity and its dislocation from lysosomes, although the levels of the GCase enzyme were initially unaltered (**Manuscript II Figure 1B-D**). Furthermore, changed levels of the autophagy markers – p62 and LC3, indicated impaired lysosomal functionality (**Manuscript II Figure 1E-F**), which has also been previously observed in cellular models carrying GBA mutations (Navarro-Romero et al. 2022, de la Mata et al. 2015, Fernandes et al. 2016).

In this manuscript, we show genome-scale modeling (GSM) application in PD metabolic phenotype investigation. Considering the role of the GBA in lipid metabolism, we anticipated that metabolic modeling would be a useful approach to derive predictions regarding GBA-N370S mutation-mediated metabolic alterations. Metabolic modeling using GSM is a systems biology tool which enables the investigation of genotype-phenotype relationships in a context-specific manner (Passi et al. 2021). We used Recon3D, which is to date the most comprehensive genome-scale human metabolic network, to reconstruct metabolic networks based on the sample-specific RNA expression (Brunk et al. 2018). Importantly, a relevant phenotype or biological task must be defined to further explore the subsequent changes in the network. In this manuscript, as well as in **Manuscript III**, we used flux variability analysis (FVA), which finds the minimum and the maximum flux for reactions, indicating the flexibility of the network under defined constraints

(Gudmundsson and Thiele 2010). GSM has been shown to provide accurate predictions regarding disease-associated metabolic alterations. For instance, GSMs have been used to study sepsis (McGarrity et al. 2018), cancer (Marin de Mas et al. 2018) and SARS-CoV-2 (Cheng et al. 2021). Similarly, we were able to derive a relevant hypothesis concerning GBA-N370S-caused metabolic changes, and further validate model predictions experimentally. Metabolic modeling predicted substantial compositional differences in sphingolipid and glycerophospholipid metabolic subsystems between GBA-PD and healthy control context-specific models (**Manuscript II Figure 2B-C**). Defining maximal ATP production as the metabolic aim of the models, we performed FVA to evaluate metabolic pathway contribution and flexibility for this metabolic state. The main finding here was that mutant models exhibited strikingly comparable flux variability in selected metabolic pathways, while the behavior of control models diverged significantly, suggesting that GBA-N370S has a fundamental effect on metabolic processes (**Manuscript II Figure 2D**). The altered lipid profile of midbrain organoids harboring the GBA-N370S mutation was further validated by liquid chromatography-mass spectrometry (LC-MS), quantifying over 2000 lipid species across 16 distinct lipid classes. Multiple lipid classes were significantly differentially abundant in GBA-N370S midbrain organoids compared to WT organoids (**Manuscript II Figure 3A, Figure S4A-D**). Notably, among the differentially abundant lipids, the two predominant phospholipids found in cell membranes, namely phosphatidylethanolamine (PE) and phosphatidylcholine (PC) were both reduced in GBA mutant organoids (**Manuscript II Figure 3A**). As demonstrated in other studies, compromised cell membrane integrity has been shown to facilitate αSyn pathology, therefore driving the progression of PD (Chaudhary et al. 2014).

The decreased activity of GCase is particularly associated with the accumulation of hexosylceramides (Wong and Krainc 2016). Although the total levels of hexosylceramides were not altered in our study, there was a significant decrease of hexosylceramides with stearic fatty acid backbone C18:0 and an increase of docosanoic acid C22:0 derived hexosylceramides. Similarly, in iPSC-derived dopaminergic neurons, it has also been shown that only several species of hexosylceramides are affected by impaired GCase activity (Fernandes et al. 2016). One of the possible explanations might be that due to compromised GCase trafficking from ER to lysosomes, coupled with altered hexosylceramide distribution within neurons, mutant GCase might hydrolyse lipid species that normally would not get degraded (Fernandes et al. 2016). Interestingly, reduced GCase activity has also been observed in sporadic PD brain samples (Gegg et al. 2012, Rocha et al. 2015) as well as in blood samples (Alcalay et al. 2015) from patients with and without GBA mutations. Moreover, LRRK2-G2019S carriers show increased GCase activity (Alcalay et al. 2015). These results suggest that altered GCase activity and downstream pathological molecular events

might be an important factor in PD pathogenesis, presenting a common feature between multiple genetic forms of PD. This opens a new research question about GCase's role in PD, which should be further investigated.

In addition, the GBA-PD metabolic models showed the absence of dopamine extracellular transport (**Manuscript II Table S4**). This prediction was also validated experimentally, by measuring secreted dopamine levels that were found significantly reduced in GBA-PD organoid samples (**Manuscript II Figure 4A**). Moreover, GBA-N370S-affected midbrain organoids demonstrated significantly decreased levels of TH, dopaminergic neuron complexity and electrophysiological activity (**Manuscript II Figure 4B-F, H**). To determine the primary cause underlying the reduction of dopaminergic neurons, we looked at the DEGs. While TH and NR4A2 (NURR1) – a transcription factor regulating differentiation and maturation of dopaminergic neurons were among the downregulated genes, SOX2 and FOXA2, both neural progenitor markers, were significantly higher expressed in GBA mutant midbrain organoids (**Manuscript II Figure 5A**). Surprisingly, neural progenitors were unable to undergo proliferation due to their arrest in the S-phase of the cell cycle (**Manuscript II Figure 5C-I**) which was accompanied by DNA damage and a senescence phenotype (**Manuscript II Figure 6**). Consistent with our results, it has been shown that Gaucher patient iPCS-derived neural progenitors harboring homozygous GBA mutations display developmental defects caused by the downregulation of the canonical WNT/β-catenin signaling, which is critical in midbrain dopaminergic neurogenesis (Awad et al. 2017). Furthermore, FOXA2 upregulation has been observed in LRRK2-G2019S mutation-carrying PD patient-derived midbrain organoids (Smits et al. 2019). This study as well as results presented in **Manuscript I** suggest that defective dopaminergic neuron differentiation is a shared phenotype between LRRK2 and GBA genetic variants.

Altogether, results of **Manuscript II** confirm GBA-N370S mutation-associated relevant PD phenotypes, such as decreased GCase activity, impaired lysosomal function and strongly altered lipid profile. Moreover, our findings suggest that GBA-N370S contributes to the neurodevelopmental aspect of PD by impairing dopaminergic neurogenesis through the undifferentiated progenitor arrest in the cell cycle and cellular senescence.

2.3. Comorbidity of Parkinson's disease and Type 2 Diabetes

As discussed in section 1.2.2, insulin resistance is one of the proposed shared disease mechanisms between PD and T2D. It has been reported that two-thirds of non-diabetic PD patients have general insulin resistance, despite normal fasting glucose levels (Hogg et al. 2018), implying that insulin resistance might be one of the underlying pathological mechanisms in PD independently of T2D. Additionally, since the blood insulin levels affect those in the brain (Wallum et al. 1987), T2D-

associated peripheral insulin resistance would have an impact on insulin action in the CNS, potentially increasing dopaminergic neuron predisposition to PD and aggravating PD progression. In **Manuscript III** we apply diabetic and non-diabetic conditions to the midbrain organoids to demonstrate insulin resistance-mediated destructive effects on healthy and PD-affected midbrain. We also show that insulin signaling gene expression is altered in GBA-N370S-associated PD. However, as discussed in section 1.2.3, T2D modeling *in vitro* is challenging due to the basal media composition, which already contains high insulin concentrations. Therefore, as part of the project, we focused on optimizing cell culture media to develop a more physiologically relevant environment, achieving a substantial reduction in insulin concentration. As shown in **Manuscript III Figure 1B**, we were able to reduce supraphysiological insulin concentration in the basal media from ~390nM to ~170nM. We showed that the reduction of insulin concentration is beneficial to cells, while standard insulin concentration represents hyperinsulinemia and promotes insulin resistance. Midbrain organoids cultured in the standard basal media displayed insulin resistance phenotype, demonstrating decreased abundance of IRS, impaired AKT phosphorylation and reduced glucose uptake, while organoids cultured in reduced insulin concentration media showed opposite phenotype and, therefore were considered as insulin sensitive (**Manuscript III Figure 1C-G, Figure S5B**).

First, we explored the insulin resistance effect on the healthy, non-PD midbrain, by evaluating dopaminergic neuron amount, neural activity and metabolic function of midbrain organoids derived from healthy individuals. We observed that insulin-resistant midbrain organoids have reduced amounts of dopaminergic neurons based on TH abundance at later time points – day 60 while maintaining equivalent TH abundance at day 30 **(Manuscript III Figure 2A-B**). This indicates that insulin resistance may primarily influence the long-term sustainability of dopaminergic neurons, rather than directly affecting their differentiation process. Furthermore, insulin-resistant organoids demonstrated significantly reduced neural activity in terms of electrical signals recorded as spikes and bursts using multi-electrode array and local field potential recordings (**Manuscript III Figure 2D-K**). Impaired neural activity and communication might be an early determinant of cognitive decline, which is observed in PD patients who are also affected by T2D (Park, Choi, and Kim 2023).

Insulin is known to regulate metabolism, and an altered cellular metabolic state might underly neural activity impairment in insulin-resistant organoids. Therefore, we aimed to discover metabolic differences between insulin-resistant and insulin-sensitive midbrain organoids. We used the metabolic modeling approach as described in **Manuscript II,** to gather a comprehensive overview of altered metabolic pathways based on insulin-resistant and insulin-sensitive organoid

RNA expression. Structural analysis of the models revealed differences in multiple lipid metabolism-related pathways (**Manuscript III Figure 3A**). Lipid quantification using LC-MS confirmed distinct lipid profiles between insulin-resistant and insulin-sensitive midbrain organoids (**Manuscript III Figure 3B**). Interestingly, one of the most differentially abundant lipid classes was cell membrane PCs. They were found in significantly decreased levels in insulin-resistant organoids and also reduced in midbrain organoids harboring the GBA-N370S mutation (**Manuscript III Figure 3E**). Other insulin resistance-mediated lipid metabolic alterations were related to arachidonic acid, cholesterol ester and fatty acid metabolism. Particularly, fatty acid oxidation demonstrated an increased involvement in mitochondrial metabolism in insulin-resistant organoids (**Manuscript III Figure 3H-I**), while insulin-sensitive organoids showed high dependency on glycolysis and increased glycolytic flux as determined by C13 isotope tracing (**Manuscript III Figure 4A-D**). We observed that insulin-resistant organoids have elevated ROS levels, which might be a direct result of metabolic differences (**Manuscript III Figure 4G-I**). These findings suggest that impaired neural functionality, metabolic alterations and accelerated ROS caused by insulin resistance in the healthy midbrain might promote dopaminergic neuron vulnerability and predisposition to PD development.

Reduction of dopaminergic neurons and severe alteration of lipid profile suggest that insulin resistance-caused phenotypes are similar to those observed in midbrain organoids derived from GBA-N370S mutation-carrying PD patients (**Manuscript II**). This observation implies that insulin resistance amplifies the susceptibility of individuals carrying the GBA-N370S mutation to develop PD and exacerbates the phenotypic manifestations associated with GBA-N370S mutation-related PD. Therefore, in **Manuscript III**, we included three PD patient lines carrying the GBA-N370S mutation and exposed them to high and reduced insulin concentrations following the same experimental procedure as for the healthy individual-derived midbrain organoids. Insulin concentration change did not promote the increase of dopaminergic neurons and dopamine in GBA mutant midbrain organoids (**Manuscript III Figure 5A-C**), however, insulin-sensitive GBA organoids demonstrated higher cellular viability and multiple lipid species abundance comparable to healthy organoids, including increased levels of PCs (**Manuscript III Figure 5D-H**). However, we found a distinct expression of insulin signaling-associated genes in GBA mutant organoids compared to healthy counterparts, supporting the idea that insulin signaling impairment plays an essential role in GBA-N370S-associated phenotype development independently of the peripheral origin of insulin resistance. Particularly, the FOXO1 transcript stood out as significantly increased in GBA mutant samples (**Manuscript III Figure 6A,D, Figure S10A**). A direct link between FOXO1 and GBA genes has not been discussed in the literature, however, it is known that elevated

expression of FOXO1 and its increased transcription factor activity are triggered by ROS and high glucose levels. Moreover, FOXO1 downstream target genes include those involved in the cell cycle arrest, autophagy regulation and metabolism (Xing et al. 2018). This could mean that GBA mutation-induced ROS and altered ceramide metabolism (as discussed in 1.2.2) might impair insulin signaling, leading to FOXO1 overactivation and contribution to GBA-N370S PD progression through disease processes presented in **Manuscript II**. We performed a knockout of FOXO1 by antisense oligonucleotides (ASOs) and observed a significant increase in the dopaminergic neuron population in GBA-N370S midbrain organoids (**Manuscript III Figure 7B-D**)**,** thus confirming FOXO1 implication in GBA-associated PD**.** Similar rescue of dopaminergic neuron levels was observed in GBA mutant organoids treated with Pioglitazone, a commonly used antidiabetic molecule (**Manuscript III Figure 7I-K**). On the other hand, mutant midbrain organoid treatment with Metformin, the first-line medication for T2D, led to a decrease in general cellular death but not to a rescue of dopaminergic neuron loss (**Manuscript III Figure 7F-H**).

Altogether, findings presented in **Manuscript III** show that T2D increases PD risk through insulin resistance, and accelerates cellular death and pathological lipid phenotypes in GBA-N370S-associated PD. Furthermore, insulin resistance-mediated FOXO1 overexpression contributes to the GBA-N370S dopaminergic neuron phenotype. Moreover, we show that early rescue of insulin signaling impairment by targeted downregulation of FOXO1 might be an efficient treatment strategy for GBA-N370S carriers to increase the levels of dopaminergic neurons. Additionally, antidiabetic treatment might delay or prevent PD development.

CHAPTER 2

Materials and Methods

A detailed description of all materials and methods used in this thesis can be found in the original articles listed in Chapter 3. The following section lists the main experimental procedures I conducted myself or took part in.

- **iPCS culture**
    - See Manuscript II
- **Derivation and culture of smNPCs and NESCs**
    - See Manuscript II; Manuscript III
- **Generation of midbrain organoids**
    - See Manuscript II; Manuscript III
- **Single-cell RNA sequencing data analysis**
    - See Manuscript I
- **Immunofluorescence stainings**
    - See Manuscript III
- **High-content image analysis with MATLAB**
    - See Manuscript III
- **Confocal microscopy**
    - See Manuscript III
- **Western blot**
    - See Manuscript III
- **Flow cytometry**
    - See Manuscript III
- **Dopamine ELISA**
    - See Manuscript III

- **Insulin ELISA**
    - See Manuscript III
- **LDH assay**
    - See Manuscript III
- **Metabolic modeling**
    - See Manuscript II; Manuscript III
- **Multielectrode array**
    - See Manuscript III
- **Local field potential recording**
    - See Manuscript III
- **ATP assay**
    - See Manuscript III
- **Bulk RNA sequencing data analysis**
    - See Manuscript III
- **Metabolomics data analysis**
    - See Manuscript III
- **Lipidomics data analysis**
    - See Manuscript III
- **Stable isotope tracing data analysis**
    - See Manuscript III
- **Seahorse fuel dependency assay**
    - See Manuscript III
- **Midbrain organoid treatment with ASOs and antidiabetic drugs**
    - See Manuscript III
- **Statistical analysis**
    - See Manuscript III

CHAPTER 3

Results

Manuscript I: Midbrain organoids mimic early embryonic neurodevelopment and recapitulate LRRK2-p.Gly2019Ser-associated gene expression (Zagare & Barmpa et al., 2022)

Manuscript II: Impaired dopaminergic neuronal differentiation in GBA associated Parkinson's disease midbrain organoids is accompanied by an increased progenitor pool in cell cycle arrest (Rosety et al., 2023)

Manuscript III: Insulin resistance disrupts midbrain metabolic & functional homeostasis and aggravates dopaminergic neuron loss in GBA-PD (Zagare et al., 2023)

3.1. Manuscript I

Midbrain organoids mimic early embryonic neurodevelopment and recapitulate LRRK2-p.Gly2019Ser-associated gene expression

Alise Zagare[1,*], Kyriaki Barmpa[1,*], Semra Smajic[1], Lisa M. Smits[1], Kamil Grzyb[1], Anne Grünewald[1], Alexander Skupin[1], Sarah L. Nickels[1,°] and Jens C. Schwamborn[1,°]

[1]Luxembourg Centre for Systems Biomedicine, University of Luxembourg, Esch-sur-Alzette, Luxembourg

* Co-first authors

° Co-corresponding author

This article has been published in the American Journal of Human Genetics

3.1.1. Contribution statement

I share the first authorship of this article with Kyriaki Barmpa and this article is included in both of our PhD theses. We both had an equivalent contribution to R script development, manuscript writing and figure preparation. I took part in the development of R scripts for the single-cell RNA-sequencing data quality control, filtering, and normalization. I also compared midbrain organoid and human embryonic midbrain genetic signatures and performed a correlation analysis of common gene expression between embryonic developmental weeks and WT or LRRK2-G2019S mutant midbrain organoids. These results are presented in panels A-C included in Figure 1 and panels C-D included in Figure 4. In addition, I analyzed cell type proportions in WT and LRRK2-G2019S mutant organoids demonstrated in plots A and B in Figure 4, and I took part in the development of the R script for the pseudotime analysis and preparation of Figure 5. The initial idea of the article was developed by J.C. Schwamborn, and this project was supervised by S.L. Nickels.

3.1.2. Preface

The main aim of this manuscript was to evaluate the extent of similarity between midbrain organoids and the human embryonic midbrain in terms of cellular composition and transcriptomic profile. We compared single-cell RNA sequencing data of human midbrain organoids generated in our lab (Smits et al. 2020), to single-cell RNA sequencing data of human embryonic midbrain at different developmental stages (La Manno et al. 2016). In addition, we aimed to compare transcriptomic profiles at the single cell level of healthy-individual derived midbrain organoids and their isogenic counterparts with introduced LRRK2-G2019S mutation, to investigate LRRK2-G2019S induced developmental alterations that eventually lead to PD.

Single-cell RNA sequencing is a powerful tool for studying cellular heterogeneity, discovering new cellular subpopulations and investigating physiological and pathological molecular mechanisms at the single-cell level (Tang et al. 2019). In this article, we make use of this technology to explore the cellular heterogeneity and quantitative proportions of different cell types present in the midbrain organoids that we use to study PD. Similar to other single-cell RNA sequencing studies of midbrain organoids, we were able to detect neural progenitor, general neuron, dopaminergic neuron, perivascular-like cell and glia populations (Fiorenzano et al. 2022). Moreover, we were able to show that the gene expression signature of cellular clusters in the midbrain organoids highly correlates with the human embryonic midbrain. The physiological resemblance of cellular populations present in midbrain organoids to the actual *in vivo* tissue is essential for accurate disease modeling. Particularly, midbrain organoids allow us to address neurodevelopmental

aspects of PD. It has been suggested that neurodevelopmental alterations might increase the predisposition to neurodegenerative diseases. In this article, we focus on the LRRK2-G2019S mutation, which is the most common cause of sporadic and familial PD (Correia Guedes et al. 2010). LRRK2 is constitutively expressed in the brain, and it is a multidomain, multifunctional protein with a variety of interaction partners, leading to its involvement in numerous cellular pathways (Milosevic et al. 2009, Biskup and West 2009). The point mutation G2019S (glycine to serine substitution at the position 2019 within LRRK2 kinase domain) is associated with LRRK2 kinase gain of function, which has been linked to αSyn pathology, neuronal survival, mitochondrial dysfunction and multiple other PD-associated phenotypes, which makes LRRK2 an attractive therapeutic target (Biskup and West 2009, Oun et al. 2022). This single-cell RNA sequencing approach allowed us to gain insight into LRRK2-G2019S mutation-mediated early molecular changes in every midbrain-specific cell type. Importantly, we detected impairments in dopaminergic neuron differentiation, which could be a critical determinant of their increased vulnerability.

Midbrain organoids mimic early embryonic neurodevelopment and recapitulate LRRK2-p.Gly2019Ser-associated gene expression

Graphical Abstract

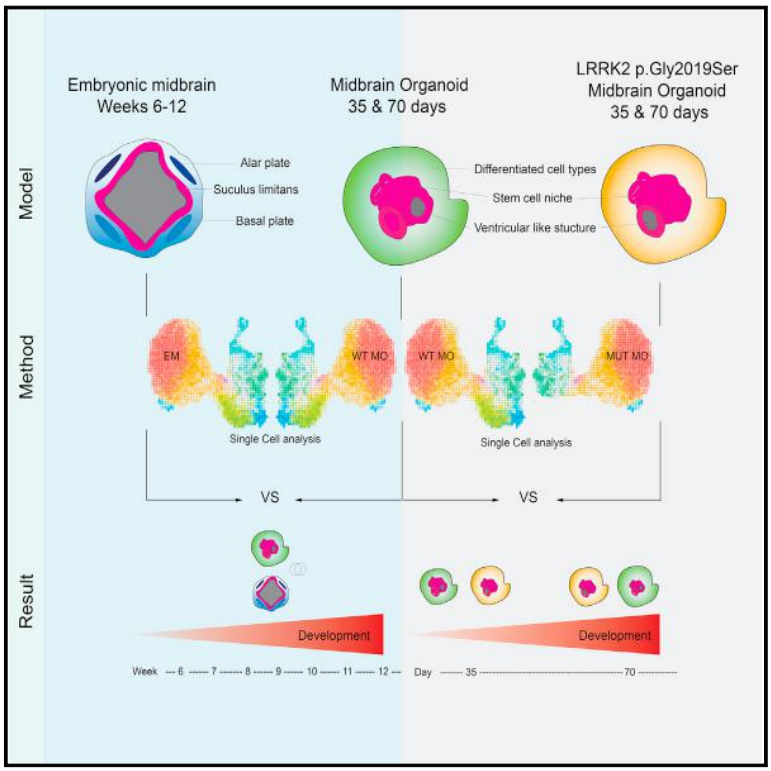

Authors

Alise Zagare, Kyriaki Barmpa, Semra Smajic, ..., Alexander Skupin, Sarah L. Nickels, Jens C. Schwamborn

Correspondence

sarah.nickels@uni.lu (S.L.N.), jens.schwamborn@uni.lu (J.C.S.)

Zagare et al., 2022, The American Journal of Human Genetics *109*, 311–327
February 3, 2022
https://doi.org/10.1016/j.ajhg.2021.12.009

Midbrain organoids mimic early embryonic neurodevelopment and recapitulate LRRK2-p.Gly2019Ser-associated gene expression

Alise Zagare,[1,2] Kyriaki Barmpa,[1,2] Semra Smajic,[1] Lisa M. Smits,[1] Kamil Grzyb,[1] Anne Grünewald,[1] Alexander Skupin,[1] Sarah L. Nickels,[1,*] and Jens C. Schwamborn[1,*]

Summary

Human brain organoid models that recapitulate the physiology and complexity of the human brain have a great potential for *in vitro* disease modeling, in particular for neurodegenerative diseases, such as Parkinson disease. In the present study, we compare single-cell RNA-sequencing data of human midbrain organoids to the developing human embryonic midbrain. We demonstrate that the *in vitro* model is comparable to its *in vivo* equivalents in terms of developmental path and cellular composition. Moreover, we investigate the potential of midbrain organoids for modeling early developmental changes in Parkinson disease. Therefore, we compare the single-cell RNA-sequencing data of healthy-individual-derived midbrain organoids to their isogenic LRRK2-p.Gly2019Ser-mutant counterparts. We show that the LRRK2 p.Gly2019Ser variant alters neurodevelopment, resulting in an untimely and incomplete differentiation with reduced cellular variability. Finally, we present four candidate genes, *APP*, *DNAJC6*, *GATA3*, and *PTN*, that might contribute to the LRRK2-p.Gly2019Ser-associated transcriptome changes that occur during early neurodevelopment.

Introduction

Parkinson disease (PD) is a multifactorial neurodegenerative disorder with varying motor and non-motor symptoms, characterized by the loss of dopaminergic neurons (DNs) in the substantia nigra pars compacta (SNpc) of the midbrain.[1] The most common mutation associated with PD is c.6055G>A (p.Gly2019Ser) in leucine-rich repeat kinase 2 (*LRRK2*) (GenBank: NM_198578.4).[2–4] LRRK2 is a multidomain protein involved in many cellular functions, including cell proliferation, survival regulation of neural stem cells (NSCs), and neurogenesis.[5,6] Altered neurogenesis and neurodevelopment have been suggested to have major implications in the development of neurodegenerative diseases, including PD.[7] Accordingly, various studies show an accelerated neuronal differentiation in *LRRK2*-mutant human cellular models, with a simultaneous impairment specifically of DN development.[8–10] In particular, the interaction of LRRK2 with the canonical Wnt/b-catenin signaling pathway has been linked to the development of DNs through the regulation of axonal guidance, dendritic morphogenesis, and synapse formation.[11–14]

Taking into consideration the complexity of the etiology of PD related to age, genetics, and environmental causes and the possibility of a neurodevelopmental component in PD, it is essential to have an adequate model, which can represent the human brain development and the manifestation of the disease. Studies on human postmortem brain tissue provided precious understanding of PD-associated alterations.[15] However, postmortem tissues are generally available at the end stage of the disease and display a late stage in the disease progression. In order to overcome the limitation of understanding the disease development throughout life, we rely on various experimental models. Our understanding of pathological mechanisms underlying the disease largely depends on models that do not fully portray the complexity of the disease pathology or the cellular composition of the human brain. Genetic and toxin-based animal models often are not able to adequately capture the critical aspects of human PD, resulting in incomplete disease phenotypes.[16] The discovery of induced pluripotent stem cells (iPSCs) and CRISPR-Cas9 technology surpassed this obstacle and enabled the access to human-derived cells for isogenic disease modeling.[17–19] Although such 2D cultures capture the specific effect of mutation-induced PD and its molecular mechanisms, they still lack the cellular diversity of the human brain. To overcome these limitations, the recent developments in self-organizing 3D human-derived midbrain organoids represent a promising advancement in modeling neurodegenerative diseases.[9,20–24]

In order to study the role of human LRRK2 p.Gly2019Ser in a physiological context of early human development, we used previously published single-cell RNA-sequencing (scRNA-seq) datasets of human embryonic midbrain between developmental week 6 and week 11[25] as well as healthy-individual-derived isogenic wild-type (WT) and LRRK2 p.Gly2019Ser midbrain organoids of 35 and 70 days of differentiation.[26] We have previously demonstrated that the respective midbrain organoids comprise different neuronal types, including dopaminergic, GABAergic,

[1]University of Luxembourg, Luxembourg Centre for Systems Biomedicine, 6, Avenue du Swing, L-4367 Belvaux, Luxembourg
[2]These authors contributed equally
*Correspondence: sarah.nickels@uni.lu (S.L.N.), jens.schwamborn@uni.lu (J.C.S.)
https://doi.org/10.1016/j.ajhg.2021.12.009.

glutamatergic, and serotonergic neurons as well as glia cells.[26] First, we sought to use the single-cell transcriptomes of healthy midbrain organoids and the human embryonic midbrain to analyze the shared cellular identities and correlation between the *in vitro* and *in vivo* systems. Further, we exploit the transcriptome of the healthy and isogenic (in which LRRK2 p.Gly2019Ser has been inserted) midbrain organoids to investigate the LRRK2-p.Gly2019Ser-dependent changes in gene expression. We report that the midbrain organoids share proportionately similar transcriptomic profile and cell-type diversity with the developing human midbrain. Additionally, our analysis shows that midbrain organoids accurately adopt human midbrain development and are able to capture a LRRK2-p.Gly2019Ser-associated gene expression profile that might underlie *LRRK2*-mutation-related phenotypes.

Material and methods

Midbrain organoid generation from midbrain floorplate neural progenitor cells

Neural progenitor cells (NPCs) were derived from iPSCs of a healthy individual and isogenic LRRK2-p.Gly2019Ser-inserted cell line. Gene-editing of the iPSCs was done with CRISP-Cas9 and piggyBac systems, and it has been described in Qing et al., 2017.[27] The derivation of NPCs from iPSCs and further organoid generation have been described in detail previously[9,26] (Table S1). In brief, NPCs were cultured in N2B27 base medium supplemented with 2.5 μM SB-431542 (SB, Ascent Scientific), 100 nM LDN-193189 (LDN, Sigma), 3 μM CHIR99021 (CHIR, Axon Medchem), 200 μM ascorbic acid (AA, Sigma), and 0.5 μM SAG (Merck). For the derivation of midbrain, 3,000 NPCs were seeded per well in an ultra-low-attachment 96-well plate. For 7 days, cells were kept under maintenance conditions, following 3 days of pre-pattering where LDN and SB were withdrawn, and CHIR concentration was reduced to 0.7 μM. On day 9 of organoid culture, the differentiation was induced by changing the medium to N2B27 with 10 ng/mL brain-derived neurotrophic factor (BDNF, Peprotech), 10 ng/mL glial-cell-derived neurotrophic factor (GDNF, Peprotech), 200 μM AA, 500 μM dibutyryl cAMP (Sigma), 1 ng/mL TGF-β3 (Peprotech), 10 μM dual antiplatelet therapy (DAPT) (Cayman), and 2.5 ng/mL ActivinA (Peprotech). The organoids were cultured under static conditions with media changes every third day for 35 or 70 days. 30 midbrain organoids of each condition (WT35, WT70, MUT35, and MUT70) were pulled for Drop-seq analysis as described in Smits et al., 2020.[26]

Immunofluorescence staining

Midbrain organoids were fixed with 4% paraformaldehyde (PFA) overnight at 4°C followed by three washes with PBS for 15 min. The washed organoids were embedded in 3%–4% low-melting point agarose in PBS. Embedded organoids were sectioned into 50 μm sections with vibratome (Leica VT1000s). Organoid sections were blocked with 0.5% Triton X-100, 0.1% sodium azide, 0.1% sodium citrate, 2% BSA, and 5% normal donkey serum in PBS for 90 min at room temperature (RT) on a shaker. We diluted the primary antibodies in the same solution but with 0.1% Triton X-100 instead. The sections were incubated with the primary antibodies for 48 h at 4°C. Next, they were washed three times with PBS and subsequently blocked for 30 min at RT on a shaker. Next, sections were incubated with the secondary antibodies diluted in 0.05% Tween-20 in PBS for 2 h at RT and subsequently washed twice with 0.05% Tween-20 in PBS and once with Milli-Q water before mounting them in Fluoromount-G mounting medium (Southern Biotech). The primary antibodies used were TH rabbit Abcam ab112, FOXA2 mouse Santa Cruz sc-101060, and EN1 goat Santa Cruz sc- 46101. The secondary antibodies used were Hoechst 33342 solution (20 mM) Invitrogen 62249, anti-rabbit secondary 488 Thermo Fisher a21206, anti-mouse secondary 568 Invitrogen A10037, and anti-goat secondary 647 Invitrogen A21447.

Data pre-processing

In this study, we used already published scRNA-seq datasets. The midbrain organoids dataset was published from our lab,[26] while the other three datasets (embryonic midbrain, embryonic prefrontal cortex, and cortical organoids) are external[25,28,29] (Figure S1). scRNA-seq data from 30 pooled midbrain organoids per cell line and time point were generated following the Drop-seq pipeline.[30] Reads were mapped to human reference genome hg38 (GRCh38.87). From midbrain organoids datasets, cells having unique feature counts over 2,500 were removed as probable doublets or multiplets. Similarly, low-quality cells or empty droplets were further filtered out with unique feature counts below 100 (for day 35 data) and 200 (for day 70 data) and mitochondrial transcripts above 30% (Figure S2). Embryonic midbrain scRNA-seq data did not include any mitochondrial (MT) genes, thus to make midbrain organoid data more comparable to the embryonic midbrain data, we removed all MT genes from midbrain organoid datasets after quality control (QC). After QC, WT35 midbrain organoids included 2,864 cells, WT70 included 2,005 cells, MUT35 included 2,946 cells, and MUT70 included 2,660 cells.

The external datasets of embryonic midbrain, prefrontal cortex, and cortex organoid did not show any outliers in terms of doublets or empty droplets. Therefore, no additional QC was applied to these datasets.

Embryonic midbrain data of developmental week 6 to 11 included in total 1,977 cells, embryonic prefrontal cortex data at developmental stages between gestational weeks 8 and 26 included 2,309 cells, and cortex organoid data from 1 month old organoid comprised 4,832 cells.

Data integration and normalization

To better transmit the biological information between *in vivo* and *in vitro* ventral midbrain datasets, midbrain organoid data (WT35, WT70, MUT35, and MUT70) and embryonic midbrain data were integrated with the Seurat integration analysis workflow.[31] Integration was performed on the basis of the top 20 dimensions. RNA assay data of integrated object were log normalized and scaled to 10,000 transcripts per cell.

Cell type identification

After the integration of embryonic midbrain and midbrain organoid datasets, integrated object was scaled and principal-component analysis (PCA) was applied. Cell clustering was performed on the basis of the top 20 principal components via Louvain algorithm modularity optimization with a resolution of 0.5. Uniform manifold approximation and projection (UMAP) was used for cell cluster visualization.[32] Nine distinct cell clusters were identified in the UMAP plot. Clusters 0 and 7 were present only in

midbrain organoids and located in a close proximity to each other in the UMAP plot, indicating their high similarity and *in vitro* specificity. Because of this overclustering both clusters were pulled, resulting in eight distinct cellular identities labeled 1–8. For cell type identification, a binarized gene list across cell types from La Manno et al., 2016[25] was used. This list of genes comprises information about the marker genes in a binarized manner, where 1 means that gene is marking a specific cell population and 0 means that it cannot be considered as a marker gene. For more details on how this list is generated, please refer to La Manno et al., 2016.[25] Expression of each cluster-defining gene was overlapped with the marker gene (1) in the marker matrix from La Manno et al., 2016.[25] The total number of marker genes of a particular cell type of La Manno et al., 2016[25] that was present in each cluster of embryonic-midbrain- and midbrain-organoid-integrated dataset is visualized in Figure S4A. Cellular subtypes described by La Manno et al., 2016[25] were grouped in five major neuronal identity clusters—neurons subdivided in dopaminergic neurons (DNs) and non-dopaminergic neurons (non-DNs), then neuroblasts (NBs), progenitors (PROGs), and radial glia cells (RGLs). In addition, we identified non-neuronal identity cell populations—pericytes and endothelial cells. Cell types were assigned on the basis of the highest number of major cluster marker genes being expressed in the respective clusters of integrated embryonic midbrain and midbrain organoid dataset.

Differential gene expression analysis

Differentially expressed genes (DEGs) were detected with the FindMarkers function of the Seurat pipeline with the default thresholds. In all comparisons, we used the MUT midbrain organoids as ident.1 and the WT midbrain organoids as ident.2.

Pathway analysis

Pathway enrichment analysis was performed with MetaCore version 21.1 build 70400 on the basis of DEGs detected with the FindMarkers function from Seurat. DEGs were filtered for fold change (FC) > 0.25 and p adj. value < 0.05. From the analysis, we obtained the most significant enriched pathways, GO processes, network processes, and related diseases lists. The most significantly enriched pathways were illustrated in GraphPad Prism 9.

Cytoscape

Cell-cluster-specific genes were identified with the FindAllMarkers function from Seurat. The top 100 marker genes of each cell cluster were visualized in the network created with the Cytoscape software version 3.8.0.

Pseudotime analysis

Pseudotime analysis was performed with the Monocle package version 3. Merged Seurat object was uploaded in the Monocle workflow. Cell clustering was performed on the basis of 150 principal components with default settings. UMAP was used for visualization. Because Monocle does not allow a full metadata integration from Seurat object, we assigned cell identities manually to correspond to the ones previously defined. For the comparison between developmental stages of embryonic midbrain and midbrain organoid, we used the align_cds function to remove the batch effect between *in vivo* and *in vitro* midbrain systems. As a starting point for cell ordering along the pseudotime trajectory, the NB *in vitro* cluster of WT35 was chosen. For the comparison between developmental stages of WT midbrain organoids and MUT midbrain organoids, the same starting point of the NB *in vitro* cluster of WT35 was chosen. Genes that vary the most over the pseudotime were computed with the fit_models function. Midbrain-organoid- and embryonic-midbrain-integrated Seurat object was subset by pseudotime genes for the visualization of their expression in midbrain organoids.

Statistical analysis

If not stated otherwise, statistical analysis of scRNA-seq data was performed with RStudio R version 3.6.2 with the ggplot2 package. For all comparison, non-parametric Kruskal-Wallis test was performed. Statistical significance between comparisons are represented with asterisks: $p < 0.05$*, $p < 0.01$**, $p < 0.001$***, $p < 0.00001$****.

In vitro and *in vivo* midbrain data comparison to the cortex

WT midbrain organoids and embryonic midbrain were merged with embryonic prefrontal cortex and integrated on the basis of the top 20 dimensions. SCTransform normalization was applied to reduce the technical variation in the data and stabilize gene abundance levels, which can be highly variable between *in vitro* and *in vivo* tissues, especially between different tissue types—midbrain and cortex.[33] We determined mutual genes between midbrain organoids, embryonic midbrain, and embryonic prefrontal cortex by intersecting row names of respective datasets. Integrated object was subset by mutual genes. The top 2,000 variable genes in this subset of complete integrated dataset were detected with the FindVariableFeature function.

For the comparison of embryonic midbrain to cortical organoid, datasets were merged, SCTranformed, and subset by the mutual genes for the correlation analysis.

Ethical approval

The responsible national ethical commission has approved the study under the CNER report no. 201901/01. Written informed consent was obtained from all individuals who donated samples to this study (Smits et al., 2020).[26] The cell lines used in this study are summarized in Table S1.

Results

Midbrain organoids show a gene expression signature comparable to the human embryonic midbrain

To assess the similarity between the *in vitro* and *in vivo* midbrain systems, we compared scRNA-seq data of midbrain organoids cultured for 35 days (WT35) and 70 days (WT70)[26] to the human embryonic midbrain of developmental weeks 6–11.[25] In addition, to investigate possible transcriptome similarities between midbrain organoids and other brain regions during early development, we compared the scRNA-seq data of midbrain organoids to scRNA-seq data of the human embryonic prefrontal cortex.[28]

The transcriptome datasets of midbrain organoids, embryonic midbrain, and embryonic prefrontal cortex were embedded into a single Seurat object (Figure S3A). The average expression of the top 500 variable mutual genes

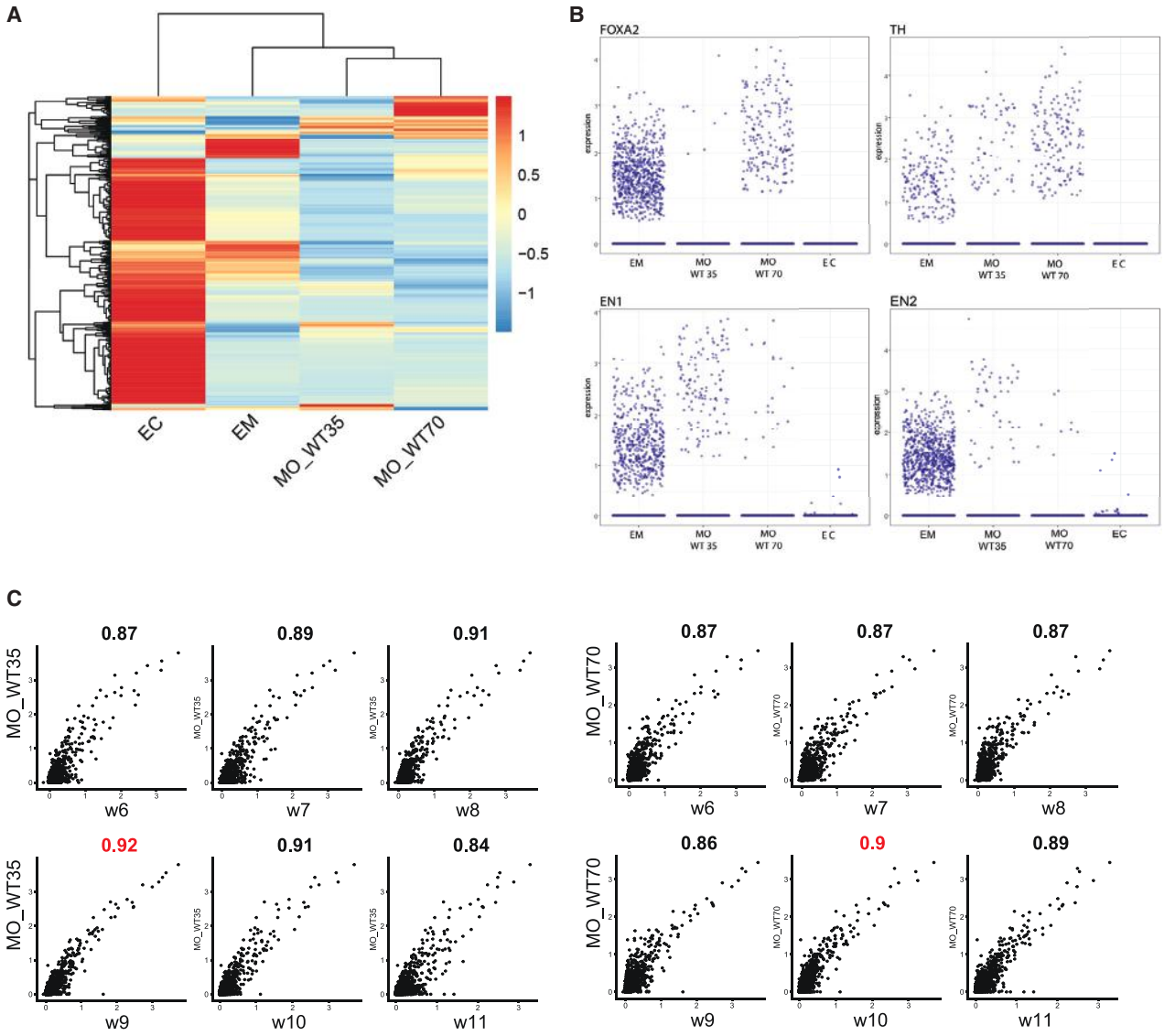

Figure 1. Midbrain organoids show a genetic signature comparable to the embryonic midbrain

(A) The top 1,000 most variable genes of Seurat integrated object of merged scRNA-seq datasets of embryonic cortex (EC), embryonic midbrain (EM), midbrain organoids 35 days of differentiation (MO_WT35), and midbrain organoids 70 days of differentiation (MO_WT70). The average gene expression visualized after *Z* score normalization.

(B) Expression of midbrain markers *FOXA2*, *TH*, *EN1*, and *EN2* in Seurat integrated object of merged scRNA-seq datasets of embryonic cortex (EC), embryonic midbrain (EM), midbrain organoids 35 days of differentiation (MO_WT35), and midbrain organoids 70 days of differentiation (MO_WT70). Each dot represents a single cell.

(C) The average common gene expression correlation between midbrain organoids 35 days of differentiation (MO_WT35) and midbrain organoids 70 days of differentiation (MO_WT70) and embryonic midbrain (EM) developmental weeks (w6–w11). The Pearson correlation coefficient is displayed above each comparison. The highest correlation between midbrain organoids and embryonic developmental time point is highlighted in red. Each dot represents a single cell.

showed a clear separation of the embryonic prefrontal cortex from midbrain organoids and the embryonic midbrain (Figure 1A). This separation indicates the expected greater similarity between midbrain organoids and the embryonic midbrain than the embryonic prefrontal cortex. The following correlation analysis of the average expression of all common genes confirmed that the transcriptome of midbrain organoids is more similar to the embryonic midbrain ($\rho > 0.7$) than to the embryonic prefrontal cortex ($\rho < 0.7$) (Figure S3B). Moreover, the embryonic midbrain and midbrain organoids express typical midbrain markers, such as *TH*, *FOXA2*, *EN1*, and *EN2*, which were absent or expressed at low levels in the embryonic prefrontal cortex (Figure 1B). The expression of TH, FOXA2, and EN1 in midbrain organoids was also validated by immunofluorescence staining (Figure S3C). In addition, we aimed to associate midbrain organoids to different time points in embryonic midbrain development by comparing the expression of the common genes between both datasets. The WT35 midbrain organoids highly correlated with embryonic

week 9 (R = 0.92), while the midbrain organoids WT70 highly correlated with the week 10 (R = 0.90) (Figure 1C). These findings not only suggest that *in-vitro*-derived midbrain organoids show high gene expression similarities with the human embryonic midbrain but also manifest a developmental pattern comparable to their *in vivo* counterpart. In order to further validate the brain regional specificity of the organoids, we compared the scRNA-seq data of the embryonic midbrain to a cortex organoid[29] in the same manner (Figure S3D). The Pearson correlation coefficient of 0.05 showed insignificant correlation between the embryonic midbrain and the cortex organoid, providing evidence that organoids derived from different brain regions exhibit no close transcriptome similarities with the developing embryonic midbrain *in vivo*.

Midbrain organoids inherit physiological-relevant cellular populations that are shared with the developing embryonic midbrain

After confirming that midbrain organoids present a gene expression signature comparable to embryonic midbrain *in vivo*, we used the integration workflow from Seurat[31] to identify shared cellular populations across the *in vivo* and *in vitro* midbrain systems. We integrated the scRNA-seq data of the embryonic midbrain with healthy control and LRRK2-p.Gly2019Ser-mutant midbrain organoids of both differentiation time points 35 and 70 days (WT35, WT70, MUT35, and MUT70, respectively). We identified eight different cell types and visualized them by using UMAP (Figure 2A). To define cellular identities, we used the cell type marker gene list proposed by La Manno and colleagues[25] and compared it to the marker gene list per cluster of the integrated object (Figure S4). We verified each marker expression in every cell cluster identified in the integrated Seurat object. The number of marker genes that were present in the cell populations (corresponding to the cell types defined in La Manno et al., 2016[25]) are shown in Figure S5A. La Manno and colleagues[25] reported the presence of 25 cellular identities in the embryonic midbrain, including several sub-clusters of radial glia, progenitors, and dopaminergic neurons. To simplify cell identification, we grouped all 25 cell identities in more generic cell type clusters, such as neurons (NEURs), neuroblasts (NBs), progenitors, glia, pericytes, and endothelial cells. Neurons were further separated in non-dopaminergic neurons (non-DNs) and dopaminergic neurons (DNs). Cell identities were assigned to cell populations within the integrated Seurat object on the basis of the highest number of marker genes defining each generic cell type (Figure S5A). Once these clusters were broadly defined, using the embryonic midbrain data,[25] we verified and refined the assigned cell identities on the basis of additional cell type and maturity-specific marker expression (Figure 2B, Figure S5B). We confirmed the particularly high expression of neuronal maturity markers[34] and dopaminergic markers[9] in DNs. Therefore, we defined DNs as mature DNs (mDNs). The neuronal cluster presenting lower expression of maturity and neuronal-type-specific marker expression, we defined as young neurons (yNEURs) (Figure S5B). The vast majority of cells in the yNEUR cluster showed a stable expression of young neuronal markers such as *NCAM1*, *STMN1*, and *DCX* (Figure 2B). The mature neuronal marker *MAP2* as well as synaptic genes such as *SYP* and *SYT1* were expressed in the mDN and non-DN clusters. Lastly, expression of the DN markers *TH*, *KCNJ6*, and *NR4A2* as well as of the DN-specific synaptic markers *ROBO1* and *DCC* were confirmed in yNEURs and mDNs. Importantly, midbrain identity markers *FOXA2* and *LMX1A* were expressed in most of the cell types (glia, progenitors, yNEURs, and mDNs). The radial glia marker *SLC1A3* and neural progenitor markers *SOX2* and *MSI1* showed high expression in the glia and progenitor clusters, suggesting that glia cells are rather immature at this stage of embryonic midbrain development and, thus, display a genetic signature of early development in midbrain organoids. However, also more specific glial markers such as *GFAP* and *S100B* were already detectable in some of the cells. Endothelial cell identity was confirmed by the positive expression of the *CDH5*, while pericyte cells showed robust expression of the blood vessel development regulator *CSPG4*. Cells belonging to the NB cluster were positive for neural stem cell marker (*SOX2*) as well as immature (*DCX*) and mature neural *(SYT1*) and DN markers (*TH* and *KCNJ6*). However, none of these markers showed a constantly high expression among all cells in the NB cluster. This suggests that the identity of NBs is rather yet undefined and might be a specific feature of *in vitro* cultures, with the potential to develop into more mature neural cell types over time.

Further, we visualized UMAP embeddings of cell types and split them by datasets to reveal common and distinct cell types across embryonic midbrain and midbrain organoids (Figure 2C). Clusters of progenitors, yNEURs, mDNs, non-DNs, and glia were present in the embryonic midbrain as well as midbrain organoids, demonstrating that most cell types are common between the *in vitro* and *in vivo* midbrain systems. We observed that the NB cluster was present mainly in midbrain organoids and not in the embryonic midbrain and therefore was called NBs *in vitro*. Pericytes were found in midbrain organoids and the embryonic midbrain, however more mature endothelial cells were only present in the embryonic midbrain.

Next, we investigated the most variable gene expression pattern between the defined cell types (Figure 2D). The top 100 most variable genes led to a clustering of yNEURS, mDNs, non-DNs, and NBs together, confirming the common neuronal expression profile of these cell types. Pericytes and endothelial cells showed rather distinct genetic signature, consistent with the fact that these cells have non-neuronal identity. Glia and progenitors formed another separate cluster with a similar transcriptomic profile, implying again an early developmental stage of the glial cells.

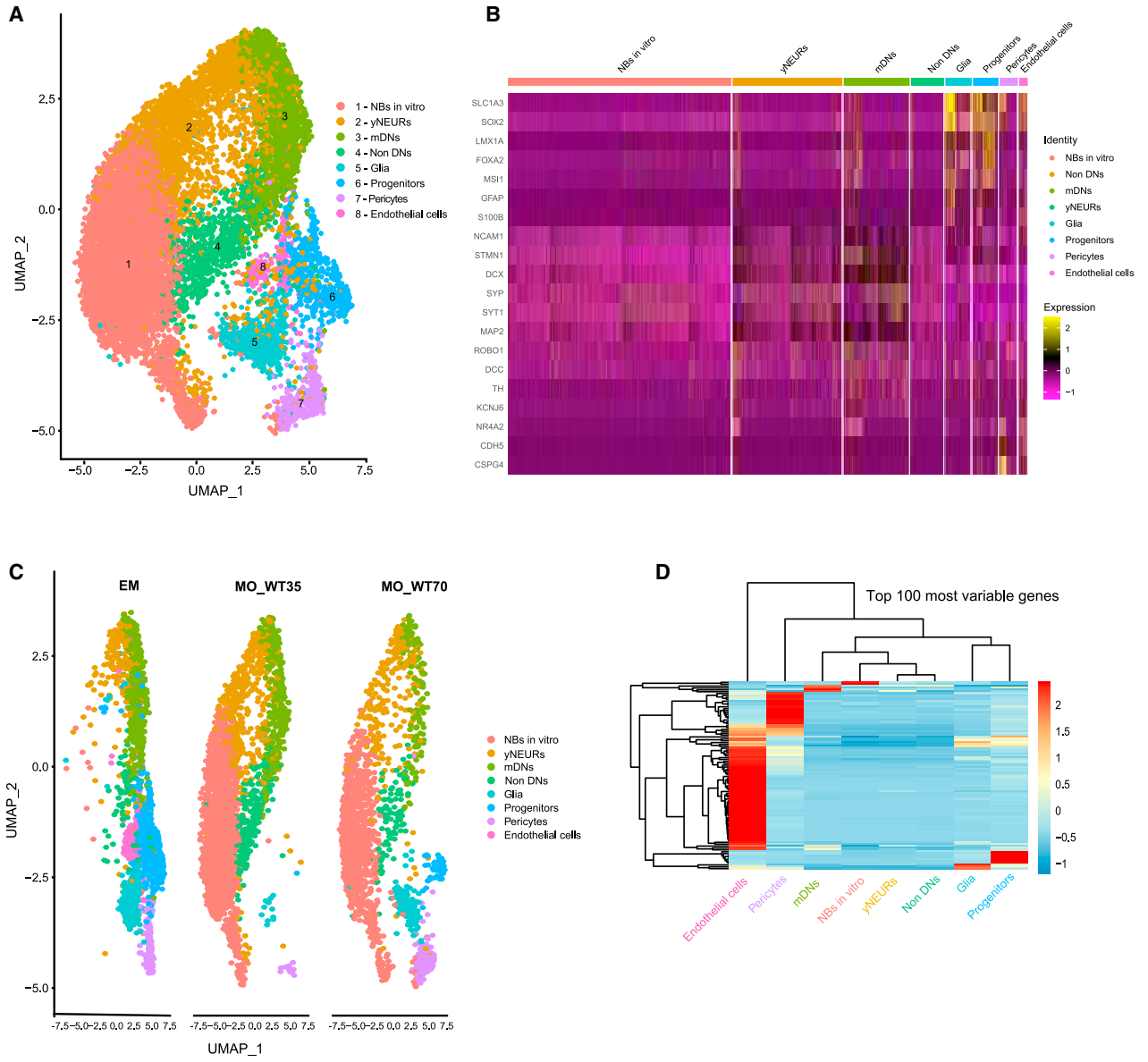

Figure 2. Midbrain organoids inherit physiological-relevant cellular populations that are shared with the developing embryonic midbrain

(A) UMAP of integrated Seurat object of merged scRNA-seq datasets of embryonic midbrain, and WT and MUT midbrain organoids 35 and 70 days of differentiation, showing cell clusters 1–8, after manual correction of oversampling. Each dot represents a single cell and is colored according to the cell identity.

(B) Identity heatmap showing cell-type-specific marker expression in identified cell clusters.

(C) UMAP of cell clusters in embryonic midbrain (EM), WT midbrain organoids of 35 days of differentiation (MO_WT35), and 70 days of differentiation (MO_WT70). Each dot represents a single cell and is colored according to the cell identity.

(D) Unsupervised hierarchical clustering of cell types, using the average expression of the top 100 most variable genes, visualized after *Z* score normalization.

Differential gene expression analysis reveals a *LRRK2*-related PD phenotype in the mutant midbrain organoids

Further, we assessed the potential of midbrain organoids in disease modeling by comparing the transcriptomic signature of the midbrain organoids derived from the healthy control where the LRRK2 p.Gly2019Ser variant was inserted with the isogenic WT counterpart.[27] As with the WT midbrain scRNA-seq data, we analyzed MUT midbrain organoid scRNA-seq data from organoids sampled at day 35 and day 70 of differentiation. We verified *LRRK2* expression in midbrain organoids and observed that it is expressed in a larger proportion of cells at later time points in both WT and MUT midbrain organoids (Figure S6A). In order to identify the key differences in the transcriptomic signature between MUT midbrain organoids and WT midbrain organoids, we computed the DEGs across both time points and all cell types with subsequent pathway enrichment analysis. The combined enrichment analysis of DEGs of both time

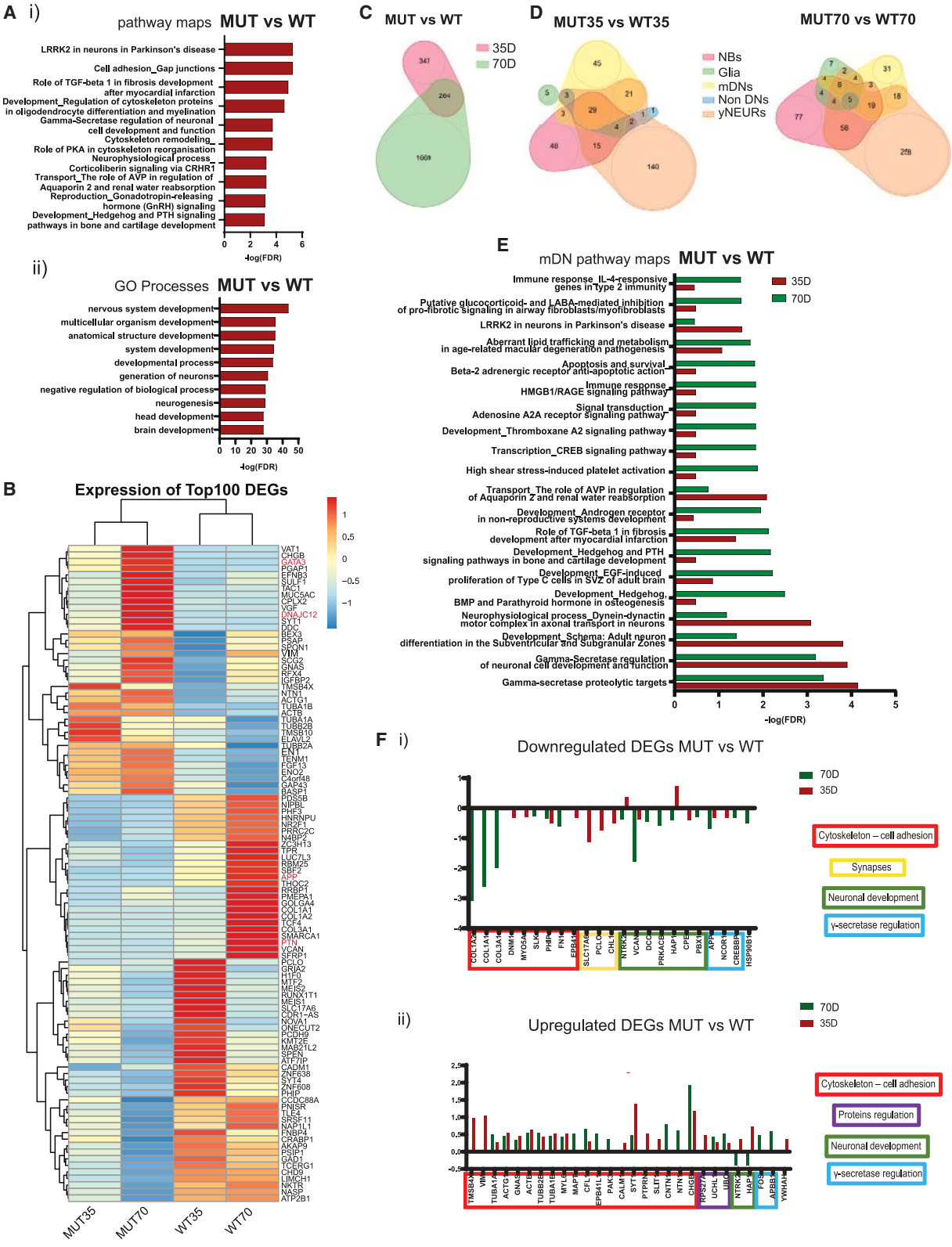

Figure 3. LRRK2-p.Gly2019Ser-mutant midbrain organoids recapitulate PD-associated pathways

(A) Pathway maps (i) and GO processes (ii) of the enrichment analysis of 294 DEG (p adj. value < 0.05) between MUT and WT midbrain organoids.

(B) Heatmap of to 100 DEG (p adj. value < 0.05) between MUT and WT midbrain organoids. Genes highlighted in red are the potential LRRK2 p.Gly2019Ser target genes involved in the neurodevelopment (see also Figure 6)

(legend continued on next page)

points showed the most significant enrichment in the pathway of LRRK2 role in neurons in PD (Figure 3Ai). Moreover, other pathways associated with *LRRK2*, such as cytoskeleton regulation and cell adhesion, were also enriched in the MUT midbrain organoids. In addition, we found a significant DEG enrichment in protein kinase cAMP-dependent signaling and the γ-secretase regulation pathway. We identified that the most significant Gene Ontology (GO) and network processes were related to the neuronal development and axonal guidance (Figure 3Aii, Figure S6Bi). Furthermore, the most enriched diseases were linked to the brain and nervous system, confirming a diseased state of MUT midbrain organoids (Figure S6Bii). Last, the top 100 DEGs (adj. p value < 0.05) clustered MUT midbrain organoids separately from the WT midbrain organoids for both time points, confirming that LRRK2 p.Gly2019Ser induced changes in gene expression (Figure 3B). Interestingly, in the WT midbrain organoids, the expression levels of the DEGs differ between the two time points of differentiation, while in the MUT35 and MUT70 midbrain organoids, DEGs showed very similar expression patterns, indicating a potential developmental impairment of MUT organoids. Similarly, the top 100 DEGs separated the majority of different cell types of the MUT midbrain organoids from the WT midbrain organoids for both time points (Figure S5C), indicating that the presence of the *LRRK2* variant is responsible for gene expression changes in all cell types in at least one of the time points. However, the pathway enrichment analysis combined for all cell types showed a higher significance in the enrichment of cytoskeleton remodeling, γ-secretase regulation, and LRRK2-related pathways for day 70, suggesting a stronger manifestation of the LRRK2-p.Gly2019Ser-associated changes overtime (Figure S6D). In support of that, we identified in total 347 DEGs (adj. p value < 0.05) at day 35 and 1,669 DEGs (adj. p value < 0.05) at day 70 between the MUT and WT midbrain organoids. 264 DEGs were common between both time points (Figure 3C). Next, we overlapped all DEGs (adj. p value < 0.05) between cell types and saw that the highest number of DEGs at both time points were present in NBs *in vitro*, yNEURs, and mDNs (Figure 3D, Figure S7A). Pathway enrichment analysis identified that the cytoskeleton-regulation-related pathways were significant in the MUT35 and MUT70 midbrain organoids in all three respective cell types, while LRRK2-PD-related pathway occurred to be highly significant in NBs *in vitro*. (Figure 3E, Figure S7Bi). In mDNs and yNEURs, the γ-secretase and neurodevelopmental regulation pathways were identified as the most enriched for both time points (Figure 3E, Figure S6Bii), additionally indicating a possible link between LRRK2 p.Gly2019Ser and γ-secretase function.

In order to investigate the gene expression profiles between the MUT and WT midbrain organoids in more detail, we visualized the fold changes of the genes involved in the most significantly enriched pathways (Figures 3Fi and 3Fii). Genes related to cytoskeleton dysregulations, such as *COL1A2*, *COL1A1*, *COL3A1*, *DNM1*, *MYO5A*, *PHIP*, *SLK*, *FN1*, and *EPB41*, were found to be downregulated with a log2FC between −0.26 and −3, while others, such as *TMSB4X*, *VIM*, *TUBA1A*, *ACTG1*, *GNAS*, *TUBB2B*, *TUBA1B*, *MYL6*, *MAPT*, *CFL1*, *EPB41L1*, *PAK3*, *CALM1*, *SYT1*, *PTPRN*, *SLIT1*, *CNTN1*, *NTN1*, and *CHGB*, were found upregulated (log2FC between 0.26 and 1.93) in MUT midbrain organoids at the majority of both time points. Synapses-related genes, such as *SLC17A6*, *PCLO*, and *CHL1*, were particularly downregulated (log2FC between −0.5 and −1.12) in MUT35 midbrain organoids, but they were not differentially expressed in MUT70 midbrain organoids. Genes that are associated with neuronal development, such as *NTRK2*, *VCAN*, *DCC*, *PRKACB*, *HAP1*, *CPE*, and *PBX1*, were also dysregulated in MUT midbrain organoids. The majority of them were downregulated (log2FC between −0.38 and −1.77) in MUT70 midbrain organoids, while *NTRK2* and *HAP1* were upregulated (log2FC 0.36 and 0.72, respectively) in MUT35 midbrain organoids. Protein regulation-associated genes, such as *RPS27A*, *UCHL1*, and *UBC*, were upregulated (log2FC between 0.25 and 0.52) at both time points. Additionally, genes that are related to the γ-secretase regulation pathway, such as *APP*, *NCOR1*, and *CREBBP*, were downregulated (log2FC between −0.31 and −0.68) in MUT35 and MUT70 midbrain organoids, but *FOS* and *APBB1* were upregulated (log2FC 0.47 and 0.59, respectively), particularly in MUT70 midbrain organoids. We also observed a dysregulation of *HSP90B1*, which was downregulated (log2FC −0.51) at MUT70 midbrain organoids and *YWHAH* showing upregulation (log2FC 0.36) in MUT35 midbrain organoids. These genes encode HSP90B1 and 14-3-3 family proteins, respectively, known as direct interacting partners with LRRK2.

Mutant midbrain organoids have a distinct cellular composition and correlate differently with the stages of embryonic development

We observed that MUT midbrain organoids differ from WT midbrain organoids in their cellular composition. In the UMAP embedding plot split by models and colored by cell types (Figure S8A), we saw that progenitors and pericytes, which are shared cellular populations between WT midbrain organoids and embryonic midbrain, are not present in MUT

(C) Venn diagram, showing the number of DEGs between MUT and WT midbrain organoids found at 35 days and 70 days of differentiation (p adj. value < 0.05).
(D) Venn diagrams, showing the number of DEGs found in each cell type between MUT and WT midbrain organoids fat 35 days and 70 days (p adj. value < 0.05).
(E) Mature DN pathway processes enrichment based on the DEGs identified in mDNs between MUT and WT midbrain organoids (p adj. value < 0.05).
(F) Fold changes of genes selected from the top enriched pathways dysregulated in mDNs.

midbrain organoids at any time point. On the contrary, we observed that the glia population is more enriched in MUT35 than in WT35 midbrain organoids. To confirm our observations, we subset the integrated Seurat object by the respective cell clusters and plotted them separately in the embryonic midbrain and in the WT as well as in the MUT midbrain organoids for both time points (Figure 4A). We saw that pericytes positive for the endothelial lineage marker *MCAM* and for the major regulator of angiogenic events, *SPARC*, are highly represented in WT70 midbrain organoids and in the embryonic midbrain but not in MUT midbrain organoids. Similarly, progenitors positive for the G2-proliferation-associated *CENPF* marker were only detected in the embryonic midbrain and WT70 midbrain organoids. A higher number of glia cells expressing *VIM* were already detected in MUT35 midbrain organoids compared to WT35 midbrain organoids. However, an increase of glia over time is more evident in WT than in MUT midbrain organoids.

Next, we calculated the proportion of each cell type present in WT and MUT midbrain organoids at both time points (Figure 4B). We saw a reduction of NBs *in vitro* (62%→51%) and yNEURs (17%→12%) from WT35 to the WT70. This reduction of less mature cells in WT35 midbrain organoids resulted in an increased variety of cell types present in WT70 midbrain organoids. Moreover, the cellular profile of WT70 midbrain organoids was quite similar to the cellular diversity observed in embryonic midbrain (Figure S8B). The major difference here was a high percentage of progenitors in the embryonic midbrain that seemed to be replaced by the presence of NBs *in vitro* in WT70 midbrain organoids.

Contrary to the WT midbrain organoids, in the MUT midbrain organoids, there was no evident difference in cell-type evolution over time. The same cell types were present in the MUT35 and MUT70 midbrain organoids, besides the fact that NBs *in vitro* almost doubled over time. Furthermore, the average gene expression correlation between MUT midbrain organoids and embryonic midbrain developmental time points showed that MUT35 midbrain organoids correlated better with embryonic development for all time points, compared to WT35 midbrain organoids (Figure 1C, Figure 4C). On the other hand, MUT70 midbrain organoids had a weaker correlation with the embryonic midbrain than the WT70 midbrain organoids, especially for week 11, which is also the latest and therefore most mature time point (R WT = 0.89 versus R MUT = 0.83). All together, these finding suggest that MUT midbrain organoids have a different developmental path compared to WT midbrain organoids and embryonic midbrain.

To further investigate the developmental differences between the MUT and WT midbrain organoids, we computed pseudotime trajectories to explore pseudotemporal ordering of midbrain organoid cell populations compared to the embryonic midbrain developmental time points. As the root, we chose WT35 NBs *in vitro* and we visualized the trajectories in UMAP plots colored by cell types and developmental time points of midbrain organoids and embryonic midbrain (Figures 4Di and 4Dii). We observed that mDNs of WT35 midbrain organoids are placed closer to embryonic developmental week 9 (branch point 2 and red circle 1 in Figure 4Dii), while mDNs of WT70 midbrain organoids were closer to embryonic developmental week 10 (branch point 2 and red circle 2 in Figure 4Dii), which is consistent with the gene average expression correlation analysis between WT midbrain organoids and embryonic midbrain. In clear contrast to this, we observed that mDNs of MUT35 and MUT70 midbrain organoids are placed closely to each other and formed a separate branch (branch point 3 to the endpoint 3 in Figure 4Di), which did not align with the embryonic midbrain trajectory. Further, we observed that glia cells of MUT70 and WT70 midbrain organoids (endpoint 2 and endpoint 8 in Figure 4Di) were arranged in close proximity to embryonic week 11 (endpoint 2 in Figure 4Dii), presenting appropriate developmental pattern, where gliogenesis follows neurogenesis. The similar distribution of MUT and WT glia within the pseudotemporal space indicates that the previously observed stagnation in glial development is linked to its number and not its quality. In general, the cells of MUT70 midbrain organoids were placed further from the embryonic developmental trajectory in the UMAP plot than the cells of WT70 midbrain organoids. This indicates that MUT midbrain organoids manifest a developmental deviation, while the development of WT midbrain organoids is more similar to embryonic midbrain *in vivo*. Moreover, MUT70 midbrain organoids demonstrated a more cyclic trajectory, confirming a limited cellular developmental path that is resulting in less variable cellular identities.

Mutant midbrain organoids compared to wild-type midbrain organoids show impaired pseudotemporal development that manifests in an untimely and incomplete differentiation

In order to further explore the developmental deviation of the MUT midbrain organoids from WT midbrain organoids, we computed a developmental pseudotime trajectory only across midbrain organoids (WT35, WT70, MUT35, and MUT70), excluding the embryonic midbrain. The cell distribution along the trajectory starting from NBs *in vitro* of WT35, demonstrated accelerated differentiation of MUT35 midbrain organoids with subsequent developmental withhold (Figure 5A). We observed that mDNs might be the most affected cellular population. We saw that mDNs of WT midbrain organoids follow a differentiation path along the pseudotime trajectory from WT35 to the edge of WT70 midbrain organoids (endpoint 4 to 9). Contrary, mDNs of MUT35 midbrain organoids were located in close proximity to mDNs of MUT70 midbrain organoids (between endpoints 1 and 6), implying the impaired mDN maturation. In addition, glia cells of MUT35 midbrain organoids were located close to the WT70 midbrain organoids on the pseudotime trajectory (between branch points 7 and 8), confirming forwarded glia differentiation of MUT35 midbrain organoids.

Next, we computed genes with a clear expression switch across the developmental trajectory between WT35 and

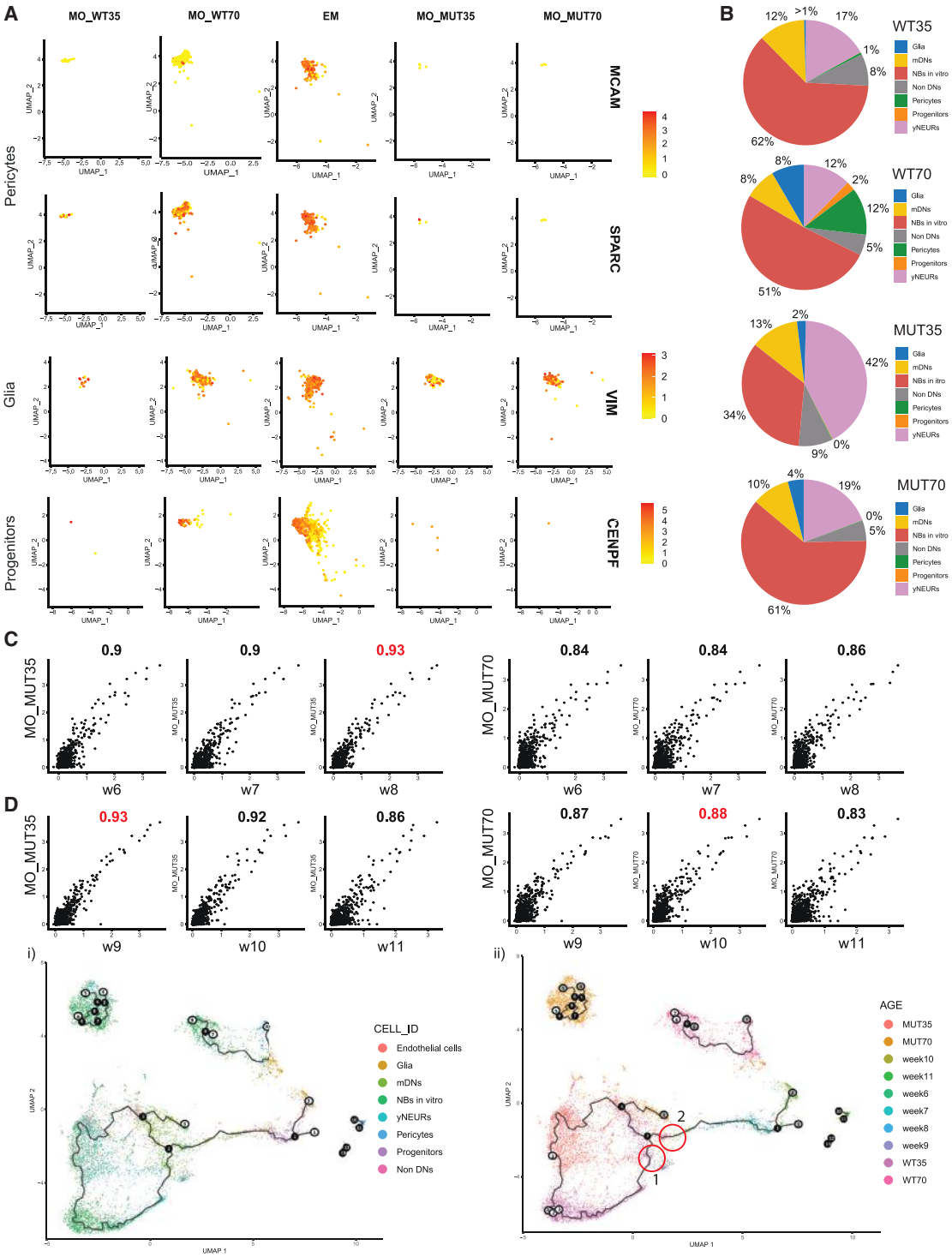

Figure 4. LRRK2-p.Gly2019Ser-mutant midbrain organoids have a different cellular composition and correlate differently with the stages of embryonic midbrain development

(A) Cell cluster identities defined by typical marker expression between WT and MUT midbrain organoids for pericytes, glia, and progenitor cells. Each dot represents a single cell and is colored according to the expression level.

(B) Percentage of cell identities in WT35, WT70, MUT35, and MUT70 midbrain organoids.

(C) The average gene expression correlation between MUT midbrain organoids 35 days of differentiation (MO_MUT35) and 70 days of differentiation (MO_MUT70) compared to the embryonic midbrain (EM) developmental weeks (w6–w11). The Pearson correlation coefficient is displayed above each comparison. Each dot represents a single cell.

(D) Batch-corrected pseudotime analysis based on the 150 dimensions. Each dot represents a single cell. The starting point is WT35 NBs *in vitro*. Cell distribution along the trajectory colored by cell identities (i) and by datasets (ii). Black nodes define branchpoints of the trajectory, white nodes define trajectory graph nodes, and gray nodes define endpoints of the certain trajectory leaf. Red circles indicate the position of mDNs of WT35 and WT70 midbrain organoids.

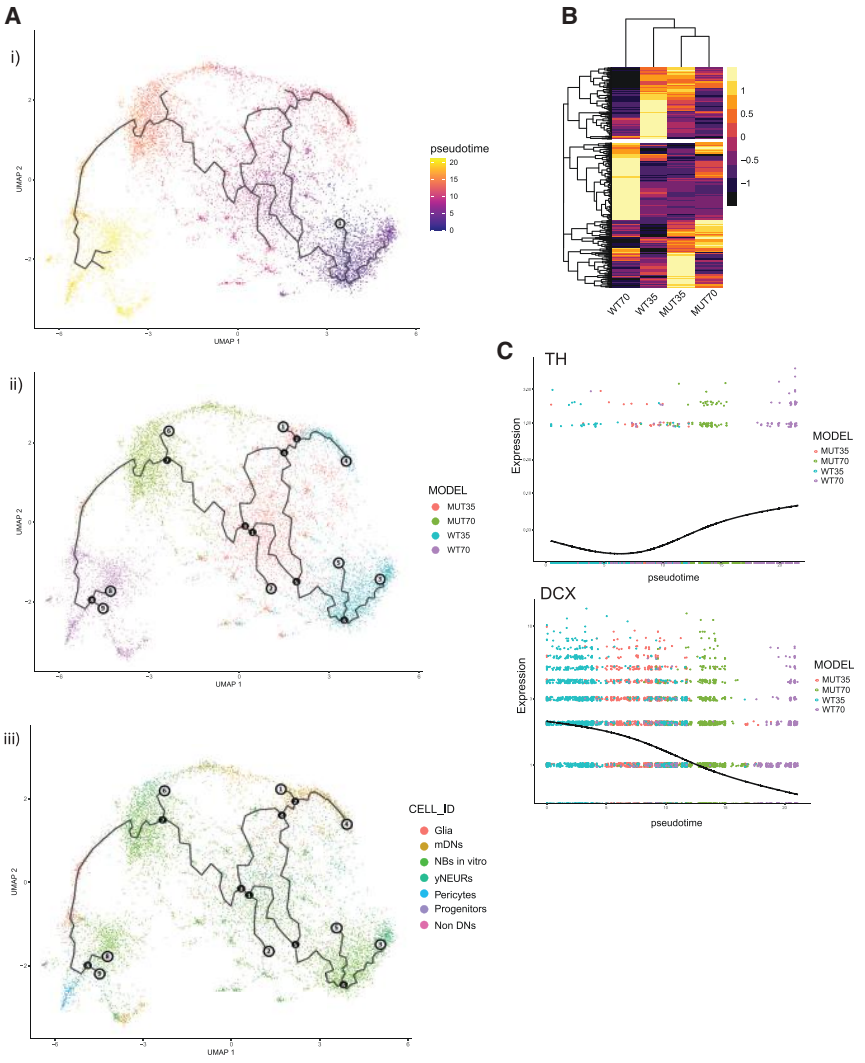

Figure 5. Transcriptome signatures over time reveal impaired development of LRRK2-p.Gly2019Ser-mutant midbrain organoids

(A) Pseudotime analysis of midbrain organoids with the root node WT35 NBs *in vitro* (i). Pseudotime trajectory, cells colored by the model: WT35, WT70, MUT35, and MUT70 (ii). Pseudotime trajectory, cells colored by cell identity (iii). Black nodes define branchpoints of the trajectory and gray nodes define endpoints/outcomes of the certain trajectory leaf.

(B) Genes with fitted expression pattern along the trajectory between WT35 and WT70 midbrain organoids, visualized in heatmap after *Z* score normalization in WT and MUT organoids.

(C) Pseudotemporal expression of *TH* and *DCX* across the cells in WT and MUT midbrain organoids. Each dot represents a single cell.

WT70 midbrain organoids (Figure 5B, Figure S8C). We investigated whether the same genes that have a temporal dynamic expression pattern in WT midbrain organoids show similar expression tendency in MUT midbrain organoids (Figure 5B). We observed that MUT midbrain organoids presented a completely different expression of the same genes, suggesting that MUT midbrain organoids do not follow the same developmental process as WT midbrain organoids. Furthermore, we highlighted the temporal expression of the rate-limiting enzyme of dopamine synthesis, tyrosine hydroxylase (*TH*), and the developing neuronal marker doublecortin (*DCX*). *TH* expression showed an increase over time in WT midbrain organoids but was impaired in the MUT midbrain organoids at both time points. *DCX* showed a clear decrease in the expression between WT35 and WT70 midbrain organoids. While in MUT35 midbrain organoids its expression was already further declined, it was still expressed at MUT70 midbrain organoids, further supporting an accelerated differentiation in MUT midbrain organoids at early time points of development accompanied by an incomplete differentiation at later developmental stages.

These results imply that mutant midbrain organoids reach a deadlock at some point during development.

Identification of potential LRRK2 p.Gly2019Ser target genes that could underlie impaired neurodevelopment and contribute to explain the PD-associated genetic signature

On the basis of the DEG analysis and after pseudotime trajectory examination, we distinguished four potentially promising candidate genes that have already been associated with PD[35–40]—*DNAJC12*, *GATA3*, *PTN*, and *APP* (Figure 3B). These genes showed a temporal dynamic expression in the developing embryo and were significantly differentially expressed in MUT midbrain organoids compared to WT midbrain organoids. Their considerable change in expression during embryonic development indicates an active role in neurodevelopment (Figure 6A). Moreover, differential expression between MUT and WT midbrain organoids further supports altered MUT midbrain organoid neurodevelopment. *DNAJC12* and *GATA3* showed a significant upregulation in every neuronal cell type and glia in MUT midbrain organoids compared to WT midbrain organoids in both time points (Figures 6B and 6C). In addition, in MUT organoids, *DNAJC12* and *GATA3* expression increased over time in contrast to the embryonic midbrain where the expression decreased after peaking at week 9. In the neuronal clusters of WT midbrain organoids, the expression pattern of these two genes was comparable to embryonic development, showing highest expression levels at 35 days (corresponding to week 9). In contrast, *PTN* and *APP* were found to be significantly downregulated

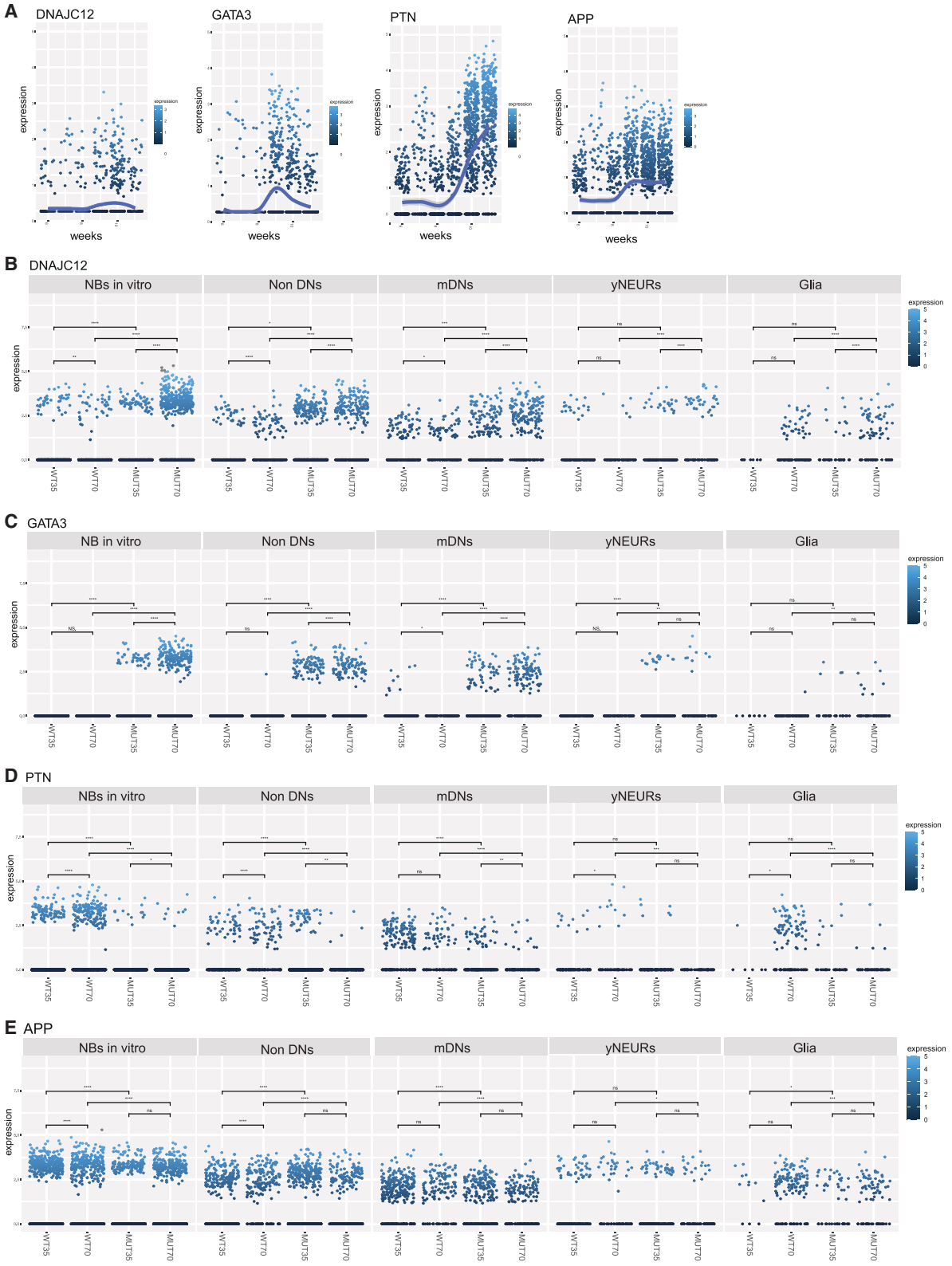

Figure 6. Discovery of potential LRRK2 p.Gly2019Ser target genes that might be involved in impaired neurodevelopment of mutant midbrain organoids

(A) *DNAJC12*, *GATA3*, *PTN*, and *APP* expression profile over the embryonic development time points (w6–w11). Each dot represents a single cell of embryonic midbrain and is colored according to the expression level.

(legend continued on next page)

in MUT midbrain organoid neuronal cell types and glia compared to WT midbrain organoids (Figures 6D and 6E). We observed that both *PTN* and *APP* expression tended to increase over time in embryonic midbrain development. A similar expression pattern was observed in NBs *in vitro*, yNEURs, and glia of WT midbrain organoid but not in MUT midbrain organoids. These results highlight a dysregulation of genes with essential roles in neuronal development and neuroprotection that might be directly associated with the LRRK2 p.Gly2019Ser variant, linking *LRRK2* to the regulation of nigrostriatal system development.

Discussion

Our analysis of scRNA-seq data of human midbrain organoids and embryonic midbrain highlights the physiological relevance of midbrain organoids and their potential in disease modeling. Over the recent years, midbrain organoids have become a widely used model in PD studies, as the midbrain is the most affected region in the brain of PD patients.[9,20,23,41,42] In the present study, we were able to show the developmental correlation of healthy control-derived midbrain organoids from 35 and 70 days of culture[9] with human embryonic midbrain.[25] Importantly, midbrain organoids showed a higher degree of correlation with embryonic midbrain development than with the embryonic prefrontal cortex, validating the midbrain identity of the organoids. In support of this, we did not find a significant correlation between the cortex organoids[29] and embryonic midbrain, which further validates the specificity of the brain regional organoids. In addition, our analysis implicates developmental maturation of midbrain organoids after long time culture (e.g., 70 days), which showed a better correlation with the later stages of embryonic midbrain development.

Previous studies have demonstrated the cellular heterogeneity of human brain organoids and their similarities with their fetal counterparts.[43,44] Similarly, our analysis showed that midbrain organoids exhibit a shared cellular composition with the developing embryonic midbrain. One interesting finding is the identification of pericytes in midbrain organoids. It has been reported that pericytes can originate from the neuroectoderm and contribute to the formation of vasculature in the CNS.[45–47] The presence of mesenchymal cells was also originally reported by Smits et al., 2020.[26] Moreover, recent studies showed that a mesenchymal-like cell population appears in the early development of the cortex, even before the beginning of neurogenesis.[48] Nevertheless, because the cells in midbrain organoids are guided toward midbrain identity by the expansion of the neuroepithelium, the presence of more mature endothelial cells is not expected. Accordingly, the endothelial cell cluster was found only in the embryonic midbrain and not in midbrain organoids. In contrast, the NB *in vitro* cluster was almost uniquely present in the midbrain organoids. Although these cells did not show a significant variable gene expression profile and clustered with neuronal cell types, there was no expression of reliable marker genes. Due to their unclear gene expression profile, NBs *in vitro* seemed to be less comparable to the physiological cell types shared between midbrain organoids and embryonic midbrain. We speculate that this NB cluster represents mfNPCs, which is the starting cell population for midbrain organoid generation. Although these cells are artificially patterned toward midbrain identity[49] and show unspecific genetic identity,[50] they can give rise to multiple physiologically relevant neuronal cell types and glia, similar to their *in vivo* neural progenitor counterpart.

When comparing MUT to WT midbrain organoids, clear differences become visible regarding their cellular composition, revealing PD-associated phenotypic differences. The MUT midbrain organoids reveal a faster differentiation profile that limits the development of a more variable and mature cellular composition. The accelerated differentiation phenotype at 35 days that we observed with pseudotime analysis has been described before in *LRRK2*-related PD.[8–10] In addition, the MUT midbrain organoids have no evident differences in the cell type populations at both time points and pseudotime analysis revealed that besides the untimely differentiation, the MUT70 midbrain organoids face a premature arrest or slowdown of the differentiation capacity. Importantly, the mDNs were the most affected population of cells. They showed no indication of maturation along the trajectory in the MUT70 compared to the MUT35 midbrain organoids and had a reduced expression of TH in MUT midbrain organoids. The doubling of the number of NBs *in vitro* in MUT70 midbrain organoids might be a compensation strategy linked to the incapacity of terminal differentiation or an increase in mature cell death. Moreover, we observed that the MUT midbrain organoids contain a higher number of glial cells than WT midbrain organoids at early time points. A situation that is inverted in longer cultures (MUT70 and WT70). The pseudotime trajectory confirmed that glial cells of MUT35 midbrain organoids were located closer to the WT70 midbrain organoids, indicating a faster gliogenesis. Finally, and most importantly, in contrast to MUT midbrain organoids, WT midbrain organoids from longer cultures are capable of capturing the cellular diversity found in human embryonic midbrain development *in vivo*.

Regarding the developmental pattern of organoids and embryonal tissue, MUT midbrain organoids showed a different developmental path compared to WT midbrain

(B–E) *DNAJC12*, *GATA3*, *PTN*, and *APP* expression across major cell types in WT and MUT midbrain organoids at 35 days and 70 days of differentiation. Each dot represents a single cell of midbrain organoid and is colored according to the expression level. Kruskal-Wallis test $p < 0.05$*, $p < 0.01$**, $p < 0.001$***, $p < 0.00001$***.

organoids. From the correlation analysis, we saw that the MUT70 midbrain organoids have lower correlation than MUT35 midbrain organoids with the different time points of embryonic midbrain development. Furthermore, cells of MUT70 midbrain organoids were positioned further away from the embryonic pseudotemporal developmental trajectory in the UMAP plot, while cells of WT70 midbrain organoids have a development trail closer to embryonic development.

On the basis of the here-presented data, we propose that LRRK2 p.Gly2019Ser could be responsible for the observed developmental defects and the impaired cellular composition. Our *LRRK2* midbrain organoid model was able to capture the dysregulation of gene expression linked to *LRRK2*-induced PD. The analysis of DEGs between MUT and WT midbrain organoids showed the significance of LRRK2-related pathway in PD and highlighted GO processes related to nervous system development. In addition to individual gene dysregulation of LRRK2-associated pathways, the overall DEG analysis showed a clear separation of the MUT and WT midbrain organoid clusters, confirming the presence of disease-associated phenotypes.

The major dysregulated pathways were cytoskeleton remodeling and cell adhesion. It is well known that LRRK2 plays an important role in actin and microtubule dynamics. LRRK2 p.Gly2019Ser has been reported to disturb the cytoskeleton processes through increased kinase activity.[51,52] The dysregulation of actin and microtubule genes, which are key components of cytoskeleton dynamics, may lead to failure of the proper cellular differentiation process.[26] Cytoskeleton-related proteins, such as MYO5A, DNM1, EPB41, ACTB, MAPT, and VIM, are direct interacting partners of LRRK2.[53] We found that the corresponding genes have a dysregulated expression in the MUT midbrain organoids, indicating that altered LRRK2 function is able to impair the gene expression profile of its interactome. Altered LRRK2 function has also been described to have a role in impaired synaptogenesis.[51,54,55] Here, we identified significant downregulation of the synapse-related genes *SLC17A6*, *PCLO*, and *CHL1* specifically in MUT35 but not in MUT70 midbrain organoids. This observation suggests an impaired synaptogenesis occurring in early neurodevelopment of MUT midbrain organoids.

Further, direct LRRK2-interacting partners such as HSP90B1 and YWHAH have also been altered upon presence of the LRRK2 p.Gly2019Ser. HSP90B1 along with the other heat-shock proteins is involved in protein folding and has been linked to PD.[56] HSP90B1 is a chaperone protein from the HSP90 family that interacts with LRRK2. This interaction is important for the proteasomal degradation of LRRK2.[57] Thus, the downregulation of *HSP90B1* in MUT70 midbrain organoids could be linked to the toxic aggregation of mutant LRRK2. *YWHAH* encodes the 14-3-3 eta, known to regulate the activity of kinases, including LRRK2.[58]

Additionally, we identified dysregulation of genes related to the γ-secretase pathway. APP belongs to this pathway and shows a severe dysregulation in MUT midbrain organoid. *APP* encodes the β-amyloid precursor protein that has an important role in the development of neurodegenerative pathologies such as Alzheimer disease because of the accumulation of its derivative amyloid-beta (Aβ) peptide, which is induced by cleavage from secretases including the γ-secretase.[59,60] A link between Aβ accumulation and LRRK2 p.Gly2019Ser PD cases has also been made. LRRK2 phosphorylates the intracellular domain (AICD) of APP, which regulates the transcription of cytoskeleton-related genes and has a role in the loss of dopaminergic neurons in the midbrain of PD cases by induced neurotoxicity.[61] APP has also an important role in neurogenesis, gliogenesis, and neuroprotection in the developing brain.[35,60,62] Therefore, dysregulation of *APP* can be associated not only with the neurodegeneration but also with the aberrations of neuronal development. Indeed, during embryonic midbrain development, we observed a strong increase of *APP* expression over time, whereas in MUT midbrain organoids, we observed a significant reduction compared to WT midbrain organoids, especially in mDNs and glia cells.

Further evidence of altered cellular development of MUT midbrain organoids comes also from the changed expression of three PD-associated DEG candidates, *DNAJC12*, *GATA3*, and *PTN*. The expression pattern of these genes in the embryonic midbrain suggests their important role in development and differentiation of the cells, although these findings would benefit from further experimental validation. DNAJC12 is described to have a role in protein folding and export. Bi-allelic mutations of *DNAJC12* have been associated with hyperphenylalaninemia and neurodevelopmental delay in children. However, recent findings link mutation in *DNAJC12* to early-onset PD because of its interaction with aromatic amino-acid hydroxylases, including TH.[37,63] GATA3 has been described as an important regulator of CNS development and neuronal fate.[36] An association with PD has been reported via GATA family transcriptional regulation of *TRPM2* and *SNCA*.[38,64] Until now, there is no reported interaction of GATA3 and DNAJC12 with LRRK2. However, the notable upregulation of *GATA3* and *DNAJC12* in MUT midbrain organoids suggests their possible dysregulation due to LRRK2 p.Gly2019Ser and might explain the accelerated differentiation phenotype, subsequent maturation decline, and decreased expression of *TH*. In contrast, we observed that *PTN* is expressed significantly higher in WT midbrain organoids. PTN is a neurotrophic factor, highly expressed during development of nigrostriatal dopamine system, and later plays a role in cellular recovery and repair.[39,40] It has been shown to restore neuronal survival and functionality in a 6-OHDA mouse model.[39] The high expression of *PTN* in NBs *in vitro* of WT midbrain organoids may explain their better developmental trail compared to MUT midbrain organoids.

In summary, we demonstrated a high degree of transcriptome similarity between human midbrain organoids and embryonic midbrain, supporting the potential of midbrain

organoids to recapitulate human brain physiology. Moreover, our study showed the ability of midbrain organoids to capture LRRK2-p.Gly2019Ser-dependent alterations in gene expression, which highlights cellular processes related to cytoskeleton regulation, cell adhesion, and γ-secretase regulation during neuronal development. Finally, we observed developmental aberrations in MUT midbrain organoids and altered gene expression patterns along pseudotemporal trajectories, supporting a neurodevelopmental component in LRRK2-p.Gly2019Ser-associated PD.

Data and code availability

WT midbrain organoid scRNA-seq datasets are available at the following doi: https://doi.org/10.17881/lcsb.20190326.01. LRRK2-G2019S MUT midbrain organoid scRNA-seq datasets are available at the following doi: https://doi.org/10.17881/rc4f-nk07. The accession number for the raw data for WT and MUT midbrain organoids is GEO: GSE133894. The accession number for the raw data for the human embryo ventral midbrain between 6 and 11 weeks is GEO: GSE76381. The accession number for the raw data for scRNA-seq data of prefrontal cortex at developmental stages between gestational weeks 8 and 26 is GEO: GSE104276. The accession number for the raw data for scRNA-seq data of human cortical organoids is GEO: GSE130238. We used data only of 1-month-old cortical organoid, which better corresponds to the developmental stage of midbrain organoids. Data were analyzed with R version 3.6.2 with single-cell analysis toolkit Seurat version 3.2.0[31,65,66] and Monocle 3.[67] All scripts used for the analysis are available via GitHub: https://github.com/LCSB-DVB.

Supplemental information

Supplemental information can be found online at https://doi.org/10.1016/j.ajhg.2021.12.009.

Acknowledgments

This work was supported by the National Centre of Excellence in Research on Parkinson Disease (NCER-PD), which is funded by the Luxembourg National Research Fund (FNR/NCER13/BM/11264123). S.S. is supported by the FNR-funded doctoral training program PARK-QC (PRIDE17/12244779/PARK-QC). L.M.S. was supported by a fellowship from the FNR (AFR, Aides à la Formation-Recherche). A.G. received funding from the FNR within the framework of the ATTRACT (FNR9631103) and INTER (INTER/DFG/19/14429377) programs. Additionally, we would like to acknowledge support by an LCSB flagship project.

Declaration of interests

J.C.S. is co-inventor on a patent covering the generation of the here-described midbrain organoids (WO2017060884A1). Furthermore, J.C.S. is co-founder and shareholder of the company OrganoTherapeutics, which makes use of the midbrain organoid technology. The other authors declare no competing interests.

Received: June 14, 2021
Accepted: December 13, 2021
Published: January 24, 2022

Web resources

Metacore, https://portal.genego.com/
nVenn, http://degradome.uniovi.es/cgi-bin/nVenn/nvenn.cgi

References

1. Inamdar, N.N., Arulmozhi, D.K., Tandon, A., and Bodhankar, S.L. (2007). Parkinson's disease: genetics and beyond. Curr. Neuropharmacol. *5*, 99–113.
2. Paisán-Ruíz, C., Jain, S., Evans, E.W., Gilks, W.P., Simón, J., van der Brug, M., López de Munain, A., Aparicio, S., Gil, A.M., Khan, N., et al. (2004). Cloning of the gene containing mutations that cause PARK8-linked Parkinson's disease. Neuron *44*, 595–600.
3. Zimprich, A., Biskup, S., Leitner, P., Lichtner, P., Farrer, M., Lincoln, S., Kachergus, J., Hulihan, M., Uitti, R.J., Calne, D.B., et al. (2004). Mutations in LRRK2 cause autosomal-dominant parkinsonism with pleomorphic pathology. Neuron *44*, 601–607.
4. Ren, C., Ding, Y., Wei, S., Guan, L., Zhang, C., Ji, Y., Wang, F., Yin, S., and Yin, P. (2019). G2019S Variation in LRRK2: An Ideal Model for the Study of Parkinson's Disease? Front. Hum. Neurosci. *13*, 306.
5. Nickels, S.L., Walter, J., Bolognin, S., Gérard, D., Jaeger, C., Qing, X., Tisserand, J., Jarazo, J., Hemmer, K., Harms, A., et al. (2019). Impaired serine metabolism complements LRRK2-G2019S pathogenicity in PD patients. Parkinsonism Relat. Disord. *67*, 48–55.
6. Liu, G.H., Qu, J., Suzuki, K., Nivet, E., Li, M., Montserrat, N., Yi, F., Xu, X., Ruiz, S., Zhang, W., et al. (2012). Progressive degeneration of human neural stem cells caused by pathogenic LRRK2. Nature *491*, 603–607.
7. Winner, B., Kohl, Z., and Gage, F.H. (2011). Neurodegenerative disease and adult neurogenesis. Eur. J. Neurosci. *33*, 1139–1151.
8. Milosevic, J., Schwarz, S.C., Ogunlade, V., Meyer, A.K., Storch, A., and Schwarz, J. (2009). Emerging role of LRRK2 in human neural progenitor cell cycle progression, survival and differentiation. Mol. Neurodegener. *4*, 25.
9. Smits, L.M., Reinhardt, L., Reinhardt, P., Glatza, M., Monzel, A.S., Stanslowsky, N., Rosato-Siri, M.D., Zanon, A., Antony, P.M., Bellmann, J., et al. (2019). Modeling Parkinson's disease in midbrain-like organoids. NPJ Parkinsons Dis. *5*, 5.
10. Schulz, C., Paus, M., Frey, K., Schmid, R., Kohl, Z., Mennerich, D., Winkler, J., and Gillardon, F. (2011). Leucine-rich repeat kinase 2 modulates retinoic acid-induced neuronal differentiation of murine embryonic stem cells. PLoS ONE *6*, e20820.
11. Le Grand, J.N., Gonzalez-Cano, L., Pavlou, M.A., and Schwamborn, J.C. (2015). Neural stem cells in Parkinson's disease: a role for neurogenesis defects in onset and progression. Cell. Mol. Life Sci. *72*, 773–797.
12. Sancho, R.M., Law, B.M.H., and Harvey, K. (2009). Mutations in the LRRK2 Roc-COR tandem domain link Parkinson's disease to Wnt signalling pathways. Hum. Mol. Genet. *18*, 3955–3968.
13. Winner, B., Melrose, H.L., Zhao, C., Hinkle, K.M., Yue, M., Kent, C., Braithwaite, A.T., Ogholikhan, S., Aigner, R., Winkler, J., et al. (2011). Adult neurogenesis and neurite outgrowth are impaired in LRRK2 G2019S mice. Neurobiol. Dis. *41*, 706–716.
14. Berwick, D.C., and Harvey, K. (2012). LRRK2 functions as a Wnt signaling scaffold, bridging cytosolic proteins and membrane-localized LRP6. Hum. Mol. Genet. *21*, 4966–4979.

15. Hartmann, A. (2004). Postmortem studies in Parkinson's disease. Dialogues Clin. Neurosci. *6*, 281–293.
16. Blesa, J., and Przedborski, S. (2014). Parkinson's disease: animal models and dopaminergic cell vulnerability. Front. Neuroanat. *8*, 155.
17. Takahashi, K., and Yamanaka, S. (2006). Induction of pluripotent stem cells from mouse embryonic and adult fibroblast cultures by defined factors. Cell *126*, 663–676.
18. Arias-Fuenzalida, J., Jarazo, J., Qing, X., Walter, J., Gomez-Giro, G., Nickels, S.L., Zaehres, H., Schöler, H.R., and Schwamborn, J.C. (2017). FACS-Assisted CRISPR-Cas9 Genome Editing Facilitates Parkinson's Disease Modeling. Stem Cell Reports *9*, 1423–1431.
19. Vermilyea, S.C., Babinski, A., Tran, N., To, S., Guthrie, S., Kluss, J.H., Schmidt, J.K., Wiepz, G.J., Meyer, M.G., Murphy, M.E., et al. (2020). In Vitro CRISPR/Cas9-Directed Gene Editing to Model LRRK2 G2019S Parkinson's Disease in Common Marmosets. Sci. Rep. *10*, 3447.
20. Monzel, A.S., Smits, L.M., Hemmer, K., Hachi, S., Moreno, E.L., van Wuellen, T., Jarazo, J., Walter, J., Brüggemann, I., Boussaad, I., et al. (2017). Derivation of Human Midbrain-Specific Organoids from Neuroepithelial Stem Cells. Stem Cell Reports *8*, 1144–1154.
21. Schwamborn, J.C. (2018). Is Parkinson's disease a neurodevelopmental disorder and will brain organoids help us to understand it? Stem Cells Dev. *27*, 968–975.
22. Chlebanowska, P., Tejchman, A., Sułkowski, M., Skrzypek, K., and Majka, M. (2020). Use of 3D organoids as a model to study idiopathic form of parkinson's disease. Int. J. Mol. Sci. *21*, 694.
23. Kim, H., Park, H.J., Choi, H., Chang, Y., Park, H., Shin, J., Kim, J., Lengner, C.J., Lee, Y.K., and Kim, J. (2019). Modeling G2019S-LRRK2 Sporadic Parkinson's Disease in 3D Midbrain Organoids. Stem Cell Reports *12*, 518–531.
24. Kwak, T.H., Kang, J.H., Hali, S., Kim, J., Kim, K.P., Park, C., Lee, J.H., Ryu, H.K., Na, J.E., Jo, J., et al. (2020). Generation of homogeneous midbrain organoids with in vivo-like cellular composition facilitates neurotoxin-based Parkinson's disease modeling. Stem Cells *38*, 727–740.
25. La Manno, G., Gyllborg, D., Codeluppi, S., Nishimura, K., Salto, C., Zeisel, A., Borm, L.E., Stott, S.R.W., Toledo, E.M., Villaescusa, J.C., et al. (2016). Molecular Diversity of Midbrain Development in Mouse, Human, and Stem Cells. Cell *167*, 566–580.e19.
26. Smits, L.M., Magni, S., Kinugawa, K., Grzyb, K., Luginbühl, J., Sabate-Soler, S., Bolognin, S., Shin, J.W., Mori, E., Skupin, A., and Schwamborn, J.C. (2020). Single-cell transcriptomics reveals multiple neuronal cell types in human midbrain-specific organoids. Cell Tissue Res. *382*, 463–476.
27. Qing, X., Walter, J., Jarazo, J., Arias-Fuenzalida, J., Hillje, A.L., and Schwamborn, J.C. (2017). CRISPR/Cas9 and piggyBac-mediated footprint-free LRRK2-G2019S knock-in reveals neuronal complexity phenotypes and α-Synuclein modulation in dopaminergic neurons. Stem Cell Res. (Amst.) *24*, 44–50.
28. Zhong, S., Zhang, S., Fan, X., Wu, Q., Yan, L., Dong, J., Zhang, H., Li, L., Sun, L., Pan, N., et al. (2018). A single-cell RNA-seq survey of the developmental landscape of the human prefrontal cortex. Nature *555*, 524–528.
29. Trujillo, C.A., Gao, R., Negraes, P.D., Gu, J., Buchanan, J., Preissl, S., Wang, A., Wu, W., Haddad, G.G., Chaim, I.A., et al. (2019). Complex Oscillatory Waves Emerging from Cortical Organoids Model Early Human Brain Network Development. Cell Stem Cell *25*, 558–569.e7.
30. Macosko, E.Z., Basu, A., Satija, R., Nemesh, J., Shekhar, K., Goldman, M., Tirosh, I., Bialas, A.R., Kamitaki, N., Martersteck, E.M., et al. (2015). Highly parallel genome-wide expression profiling of individual cells using nanoliter droplets. Cell *161*, 1202–1214.
31. Stuart, T., Butler, A., Hoffman, P., Hafemeister, C., Papalexi, E., Mauck, W.M., 3rd, Hao, Y., Stoeckius, M., Smibert, P., and Satija, R. (2019). Comprehensive Integration of Single-Cell Data. Cell *177*, 1888–1902.e21.
32. Becht, E., McInnes, L., Healy, J., Dutertre, C.A., Kwok, I.W.H., Ng, L.G., Ginhoux, F., and Newell, E.W. (2018). Dimensionality reduction for visualizing single-cell data using UMAP. Nat. Biotechnol. *37*, 38–47.
33. Hafemeister, C., and Satija, R. (2019). Normalization and variance stabilization of single-cell RNA-seq data using regularized negative binomial regression. Genome Biol. *20*, 296.
34. Chen, X., Zhang, K., Zhou, L., Gao, X., Wang, J., Yao, Y., He, F., Luo, Y., Yu, Y., Li, S., et al. (2016). Coupled electrophysiological recording and single cell transcriptome analyses revealed molecular mechanisms underlying neuronal maturation. Protein Cell *7*, 175–186.
35. Zhou, Z.D., Chan, C.H.S., Ma, Q.H., Xu, X.H., Xiao, Z.C., and Tan, E.K. (2011). The roles of amyloid precursor protein (APP) in neurogenesis, implications to pathogenesis and therapy of alzheimer Disease (AD). Cell Adh. Migr. *5*, 280–292.
36. Tsarovina, K., Reiff, T., Stubbusch, J., Kurek, D., Grosveld, F.G., Parlato, R., Schütz, G., and Rohrer, H. (2010). The Gata3 transcription factor is required for the survival of embryonic and adult sympathetic neurons. J. Neurosci. *30*, 10833–10843.
37. Cortès-Saladelafont, E., Lipstein, N., and García-Cazorla, À. (2018). Presynaptic disorders: a clinical and pathophysiological approach focused on the synaptic vesicle. J. Inherit. Metab. Dis. *41*, 1131–1145.
38. Scherzer, C.R., Grass, J.A., Liao, Z., Pepivani, I., Zheng, B., Eklund, A.C., Ney, P.A., Ng, J., McGoldrick, M., Mollenhauer, B., et al. (2008). GATA transcription factors directly regulate the Parkinson's disease-linked gene α-synuclein. Proc. Natl. Acad. Sci. USA *105*, 10907–10912.
39. Gombash, S.E., Lipton, J.W., Collier, T.J., Madhavan, L., Steece-Collier, K., Cole-Strauss, A., Terpstra, B.T., Spieles-Engemann, A.L., Daley, B.F., Wohlgenant, S.L., et al. (2012). Striatal pleiotrophin overexpression provides functional and morphological neuroprotection in the 6-hydroxydopamine model. Mol. Ther. *20*, 544–554.
40. Marchionini, D.M., Lehrmann, E., Chu, Y., He, B., Sortwell, C.E., Becker, K.G., Freed, W.J., Kordower, J.H., and Collier, T.J. (2007). Role of heparin binding growth factors in nigrostriatal dopamine system development and Parkinson's disease. Brain Res. *1147*, 77–88.
41. Galet, B., Cheval, H., and Ravassard, P. (2020). Patient-Derived Midbrain Organoids to Explore the Molecular Basis of Parkinson's Disease. Front. Neurol. *11*, 1005.
42. Nickels, S.L., Modamio, J., Mendes-Pinheiro, B., Monzel, A.S., Betsou, F., and Schwamborn, J.C. (2020). Reproducible generation of human midbrain organoids for in vitro modeling of Parkinson's disease. Stem Cell Res. (Amst.) *46*, 101870.
43. Quadrato, G., Nguyen, T., Macosko, E.Z., Sherwood, J.L., Min Yang, S., Berger, D.R., Maria, N., Scholvin, J., Goldman, M., Kinney, J.P., et al. (2017). Cell diversity and network dynamics in photosensitive human brain organoids. Nature *545*, 48–53.
44. Camp, J.G., Badsha, F., Florio, M., Kanton, S., Gerber, T., Wilsch-Bräuninger, M., Lewitus, E., Sykes, A., Hevers, W.,

Lancaster, M., et al. (2015). Human cerebral organoids recapitulate gene expression programs of fetal neocortex development. Proc. Natl. Acad. Sci. USA *112*, 15672–15677.
45. Payne, L.B., Hoque, M., Houk, C., Darden, J., and Chappell, J.C. (2020). Pericytes in Vascular Development. Curr. Tissue Microenviron. Rep. *1*, 143–154.
46. Korn, J., Christ, B., and Kurz, H. (2002). Neuroectodermal origin of brain pericytes and vascular smooth muscle cells. J. Comp. Neurol. *442*, 78–88.
47. Yamazaki, T., and Mukouyama, Y.S. (2018). Tissue Specific Origin, Development, and Pathological Perspectives of Pericytes. Front. Cardiovasc. Med. *5*, 78.
48. Eze, U., Bhaduri, A., Haeussler, M., Nowakowski, T., and Kriegstein, A. (2020). Single-Cell Atlas of Early Human Brain Development Highlights Heterogeneity of Human Neuroepithelial Cells and Early Radial Glia. Nat. Neurosci. *1*, 143–154.
49. Reinhardt, P., Glatza, M., Hemmer, K., Tsytsyura, Y., Thiel, C.S., Höing, S., Moritz, S., Parga, J.A., Wagner, L., Bruder, J.M., et al. (2013). Derivation and expansion using only small molecules of human neural progenitors for neurodegenerative disease modeling. PLoS ONE *8*, e59252.
50. van den Hurk, M., and Bardy, C. (2019). Single-cell multimodal transcriptomics to study neuronal diversity in human stem cell-derived brain tissue and organoid models. J. Neurosci. Methods *325*, 108350.
51. Jeong, G.R., and Lee, B.D. (2020). Pathological Functions of LRRK2 in Parkinson's Disease. Cells *9*, 1–19.
52. Häbig, K., Gellhaar, S., Heim, B., Djuric, V., Giesert, F., Wurst, W., Walter, C., Hentrich, T., Riess, O., and Bonin, M. (2013). LRRK2 guides the actin cytoskeleton at growth cones together with ARHGEF7 and Tropomyosin 4. Biochim. Biophys. Acta *1832*, 2352–2367.
53. Manzoni, C., Denny, P., Lovering, R.C., and Lewis, P.A. (2015). Computational analysis of the LRRK2 interactome. PeerJ *3*, e778.
54. Matikainen-Ankney, B.A., Kezunovic, N., Mesias, R.E., Tian, Y., Williams, F.M., Huntley, G.W., and Benson, D.L. (2016). Altered development of synapse structure and function in striatum caused by Parkinson's disease-linked LRRK2-G2019S mutation. J. Neurosci. *36*, 7128–7141.
55. Lamonaca, G., and Volta, M. (2020). Alpha-Synuclein and LRRK2 in Synaptic Autophagy: Linking Early Dysfunction to Late-Stage Pathology in Parkinson's Disease. Cells *9*, 1115.
56. Vergara, D., Gaballo, A., Signorile, A., Ferretta, A., Tanzarella, P., Pacelli, C., Di Paola, M., Cocco, T., and Maffia, M. (2017). Resveratrol Modulation of Protein Expression in *parkin*-Mutant Human Skin Fibroblasts: A Proteomic Approach. Oxid. Med. Cell. Longev. *2017*, 2198243.
57. Ko, H.S., Bailey, R., Smith, W.W., Liu, Z., Shin, J.H., Lee, Y.I., Zhang, Y.J., Jiang, H., Ross, C.A., Moore, D.J., et al. (2009). CHIP regulates leucine-rich repeat kinase-2 ubiquitination, degradation, and toxicity. Proc. Natl. Acad. Sci. USA *106*, 2897–2902.
58. Obsilova, V., and Obsil, T. (2020). The 14-3-3 proteins as important allosteric regulators of protein kinases. Int. J. Mol. Sci. *21*, 1–16.
59. Zhang, X., Li, Y., Xu, H., and Zhang, Y.W. (2014). The γ-secretase complex: from structure to function. Front. Cell. Neurosci. *8*, 427.
60. O'Brien, R.J., and Wong, P.C. (2011). Amyloid precursor protein processing and Alzheimer's disease. Annu. Rev. Neurosci. *34*, 185–204.
61. Chen, Z.C., Zhang, W., Chua, L.L., Chai, C., Li, R., Lin, L., Cao, Z., Angeles, D.C., Stanton, L.W., Peng, J.H., et al. (2017). Phosphorylation of amyloid precursor protein by mutant LRRK2 promotes AICD activity and neurotoxicity in Parkinson's disease. Sci. Signal. *10*, 1–12.
62. Bergström, P., Agholme, L., Nazir, F.H., Satir, T.M., Toombs, J., Wellington, H., Strandberg, J., Bontell, T.O., Kvartsberg, H., Holmström, M., et al. (2016). Amyloid precursor protein expression and processing are differentially regulated during cortical neuron differentiation. Sci. Rep. *6*, 29200.
63. Straniero, L., Guella, I., Cilia, R., Parkkinen, L., Rimoldi, V., Young, A., Asselta, R., Soldà, G., Sossi, V., Stoessl, A.J., et al. (2017). DNAJC12 and dopa-responsive nonprogressive parkinsonism. Ann. Neurol. *82*, 640–646.
64. Zhou, Y., and Han, D. (2017). GATA3 modulates neuronal survival through regulating TRPM2 in Parkinson's disease. Int. J. Clin. Exp. Med. *10*, 15178–15186.
65. Hao, Y., Hao, S., Andersen-nissen, E., Iii, W.M.M., Zheng, S., Lee, M.J., Wilk, A.J., Darby, C., Zagar, M., Hoffman, P., et al. (2020). Integrated analysis of multimodal single-cell data. bioRxiv. https://doi.org/10.1101/2020.10.12.335331.
66. Butler, A., Hoffman, P., Smibert, P., Papalexi, E., and Satija, R. (2018). Integrating single-cell transcriptomic data across different conditions, technologies, and species. Nat. Biotechnol. *36*, 411–420.
67. Cao, J., Spielmann, M., Qiu, X., Huang, X., Ibrahim, D.M., Hill, A.J., Zhang, F., Mundlos, S., Christiansen, L., Steemers, F.J., et al. (2019). The single-cell transcriptional landscape of mammalian organogenesis. Nature *566*, 496–502.

The American Journal of Human Genetics, Volume *109*

Supplemental information

Midbrain organoids mimic early embryonic neurodevelopment and recapitulate LRRK2-p.Gly2019Ser-associated gene expression

Alise Zagare, Kyriaki Barmpa, Semra Smajic, Lisa M. Smits, Kamil Grzyb, Anne Grünewald, Alexander Skupin, Sarah L. Nickels, and Jens C. Schwamborn

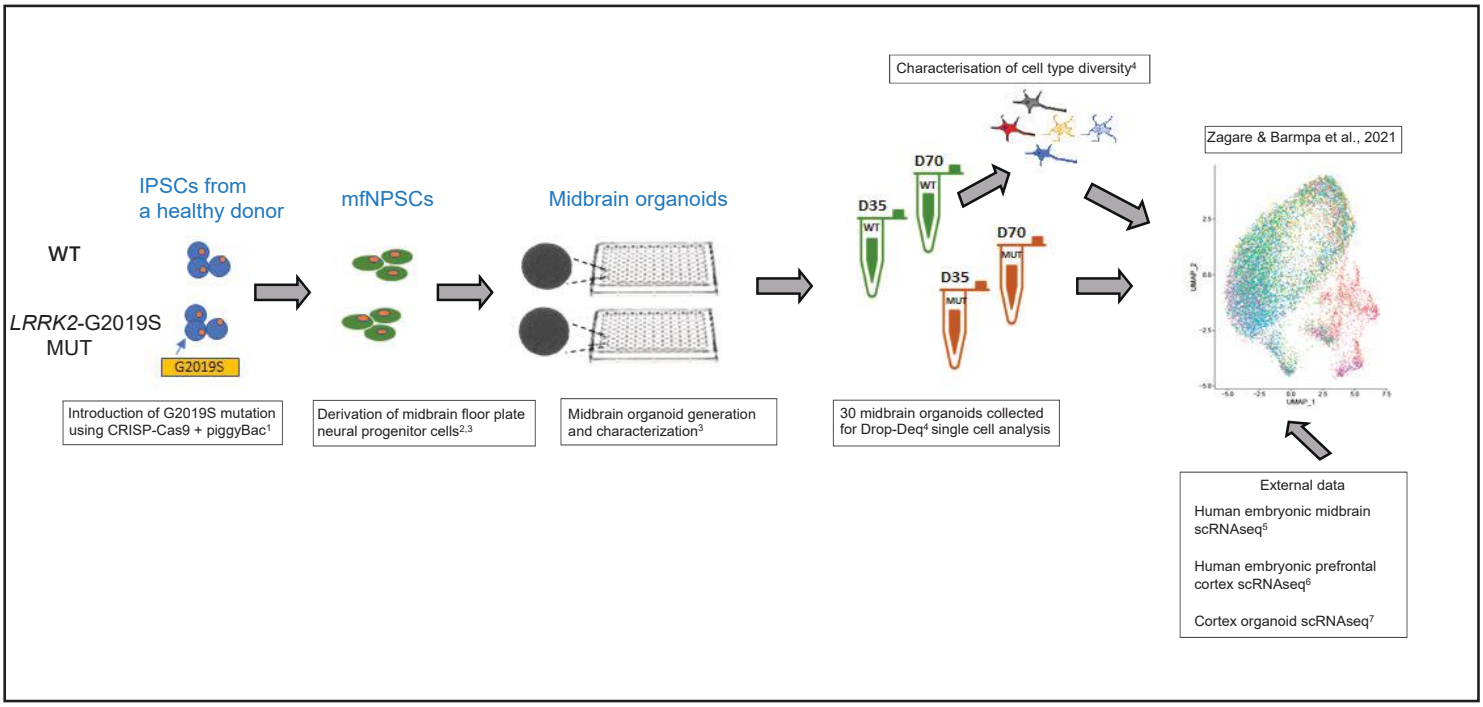

Figure S1. Graphical representation showing the origin of the data used in this study. WT and LRRK2 MUT midbrain organoids were generated in paralel in our lab. WT midbrain organoids were characterized in previous studies of Smits et al. [3,4] The present study comprises analysis of internal scRNAseq data from the respective midbrain organoids and comparison to external datasets [5,6,7].

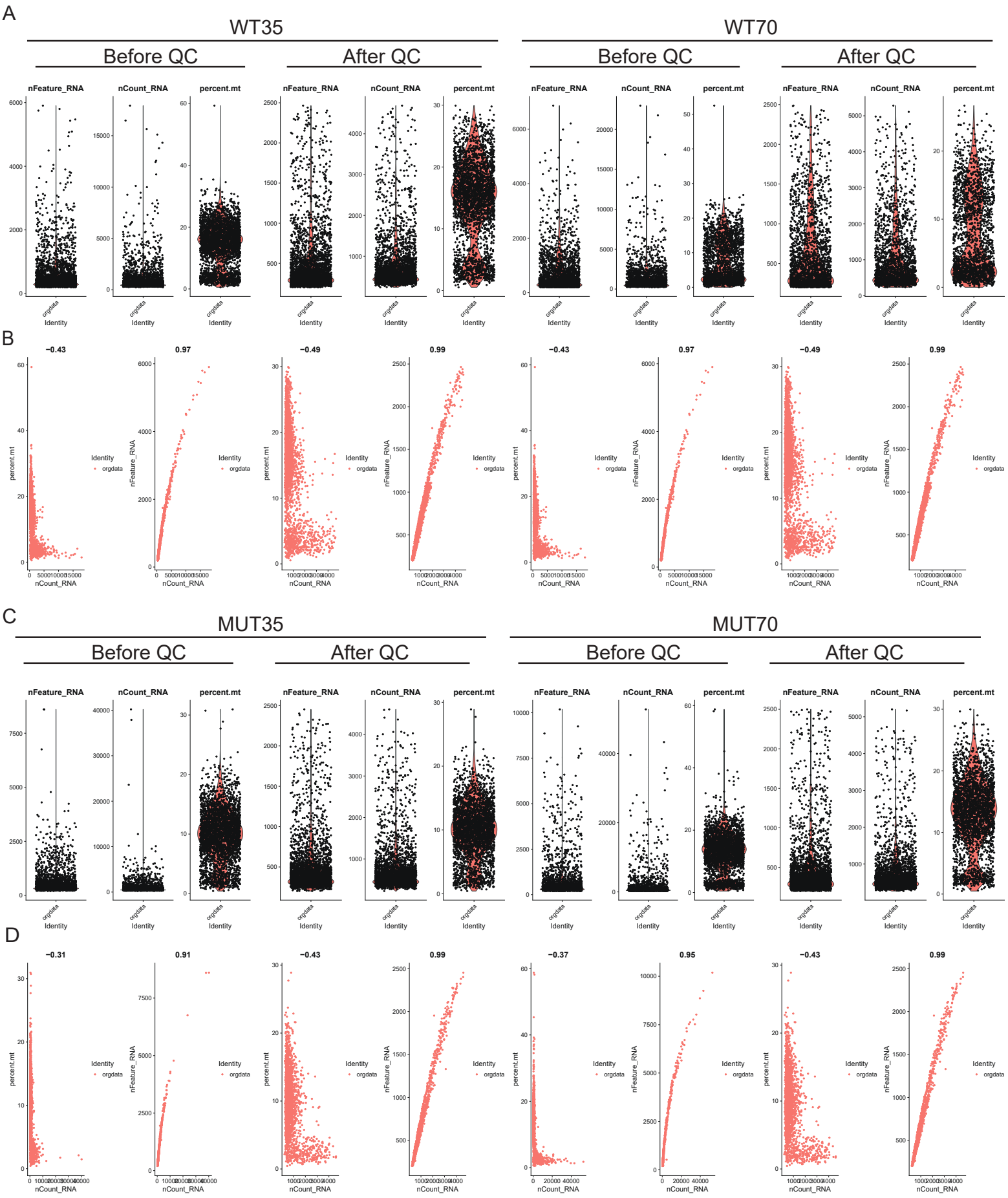

Figure S2. Quality control of midbrain organoid scRNAseq datasets. **A)** Number of genes (nFeature_RNA), total number of molecules (nCount), percent of mitochondrial genes, detected in each cell for WT35 and WT70 midbrain organoids, before and after quality control. **B)** Correlations between percentage of mitochondrial genes, the number of genes and the total number of molecules for WT35 and WT70 midbrain organoids, before and after quality control. **C)** Same as (A), for MUT35 and MUT70 midbrain organoids. **D)** Same as (B), for MUT35 and MUT70 midbrain organoids.

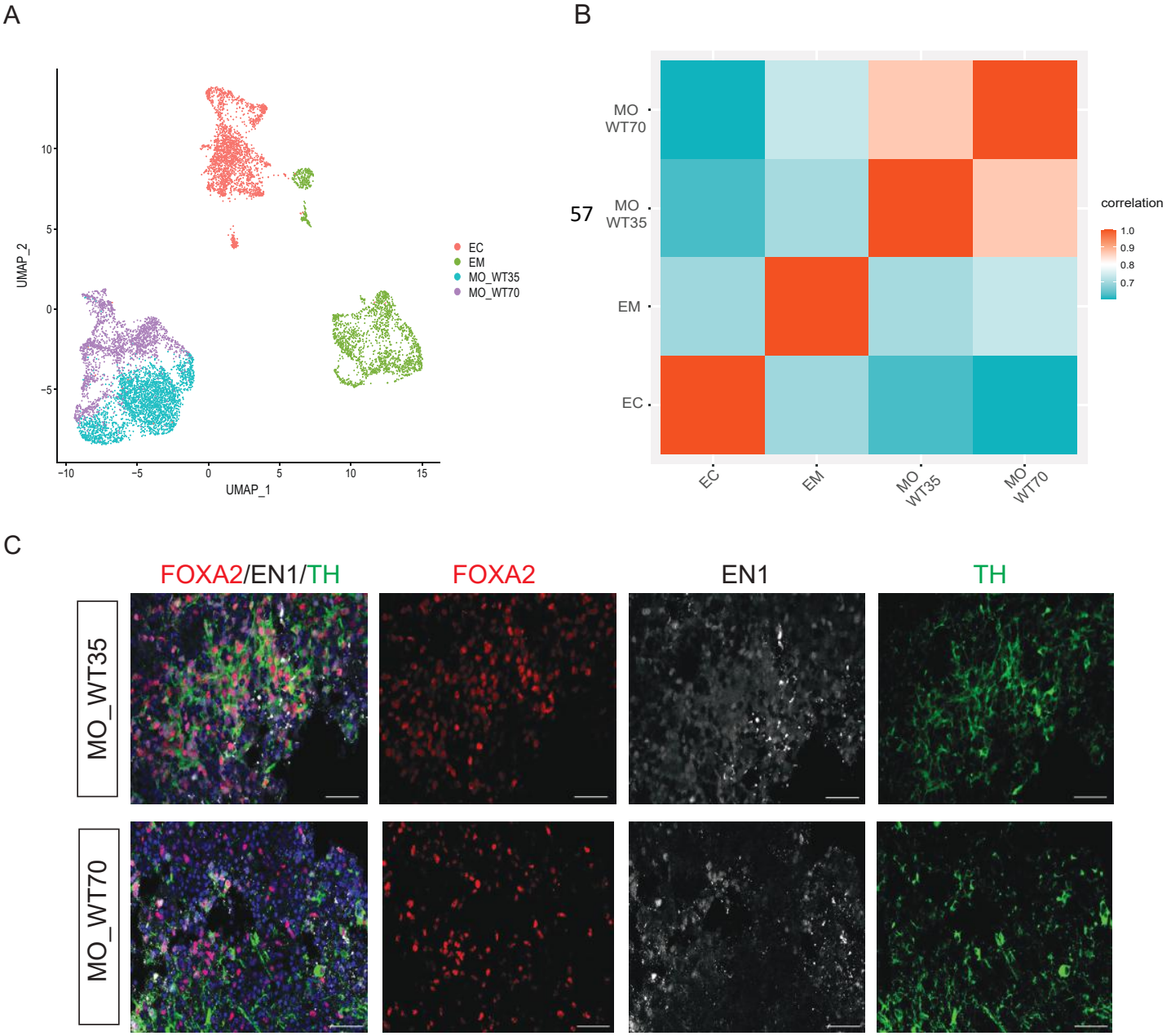

Figure S3. Validation of midbrain organoid identity. **A)** UMAP of integrated Seurat object of merged embryonic prefrontal cortex (EC), embryonic midbrain (EM), WT midbrain organoids of 35 days of differentiation (MO_WT35) and 70 days of differentiation (MO_WT70) after SCTransform. **B)** Spearman correlation of mutual gene average expression between the embryonic prefrontal cortex (EC), embryonic midbrain (EM), WT midbrain organoids of 35 days of differentiation (MO_WT35) and 70 days of differentiation (MO_WT70). **C)** Immunofluorescent staining of midbrain identity markers: FOXA2, EN1 and TH in midbrain organoid sections. Scale bar: 50µm. **D)** The average gene expression correlation of the non-integrated embryonic midbrain (EM) and cortical organoid (CO).

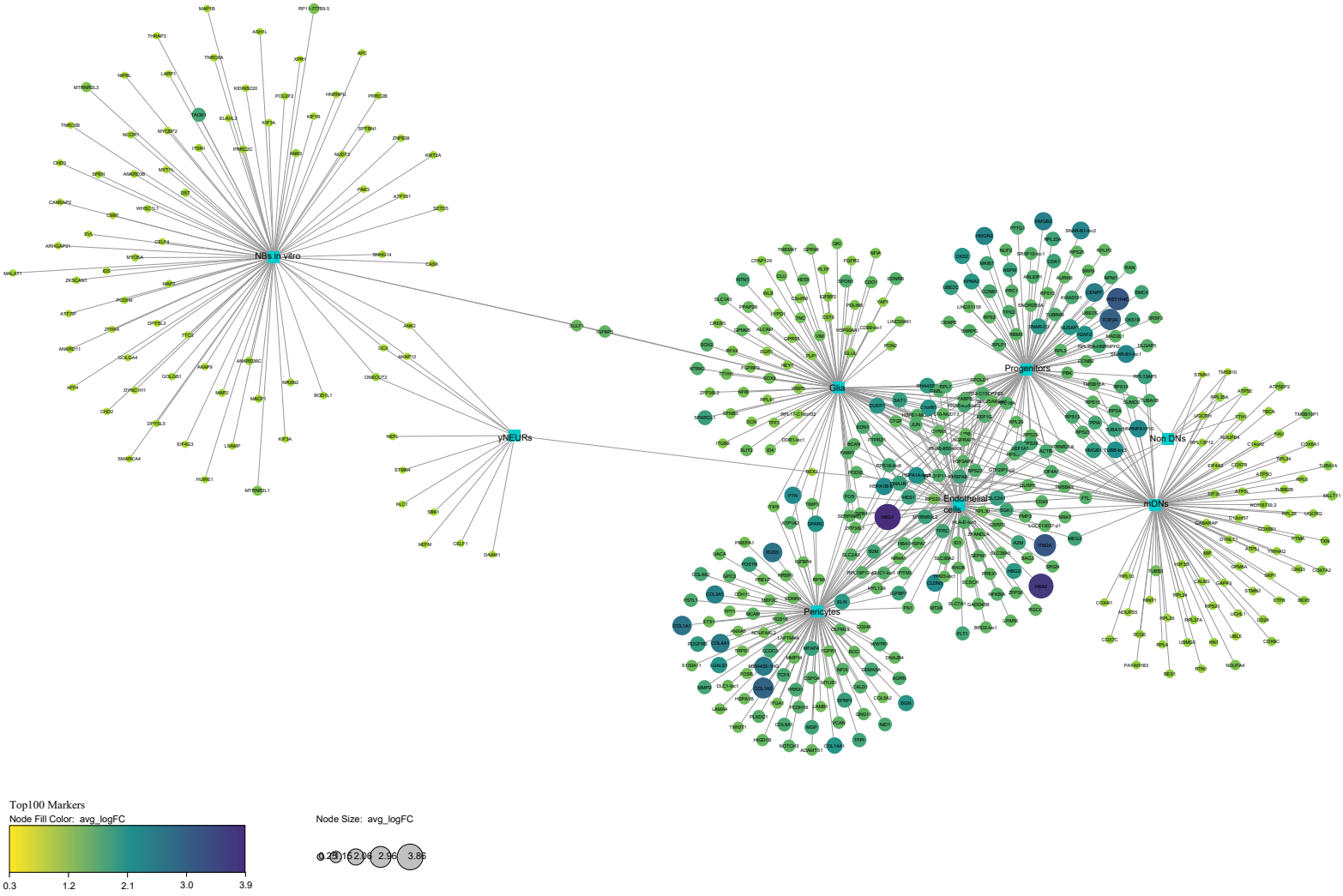

Figure S4. Network representing top marker genes for each cell cluster.
The top 100 cell type markers identified by the FindAllMarkers function. The size and color of nodes represent logarithmic fold change (avg_logFC) of each marker expression in the particular cell type compared to its expression in other cell clusters.

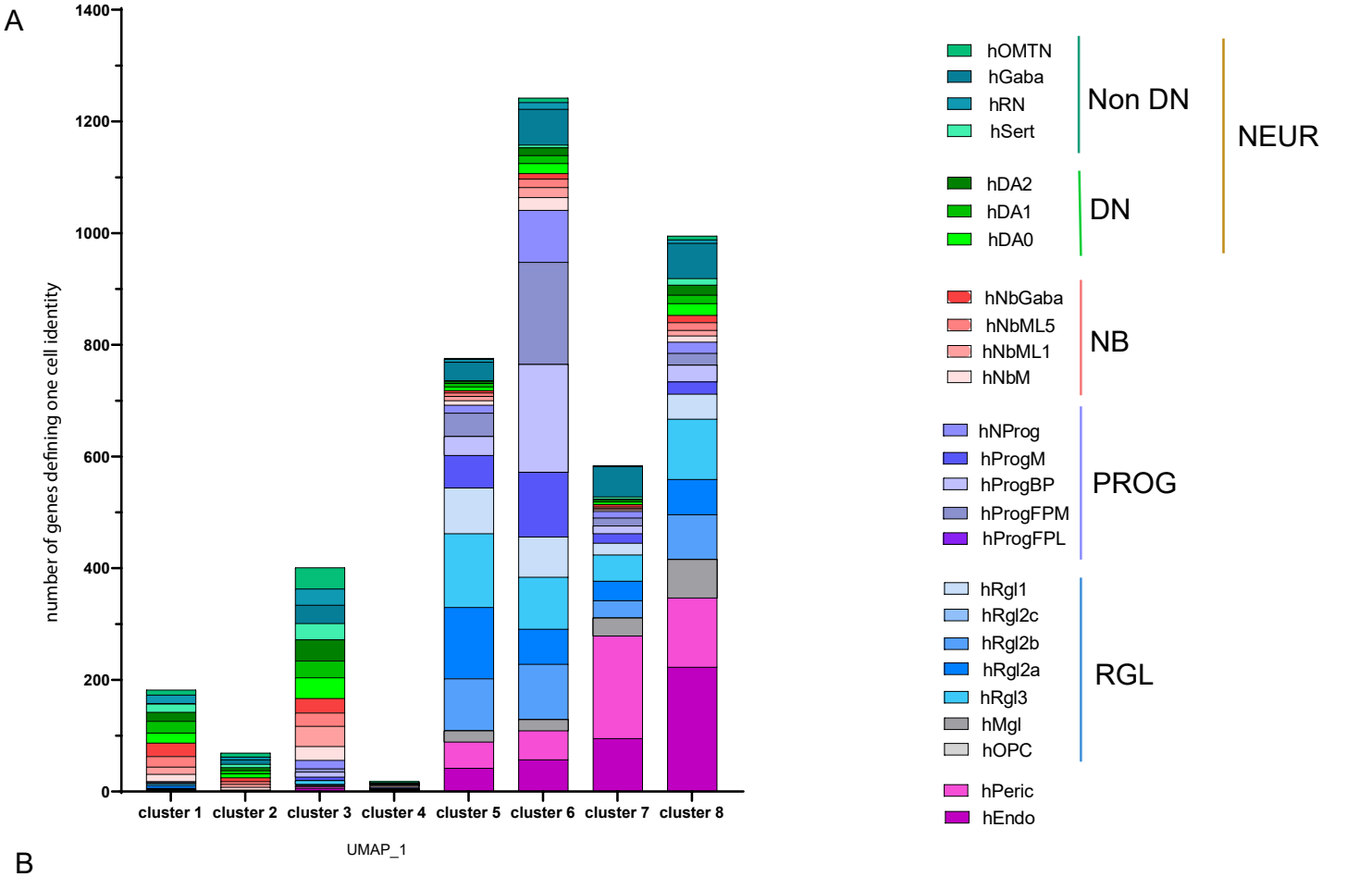

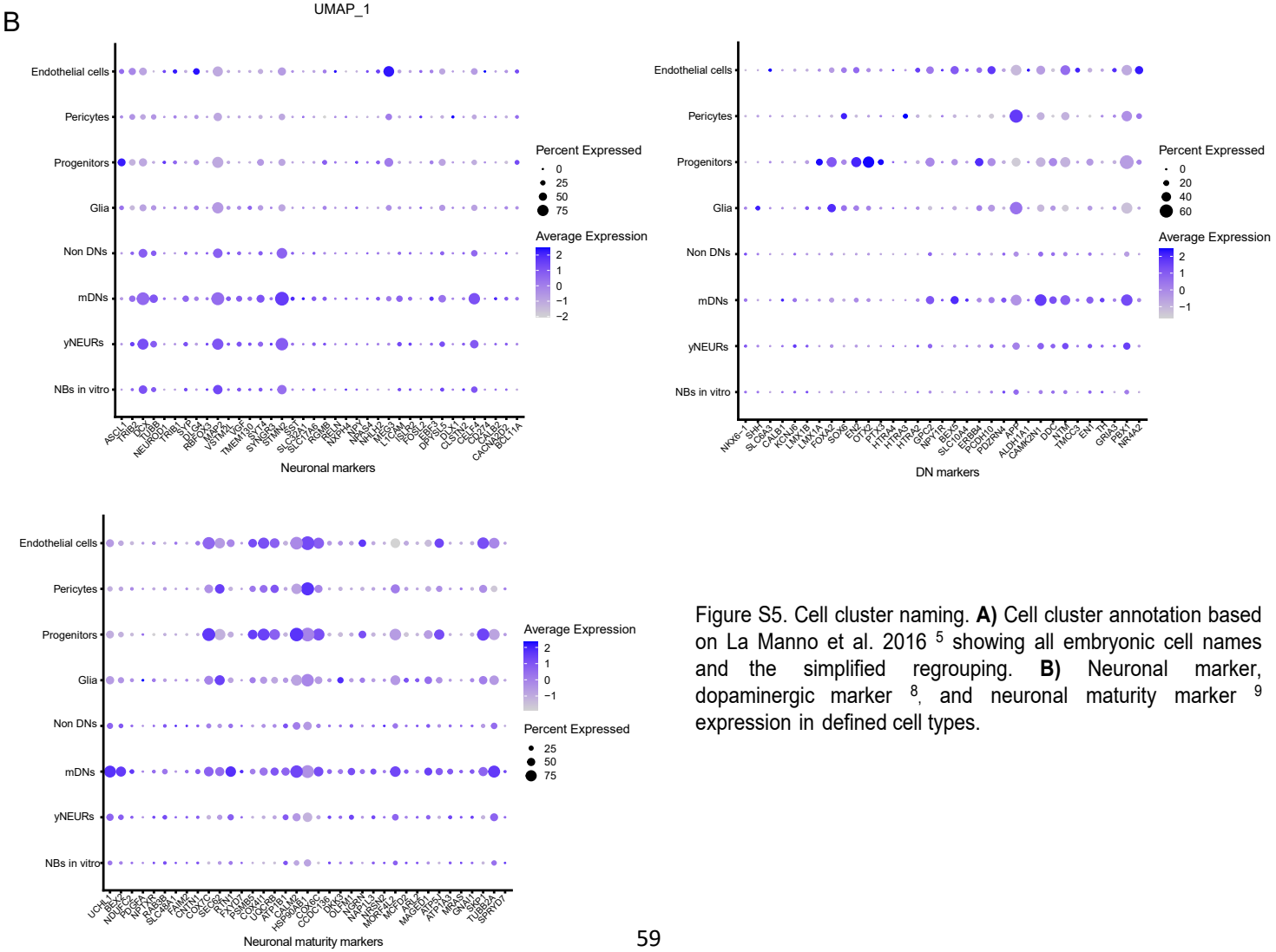

Figure S5. Cell cluster naming. **A)** Cell cluster annotation based on La Manno et al. 2016 [5] showing all embryonic cell names and the simplified regrouping. **B)** Neuronal marker, dopaminergic marker [8], and neuronal maturity marker [9] expression in defined cell types.

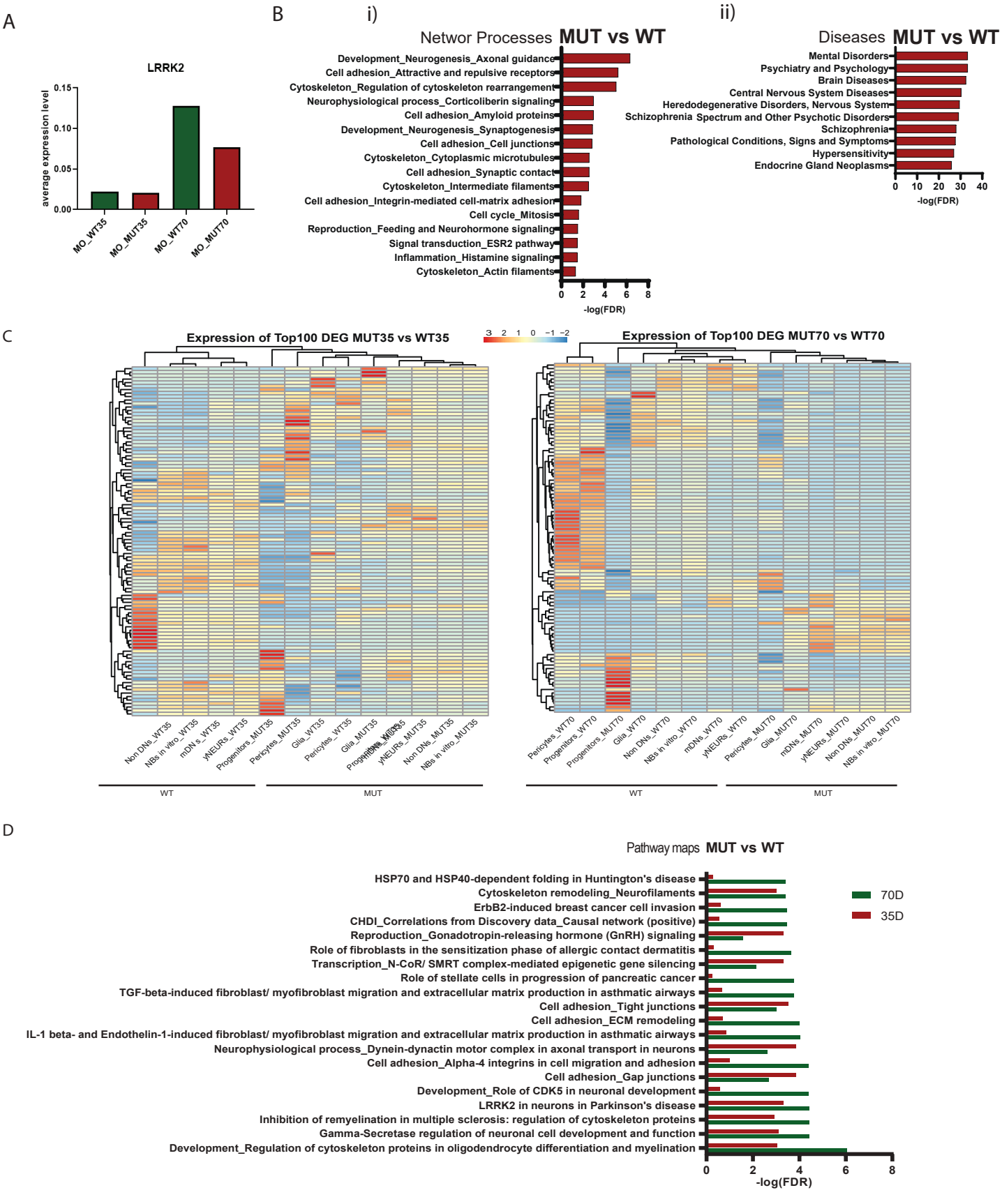

Figure S6. Differentially expressed gene analysis I. **A)** The bulk average *LRRK2* expression in midbrain organoids. **B)** i) Network processes and ii) diseases from the enrichment analysis of 294 DEGs (adjusted p-value < 0.05) between MUT and WT midbrain organoids. **C)** Heatmaps of top 100 DEGs (adjusted p-value < 0.05) at day 35 and day 70 respectively, showing the cell type unsupervised clustering between MUT and WT organoids. **D)** Pathway processes based on MUT vs WT midbrain organoid DEGs (adjusted p-value < 0.05).

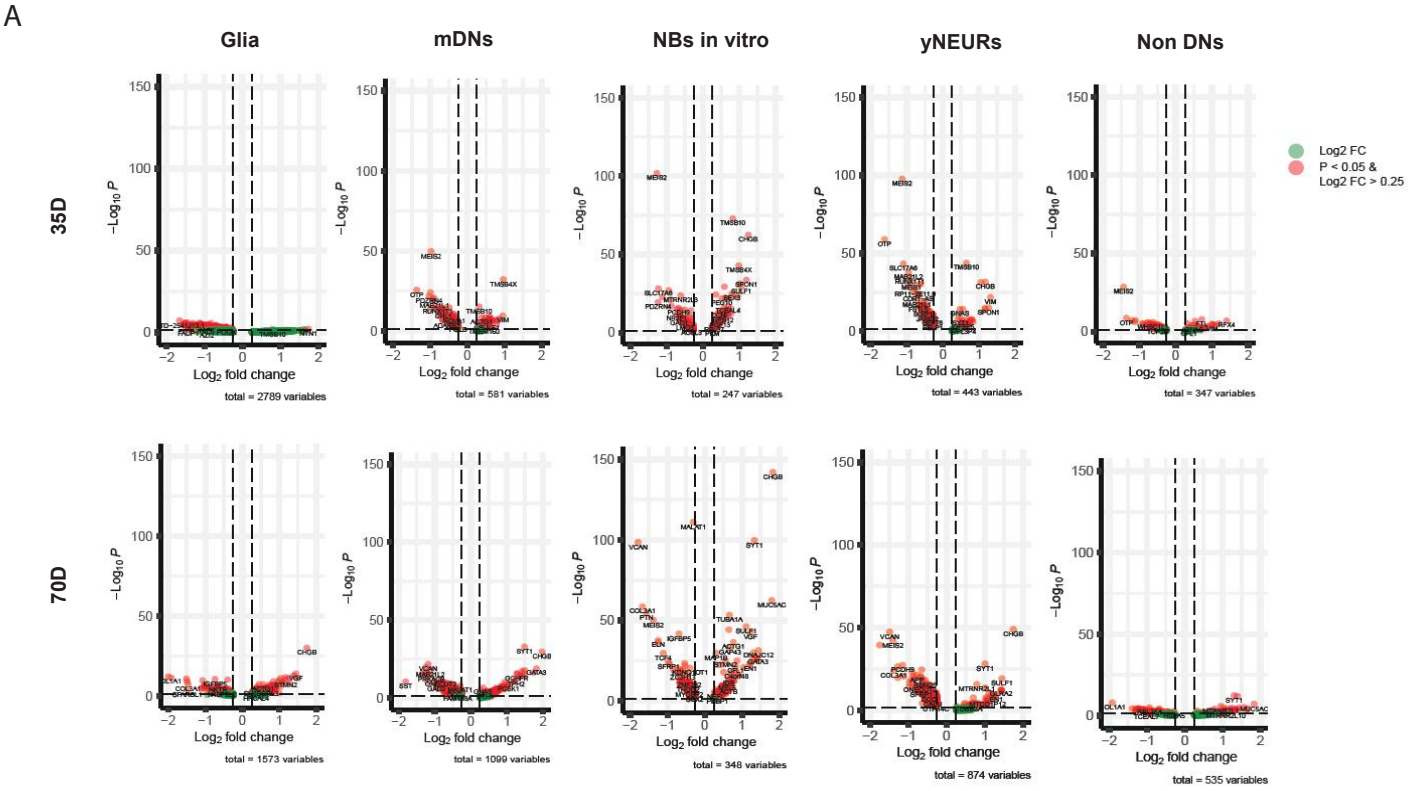

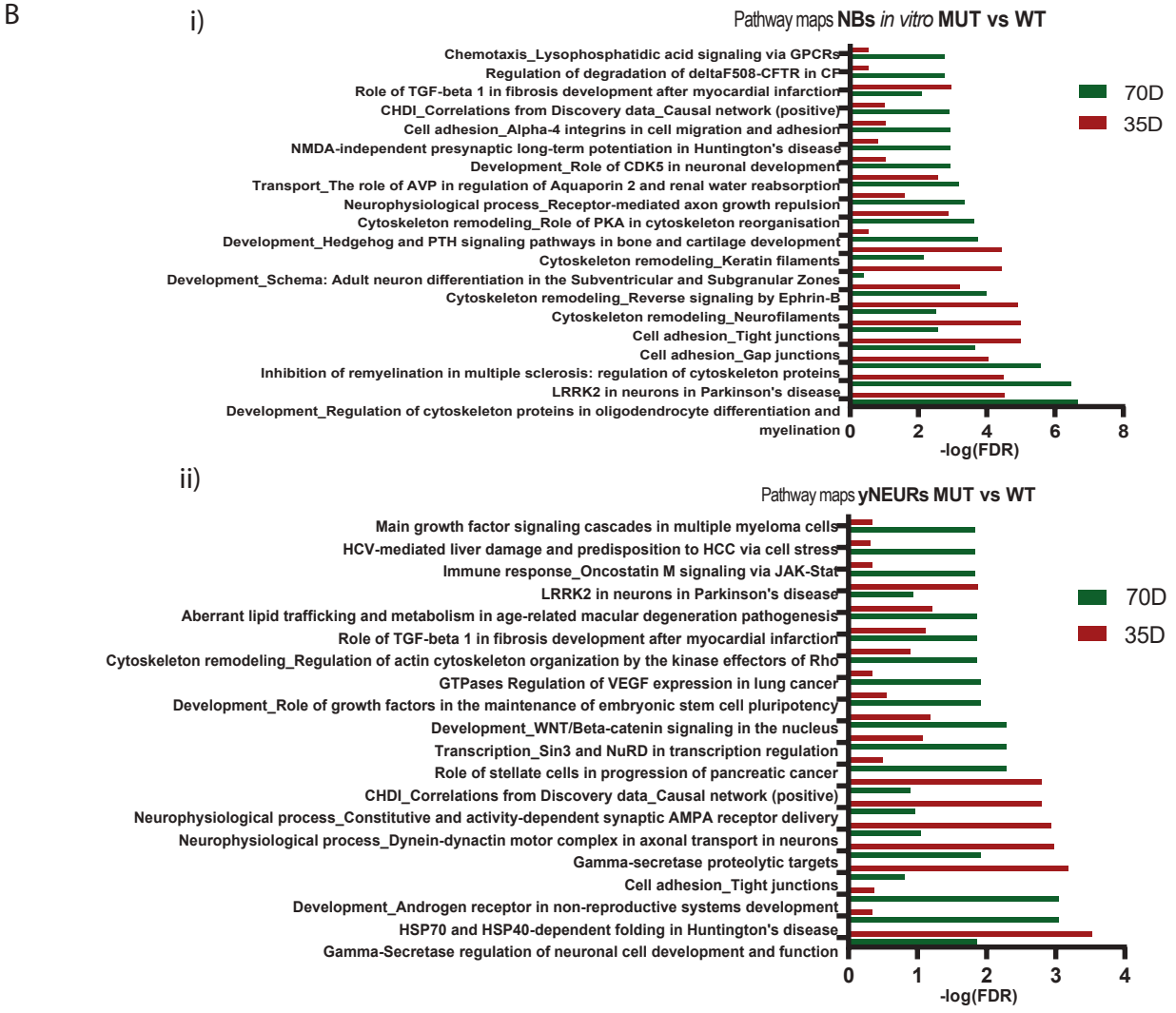

Figure S7. Differentially expressed gene analysis II. **A)** Volcano plots showing DEG fold changes in cell clusters between MUT and WT midbrain organoids. **B)** Pathway enrichment analysis in i) yNEURs and ii) NBs in vitro based on the DEGs in the respective cell clusters (adjusted p-value < 0.05).

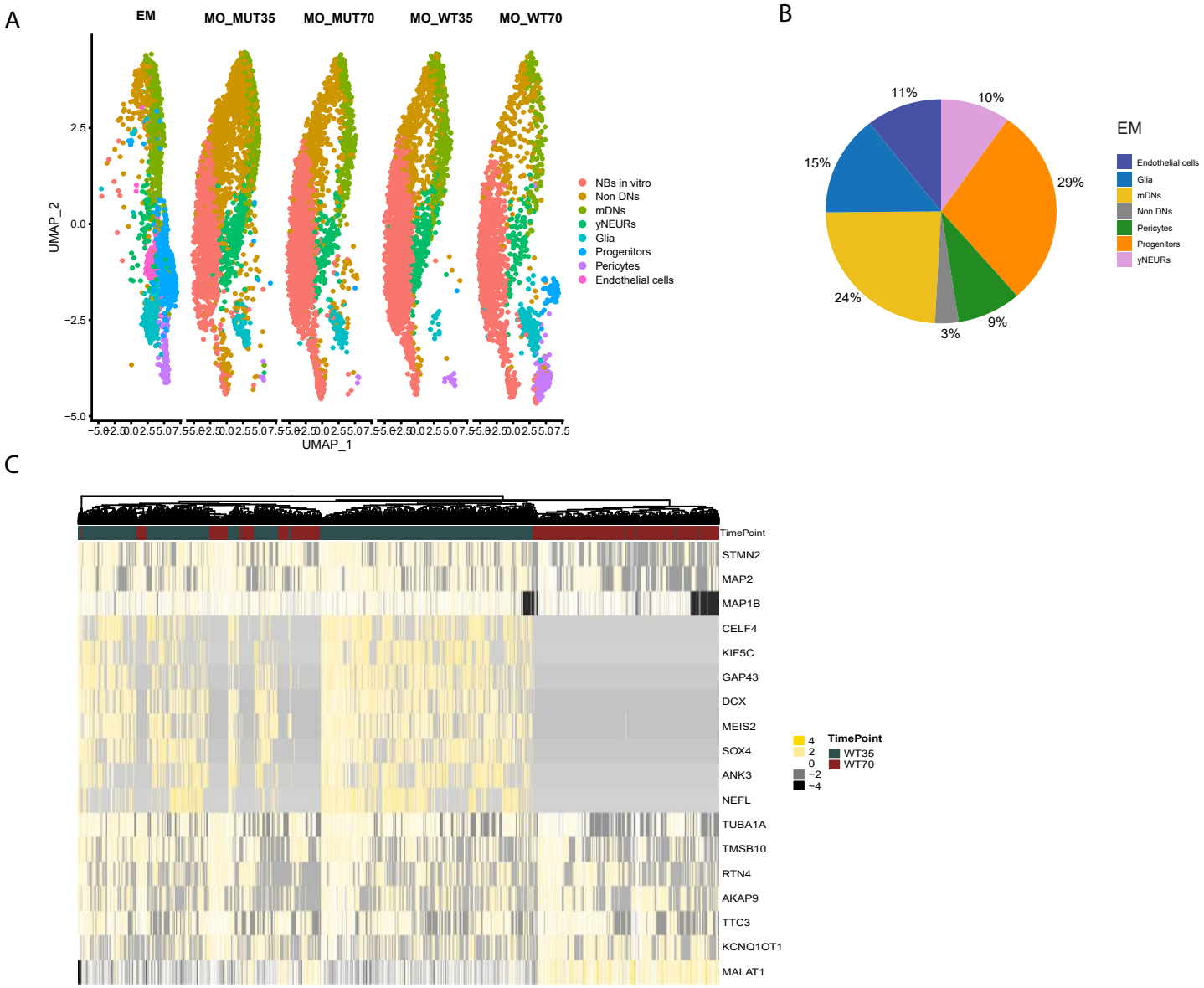

Figure S8. *LRRK2*-G2019S mutant midbrain organoids have a different cellular composition and altered developmental path. **A)** UMAP of integrated Seurat object of merged scRNAseq datasets of embryonic midbrain, and WT and MUT midbrain organoids 35 and 70 days of differentiation, colored by cell clusters and split by the dataset. **B)** Percentage of cell identities present in the embryonic midbrain (EM). **C)** Heatmap of genes with changed expression pattern in at least 50% of cells between WT35 and WT70 midbrain organoids.

Source of iPSCs	Mutation	Age at sampling	Sex	Corresponding midbrain organoid culture
The Wellcome Trust Sanger Institute, Cambridge, UK	-	55	Male	MO_WT35 MO_WT70
The Wellcome Trust Sanger Institute, Cambridge, UK	Introduced LRRK2 G2019S[1]	55	Male	MO_MUT35 MO_MUT70

Table S1. Cell lines used to generate midbrain floor plate neural progenitor cells and further the midbrain organoids for scRNAseq.

References of Supplemental Data

1. Qing, X., Walter, J., Jarazo, J., Arias-Fuenzalida, J., Hillje, A.L., and Schwamborn, J.C. (2017). CRISPR/Cas9 and piggyBac-mediated footprint-free LRRK2-G2019S knock-in reveals neuronal complexity phenotypes and α-Synuclein modulation in dopaminergic neurons. Stem Cell Res. *24*, 44–50.

2. Smits, L.M., Reinhardt, L., Reinhardt, P., Glatza, M., Monzel, A.S., Stanslowsky, N., Rosato-Siri, M.D., Zanon, A., Antony, P.M., Bellmann, J., et al. (2019). Modeling Parkinson's disease in midbrain-like organoids. Npj Park. Dis. *5*,.

3. Reinhardt, P., Glatza, M., Hemmer, K., Tsytsyura, Y., Thiel, C.S., Höing, S., Moritz, S., Parga, J.A., Wagner, L., Bruder, J.M., et al. (2013). Derivation and Expansion Using Only Small Molecules of Human Neural Progenitors for Neurodegenerative Disease Modeling. PLoS One *8*,.

4. Smits, L.M., Magni, S., Kinugawa, K., Grzyb, K., Luginbühl, J., Sabate-Soler, S., Bolognin, S., Shin, J.W., Mori, E., Skupin, A., et al. (2020). Single-cell transcriptomics reveals multiple neuronal cell types in human midbrain-specific organoids. Cell Tissue Res. *382*, 463–476.

5. La Manno, G., Gyllborg, D., Codeluppi, S., Nishimura, K., Salto, C., Zeisel, A., Borm, L.E., Stott, S.R.W., Toledo, E.M., Villaescusa, J.C., et al. (2016). Molecular Diversity of Midbrain Development in Mouse, Human, and Stem Cells. Cell 167, 566-580.e19.

6. Zhong, S., Zhang, S., Fan, X., Wu, Q., Yan, L., Dong, J., Zhang, H., Li, L., Sun, L., Pan, N., et al. (2018). A single-cell RNA-seq survey of the developmental landscape of the human prefrontal cortex. Nature 555, 524–528.

7. Trujillo, C.A., Gao, R., Negraes, P.D., Gu, J., Buchanan, J., Preissl, S., Wang, A., Wu, W., Haddad, G.G., Chaim, I.A., et al. (2019). Complex Oscillatory Waves Emerging from Cortical Organoids Model Early Human Brain Network Development. Cell Stem Cell 25, 558-569.e7.

8. Paisán-Ruíz, C., Jain, S., Evans, E.W., Gilks, W.P., Simón, J., Van Der Brug, M., De Munain, A.L., Aparicio, S., Gil, A.M., Khan, N., et al. (2004). Cloning of the gene containing mutations that cause PARK8-linked Parkinson's disease. Neuron 44, 595–600.

9. Ren, C., Ding, Y., Wei, S., Guan, L., Zhang, C., Ji, Y., Wang, F., Yin, S., and Yin, P.(2019). G2019S Variation in LRRK2: An Ideal Model for the Study of Parkinson's Disease? Front. Hum. Neurosci. 13, 1–6.

3.2. Manuscript II

Impaired dopaminergic neuronal differentiation in GBA associated Parkinson's disease midbrain organoids is accompanied by an increased progenitor pool in cell cycle arrest

Isabel Rosety[1,7*], Alise Zagare[1], Claudia Saraiva[1], Sarah Nickels[1], Paul Antony[2], Catarina Almeida[1], Enrico Glaab[5], Rashi Halder[4], Sergiy Velychko[6], Thomas Rauen[6], Hans R. Schöler[6], Silvia Bolognin[1], Thomas Sauter[3], Javier Jarazo[1,7], Rejko Krueger[2,8], Jens C. Schwamborn[1,°]

[1]Developmental and Cellular Biology, Luxembourg Centre for Systems Biomedicine (LCSB), University of Luxembourg, Esch-sur-Alzette, Luxembourg.

[2]Translational Neuroscience, Luxembourg Centre for Systems Biomedicine, University of Luxembourg, Esch-sur-Alzette, Luxembourg.

[3]Department of Life Sciences and Medicine, University of Luxembourg, Belvaux, 4367, Luxembourg.

[4]Systems Ecology Group, Luxembourg Centre for Systems Biomedicine, University of Luxembourg, Esch-sur-Alzette, Luxembourg.

[5]Biomedical Data Science group, Luxembourg Centre for Systems Biomedicine, University of Luxembourg, Esch-sur-Alzette, Luxembourg.

[6]Max Planck Institute for Molecular Biomedicine, MPG White Paper Group - Animal Testing in the Max Planck Society, Muenster, Germany

[7]OrganoTherapeutics SARL-S, Esch-sur-Alzette, Luxembourg

[8]Transversial Translational Medicine, Luxembourg Institute of Health (LIH), 1 A-B rue Thomas Ediison, L-1445 Strassen, Luxembourg

* First author

° Corresponding author

This article has been accepted to Npj Parkinson's Disease

3.2.1. Contribution statement

I contributed to this article by performing metabolic modeling to explore and predict metabolic alterations driven by the GBA-N370S mutation. I generated context-specific metabolic models by integrating RNA sequencing data of two GBA-PD patient and two healthy control-derived midbrain organoids into the generic human metabolic model Recon3. With the support of Prof T. Sauter, I performed flux variability analysis and calculated the similarity index. To visualize the modeling results, I prepared plots A-D included in Figure 2 of the manuscript. In addition, I described the metabolic modeling method in the Materials and Methods section and reviewed the interpretation of metabolic modeling results in the main text of the article. The project was supervised by J.C. Schwamborn.

3.2.2. Preface

The aim of the manuscript was to characterize the GBA-N370S mutation-caused PD-associated phenotypes, particularly focusing on early neurodevelopmental changes that might reveal the underlying causes of dopaminergic neuron vulnerability.

The heterozygous missense mutation c1226A>G (N370S) is one of the most common variants in GBA among PD patients (Smith and Schapira 2022). It is worth noting that homozygous mutations in GBA cause Gaucher disease, which is an inherited lysosomal storage disorder. Gaucher disease is characterized by the accumulation of glucosylceramides due to the GCase deficient activity leading to multiorgan dysfunction, including neurological complications (Almeida Mdo 2012). Observation of parkinsonism among Gaucher disease patients led to the discovery of GBA mutation contribution to PD development (Smith and Schapira 2022). In general, pathogenetic mechanisms that link mutations in GBA with PD are related to decrease of GCase enzymatic activity, ER stress caused by misfolded GCase protein, lysosomal dysfunction and altered lipid homeostasis (Smith and Schapira 2022, Fernandes et al. 2016, Ginns et al. 2014, Galvagnion et al. 2016). In this article, we were able to reproduce these typical GBA mutation-associated phenotypes in midbrain organoids generated from three patient-derived iPSC lines carrying GBA-N370S mutation. In addition, we discovered that GBA-N370S mutant organoids display severely impaired dopaminergic neurogenesis that might be an essential factor for PD development.

Detailed GBA-N370S PD phenotype characterization, presented in this article, allowed us to understand the mutation-caused pathogenesis to further develop treatment strategies for GBA-N370S PD as well as explore GBA-N370S course under different conditions, for instance, under changed insulin signaling activity (Manuscript III).

Impaired dopaminergic neuronal differentiation in GBA associated Parkinson's disease midbrain organoids is accompanied by an increased progenitor pool in cell cycle arrest

Authors

Isabel Rosety[1,7], Alise Zagare[1], Claudia Saraiva[1], Sarah Nickels[1], Paul Antony[2], Catarina Almeida[1], Enrico Glaab[5], Rashi Halder[4], Sergiy Velychko[6], Thomas Rauen[6], Hans R. Schöler[6], Silvia Bolognin[1], Thomas Sauter[3], Javier Jarazo[1,7], Rejko Krueger[2,8], Jens C. Schwamborn[1,*]

Affiliations

[1] Developmental and Cellular Biology, Luxembourg Centre for Systems Biomedicine (LCSB), University of Luxembourg, Esch-sur-Alzette, Luxembourg.

[2] Translational Neuroscience, Luxembourg Centre for Systems Biomedicine, University of Luxembourg, Esch-sur-Alzette, Luxembourg.

[3] Department of Life Sciences and Medicine, University of Luxembourg, Belvaux, 4367, Luxembourg.

[4] Systems Ecology Group, Luxembourg Centre for Systems Biomedicine, University of Luxembourg, Esch-sur-Alzette, Luxembourg.

[5] Biomedical Data Science group, Luxembourg Centre for Systems Biomedicine, University of Luxembourg, Esch-sur-Alzette, Luxembourg.

[6] Max Planck Institute for Molecular Biomedicine, MPG White Paper Group - Animal Testing in the Max Planck Society, Muenster, Germany

[7] OrganoTherapeutics SARL-S, Esch-sur-Alzette, Luxembourg.

[8] Transversial Translational Medicine, Luxembourg Institute of Health (LIH), 1 A-B rue Thomas Ediison, L-1445 Strassen, Luxembourg

*__Corresponding Author:__ Jens C. Schwamborn, Luxembourg Centre for Systems Biomedicine University of Luxembourg, 7 avenue des Hauts-Fourneaux, L-4362, Esch-sur-Alzette, Luxembourg. jens.schwamborn@uni.lu

Abstract

The mechanisms underlying Parkinson's disease (PD) etiology are only partially understood despite intensive research conducted in the field. Recent evidence suggests that early neurodevelopmental defects might play a role in cellular susceptibility to neurodegeneration. To study the early developmental contribution of GBA mutations in PD we used patient-derived iPSCs carrying a heterozygous N370S mutation in the GBA gene. Patient-specific midbrain organoids displayed GBA-PD relevant phenotypes such as reduction of GCase activity, autophagy impairment, and mitochondrial dysfunction. Genome-scale metabolic (GEM) modeling predicted changes in lipid metabolism which were validated with lipidomics analysis, showing significant differences in the lipidome of GBA-PD. In addition, patient-specific midbrain organoids exhibited a decrease in the number and complexity of dopaminergic neurons. This was accompanied by an increase in the neural progenitor population showing signs of oxidative stress-induced damage and premature cellular senescence. These results provide insights into how GBA mutations may lead to neurodevelopmental defects thereby predisposing to PD pathology.

Introduction

Parkinson's disease (PD) is considered the second most common neurodegenerative disorder. It is characterized by the loss of dopaminergic (DA) neurons in the substantia nigra pars compacta of the midbrain. Heterozygous mutations in the GBA1 gene represent the most common genetic risk factor for PD[1]. The GBA1 gene encodes the lysosomal enzyme β-glucocerebrosidase (GCase), which catalyzes the hydrolysis of glucosylceramide (GlcCer) into ceramide and glucose[2]. Homozygous GBA mutations cause Gaucher disease (GD), the most prevalent lysosomal storage disorder, which is characterized by the accumulation of GlcCer in different tissues[3]. However, the underlying molecular mechanisms through which mutant GCase leads to PD is not yet fully understood. Both toxic gain of and loss of GCase function have been proposed[4], although the two hypotheses are not mutually exclusive.

PD is classically considered an age-related disorder. However, increasing evidence suggests that neurodevelopmental defects might increase the susceptibility to develop PD[5-8]. Neurodevelopmental alterations such as impaired midbrain dopaminergic (mDA) neuron differentiation or metabolic perturbations could affect the viability and resistance to insults and stressors of adult mDA neurons. Interestingly, recent reports have associated PD with metabolic alterations[9-11]. In addition, Gaucher disease (GD) patients, who carry a homozygous mutation in the GBA1 gene, are known to experience metabolic disturbances[12]. This led to the hypothesis that the GBA-N370S heterozygous mutation may result in metabolic changes that could have an impact in neurodevelopment.

Human induced pluripotent stem cell (iPSC) technology has allowed the opportunity to investigate the role of genetic mutations in the pathogenesis of PD. A recent breakthrough was achieved in the field with the derivation of human midbrain organoids (MOs) from iPSCs. This allowed the generation of 3D human tissue *in vitro* that recapitulates the physiology and complexity of the human brain[13]. Moreover, midbrain organoids derived from iPSCs mimic early embryonic neurodevelopment[14], thereby constituting an ideal model to investigate PD-related neurodevelopmental phenotypes.

In this study, we generated midbrain organoids from patients carrying a heterozygous GBA-N370S mutation. We exploited gene expression data to reconstruct a context-specific metabolic model in order to generate predictions which were validated with experimental data. The main metabolic subsystems deregulated as a result of the GBA-N370S mutation were the sphingolipid pathway and metabolite extracellular transport reactions. Moreover, we showed that GBA-PD organoids displayed relevant disease phenotypes such as reduced GCase enzymatic activity as well as mitochondrial and autophagic dysfunction. Our results suggest that the heterozygous GBA-N370S mutation has a negative effect in the differentiation of neural precursors to neurons. These data underline the early pathogenic contribution of GCase function and may explain the selective mDA neuronal vulnerability in GBA-PD.

Results

Generation and characterization of GBA-PD patient-specific MOs

To investigate whether mutant GCase is linked to an altered metabolism leading to neurodevelopmental defects, iPSCs derived from 3 healthy controls (CTRL1, CTRL2 and CTRL3) and 3 GBA-PD patients (PD1, PD2 and PD3) were used to generate midbrain organoid models (Supplementary Table 1). All iPSC lines displayed embryonic stem cell-like morphology and expressed the pluripotency markers SOX2, TRA-1-81, TRA-1-60, OCT4, SSEA4 and NANOG, as well as presenting a normal karyotype. They were subsequently screened for the GBA-N370S heterozygous mutation, which was absent in all the healthy controls and was confirmed in all three GBA-PD cell lines. In addition, the LRRK2-G2019S mutation was discovered in the patient PD3 (Full iPSC characterization available in "Resource availability"). Human iPSCs were differentiated into midbrain floorplate neural precursors (mfNPCs) as described before[15]. The successful derivation of mfNPCs was assessed by confirming the expression of the neural stem cell markers Nestin and SOX2 along with the absence of the dorsal marker Pax6 (Fig. S1A-B). Next, we generated midbrain organoids (MOs) from the mfNPCs based on a protocol previously described[16]. Organoids were either embedded in a droplet of geltrex or kept unembedded in a low-attachment 96-well plate (Fig. 1A, Fig. S2), depending on the intended downstream assays.

We then sought to confirm the decrease of GCase activity that is associated with the N370S mutation. As expected, the enzyme activity of GCase in GBA-PD MOs was significantly reduced (Fig. 1B). No differences were found in the levels of GCase protein at 30 days of *in vitro* organoid differentiation (DIV) (Fig. 1C), but they were significantly decreased at DIV60 (Fig. S3A). Moreover, mutations in the GBA gene are known to cause GCase retention in the ER, leading to reduced levels of the enzyme in the lysosomes[17,18]. Therefore, we measured the amount of GCase protein found in lysosomes by colocalization analysis with the lysosomal marker LAMP1 and found a significant reduction of the enzyme located in lysosomes (Fig. 1D).

GCase deficiency has been shown to impair the lysosomal degradation capacity of dopaminergic neurons [18], we therefore examined the glycohydrolase activity of the lysosomal enzymes β-hexosaminidase, β-galactocerebrosidase and β-galactosidase. No significant differences were observed in β-hexosaminidase or β-galactocerebrosidase activity of GBA-PD MOs compared to unaffected controls, however, an increase in β-galactosidase activity was detected in patient-derived MOs (Fig. S3B). To further investigate a possible impairment of the lysosomal degradation capacity, we examined the autophagy markers p62/SQSTM1 and LC3 to assess autophagy flux. We found that p62 levels were increased in GBA-PD MOs under basal conditions (Fig. 1E) as previously shown[18], whereas LC3-II levels as well as LC3-II/-LC3 I ratio were decreased (Fig. 1F, Fig S3C), suggesting that the formation of autophagosomes might be impaired.

Mitochondrial dysfunction has been proposed as a key mechanism in the pathogenesis of PD and has been reported in GBA-PD cellular and animal models[19-21]. We investigated mitochondrial mass by quantification of the mitochondrial membrane proteins VDAC and TOM20. Whereas we found no differences in TOM20 levels (Fig. S3D), there was a significant decrease in VDAC (Fig. S3E), probably indicating that while the mitochondrial content is unaffected in GBA-PD MOs, their content in the voltage-dependent anion channel, VDAC, is reduced. Based on this, we speculated that mitochondria functionality might be impaired. In order to evaluate this, we measured mitochondrial oxygen consumption rates (OCRs); indeed, GBA-PD organoids displayed significantly reduced mitochondrial ATP as well as decreased coupling efficiency, and higher proton leak compared to unaffected controls (Fig. S3F), which clearly indicates that mitochondrial functionality is compromised.

In summary, patient-specific midbrain organoids exhibit characteristic pathological features of GBA-associated PD, such as impaired GCase activity, reduced lysosomal content of GCase, impaired autophagy flux and mitochondrial phenotypes.

Computational modeling shows that the GBA-N370S mutation has a high impact on cellular metabolism

After the establishment and validation of a midbrain PD model consistent with GBA-PD-associated phenotypes, we addressed the effect of the heterozygous GBA-N370S mutation on metabolic changes. Genome-scale metabolic (GEM) models are an *in silico* tool for the identification of metabolic flux alterations underlying disease phenotypes and has proven to be useful to generate accurate predictions and relevant hypothesis for metabolism research[22,23]. Here, we use one of the most comprehensive human metabolic models, Recon3[24] to reconstruct context-specific models of healthy and GBA-PD midbrain organoids. RNA-seq analysis was conducted on DIV30 midbrain organoids from the CTRL1, CTRL2, PD1 and PD2 cell lines and was used to build cell line-specific models with rFASTCORMICS[25] capturing GBA-N370S associated metabolic alterations.

First, we performed structural model analysis to identify differences between the control and GBA-PD models in gene, metabolite, and reaction composition (Fig. 2A and Table S3). We identified 97 genes, 449 reactions and 302 unique metabolites present only in the control models but not in patient-derived models. In contrast, GBA-PD models shared 71 genes, 1055 reactions, and 676 unique metabolites that were absent in the control models. Next, we performed gene enrichment analysis for the control and patient model unique genes (Fig. S4A). We found that the most enriched biological processes of control-specific genes were associated to lipid metabolism, transmembrane transport and polyol transport, while GBA-PD model-specific genes showed a particular enrichment in the glycosylation and carbohydrate metabolic processes. Further, we analyzed the Recon3 subsystems of the control and patient-specific reactions (Fig.2B). Among the top five subsystems containing the highest number of control-specific reactions we identified mitochondrial transport, sphingolipid metabolism, extracellular transport, and fatty acid oxidation. The highest number of reactions specific to the GBA-PD models belong to glycerophospholipid metabolism, fatty acid oxidation, peptide metabolism, and extracellular transport (Fig. 2B). Importantly, within the extracellular metabolite transport reactions, dopamine extracellular transport belongs to the subset of reactions present only in control models and was not found in the GBA-PD models (Table S4). Next, we pooled the count of control- and mutant-specific reactions per subsystem in order to identify metabolic pathways with the most different reaction composition between the two conditions (Fig. 2C, Table S5). The subsystems with the most different reactions were extracellular metabolite transport, exchange/demand reactions and peptide metabolism, followed by fatty acid oxidation, sphingolipid metabolism, and glycerophospholipid metabolism. We then performed flux variability analysis (FVA) on these subsystems optimizing for ATP production to mimic a situation of high energetic demand similar to the physiological state of a mDA neuron[26]. We included in our analysis the central energy pathways as there is evidence that these pathways could be dysregulated[27]. For the subsystems of interest, we then compared flux distribution similarity based on FVA between mutants and controls using a similarity index (SI) (Fig. 2D). In addition, we computed the SI between both control models and between both mutant models separately (Fig. 2D). This allowed us to assess the variability between cell lines of the same condition. We found that in a situation of high ATP demand, the most different flux distribution was observed in exchange/demand reactions and extracellular transport, followed by sphingolipid

and glycerophospholipid metabolism. However, when considering the subsystems with a relative low variability within the same condition, the biggest differences between patients and controls were observed in the glycolysis pathway, after exchange/demand reactions and extracellular metabolite transport.

Interestingly, we observed that the SI between both mutant models were, in general, higher than between both control models for all the metabolic pathways of interest. This indicates that the variability within the GBA-PD condition is lower than in the controls, suggesting that the GBA-N370S mutation has a substantial effect on metabolism.

Overall, these findings suggest that lipid metabolism in GBA-PD organoids could be largely affected, along with important disturbances in the extracellular transport.

Lipid alterations in PD-N370S midbrain organoids

Among the predicted metabolic changes, glycerophospholipid metabolism and sphingolipid metabolism were recurrently highlighted pathways (Fig. 2B-D), implying that lipid metabolism in GBA-PD organoids could be largely affected. In order to confirm that, we performed a comprehensive lipidomic analysis including over 2000 lipid species across 16 different lipid classes. We visualized the results using the t-SNE dimensionality reduction technique and observed that the lipidomics data from GBA-N370s MOs and controls formed two clearly separated distinct clusters (Fig. S4B), respectively, suggesting a dramatic difference in the lipidomes between the two conditions. We further scrutinized these results by analyzing the levels of hexosylceramides (HexCer), which comprise glucosylceramide (GlcCer), the primary physiological substrate of GCase, as well as galactosylceramide. The predominant HexCer species was C18:0 (Fig. S4C) as reported in the human brain[28,29] and its levels were significantly lower in GBA-PD organoids, whereas HexCer C22:0 was significantly higher (Fig. S4C). However, the total HexCer levels where not significantly different in GBA-PD MOs compared to controls (Fig. 3A).

Interestingly, the two most abundant phospholipids in the brain, phosphatidylethanolamine (PE) and phosphatidylcholine (PC)[30], were both decreased in GBA-PD derived organoids (Fig. 3A), this was accompanied with statistically significant differences in other lipid classes, such as triglycerides (TG), monoglycerides (MG) and phosphatidylglycerol (PG) (Fig, S4D). Even though there were no differences in the total levels of phosphatidylinositol (PI), there was an important dissimilarity in the PI species composition (Fig. 3B-C). A total of 45 lipid species were found to differ significantly in their abundance between the two conditions. A lipidomics study of the human PD brain identified a specific decrease in PI (38:5) accompanied by an increase in PI (36:1) and PI (40:4) in the visual cortex[31]. In agreement with this report, the same differences were detected here (Fig. 3C). PIs are the precursors of phosphoinositides (PIPs), that are signaling molecules required for many important cellular processes. The fatty-acyl chain profiles of PIPs correlate with that of PIs[32], we therefore assumed that the significant differences observed in PI molecular species would translate to an abnormal PIP profile. Consistently, many phosphoinositide signaling genes expressed in the human fetal brain[33] were differentially expressed in GBA-PD organoids (Fig. S4E).

Surprisingly, we did not detect any differences in total levels of sphingomyelins (Fig. 3A), which are synthesized from ceramide and PC, both of which were significantly reduced in patient-derived MOs. However, their species profile was significantly different between the two conditions in terms of fatty acid composition (Fig. 3D).

Our lipidomics results indicate that GBA-PD organoids present a drastically deregulated lipid profile, including differences in steady-state levels for several lipid classes, as well as significant changes in the molecular

species within the same class. Strikingly, they recapitulate lipid composition differences that previously have been described in the brain of human PD patients[31].

Impaired Dopaminergic neuronal differentiation in GBA-PD midbrain organoids

Based on the metabolic modeling, the most affected subsystem is the extracellular transport (Fig. 2B-D), since some of the reactions present exclusively in control models belong to the dopamine extracellular transport (Table S4), we sought to experimentally validate whether dopamine release was impaired in GBA-PD organoid cultures. Indeed, we found that dopamine extracellular levels were profoundly decreased in all the organoids with the GBA-N370S mutation compared with control-derived organoids at DIV60 (Fig. 4A). Next, we assessed the levels of tyrosine hydroxylase (TH), the rate-limiting enzyme in the biosynthesis of dopamine, and found that they were equally reduced, not only at DIV60 (Fig. 4B) but also at every time point collected from DIV15 to DIV90 (Fig. S5A). To determine whether decreased levels of DA and TH result from a lower enzymatic content in cells or rather a lower number of DA neurons in patient MOs, we quantified the amount of dopaminergic neurons using an automated image analysis algorithm. The proportion of TH+ neurons was significantly decreased (Fig. 4C-E, S5B-D) in GBA-PD organoids compared to controls, at DIV30 and DIV60, but also at earlier timepoints (Fig. S5B). Moreover, the neurites of these dopaminergic neurons seemed to be less ramified (Fig. 4F), quantified by the number of links and nodes and this difference becomes even more significant at later timepoints (Fig. S5E). In addition to a less complex arborization, the neurites of these dopaminergic neurons presented a higher fragmentation index (Fig. S5F), which can be an early sign of neurodegeneration[34].

We performed an enrichment analysis by process networks on the transcriptomic data obtained from the two control lines (CTRL1 and CTRL2) and the two GBA-PD lines (PD1 and PD2), in order to gain insight into the deregulated processes that might explain the inefficient dopaminergic differentiation in all the GBA-PD organoids (Fig. 4G). Most of the enriched processes were related to neurogenesis and neuronal differentiation, which led us to hypothesize that the defects in neuronal differentiation observed might not be specific to the dopaminergic system but the general neuronal population. Accordingly, we measured the levels of TUJ1+ and MAP2+ cells which are significantly lower at every time point assessed between DIV15 and DIV90 in the PD models (Fig. S6A-B), thereby confirming a generalized neuronal deficit in GBA-N370S mutant MOs. These results were confirmed by western blot (WB) analysis of TUJ1 (Fig. S6C).

In order to investigate whether the reduction in the neuronal population is already present during the early differentiation process, we evaluated the amount of neuroblast-like cells. These were identified by the expression of doublecortin (DCX), which is expressed during a limited phase in the brain development and is a reliable marker of neurogenesis[35,36], and Nestin, a neural stem cell marker whose expression persists in immature neurons[37]. The proportion of DCX+/Nestin+ cells is significantly decreased in the PD models (Fig. S6D-E), confirming that an immature neuronal population is not prevalent in GBA-N370S MOs and there is indeed an impairment in the differentiation process.

Finally, this neuronal differentiation defect was further confirmed by extracellular neuronal activity recordings using a multi-electrode array (MEA), which showed lower electrophysiological activity in patient-specific MOs (Fig. 4H and S6F-G).

To determine if the lower proportion of dopaminergic neurons in patient-specific MOs was simply a consequence of an impaired general neuronal differentiation, we quantified the amount of TH+ neurons and normalized to the total amount of neurons. This analysis confirmed that although general neurogenesis was

impaired, the DA system was even more profoundly affected (Fig. 4I). Altogether, these data indicate that the amount of dopaminergic neurons is reduced in patient-specific midbrain organoids, whereby recapitulating the cardinal feature of PD.

Increased number of neural progenitor cells in GBA-N370S mutant MOs in cell cycle arrest

To better understand the mechanisms leading to decreased amounts of DA neurons, we investigated the genes involved in dopaminergic differentiation (Fig. 5A), among the top 10 DEGs, a downregulation of NR4A (NURR1) was identified, which is a well-known essential transcription factor for the differentiation, maturation, and maintenance of midbrain DA neurons[38-40]. TH expression was equally decreased, consistent with our immunofluorescence and WB data. Additionally, RET receptor tyrosine kinase, was downregulated along with its interactive partners, including GDNF, a known neurotrophic factor (Fig. S7A).

Interestingly, FOXA2 and SOX2 were upregulated (Fig. 5A), both of which are known to be highly expressed in dopaminergic neural progenitors[41,42]. An increase of FOXA2+ progenitor cells has been reported in MOs from PD patients carrying the LRRK2-G2019S mutation[15]. This might indicate that although the neural progenitors do not differentiate into neurons, they do not differentiate into other cell types either and remain in an undifferentiated state instead. Thus, we quantified the amount of cells expressing the neural progenitor marker SOX2 (Fig. 5B-C) and FOXA2 (Fig. S7B-D), which proved to be significantly higher in GBA-PD organoids compared to controls. We confirmed these results via WB (Fig. 5D) and found SOX2 levels to remain markedly increased at later time points as well (Fig. S7E). This would indicate a defect in the differentiation of neural stem cells, which probably leads to an enlarged progenitor pool in GBA-PD organoids.

We hypothesized that an upregulation of the neural progenitor population might be a compensatory response to an impaired DA neuron specification, as similar compensatory mechanisms have been reported in PD before[43]. However, such a response would be accompanied by an increase in organoid size and proliferation markers. Nevertheless, we did not find differences in size between the two conditions throughout the differentiation process (Fig. S8A-B). Likewise, we measured the expression of the proliferation marker Ki67 at DIV15 and DIV30 and found no evidence of increased levels in patient-derived organoids (Fig. S8C). To exclude that differences were masked by other cell types we assessed the proliferating neural stem precursors by quantifying cells expressing both Ki67 and SOX2. Surprisingly, we found a decrease in the co-expression of the two markers in patient-specific MOs (Fig. 5E-F and S8D), implying that even though there is a higher proportion of neural progenitors in the GBA-PD condition, they have a lower proliferative capacity. This is an indicator that the progenitors in GBA-PD MOs might be under cell cycle arrest. In the pathway enrichment analysis of the transcriptomics data, we indeed detected several pathways related to cell cycle regulation (Fig. S8E). Thus, we analyzed the cell cycle by flow cytometry using propidium iodide (PI) staining. Although we found no differences in the proportions of cells in G0–G1 or G2–M phase, there was a significant accumulation of cells in the S-phase population (Fig. 5G-H). To further monitor S-phase progression, the thymidine analogue, EdU (5-ethynyl-2′-deoxyuridine) was used to tag cells in S-phase as it is incorporated into cellular DNA during replication. As expected, immediately after the EdU pulse, the proportion of neural precursors that incorporated the dye was similar between CTRL and GBA-PD DIV30 MOs (Fig. 5I and S9). However, because of dilution through multiple cell divisions, the EdU signal was lost completely in pulse-labeled progenitors of control organoids after 7 days from initial EdU pulse, whereas it was retained in GBA-PD organoids (Fig. 5I and S10), indicating that the neural precursors of patient-derived MOs did not divide and were therefore arrested in S phase.

Neural progenitors of GBA-PD organoids display signs of oxidative damage and cellular senescence

A common trigger of cell cycle checkpoint activation is DNA damage[44], and a significant amount of the damage is caused by reactive oxygen species (ROS)[45]. Moreover, oxidative stress is known to play an important role in PD pathogenesis, therefore we assessed DNA oxidative damage by measuring the levels of 8-Hydroxydeoxyguanosine (8-OHdG), a major oxidative DNA-damage product[45]. The levels of 8-OHdG released into the medium was significantly increased in the GBA-N370S condition (Fig. 6A), indicating that patient-derived MOs are under severe oxidative stress, thereby restraining the cell cycle progression.

Persistent DNA damage response may result in a permanent cell cycle arrest, leading to cellular senescence[46,47]. A well-established marker for senescence is the loss of nuclear LAMINB1[48]. Accordingly, we quantified the expression of nuclear LAMINB1 in the neural precursor population and were able to detect a significant decrease (Fig. 6B and S11). The senescent phenotype is associated with the loss of heterochromatin, which can be assessed by immunostaining of heterochromatin protein 1 gamma (HP1γ) [49,50]. Organoids from GBA-PD patients present a lower mean fluorescence intensity (MFI) than control-derived organoids (Fig. 6C-D left and S12A), despite the presence of a bright dotted pattern in GBA-PD MOs resembling senescence-associated heterochromatin foci (SAHF)[51], which is absent in control MOs (Fig. S12B-C). When the threshold of the image analysis quantification was adjusted to account for this, in order to identify a population that uniformly expresses high levels of HP1γ, the decrease in GBA-PD MOs became more significant (Fig. 6D right). Moreover, the activity of the lysosomal enzyme beta-galactosidase (β-gal) is commonly used as a marker for senescent cells[52] and increased activity of this enzyme in GBA-PD MOs was already shown in (Fig. S3B). To confirm these results, we performed senescence-associated beta-galactosidase (SA-β-gal) staining, showing an accumulation of SA-β-gal positive cells in GBA-PD organoids (Fig. 6E).

Collectively, these data suggest that GBA-N370S mutation causes cell cycle arrest and cellular senescence in neural progenitor cells, resulting in impaired neurogenesis.

Discussion

In this study in silico metabolic network modeling identified several pathways that potentially play a role in GBA-N370S associated PD. These pathways could not only be validated by extensive phenotyping but also led to the discovery of novel potential mechanisms of action of GBA-N370S on neurodevelopment and in PD pathogenicity.

By using patient-specific midbrain organoids we confirmed decreased GCase activity, a dysregulation of autophagy, altered mitochondrial function and highlighted the role of the heterozygous GBA-N370S mutation in lipid dysregulation. We showed differences in steady-state levels of several lipid classes as well as differences in lipid composition within the same class, which may decisively distort cell homeostasis. For instance, we observed a decrease in triglycerides (TG), which could have an effect in α-synuclein aggregation in later stages of the disease, as TGs are protective against α-synuclein cytotoxicity and ER trafficking defects [53,54]. Likewise, the depletion of PE, might explain the lower levels of LC3-II observed, as in order for LC3-I to become LC3-II upon autophagy induction, it needs to be conjugated to PE[55,56]. Interestingly, a decrease in PE has also been observed in PD patients using magnetic resonance spectroscopic imaging[57].

While homozygous mutations in the GBA gene are associated with accumulation of GlcCer in Gaucher disease, it remains controversial whether heterozygosity is equally associated with substrate accumulation as it has not yet been demonstrated in GBA-PD patient brains[28,58]. In patient-derived iPSC neuronal cultures, both an accumulation[59] and unchanged levels[18] have been reported. Consistent with the latter, we did not observe an increase in total levels of hexosylceramides. However, it is of note that differences in GlcCer could have been masked by the levels of galactosylceramide, since technically it was impossible to distinguish the two.

Moreover, we demonstrated that the impaired dopamine transport stems from a lower number and notably more dysfunctional DA neurons. A defective specification of DA neurons will likely affect their vulnerability. The transcription factor NURR1, essential for the differentiation, maturation, and maintenance of mDA neurons[60] was significantly decreased in GBA-PD organoids (Fig. 5A). An early reduced expression of NURR1 has been shown to result in a lower DA yield and an increased susceptibility of these neurons[61,62]. Moreover, NURR1 is essential for the expression of the RET protein in midbrain DA neurons[63,64], consistently, the Ret-GDNF signaling pathway was downregulated in GBA-PD organoids. GDNF is an important neurotrophic factor in the midbrain DA system and increasing evidence suggests that GDNF/Ret signaling is an important modulator of development and maintenance in midbrain dopaminergic neurons[65,66]. Together, these results suggest that neurodevelopment is strongly impaired in GBA-N370S midbrain organoids.

The reduction of neurons during differentiation was accompanied by an accumulation of undifferentiated cells. This observation offers an explanation for the big differences in flux variability analysis (FVA) for the glycolysis pathway between patients and controls when maximizing for ATP production, since neural stem cells depend mainly on glycolysis for meeting their energetic demand[67]. These neural stem cells were, however, not proliferative, which was accompanied by increased DNA oxidative damage, leading to cell cycle arrest at the S-phase, thereby potentially explaining the lower amount of differentiated neurons in GBA-PD organoids. Moreover, these non-proliferative neural stem cells showed signs of premature senescence, supported by a loss of LAMINB1, as well as an upregulation of β-gal and a downregulation of HPIγ, three well-known hallmarks of senescence[49,50,52]. But although there was a general decrease of HPIγ expression, GBA-N370S organoids exhibited a punctate staining, as opposed to control organoids, that might indicate

the presence of senescence-associated heterochromatin foci (SAHF), which are thought to contribute to the maintenance of the senescent phenotype[51].

An altered transition between a neural precursor state and a differentiated neuron has already been reported in other forms of PD[15,68]. Nevertheless, the neurodevelopmental contribution of GBA mutations has not been extensively investigated. A previous study showed that iPSC-derived neurons from monozygotic twins harboring the heterozygous GBA-N370S but clinically discordant for PD had reduced capacity to synthesize and release dopamine[69], although differentiation efficiency was not assessed. Moreover, in a Gaucher disease *in vitro* model harboring a homozygous mutation in the GBA gene, the ability of neural progenitors to differentiate to DA neurons was significantly reduced[70]. However, impaired DA neurogenesis has not yet been described in GBA-PD *in vitro* models, this could be explained by the differences in DA neuron differentiation protocols or the number of cell lines used. This further proves that iPSC-derived 3D organoids, which have a higher resemblance to in vivo cell organization and organ structure than standard 2D cultures[13,71], can be used to identify potential early developmental defects in neurodegenerative diseases such as PD.

β-Glucocerebrosidase (GCase) activity is reduced not only in mutation carriers but also in idiopathic PD and healthy individuals at older age[72,73], pointing toward a general role for GCase in neurodegenerative processes. It would be necessary to find out from a mechanistic point of view, if autophagy upregulation would be enough to increase the neuronal differentiation efficiency as observed in other organoid PD models [68], or whether the phenotypes observed are a consequence of other pathological processes such as ER stress or oxidative damage, which are more likely to cause cell cycle arrest and the subsequent low differentiation yield. On the other hand, emerging evidence supporting a role of lipid metabolism in neural stem cell proliferation and neurogenesis has gained attention recently[74,75]. In line with this, many phosphoinositide signaling genes were differentially expressed in GBA-PD MOs, some of which are known to be required for neural tube morphogenesis and differentiation during embryonic development, such as PTEN, GAP43, SYT1 and CFL1[33,76]. This offers exciting new possible mechanisms through which an altered lipidome due to mutant GCase affects stem cell regulation and neuronal differentiation. Pharmacological rescue of GCase activity using recombinant GCase or chemical chaperones will allow further exploration of the mechanisms by which GBA-N370S mutation leads to the developmental defects observed and may provide promising therapeutic strategies to treat PD.

In summary, we here show that PD patient-specific midbrain organoids recapitulate cardinal disease features *in vitro*. Furthermore, we used this model to identify a cellular process, stress-induced cell cycle arrest of neural progenitor cells, as potentially underlying cause for deficiencies in dopaminergic neurons. These findings support the notion that PD has a neurodevelopmental component and opens new avenues for therapeutics developments targeting these mechanisms.

Materials and Methods

iPSCs, mfNPCs and organoid culture:

Patient GBA-PD1 sample was obtained from Coriell Institute and Patients GBA-PD2 and GBA-PD3 were provided by University College London. Healthy controls 1 and 2 were generated at the Max Planck Institute and healthy control 3 was provided by StemBANCC. From each donor, one clone per iPSC line was used in this study. More information is detailed in (Table S1). Full characterization of iPSCs is available at https://doi.org/10.17881/xfh3-a153. iPSCs were cultured in Essential 8 medium (Thermo Fisher, A1517001) with 1% Penicillin/Streptomycin (Invitrogen, 15140122) in Matrigel-coated plates (Corning, 354277). Splitting was performed using EDTA 0.5mM (Invitrogen, 15575020) and ROCK inhibitor Y-27632 (Merck Milipore, cat no. 688000) was added to the media at 10uM for 6-24h after seeding.

Midbrain floor plate neural progenitor cells (mfNPCs) were derived from iPSCs as previously described in[15]. mfNPCs were maintained in Matrigel-coated plates and cultured in freshly supplemented N2B27 as described in[16]. In order to obtain a homogeneous population of mfNPCs, the cells were passaged at least 5 times before doing an immunofluorescence staining to confirm the neural stem cell identity, which we validated by the expression of the neural stem cell markers SOX2 and NESTIN and we confirmed absence of expression of PAX6, thereby excluding a dorsal identity (Fig. S1).

Once the quality of the derivation was confirmed by immunostaining, ventral midbrain organoids were generated as detailed in[16], using a reduced seeding density of 6000 cells. For each organoid generation, the passage of mfNPCs was the same between controls and GBA-PD cell lines. The MOs were embedded in Geltrex (Invitrogen, cat no. A1413302) at day 8 of differentiation and kept at 37C, 5% CO2 under dynamic conditions (80 rpm) for up to 90 days or were left in 96-well ultralow adhesion plates (round bottom, Corning).

GBA-N370S mutation screening

Cell lines coming from GBA-PD patients were screened for the N370S mutation in the GBA gene by extracting genomic DNA from blood samples using the GenElute™ Blood Genomic DNA Kit (Sigma, NA2020-1KT), PCR reactions were carried out using GoTaq® G2 Hot Start Master Mix (M7423, Promega). Primer sequences were F: TGTGTGCAAGGTCCAGGATCAG, R: ACCACCTAGAGGGGAAAGTG, which do not amplify the GBA pseudogene. Samples were sent for sequencing to Microsynth Seqlab and mutations were confirmed (see “Resource availability”).

Cell cycle analysis by flow cytometry

For flow cytometry analysis, four embedded organoids of each cell line were pooled and incubated with 500 µL of papain (0.18% Papain, Sigma; 0.04 % EDTA, Sigma; 0.04 % L-Cystein; DMEM-F12, Invitrogen) for 40 minutes at 37°C. After 40 minutes, papain was removed and 300 µL of Accutase (Sigma) were added, organoids were then immediately disrupted into a homogeneous suspension by pipetting, in order to stop the digestion, 1mL of PBS containing 0.5 % trypsin inhibitor and 0.5% of BSA was added. The samples were then centrifuged for 5 minutes at 500g and washed once in ice cold PBS. For cell fixation, 70% (v/v) of ice-cold ethanol was added to the pellet dropwise while vortexing. Cells were fixed for 30 min at 4 °C on a rotor. After fixation, cells were washed twice with 1mL of PBS and centrifuged at 850g for 5min.

The pellet was then resuspended in 250uL of propidium iodide working solution (PI; P4864, Sigma 40ug/mL, and RNase A 20ug/mL in PBS) and incubated for 15min at room temperature.

Cells were then analyzed by fluorescence-activated cell sorting (FACS) on the BD LSRFortessa Cell Analyzer using the 488 nm laser for excitation. Data were analyzed using FlowJo v10 software and cell cycle phases were quantified by the Watson Pragmatic algorithm.

GCase activity

GCase activity was measured as described previously[18,77]. Briefly, non-embedded organoids were lysed in GCase lysis buffer (citrate phosphate buffer supplemented with 0.25 % (v/v) Triton-X100 and 0.25% (w/v) taurocholic acid pH 5.4). Following incubation on ice for 30 minutes, samples were centrifuged for 20 minutes at 4°C, 20 000g. The supernatant was incubated with 1mM 4-methylumbelliferyl β-D-glucopyranoside (Sigma, M3633) and incubated at 37 °C for 40 min. The reaction was stopped by adding equi-volume of glycine (1M, pH 12.5) and resulting fluorescence detected on a Microplate Reader Cytation5M (BioTek). Excitation at 355 nm and emission 460 nm was used. GCase activity was normalized to the total protein content of the lysates using the Pierce™ BCA Protein Assay Kit (Thermo Fischer). Values from samples treated with 3mM conduritol B epoxide (Santa Cruz, sc-201356) were subtracted from non-CBE-treated samples to obtain activity derived from GBA1. GCase activity was normalized to the mean of the controls per experiment and results were expressed as percentage of controls.

Other lysosomal enzyme assays

Measurements of total β-hexosaminidase and β-galactosidase enzymatic activity were determined in 30DIV non-embedded organoids using the substrates 4-methylumbelliferyl-N-acetyl-b-D-glucosaminide (MUG, 0.05 mM; Sigma, M2133) and 4-methylumbel-liferyl-β-D-galactopyranoside (MUbGal, 0.56 mM; Sigma, M1633), as described previously[78]. The readouts were not normalized to the protein content due to the interference of BSA from the extraction buffer with the protein quantification. To measure β-galactocerebrosidase activity, samples were processed as described before[79]. Briefly, 30DIV non-embedded organoids were lysed in 0.25% Triton X-100 and 0.25% sodium taurocholate, 10 µL of the lysate were then added to 20 µL of substrate reagent consisting of 0.4 mM 6-hexadecanoylamino-4-methylumbelliferyl-β-D-galactopyranoside (HMUGal; Creative Enzymes, CSUB-0720), 0.3% sodium taurocholate, and 0.18% oleic acid in citric acid/phosphate buffer (pH 5.2). The enzymatic reaction was carried out at 37 °C for 6 h, and then was stopped by addition of 60 µL 0.2 M glycine-NaOH buffer (pH 10.7) with 0.1% SDS and 0.15% Triton X-100. Measured fluorescence (excitation 404 nm; emission 460 nm) was normalized to total protein concentration (Pierce™ BCA Protein Assay Kit. Thermo Fischer).

Dopamine extracellular release

Dopamine ELISA (Immusmol BA-E-5300) was performed for the quantitative determination of dopamine secreted by midbrain organoids at DIV60 from five independent non-embedded organoid differentiations. Media was changed two days before collection, on the day of the collection, 270 µl of medium were taken and diluted with 30 µl of HCl buffer (0.01 N HCl, 4 mM Na2O5S2, and 1 mM EDTA), they were then snap frozen in liquid nitrogen and stored at -80 °C until the day of the analysis. The ELISA was performed according to the manufacturer's instructions with 50 µl sample volume. Values were normalized to the size (area) of the organoids.

Western blot

For western blot, five non-embedded organoids were lysed using RIPA buffer (Abcam) with Complete protease inhibitor cocktail (Roche) for 20min on ice. In order disrupt DNA, lysates were sonicated for 10 cycles (30s on / 30s off) using the Bioruptor Pico (Diagenode). Samples were then centrifuged at 4 °C for 20 min at 14 000 g. The protein concentration was determined using the Pierce™ BCA Protein Assay Kit (Thermo Fischer). Samples were brought to the same concentration and boiled at 95 °C for 5 min in denaturating loading buffer. Protein separation was achieved using SDS polyacrylamide gel electrophoresis (Bolt™ 4-12% Bis-Tris Plus Gel, Thermo Fischer) and transferred onto PVDF membrane using iBlot™ 2 Gel Transfer Device (Thermo Fischer). Membranes were blocked for 1 h at RT in 5% skimmed milk powder in PBS before incubating overnight at 4◦C with the primary antibodies prepared in 5% BSA and 0.02% Tween (see Table S2 for list of antibodies used). Membranes were then washed 3x for 5 min with PBST and incubated with DyLight™ secondary antibodies (anti-rabbit IgG (H+L) 800 or anti-mouse IgG (H+L) 680). Membranes were scanned in the Odyssey® Fc 2800 Imaging System. Western blots were analyzed using ImageJ software.

Immunofluorescence stainings for cell characterization

Immunofluorescent stainings for iPSCs and mfNPCs were performed as described in[80] and[15], respectively. A commercially available control cell line (Alstem, Cat# iPS15) was derived into small molecule neural precursor (smNPC)[81] and used as a positive control for Pax6 immunostaining (Fig. S1B).

Immunofluorescence stainings of organoid sections

Immunofluorescence staining of organoids was carried out using a modified published protocol[16]. Embedded organoids were fixed with 4 % paraformaldehyde overnight at RT and washed with PBS 3x 15 min. One organoid per cell line, condition and experiment were embedded in 3% low-melting point agarose, the solid agarose block with the organoid was sectioned into 70 µm sections using a vibrating blade microtome (Leica VT1000s). The sections were permeabilized and blocked with blocking buffer (BB) (2.5 % donkey serum or normal goat serum, 2.5 % BSA, and 0.1 % sodium azide) containing 0.5 % Triton X-100. Sections were incubated for 72 h at 4 °C on an orbital shaker with primary antibodies (see Table S2) in BB containing 0.1% Triton X-100.

Incubation with secondary antibodies and mounting of the sections were performed as described in[16].

For high-content image analysis, stained sections from at least three independent organoid differentiations were acquired on Yokogawa CV8000 high content screening microscope with a 20x Objective (33 planes, 3,2 µm interval).

For quantitative analysis at 60x, a confocal laser scanning microscope (Zeiss LSM 710) was used, two randomly selected fields per organoid section were acquired of three independent organoid differentiations, keeping the same acquisition settings.

For qualitative images, organoid sections were acquired with a confocal laser scanning microscope (Zeiss LSM 710) with either a 20x, 40x or 60x objective. Three-dimensional surface reconstructions of confocal z-stacks were created using Imaris software (Bitplane)

Representative images were cropped and rescaled using Adobe illustrator for visualization purposes, all originals can be found at https://doi.org/10.17881/xfh3-a153.

EdU incorporation assay

For EdU incorporation assay, 30DIV embedded organoids were incubated with Edu for 8h and then fixed with 4% PFA immediately or maintained in culture for 7 days after EdU removal. Staining was performed using the Click-iT Plus EdU Alexa Fluor Imaging Kit (Thermo Fisher, Cat # C10638) according to the manufacturer's protocol, sections were then immunostained for additional markers using the protocol described above.

Image processing and analysis

Immunofluorescence 3D images of each organoid were processed and analyzed in Matlab (2020a, Mathworks) using a custom image-analysis algorithm as described previously[82,83].

Transcriptomics analysis

Total RNA was isolated from 3 independent organoid generations at DIV30, for each sample, 8 embedded organoids of the same batch were pooled from CTRL1, CTRL2, PD1 and PD2 using Trizol reagent (cat. no. 15596026, ThermoFischer) according to the manufacturer's protocol. mRNA library preparation and sequencing were conducted as described before[84]. Sequencing of samples was done in two individual runs, PD1 and CTRL2 were analyzed in parallel during the first run, CTRL2 and PD1 were analyzed together during the second run.

Analysis of transcriptomics data

Gene expression analysis based on the RNAseq data was done following the method described in[84]. p-value significance scores from of the two individual datasets (PD1 vs CTRL2 and PD2 vs CTRL1) were combined using the weighted meta-analysis method by Marot and Mayer[85], focusing only on the genes with shared sign of the log fold-change. The final integrated p-values were then adjusted for multiple hypothesis testing using the Benjamini-Hochberg approach. The combined log fold change is expressed as the mean of the log fold change from the two datasets.

Lipidomics analysis

For lipidomics analysis, four embedded organoids at DIV30 were pooled per cell line for each experiment. Analysis was performed on two of the controls (CTRL1 and CTRL2) and all of the GBA-PD lines (PD1 and PD2 and PD3). On the day of the collection, organoids were washed once with ice-cold PBS and snap frozen with liquid nitrogen. Lipid species were analyzed by Lipometrix (http://www.lipometrix.be) using HILIC LC-MS/MS. Results were normalized to DNA content. Analysis was carried out on samples from four independent organoid generations. p-values were calculated using a one-way ANOVA test, assuming equal variance (homoscedasticity) in the 2 groups. FDR adjusted p-values were calculated using the Benjamini–Hochberg[86] procedure.

Microelecrode array (MEA)

MEA recordings were conducted using the Maestro system from Axion BioSystems using a protocol adapted from[84]. 10-day-old non-embedded organoids were placed on a 96-well MEA plate containing 8-electrodes per well and precoated with 0.1 mg/ml poly-D-lysine hydrobromide (Sigma, P7886) and 10 µg/ml laminin (Sigma, L2020), a droplet of geltrex (Invitrogen, A1413302) was added on top to secure the organoid on the right position. The recording of the firing activity was carried out as described before [13,84]. The Axion

Integrated Studio software (AxIS 2.1), was used to analyze MEA recordings. To minimize false positives and missed detections, a Butterworth band pass filter with 200-3000 Hz cutoff frequency and a threshold of 6 x SD were used. Electrodes were defined as active when the average activity detected was ≥5 spikes/min. Neural stat compiler files generated from the recordings were used for the data analysis. Further details regarding the analysis were previously described[84]. Script for data analysis is uploaded in the corresponding Gitlab repository.

Metabolic modeling

RNA sequencing Transcripts Per Kilobase Million (TPM) reads were filtered to exclude genes with expression of 0 among all technical replicates of each cell line. After filtering, the median of TPM expression between technical replicates was calculated. In case of gene isoforms, the isoform with the highest median value was considered. Using clusterProfiler package (version 3.9) in R (version 3.6.2) gene symbols were assigned to EntrezIDs, which are required for the model generation.

For every cell line (two mutants and two healthy controls) a context-specific metabolic model was reconstructed with the rFASTCORMICS pipeline[25] using Recon3[24]. Models were constrained by the media composition. Generated models were further analyzed using the COBRA toolbox[87] in Matlab (version 2019b). Models were compared regarding their gene, reaction and metabolite composition. Shared genes, reactions and metabolites between both control models (CTRL1 and CTRL2) and then between both GBA-PD models (PD1 and PD2) were identified using the intersect function of Matlab. Unique genes, reactions and metabolites for control models and mutant models were found using the setdiff function of Matlab. Identified reactions being uniquely present in healthy or PD models were assigned to Recon3 subsystems. Unique gene functional classification was analyzed using the David enrichment tool freely available online at https://david.ncifcrf.gov/home.jsp.

Flux variability analysis (FVA) for the subsystems of interest was done with model optimization for ATP demand using the IBM_CPLEX solver (version 12.10). Subsystems of interest were defined based on the sum of reactions being present uniquely in healthy or in PD models. For most of the subsystems this reaction count was directly correlating with the size of subsystem in Recon3, therefore the number of reactions was expressed as percentage of the total amount of reactions in the respective subsystem in Recon3. Subsystems with a total size larger than 20 reactions in Recon3 and with more than 20% of reactions being different between control and PD models were additionally considered for the FVA. Peptide metabolism and Keratan sulfate synthesis subsystems were not analyzed with FVA because they were not present in the control models, as no comparison would be possible. In addition, central energy metabolism subsystems – Glycolysis, Pentose Phosphate pathway, Citric acid cycle and Oxidative phosphorylation were included in the downstream analysis.

A similarity index (SI) was calculated to assess the differences in flux variability for the subsystems of interest between healthy and PD models, using the formula:

SI=max(0,(min(v1max,v2max)-max(v1min,v2min)+eps)/(max(v1max,v2max) min(v1min,v2min)+eps))

Where v1max is the maximal predicted flux of model 1, v2max is the maximal predicted flux of model 2, v1min is the minimal predicted flux of model 1, v2min is the minimal predicted flux of model 2 and eps=0 because SI was calculated only for the shared reactions between the models.

Since SI can be calculated between two models, we computed SI for the following comparisons: CTRL1vsPD1; CTR1vsPD2; CTRL2vsPD1; CTRL2vsPD2; CTRL1vsCTRL2 and PD1vsPD2. Then the mean value of SI of the comparisons CTRL1vsPD1; CTR1vsPD2; CTRL2vsPD1; CTRL2vsPD2 was further

estimated to obtain a representative SI between CTRL vs GBA-PD models. SI of 0 represents a complete mismatch in flux variability between the models, and SI of 1 represents the highest similarity in flux variability

Extracellular Flux Analysis (SeaHorse Measurements)

Non-embedded organoids were seeded in a XF 96-well spheroid plate (Agilent Technologies, 102905-100) coated with Cell-Tak (Corning, 354240) and analyzed using an XFe96 Extracellular Flux Analyzer (Seahorse Biosciences) at DIV30. Seahorse XF Cell Mito Stress Tests were carried out using sequential injections of Oligomycin (5 µM), FCCP (1 µM), and Rotenone plus Antimycin A (1 µM). Values were normalized to the size (area) of the organoids. Three baseline measures and three measurements after each compound injection were performed.

DNA oxidative damage

8-hydroxy-2-deoxy Guanosine (8-OHdG) was measured in the extracellular medium of non-embedded organoids at DIV30 (Abcam, ab201734). The ELISA was performed following the manufacturer's instructions.

SA-β-Galactosidase staining

Staining was performed on PFA-fixed embedded organoid sections with the Senescence Detection Kit (Abcam, ab65351) following the manufacturer's instructions. Images were acquired at 4X and 10x on an Olympus IX83 microscope and enhanced using ImageJ software to account solely for differences in the background levels of light.

Statistical analysis

The data was processed in R software (R version 3.5.1 -- "Feather Spray"). First, data for each cell line and experiment was grouped by differentiation experiment and condition and the mean of the measurements was calculated. Statistical significance was tested using the Wilcoxon signed-rank test for comparison between the two conditions (Control and GBA-PD). The statistical analysis of EdU staining was done by comparing the groups with Kruskal–Wallis H test, followed by a post hoc Dunn test. Each data point in the graphs corresponds to the data from one cell line for one individual differentiation experiment.

For analysis of lipidomics data, p-values were calculated using a one-way ANOVA test, assuming equal variance (homoscedasticity) in the 2 groups (CTRL and GBA-PD). FDR adjusted p-values were calculated using the Benjamini–Hochberg procedure approach[86]. In order to compare the levels of all lipid species within the same lipid class, the sum of all species for each class was calculated and a Mann-Whitney u-test was used using GraphPad prism 9 to test the significance between the two conditions.

For gene-level differential expression analysis of transcriptomics data, p-value significance scores from of the two individual datasets (PD1 vs CTRL2 and PD2 vs CTRL1) were integrated using the Marot and Mayer method[85]. The final combined p-values were then adjusted for multiple hypothesis testing using the Benjamini-Hochberg procedure.

Data availability

All original and processed data as well as scripts that support the findings of this study are public available at this https://doi.org/10.17881/xfh3-a153.

Ethics Statement

The use of existing iPSC lines obtained from previous studies was approved by the local ethical committee (Comité National d'Ethique de Recherche). Cell lines used in this study are summarized in Supplementary Table 1.

Acknowledgments

We thank Dr. Nico J. Diederich and Laura Longhino from Centre Hospitalier de Luxembourg, Dr. Anna-Lena Hallmann from the Max Planck Institute, Anthony Schapira, David Chau and Revital Golan from University College London, StemBANCC and the Coriell Institute for providing cell lines. Dr. Anna Monzel for iPSC characterization and Michele Bassis for technical assistance. Microscopy and flow cytometry were supported by the LCSB bio-imaging platform. We thank the Disease Modeling Screening Platform from LCSB and LIH for their help with performing automated and high-throughput procedures. We also thank the private donors who support our work at the Luxembourg Center for Systems Biomedicine.

This work leading to this manuscript was supported by the following funding:

Fonds National de la Recherche (FNR) Luxembourg AFR program; Fonds National de la Recherche (FNR) Luxembourg INTER/JPND/15/11092422; Fonds National de la Recherche (FNR) Luxembourg, National Centre of Excellence in Research on Parkinson's Disease (NCER-PD) FNR/NCER13/BM/11264123; National Institutes of Health grant U12AV123456; National Institutes of Health grant R01AB123456; William K. Bowes Jr Foundation; German Research Foundation grant AB 1234/1-1; Max Planck Society’s White Paper-Project: Brain Organoids: Alternatives to Animal Testing in Neuroscience; Office of Biological and Environmental Research of the U.S. Department of Energy Atmospheric System Research Program Interagency Agreement grant DE-SC0000001; National Institute of Health Research UK.

Competing interests

The authors J.J., S.B., and J.C.S. declare financial and non-financial competing interests as cofounders and shareholders of OrganoTherapeutics société à responsabilité limitée (SARL).

Author contributions

I.R. conceived, designed, collected data, performed data analysis and interpretation of results. A.Z. developed the metabolic model. C.S. and C.A. contributed with experiments. R.H. generated snRNA-seq data and E.G. performed the analysis. P.A. helped with the automated-image analysis. SV, TR and HRS did reprogramming of fibroblasts into iPSC. The work was supervised by J.C.S., I.R., and A.Z. wrote the original manuscript. S.N., C.S., T.S., S.B., R.K., J.J. and J.C.S. revised and edited the manuscript.

References

1. Sidransky, E.*, et al.* Multicenter analysis of glucocerebrosidase mutations in Parkinson's disease. *N Engl J Med* **361**, 1651-1661 (2009).
2. Boer, D.E.C., van Smeden, J., Bouwstra, J.A. & Aerts, J. Glucocerebrosidase: Functions in and Beyond the Lysosome. *J Clin Med* **9**(2020).
3. Sun, A. Lysosomal storage disease overview. *Ann Transl Med* **6**, 476 (2018).
4. Sidransky, E. & Lopez, G. The link between the GBA gene and parkinsonism. *Lancet Neurol* **11**, 986-998 (2012).
5. Schwamborn, J.C. Is Parkinson's Disease a Neurodevelopmental Disorder and Will Brain Organoids Help Us to Understand It? *Stem Cells Dev* **27**, 968-975 (2018).
6. Wulansari, N.*, et al.* Neurodevelopmental defects and neurodegenerative phenotypes in human brain organoids carrying Parkinson's disease-linked DNAJC6 mutations. *Sci Adv* **7**(2021).
7. Walter, J.*, et al.* The Parkinson's-disease-associated mutation LRRK2-G2019S alters dopaminergic differentiation dynamics via NR2F1. *Cell Reports* **37**, 109864 (2021).
8. Akrioti, E.*, et al.* Early Signs of Molecular Defects in iPSC-Derived Neural Stems Cells from Patients with Familial Parkinson's Disease. in *Biomolecules*, Vol. 12 (2022).
9. Masato, A., Plotegher, N., Boassa, D. & Bubacco, L. Impaired dopamine metabolism in Parkinson's disease pathogenesis. *Molecular Neurodegeneration* **14**, 35 (2019).
10. Sonninen, T.-M.*, et al.* Metabolic alterations in Parkinson's disease astrocytes. *Scientific Reports* **10**, 14474 (2020).
11. Shao, Y.*, et al.* Comprehensive metabolic profiling of Parkinson's disease by liquid chromatography-mass spectrometry. *Molecular Neurodegeneration* **16**, 4 (2021).
12. Kałużna, M., Trzeciak, I., Ziemnicka, K., Machaczka, M. & Ruchała, M. Endocrine and metabolic disorders in patients with Gaucher disease type 1: a review. *Orphanet J Rare Dis* **14**, 275 (2019).
13. Monzel, A.S.*, et al.* Derivation of Human Midbrain-Specific Organoids from Neuroepithelial Stem Cells. *Stem Cell Reports* **8**, 1144-1154 (2017).
14. Zagare, A.*, et al.* Midbrain organoids mimic early embryonic neurodevelopment and recapitulate LRRK2-p.Gly2019Ser-associated gene expression. *The American Journal of Human Genetics* **109**, 311-327 (2022).
15. Smits, L.M.*, et al.* Modeling Parkinson's disease in midbrain-like organoids. *npj Parkinson's Disease* **5**, 5 (2019).
16. Nickels, S.L.*, et al.* Reproducible generation of human midbrain organoids for in vitro modeling of Parkinson's disease. *Stem Cell Res* **46**, 101870 (2020).
17. García-Sanz, P.*, et al.* N370S-GBA1 mutation causes lysosomal cholesterol accumulation in Parkinson's disease. *Mov Disord* **32**, 1409-1422 (2017).
18. Fernandes, H.J.*, et al.* ER Stress and Autophagic Perturbations Lead to Elevated Extracellular α-Synuclein in GBA-N370S Parkinson's iPSC-Derived Dopamine Neurons. *Stem Cell Reports* **6**, 342-356 (2016).
19. Schöndorf, D.C.*, et al.* The NAD+ Precursor Nicotinamide Riboside Rescues Mitochondrial Defects and Neuronal Loss in iPSC and Fly Models of Parkinson's Disease. *Cell Rep* **23**, 2976-2988 (2018).
20. Morén, C.*, et al.* GBA mutation promotes early mitochondrial dysfunction in 3D neurosphere models. *Aging (Albany NY)* **11**, 10338-10355 (2019).
21. Li, H.*, et al.* Mitochondrial dysfunction and mitophagy defect triggered by heterozygous GBA mutations. *Autophagy* **15**, 113-130 (2019).
22. Gu, C., Kim, G.B., Kim, W.J., Kim, H.U. & Lee, S.Y. Current status and applications of genome-scale metabolic models. *Genome Biology* **20**, 121 (2019).
23. Wang, H.*, et al.* Genome-scale metabolic network reconstruction of model animals as a platform for translational research. *Proc Natl Acad Sci U S A* **118**(2021).
24. Brunk, E.*, et al.* Recon3D enables a three-dimensional view of gene variation in human metabolism. *Nature Biotechnology* **36**, 272-281 (2018).
25. Pacheco, M.P.*, et al.* Identifying and targeting cancer-specific metabolism with network-based drug target prediction. *EBioMedicine* **43**, 98-106 (2019).
26. Pissadaki, E.K. & Bolam, J.P. The energy cost of action potential propagation in dopamine neurons: clues to susceptibility in Parkinson's disease. *Front Comput Neurosci* **7**, 13 (2013).

27. Błaszczyk, J.W. The Emerging Role of Energy Metabolism and Neuroprotective Strategies in Parkinson's Disease. *Frontiers in Aging Neuroscience* **10**(2018).
28. Gegg, M.E.*, et al.* No evidence for substrate accumulation in Parkinson brains with GBA mutations. *Mov Disord* **30**, 1085-1089 (2015).
29. Boutin, M., Sun, Y., Shacka, J.J. & Auray-Blais, C. Tandem Mass Spectrometry Multiplex Analysis of Glucosylceramide and Galactosylceramide Isoforms in Brain Tissues at Different Stages of Parkinson Disease. *Analytical Chemistry* **88**, 1856-1863 (2016).
30. Choi, J.*, et al.* Comprehensive analysis of phospholipids in the brain, heart, kidney, and liver: brain phospholipids are least enriched with polyunsaturated fatty acids. *Mol Cell Biochem* **442**, 187-201 (2018).
31. Cheng, D.*, et al.* Lipid pathway alterations in Parkinson's disease primary visual cortex. *PLoS One* **6**, e17299 (2011).
32. Traynor-Kaplan, A.*, et al.* Fatty-acyl chain profiles of cellular phosphoinositides. *Biochim Biophys Acta Mol Cell Biol Lipids* **1862**, 513-522 (2017).
33. Raghu, P., Joseph, A., Krishnan, H., Singh, P. & Saha, S. Phosphoinositides: Regulators of Nervous System Function in Health and Disease. *Frontiers in Molecular Neuroscience* **12**(2019).
34. Salvadores, N., Sanhueza, M., Manque, P. & Court, F.A. Axonal Degeneration during Aging and Its Functional Role in Neurodegenerative Disorders. *Front Neurosci* **11**, 451 (2017).
35. Francis, F.*, et al.* Doublecortin is a developmentally regulated, microtubule-associated protein expressed in migrating and differentiating neurons. *Neuron* **23**, 247-256 (1999).
36. Gleeson, J.G., Lin, P.T., Flanagan, L.A. & Walsh, C.A. Doublecortin is a microtubule-associated protein and is expressed widely by migrating neurons. *Neuron* **23**, 257-271 (1999).
37. Bott, C.J.*, et al.* Nestin in immature embryonic neurons affects axon growth cone morphology and Semaphorin3a sensitivity. *Mol Biol Cell* **30**, 1214-1229 (2019).
38. Zetterström, R.H.*, et al.* Dopamine Neuron Agenesis in Nurr1-Deficient Mice. *Science* **276**, 248-250 (1997).
39. Saucedo-Cardenas, O.*, et al.* Nurr1 is essential for the induction of the dopaminergic phenotype and the survival of ventral mesencephalic late dopaminergic precursor neurons. *Proc Natl Acad Sci U S A* **95**, 4013-4018 (1998).
40. Smith, G.A.*, et al.* A Nurr1 agonist causes neuroprotection in a Parkinson's disease lesion model primed with the toll-like receptor 3 dsRNA inflammatory stimulant poly(I:C). *PLoS One* **10**, e0121072 (2015).
41. Ferri, A.L.*, et al.* Foxa1 and Foxa2 regulate multiple phases of midbrain dopaminergic neuron development in a dosage-dependent manner. *Development* **134**, 2761-2769 (2007).
42. Xi, J.*, et al.* Specification of midbrain dopamine neurons from primate pluripotent stem cells. *Stem Cells* **30**, 1655-1663 (2012).
43. Blesa, J.*, et al.* Compensatory mechanisms in Parkinson's disease: Circuits adaptations and role in disease modification. *Experimental Neurology* (2017).
44. Bartek, J. & Lukas, J. DNA damage checkpoints: from initiation to recovery or adaptation. *Current Opinion in Cell Biology* **19**, 238-245 (2007).
45. Barzilai, A. & Yamamoto, K. DNA damage responses to oxidative stress. *DNA repair* (2004).
46. Di Micco, R., Krizhanovsky, V., Baker, D. & d'Adda di Fagagna, F. Cellular senescence in ageing: from mechanisms to therapeutic opportunities. *Nat Rev Mol Cell Biol* **22**, 75-95 (2021).
47. Raghuram, G.V. & Mishra, P.K. Stress induced premature senescence: a new culprit in ovarian tumorigenesis? *Indian J Med Res* **140 Suppl**, S120-129 (2014).
48. Freund, A., Laberge, R.M., Demaria, M. & Campisi, J. Lamin B1 loss is a senescence-associated biomarker. *Mol Biol Cell* **23**, 2066-2075 (2012).
49. Lee, J.H., Kim, E.W., Croteau, D.L. & Bohr, V.A. Heterochromatin: an epigenetic point of view in aging. *Exp Mol Med* **52**, 1466-1474 (2020).
50. Wasserzug-Pash, P.*, et al.* Loss of heterochromatin and retrotransposon silencing as determinants in oocyte aging. *Aging Cell* **21**, e13568 (2022).
51. Zhang, R., Chen, W. & Adams, P.D. Molecular dissection of formation of senescence-associated heterochromatin foci. *Mol Cell Biol* **27**, 2343-2358 (2007).
52. Hernandez-Segura, A., Nehme, J. & Demaria, M. Hallmarks of Cellular Senescence. *Trends Cell Biol* **28**, 436-453 (2018).

53. Cha, S.H.*, et al.* Loss of parkin promotes lipid rafts-dependent endocytosis through accumulating caveolin-1: implications for Parkinson's disease. *Mol Neurodegener* **10**, 63 (2015).
54. Fanning, S.*, et al.* Lipidomic Analysis of α-Synuclein Neurotoxicity Identifies Stearoyl CoA Desaturase as a Target for Parkinson Treatment. *Mol Cell* **73**, 1001-1014.e1008 (2019).
55. Kabeya, Y.*, et al.* LC3, GABARAP and GATE16 localize to autophagosomal membrane depending on form-II formation. *J Cell Sci* **117**, 2805-2812 (2004).
56. Sou, Y.S., Tanida, I., Komatsu, M., Ueno, T. & Kominami, E. Phosphatidylserine in addition to phosphatidylethanolamine is an in vitro target of the mammalian Atg8 modifiers, LC3, GABARAP, and GATE-16. *J Biol Chem* **281**, 3017-3024 (2006).
57. Hattingen, E.*, et al.* Phosphorus and proton magnetic resonance spectroscopy demonstrates mitochondrial dysfunction in early and advanced Parkinson's disease. *Brain* **132**, 3285-3297 (2009).
58. Blumenreich, S.*, et al.* Elevation of gangliosides in four brain regions from Parkinson's disease patients with a GBA mutation. *npj Parkinson's Disease* **8**, 99 (2022).
59. Schöndorf, D.C.*, et al.* iPSC-derived neurons from GBA1-associated Parkinson's disease patients show autophagic defects and impaired calcium homeostasis. *Nat Commun* **5**, 4028 (2014).
60. Rodríguez-Traver, E.*, et al.* Role of Nurr1 in the Generation and Differentiation of Dopaminergic Neurons from Stem Cells. *Neurotox Res* **30**, 14-31 (2016).
61. Le, W.*, et al.* Selective agenesis of mesencephalic dopaminergic neurons in Nurr1-deficient mice. *Exp Neurol* **159**, 451-458 (1999).
62. Saijo, K.*, et al.* A Nurr1/CoREST pathway in microglia and astrocytes protects dopaminergic neurons from inflammation-induced death. *Cell* **137**, 47-59 (2009).
63. Wallén, A.A.*, et al.* Orphan nuclear receptor Nurr1 is essential for Ret expression in midbrain dopamine neurons and in the brain stem. *Mol Cell Neurosci* **18**, 649-663 (2001).
64. Galleguillos, D.*, et al.* Nurr1 regulates RET expression in dopamine neurons of adult rat midbrain. *J Neurochem* **114**, 1158-1167 (2010).
65. Kramer, E.R.*, et al.* Absence of Ret signaling in mice causes progressive and late degeneration of the nigrostriatal system. *PLoS Biol* **5**, e39 (2007).
66. Conway, J.A., Ince, S., Black, S. & Kramer, E.R. GDNF/RET signaling in dopamine neurons in vivo. *Cell Tissue Res* **382**, 135-146 (2020).
67. Teslaa, T. & Teitell, M.A. Pluripotent stem cell energy metabolism: an update. *Embo j* **34**, 138-153 (2015).
68. Jarazo, J.*, et al.* Parkinson's Disease Phenotypes in Patient Neuronal Cultures and Brain Organoids Improved by 2-Hydroxypropyl-β-Cyclodextrin Treatment. *Mov Disord* **37**, 80-94 (2022).
69. Woodard, C.M.*, et al.* iPSC-derived dopamine neurons reveal differences between monozygotic twins discordant for Parkinson's disease. *Cell Rep* **9**, 1173-1182 (2014).
70. Awad, O.*, et al.* Altered Differentiation Potential of Gaucher's Disease iPSC Neuronal Progenitors due to Wnt/β-Catenin Downregulation. *Stem Cell Reports* **9**, 1853-1867 (2017).
71. Lancaster, M.A. & Knoblich, J.A. Organogenesis in a dish: modeling development and disease using organoid technologies. *Science* **345**, 1247125 (2014).
72. Gegg, M.E.*, et al.* Glucocerebrosidase deficiency in substantia nigra of parkinson disease brains. *Ann Neurol* **72**, 455-463 (2012).
73. Rocha, E.M.*, et al.* Progressive decline of glucocerebrosidase in aging and Parkinson's disease. *Ann Clin Transl Neurol* **2**, 433-438 (2015).
74. Knobloch, M.*, et al.* A Fatty Acid Oxidation-Dependent Metabolic Shift Regulates Adult Neural Stem Cell Activity. *Cell Rep* **20**, 2144-2155 (2017).
75. Madsen, S., Ramosaj, M. & Knobloch, M. Lipid metabolism in focus: how the build-up and breakdown of lipids affects stem cells. *Development* **148**(2021).
76. Shimojo, M.*, et al.* Synaptotagmin-11 mediates a vesicle trafficking pathway that is essential for development and synaptic plasticity. *Genes Dev* **33**, 365-376 (2019).
77. Mazzulli, J.R.*, et al.* Activation of β-Glucocerebrosidase Reduces Pathological α-Synuclein and Restores Lysosomal Function in Parkinson's Patient Midbrain Neurons. *J Neurosci* **36**, 7693-7706 (2016).
78. Tropak, M.B., Reid, S.P., Guiral, M., Withers, S.G. & Mahuran, D. Pharmacological enhancement of beta-hexosaminidase activity in fibroblasts from adult Tay-Sachs and Sandhoff Patients. *J Biol Chem* **279**, 13478-13487 (2004).

79. Meng, X.L.*, et al.* Induced pluripotent stem cells derived from mouse models of lysosomal storage disorders. *Proc Natl Acad Sci U S A* **107**, 7886-7891 (2010).
80. Gomez-Giro, G.*, et al.* Synapse alterations precede neuronal damage and storage pathology in a human cerebral organoid model of CLN3-juvenile neuronal ceroid lipofuscinosis. *Acta Neuropathologica Communications* **7**, 222 (2019).
81. Reinhardt, P.*, et al.* Derivation and expansion using only small molecules of human neural progenitors for neurodegenerative disease modeling. *PLoS One* **8**, e59252 (2013).
82. Monzel, A.S.*, et al.* Machine learning-assisted neurotoxicity prediction in human midbrain organoids. *Parkinsonism Relat Disord* **75**, 105-109 (2020).
83. Bolognin, S.*, et al.* 3D Cultures of Parkinson's Disease-Specific Dopaminergic Neurons for High Content Phenotyping and Drug Testing. *Advanced science* (2018).
84. Modamio, J.*, et al.* Synaptic decline precedes dopaminergic neuronal loss in human midbrain organoids harboring a triplication of the SNCA gene. *bioRxiv*, 2021.2007.2015.452499 (2021).
85. Marot, G., Foulley, J.L., Mayer, C.D. & Jaffrézic, F. Moderated effect size and P-value combinations for microarray meta-analyses. *Bioinformatics* **25**, 2692-2699 (2009).
86. Benjamini, Y. & Hochberg, Y. Controlling the False Discovery Rate: A Practical and Powerful Approach to Multiple Testing. *Journal of the Royal Statistical Society: Series B (Methodological)* **57**, 289-300 (1995).
87. Heirendt, L.*, et al.* Creation and analysis of biochemical constraint-based models using the COBRA Toolbox v.3.0. *Nature Protocols* **14**, 639-702 (2019).

Figure Legends

Figure 1: Generation and Characterization GBA-PD midbrain organoids.

- **A)** Schematic overview of the protocol used for the generation of midbrain organoids. mfNPCs, floorplate neural precursors.
- **B)** GCase enzyme activity in differentiated MO cultures was significantly decreased (40% reduction) when compared with controls. The data represent a summary of three independent differentiation experiments per line each analyzed in triplicate at DIV30. Values are normalized to the average of controls per experiment. Wilcoxon T-test.; ***p < 0.001.
- **C)** GCase protein levels are not altered at DIV30. Representative western blot analysis and respective quantification. The data represent a summary of at least three independent differentiation experiments per line each analyzed in triplicate. Values are normalized to the average of controls per experiment.
- **D)** Decreased percentage of colocalization of GCase with lysosomes in GBA-PD organoids at DIV30. GCase (red), LAMP1 (green). Representative confocal images with their respective zoomed region of interest (ROI) and their quantification (scale bar, 10 µm). The data represent a summary of three independent differentiation experiments for all cell lines, normalized to the average of controls per experiment. Wilcoxon T-test.; *p < 0.05.
- **E) - F)** Representative western blot and quantification of expression of the autophagy markers p62 and LC3 at DIV30. Data represents a summary of at least five independent differentiation experiments. Values are normalized to the average of controls per experiment. Wilcoxon T-test.; ***p < 0.001.

Figure 2: Metabolic modeling of GBA-PD.

- **A)** Venn diagram representation of the structural model analysis.
- **B)** Comparison of model composition by reactions. Reactions found exclusively in control models (green) or in GBA-PD (purple) were mapped to the Recon 3 subsystems, and the top five most different subsystems based on the reaction number are listed for each condition. EDR = exchange/demand reaction, GP = glycerophospholipid.
- **C)** The top 10 most different subsystems between control (CTRL1 and CTRL2) and GBA-PD (PD1 and PD2) models after pooling the exclusive reactions of the two conditions. The size and color of the dot represents the number of reactions per subsystem. The location in relation to the x-axis represents the size of the subsystem in the generic Recon3. Subsystems are positioned on the y-axis in alphabetical order. GP = glycerophospholipid, ER = endoplasmic reticulum.
- **D)** Similarity index of flux variability analysis optimizing for ATP demand for subsystems of interest. SI between CTRL1 vs CTRL2 and SI between PD1 and PD2 models were compared, as well as the SI between the CTRL (CTRL1 and CTRL2) and GBA-PD (PD1 and PD2). SI of 0 represents a complete mismatch in flux variability between the models, whereas a SI of 1 represents the highest similarity in flux variability. PI = Phosphatidylinositol, ER = endoplasmic reticulum, GP = glycerophospholipid.

Figure 3: Lipidomics analysis showing differences in lipid classes and lipid species composition.

- **A)** Differences in phosphatidylethanolamine (PE) and phosphatidylcholine (PC) levels but not hexosylceramides (HexCer), sphingomyelins (SM) or phosphatidylinositol (PI) in HILIC LC-MS/MS

based lipidomic analysis of DIV30 organoids. Data represent a summary of four independent organoid differentiations, Mann-Whitney U test. **p < 0.01, ****p < 0.0001.

B) Pairwise comparison between GBA-PD vs control of phosphatidylinositol (PI) lipid species denoted by their sum notation. Data expressed as the Log2 of the fold change.

C) Plots for PI molecular species PI (38:5), PI (36:1), PI (40:4), each plot corresponds to the most enriched species for that sum notation: (18:1/20:4), PI (18:0/18:1) and PI (18:0/22:4), respectively. Data represent a summary of four independent organoid differentiations and is expressed as the percentage of the entire PI class. p-values were calculated using a one-way ANOVA test. FDR adjusted p-values were calculated using the Benjamini–Hochberg procedure. **p < 0.01, ****p < 0.0001.

D) Fatty acid composition of the lipid species within the sphingomyelin lipid class. Data represent a summary of four independent organoid differentiations expressed as relative quantification, where each species is normalized to the total amount of lipid of its class. p-values were calculated using a one-way ANOVA test. FDR adjusted p-values were calculated using the Benjamini–Hochberg procedure. *p < 0.05, **p < 0.01, ***p < 0.001, ****p < 0.0001.

Figure 4: Impaired dopaminergic and general neuronal differentiation in GBA-PD patient-specific midbrain organoids.

A) Levels of extracellular dopamine in culture media at DIV60 were lower for GBA-PD organoids when compared with controls, measured by ELISA. The data represent a summary of five independent differentiation experiments for all cell lines. Wilcoxon T-test.; ***p < 0.001.

B) Quantification of TH protein levels and representative western blot at DIV60 showing decreased levels of the protein in heterozygous GBA-N370S organoids. Data represents a summary of five independent differentiation experiments normalized to the mean of the controls per batch. Wilcoxon T-test.; ***p < 0.001.

C) Representative images of DIV30 midbrain organoids sections stained for TH (red), MAP2 (green), nuclei (blue) (scalebar, 200 µm).

D) Immunofluorescence images of sections from Fig. 3C acquired at 40x (scalebar, 50 µm).

E) High-content automated image analysis of immunofluorescence stainings of dopaminergic neurons in organoids at DIV30 expressed as the proportion of cells expressing TH normalized by total nuclei. Data represents a summary of six independent differentiation experiments normalized to the mean of the controls per batch. Wilcoxon T-test.; ***p < 0.001.

F) Neurite branching is less complex in dopaminergic neurons from GBA-PD organoids at DIV30 when compared with controls, measured by the number of nodes (branching points) and links (branches) extracted from the skeletonization of TH mask by the algorithm used for image analysis. Representative immunofluorescence images of TH+ neurons (yellow) showing less complex arborization in GBA-PD condition (Scalebar, 50 µm) and graphic illustration of the morphometric features; links, nodes and skeleton. Data is normalized to the mean of the controls per experiment. n=6, Wilcoxon T-test.; *p < 0.05.

G) GeneGO MetaCore™ enrichment analysis by process networks showing the top 20 overrepresented processes in DIV30 organoids.

H) Mean firing rate detected by individual electrodes of a multielectrode array (MEA) system at DIV15 showing that mutant organoids are less electrophysiologically active. The data represent a summary

of four independent differentiation experiments for all cell lines. Values are normalized to the mean of the controls per experiment. Wilcoxon T-test.; ***p < 0.001. Upper panel shows a representative image of a midbrain organoid positioned on an 8-electrode array in a 96-well tissue culture plate (scalebar, 500 µm).

I) Decreased levels of TH+ cells normalized to the total neuronal population at DIV15 using the early neuronal marker TUJ1 and DIV30 using the late neuronal marker MAP2.

Figure 5: Increased levels of SOX2 and cell cycle arrest in GBA-PD organoids.

A) DEGs involved in dopaminergic differentiation (PathCards) depicted via protein-protein associations obtained from the STRING database. The border of the nodes represents the log fold-change (logFC) of the gene expression in the comparison of control GBA-PD organoids vs controls. Edges depict protein-protein associations.

B) Representative immunofluorescence staining of SOX2 (red) in midbrain organoid sections at DIV15 (CTRL1 and PD1), along with an amplified region of interest (ROI) of the original. Nuclei stained with Hoechst 33342 (blue), scalebar is 200 µm and 25 µm, respectively.

C) Quantitative analyses of SOX+ population shows increased proportion of cells expressing the neural stem cell marker in GBA-PD MOs at DIV15 and DIV30. Each data point represents the average of technical replicates for each independent differentiation. Values are normalized to the mean of the controls per experiment. Wilcoxon T-test.; Wilcoxon T-test.; *p < 0.05, **p < 0.01, n=3.

D) Validation of the immunofluorescence results by immunoblotting against SOX2 in whole cell lysates obtained from organoids at DIV15. The data represent a summary of four independent differentiations. Values are normalized to the mean of the controls per experiment. Wilcoxon T-test.; ***p < 0.001.

E) Representative images CTRL2 and PD2 expressing SOX2 (red) and Ki67(green) at DIV15. Nuclei stained with Hoechst 33342 (blue) (scalebar, 20 µm).

F) Decreased proportion of proliferative neural stem cells in mutant MOs (DIV30) compared to controls, represented by cells expressing both SOX2 and Ki67. Values are normalized to the mean of the controls per experiment. Wilcoxon T-test.; *p < 0.05.

G) - H) Propidium iodide (PI) fluorescence profiles of CTRL3 and PD3 with cell cycle distribution (Watson pragmatic model) (G). Percentage of cells in each cycle phase analyzed by flow cytometry using propidium iodide showing accumulation of cells in the S phase at DIV30 in GBA-PD organoids. The experiment was repeated five times using organoids from five independent differentiations. Wilcoxon T-test.; *p < 0.05.

I) Representative images (left) of EdU staining (green) for evaluation of the proliferation of SOX+ neural precursors (red) at the day of the exposure (day 0) and 7 days after the initial exposure to EdU (day 7). Images correspond to organoids at DIV30 of CTRL1 and PD1 cell lines (scalebar, 50 µm). Respective quantification (right) of the proportion of neural precursors with a positive signal for EdU showing a significant loss of the EdU staining in CTRL organoids at day 7 after EdU exposure. Data represents a summary of at least three independent differentiation experiments. Kruskal–Wallis with post hoc Dunn tests.; **p < 0.01, ****p < 0.0001.

Figure 6: DNA oxidative damage and signs of senescence in GBA-PD organoids.

A) Extracellular concentration of 8-OHdG in DIV30 organoids measured by ELISA. The data represent a summary of four independent differentiation experiments for all cell lines. Wilcoxon T-test.; ***p < 0.001.

B) High content automated image analysis showed decreased MFI of LAMINB1 (green) within Sox+ population (red). Data is a summary of eight independent differentiation experiments, normalized to the average of controls per organoid batch. Wilcoxon T-test.; **p < 0.01 (scalebar, 20 µm).

C) - D) Representative images of HP1γ (green) and SOX2 (red) in CTRL2 and PD2 organoid sections acquired at 60x (C) (scalebar, 10 µm). Quantification of MFI of HP1γ within the SOX2+ population (D left) and proportion of neural precursor cells (SOX2+) expressing high levels of HP1γ (D right) in DIV30 organoid sections acquired at 20× using the automated image analysis pipeline. Data represents a summary of five independent differentiation experiments normalized to the mean of the controls per batch. Wilcoxon T-test.; *p < 0.05, **p < 0.01.

E) Senescence-associated β-galactosidase staining (blue) of DIV30 organoids (scalebar, 200 µm, 4x; 100 µm, 10x).

Figure 1: Generation and Characterization GBA-PD midbrain organoids.

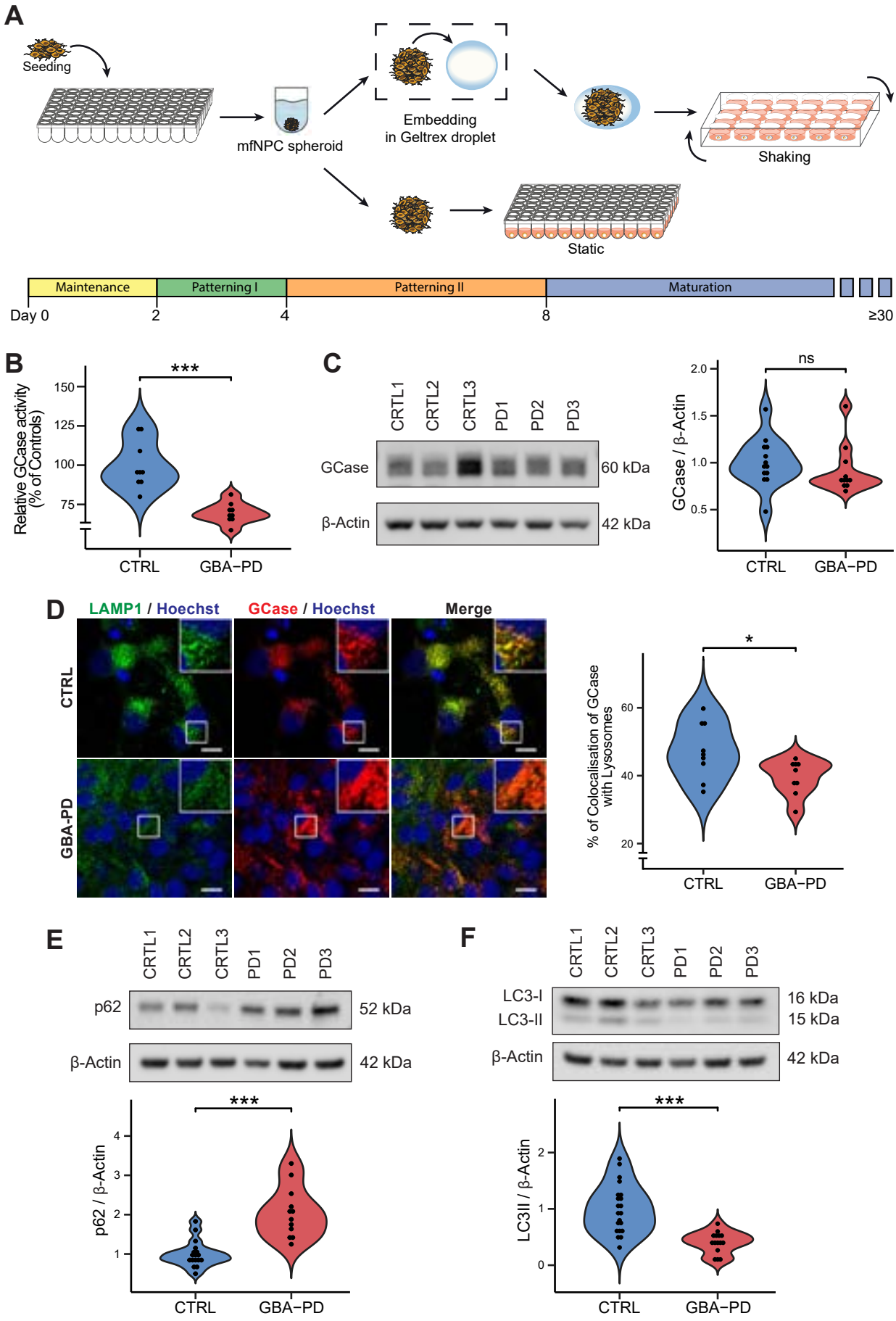

Figure 2: Metabolic modeling of GBA-PD.

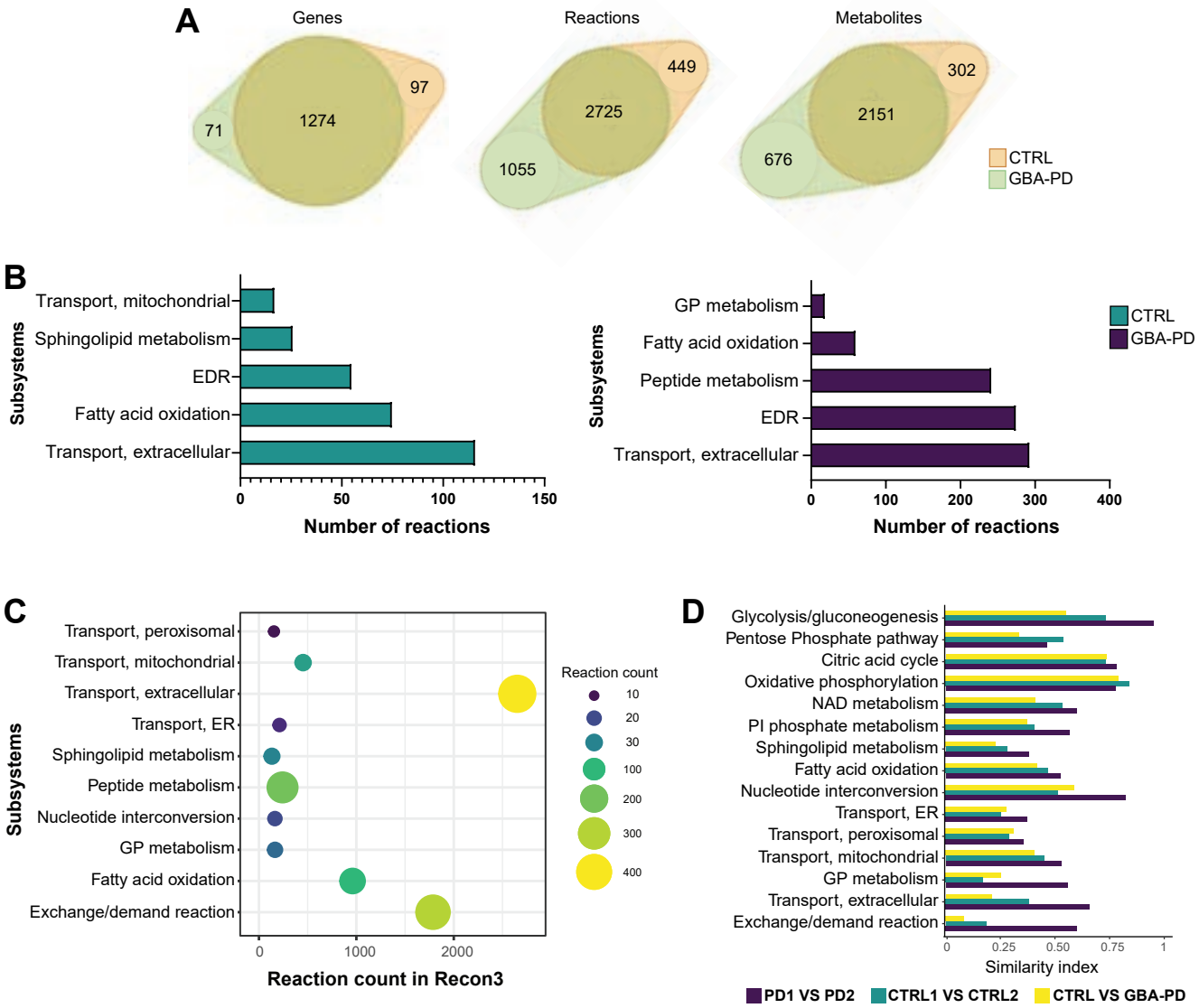

Figure 3: Lipidomics analysis showing differences in lipid classes and lipid species composition.

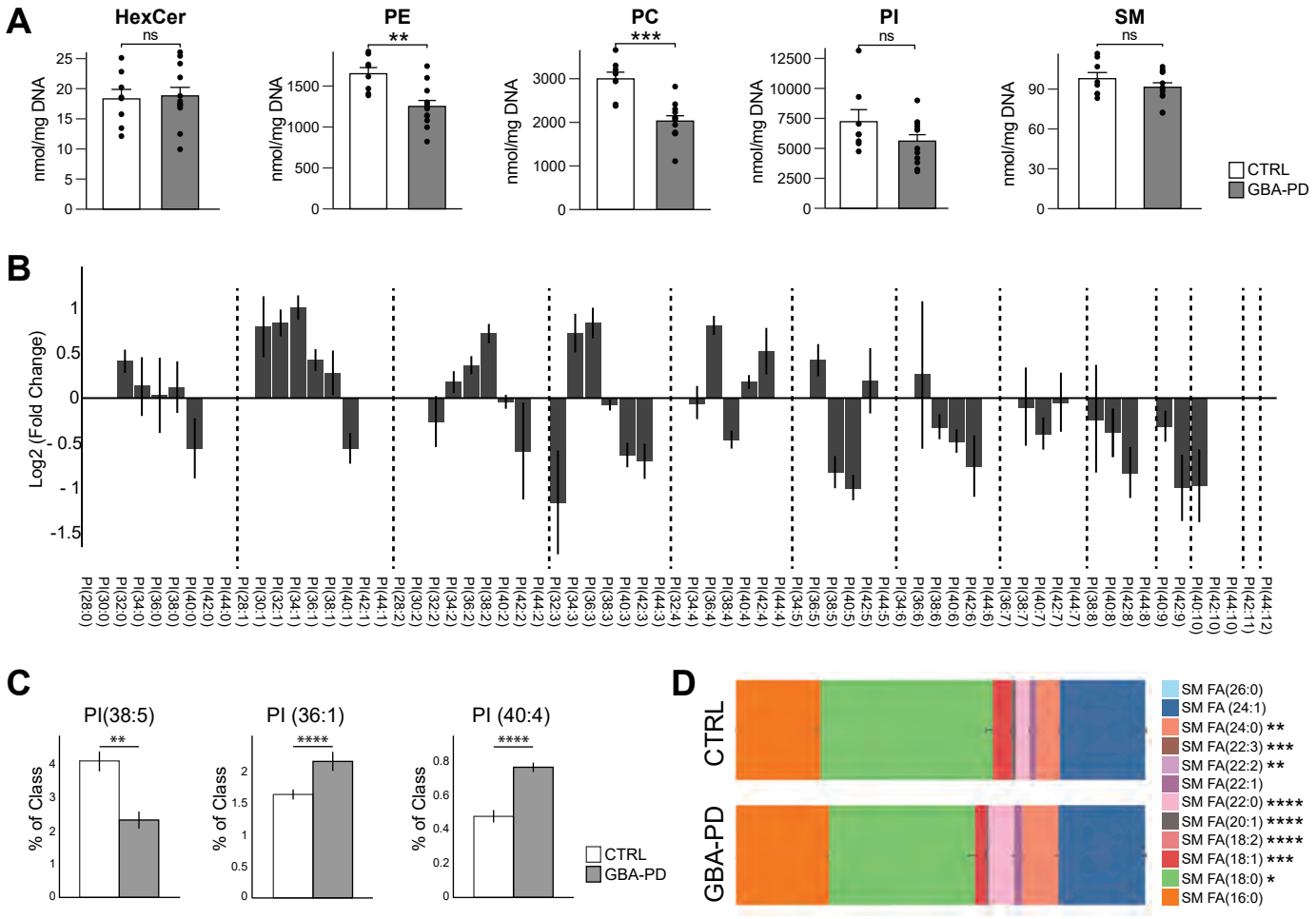

Figure 4: Impaired dopaminergic and general neuronal differentiation in GBA-PD patient-specific midbrain organoids.

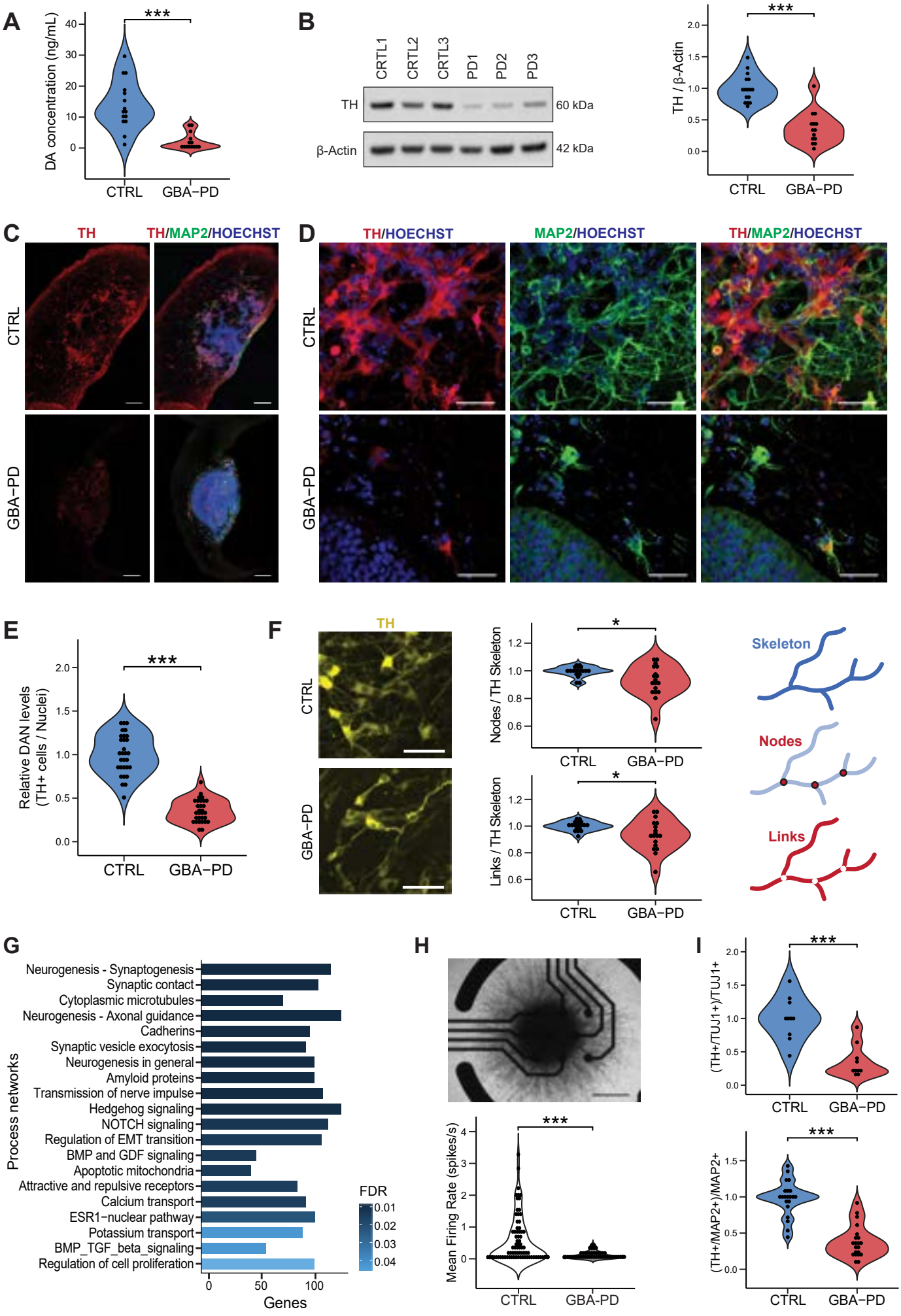

Figure 5: Increased levels of SOX2 and cell cycle arrest in GBA-PD organoids.

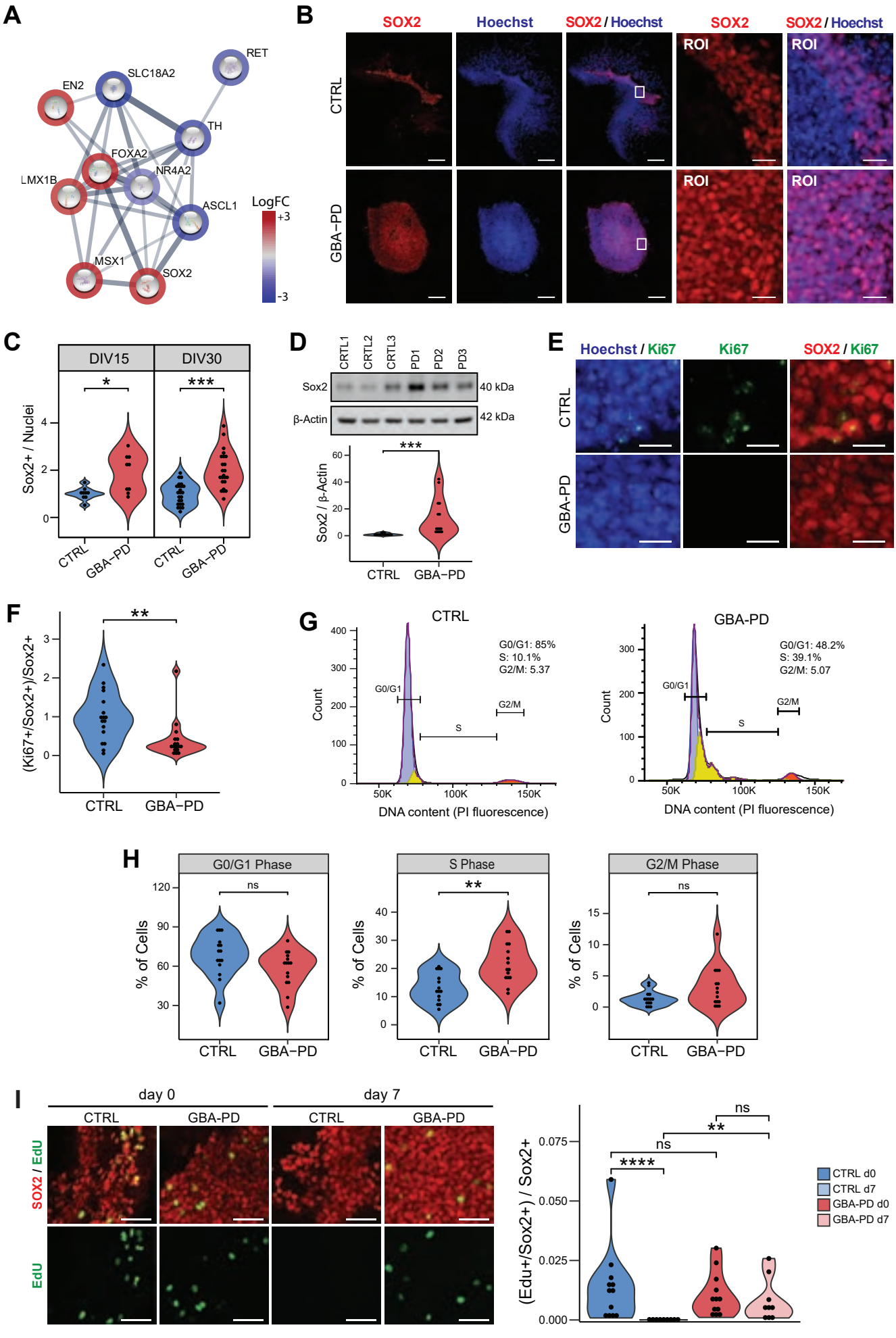

Figure 6: DNA oxidative damage and signs of senescence in GBA-PD organoids.

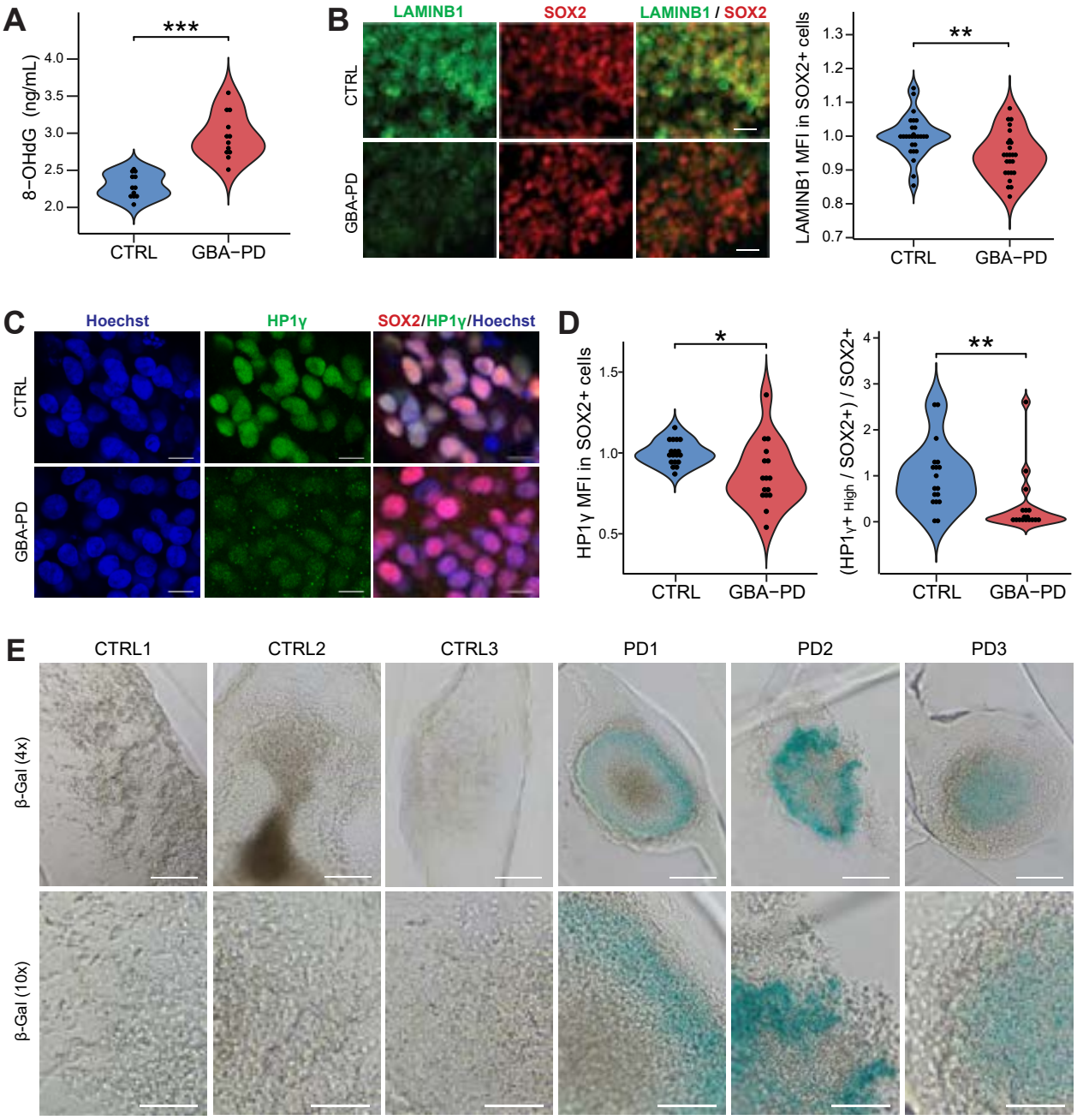

Supplementary Information

Impaired dopaminergic neuronal differentiation in GBA associated Parkinson's disease midbrain organoids is accompanied by an increased progenitor pool in cell cycle arrest

Isabel Rosety[1,7*], Alise Zagare[1], Claudia Saraiva[1], Sarah Nickels[1], Paul Antony[2], Catarina Almeida[1], Enrico Glaab[5], Rashi Halder[4], Sergiy Velychko[6], Thomas Rauen[6], Hans R. Schöler[6], Silvia Bolognin[1], Thomas Sauter[3], Javier Jarazo[1,7], Rejko Krueger[2,8], Jens C. Schwamborn[1,°]

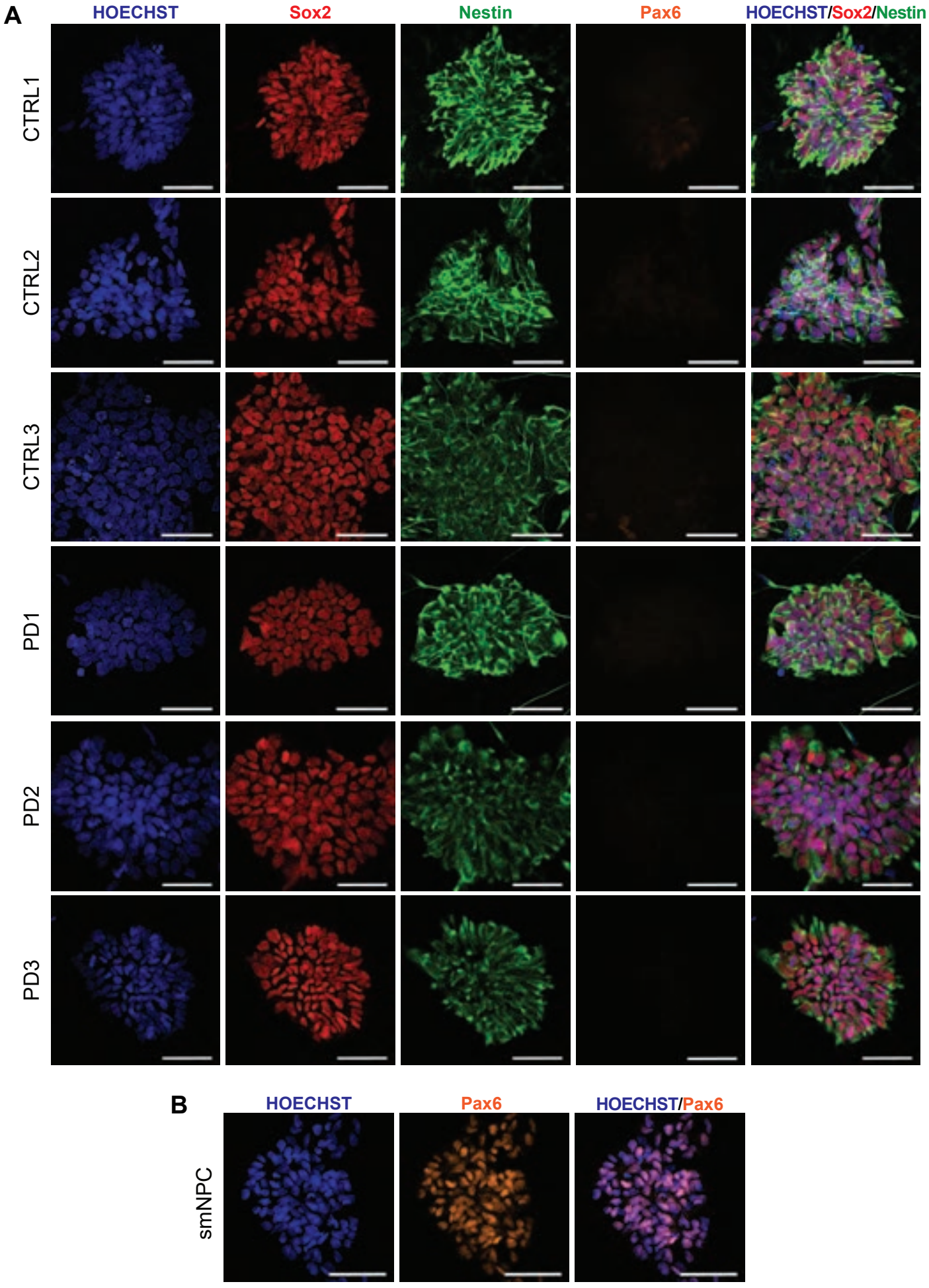
A
HOECHST
Sox2
Nestin
Pax6
HOECHST/Sox2/Nestin
CTRL1
CTRL2
CTRL3
PD1
PD2
PD3
B
HOECHST
Pax6
HOECHST/Pax6
smNPC

Supp Fig. S1. Derivation of mfNPCs from iPSCs.

A) Immunostaining of mfNPCs for Nestin (green), Sox2 (red) and Pax6 (orange). Nuclei were counterstained with Hoechst (blue) (scalebar 50 µm).
B) Positive control for Pax6 immunofluorescence staining of a healthy smNPC line Pax6 (orange). Nuclei were counterstained with Hoechst (blue) (scalebar 50 µm).

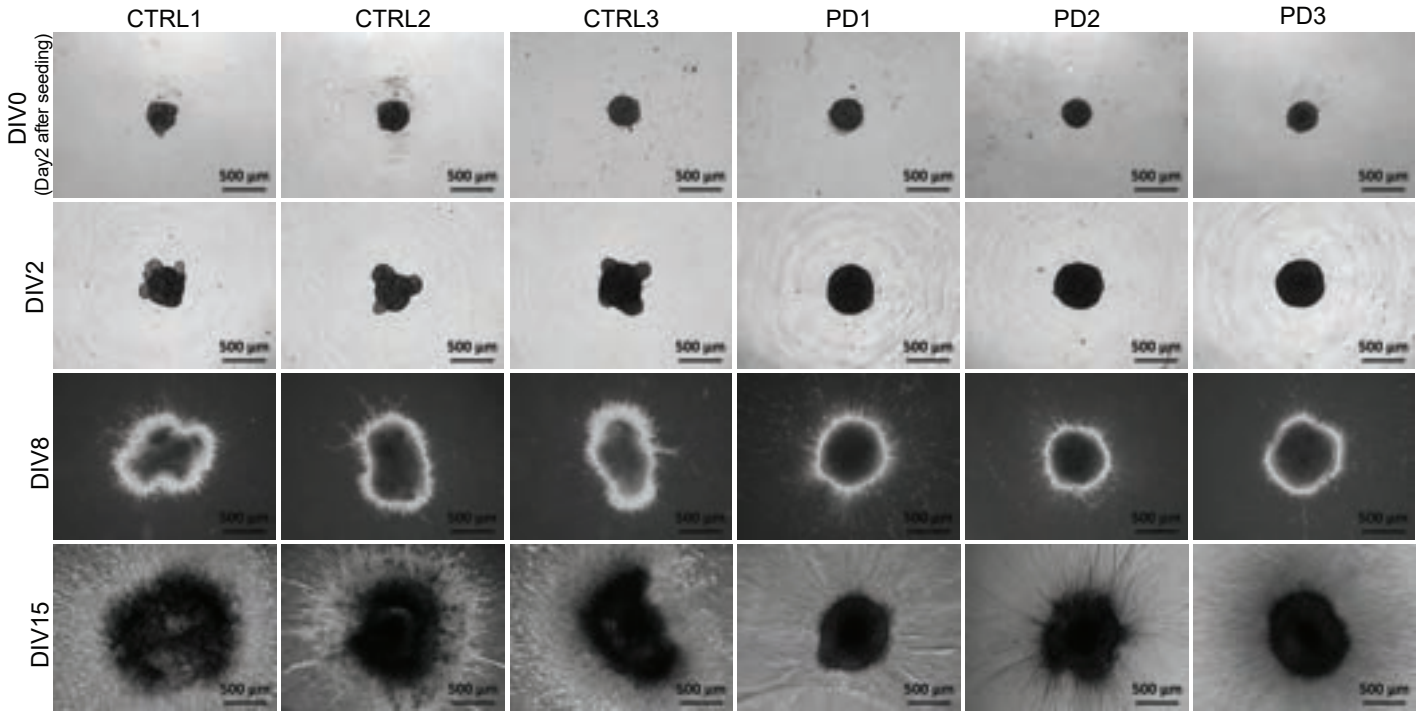
CTRL1
CTRL2
CTRL3
PD1
PD2
PD3
DIV0
(Day2 after seeding)
DIV2
DIV8
DIV15
500 µm

Supp Figure 2. Brightfield images of organoid development:

Representative bright-field images showing organoid development from day 2 of the seeding (DIV0) to DIV15. Images from DIV0 and DIV2 correspond to non-embedded organoids, images from DIV8 and DIV15 correspond to organoids after embedding on DIV6 (scalebar 500 µm).

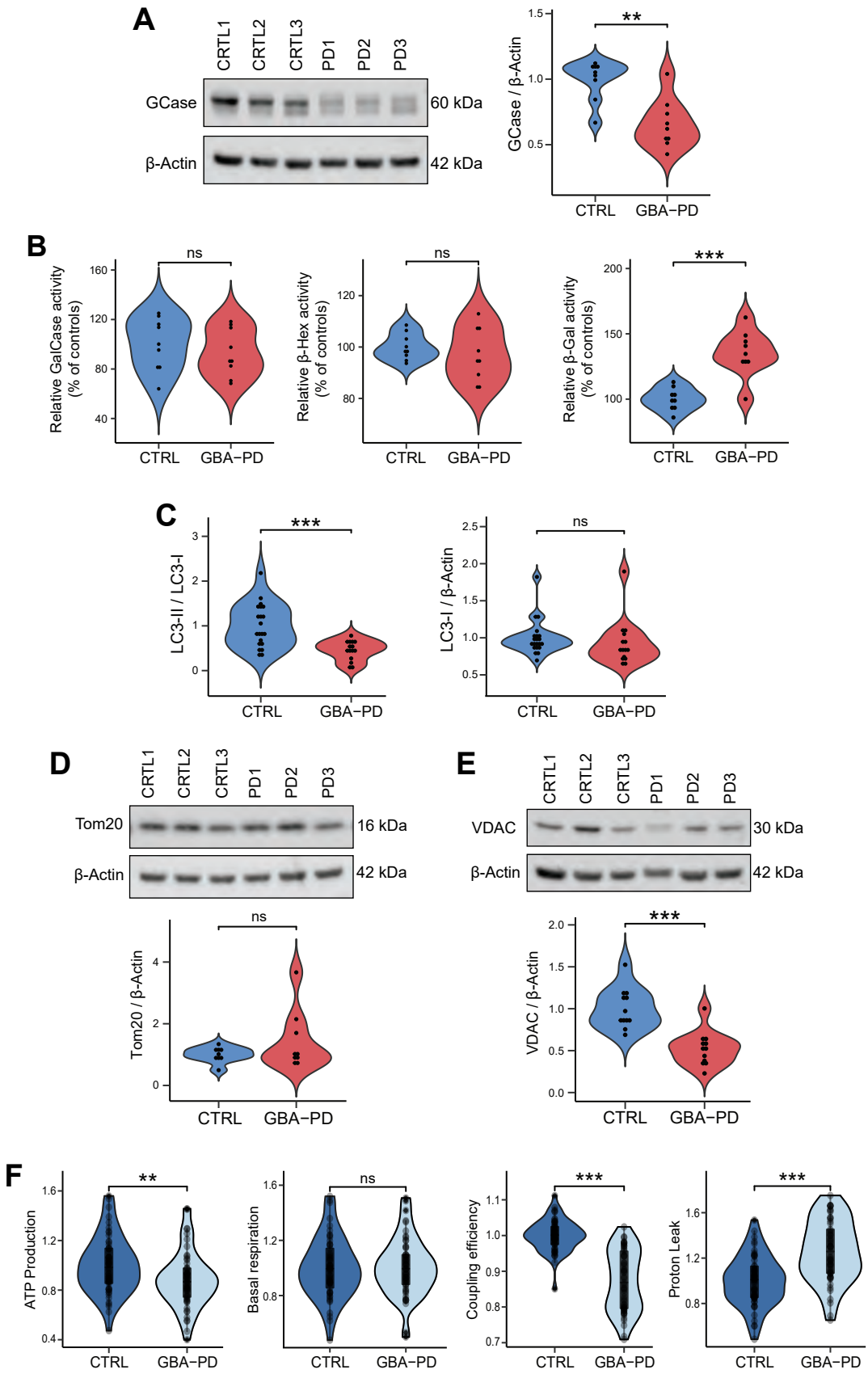
A
CRTL1
CRTL2
CRTL3
PD1
PD2
PD3
GCase
60 kDa
β-Actin
42 kDa
GCase / β-Actin
**
CTRL
GBA−PD
B
Relative GalCase activity (% of controls)
ns
Relative β-Hex activity (% of controls)
ns
Relative β-Gal activity (% of controls)
***
C
LC3-II / LC3-I
***
LC3-I / β-Actin
ns
D
Tom20
16 kDa
β-Actin
42 kDa
Tom20 / β-Actin
ns
E
VDAC
30 kDa
β-Actin
42 kDa
VDAC / β-Actin
***
F
ATP Production
**
Basal respiration
ns
Coupling efficiency
***
Proton Leak
***

Supp Figure 3. Autophagic and mitochondrial phenotypes in GBA-PD organoids:

A) GCase protein levels are significantly decreased at DIV60. Representative western blot analysis and respective quantification. The data represent a summary of at least three independent differentiation experiments, normalized to the average of controls per organoid batch. Wilcoxon T-test.; **p < 0.01.

B) Relative activities of lysosomal hydrolases β-galactocerebrosidase (GalCase), β-hexosaminidase (β-Hex) and β-galactosidase (β-Gal) in differentiated MO cultures. The data represent a summary of three independent differentiation experiments per cell line at DIV30. Values are normalized to the average of controls per experiment. Wilcoxon T-test.; ***p < 0.001.

C) Western blot quantification of LC3-II/LC3-I ratio and LC3-I protein at DIV30. Data represents a summary of five independent experiments, normalized to the mean of controls per batch. Wilcoxon T-test.; ***p < 0.001.

D) - E) Western blot analysis showing levels of mitochondrial proteins Tom20 and VDAC at DIV30. The data represent a summary of at least three independent differentiation experiments, normalized to the average of controls per organoid batch. Wilcoxon T-test.; ***p < 0.001.

F) Quantification of basal and ATP-linked mitochondrial respiration along with coupling efficiency and proton leak. Data are normalized to organoid size (area). The data represent a summary of three independent experiments for all cell lines, normalized to the mean of controls per batch. Wilcoxon T-test.; **p < 0.01, ***p < 0.001.

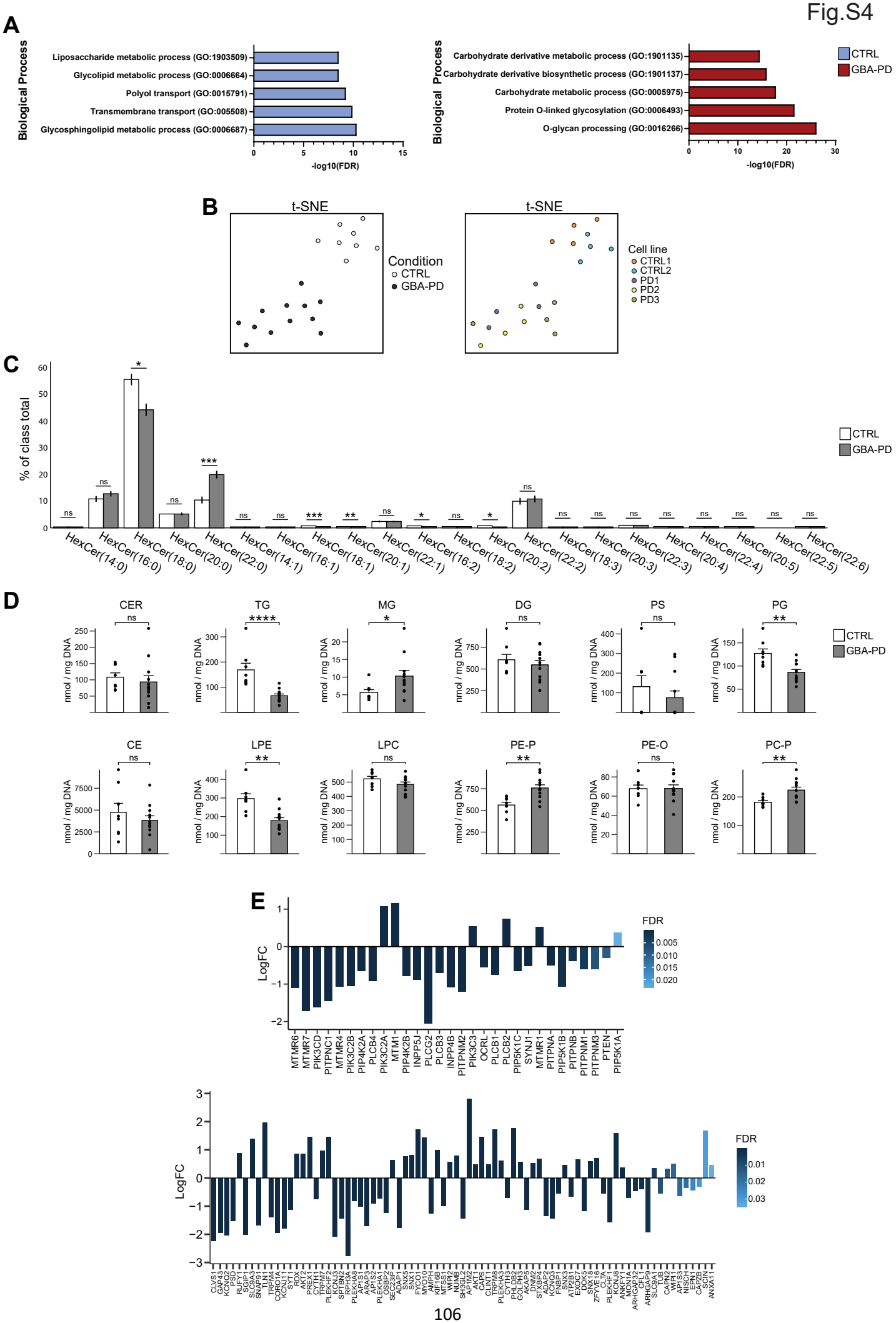
A
Biological Process
Liposaccharide metabolic process (GO:1903509)
Glycolipid metabolic process (GO:0006664)
Polyol transport (GO:0015791)
Transmembrane transport (GO:005508)
Glycosphingolipid metabolic process (GO:0006687)
-log10(FDR)
Carbohydrate derivative metabolic process (GO:1901135)
Carbohydrate derivative biosynthetic process (GO:1901137)
Carbohydrate metabolic process (GO:0005975)
Protein O-linked glycosylation (GO:0006493)
O-glycan processing (GO:0016266)
CTRL
GBA-PD
B
t-SNE
Condition
CTRL
GBA-PD
Cell line
CTRL1
CTRL2
PD1
PD2
PD3
C
% of class total
HexCer(14:0)
HexCer(16:0)
HexCer(18:0)
HexCer(20:0)
HexCer(22:0)
HexCer(14:1)
HexCer(16:1)
HexCer(18:1)
HexCer(20:1)
HexCer(22:1)
HexCer(16:2)
HexCer(18:2)
HexCer(20:2)
HexCer(22:2)
HexCer(18:3)
HexCer(20:3)
HexCer(22:3)
HexCer(20:4)
HexCer(22:4)
HexCer(20:5)
HexCer(22:5)
HexCer(22:6)
D
CER
TG
MG
DG
PS
PG
CE
LPE
LPC
PE-P
PE-O
PC-P
nmol / mg DNA
E
LogFC
FDR
MTMR6
MTMR7
PIK3CD
PITPNC1
MTMR4
PIK3C2B
PIP4K2A
PLCB4
PIK3C2A
MTM1
PIP4K2B
INPP5J
PLCG2
PLCB3
INPP4B
PITPNM2
PIK3C3
OCRL
PLCB1
PLCB2
PIP5K1C
SYNJ1
MTMR1
PITPNA
PIP5K1B
PITPNB
PITPNM1
PITPNM3
PTEN
PIP5K1A

Supp Figure 4. Metabolic modeling of GBA-N370S and wild-type organoids and lipidomics analysis

A) Gene enrichment analysis of genes found exclusively in control models (blue) and in GBA-PD models (red).

B) t-SNE scatter plots of the complete lipidomics dataset showing a clear clustering of patients (PD1, PD2 and PD3) and controls (CTRL1 and CTRL2).

C) Different hexosylceramide (HexCer) species measured by HILIC LC-MS/MS DIV30 organoids. Data represent a summary of four independent organoid differentiations, FDR adjusted p-values were calculated using the Benjamini–Hochberg procedure. *p < 0.05, **p < 0.01, ***p < 0.001.

D) HILIC LC-MS/MS based lipidomic analysis of different lipid classes of DIV30 organoids. ceramides (CER), triacylglycerides (TG), monoacylglycerides (MG), diacylglycerides (DG), phosphatidylserine (PS), phosphatidylglycerol (PG), cholesterol esters (CE), lysophosphatidylethanolamine (LPE), lysophosphatidylcholine (LPC), 1-alkenyl,2-acylphosphatidylethanolamines (PE-P), 1-alkyl,2-acylphosphatidylethanolamines (PE-O), 1-alkenyl,2-acylphosphatidylcholine (PC-P). Data represent a summary of four independent organoid differentiations, Mann-Whitney U test. *p < 0.05, **p < 0.01, ***p < 0.001 ****p < 0.0001.

E) Expression of phosphoinositide signaling genes in DIV30 hMOs. Top panel shows the DEGs of phospholipases, lipid transfer proteins, kinases and phosphatases. Bottom panel shows the DEGs of phosphoinositide binding proteins. Data is expressed as the logFC of the genes in the comparison patientderived organoids vs controls.

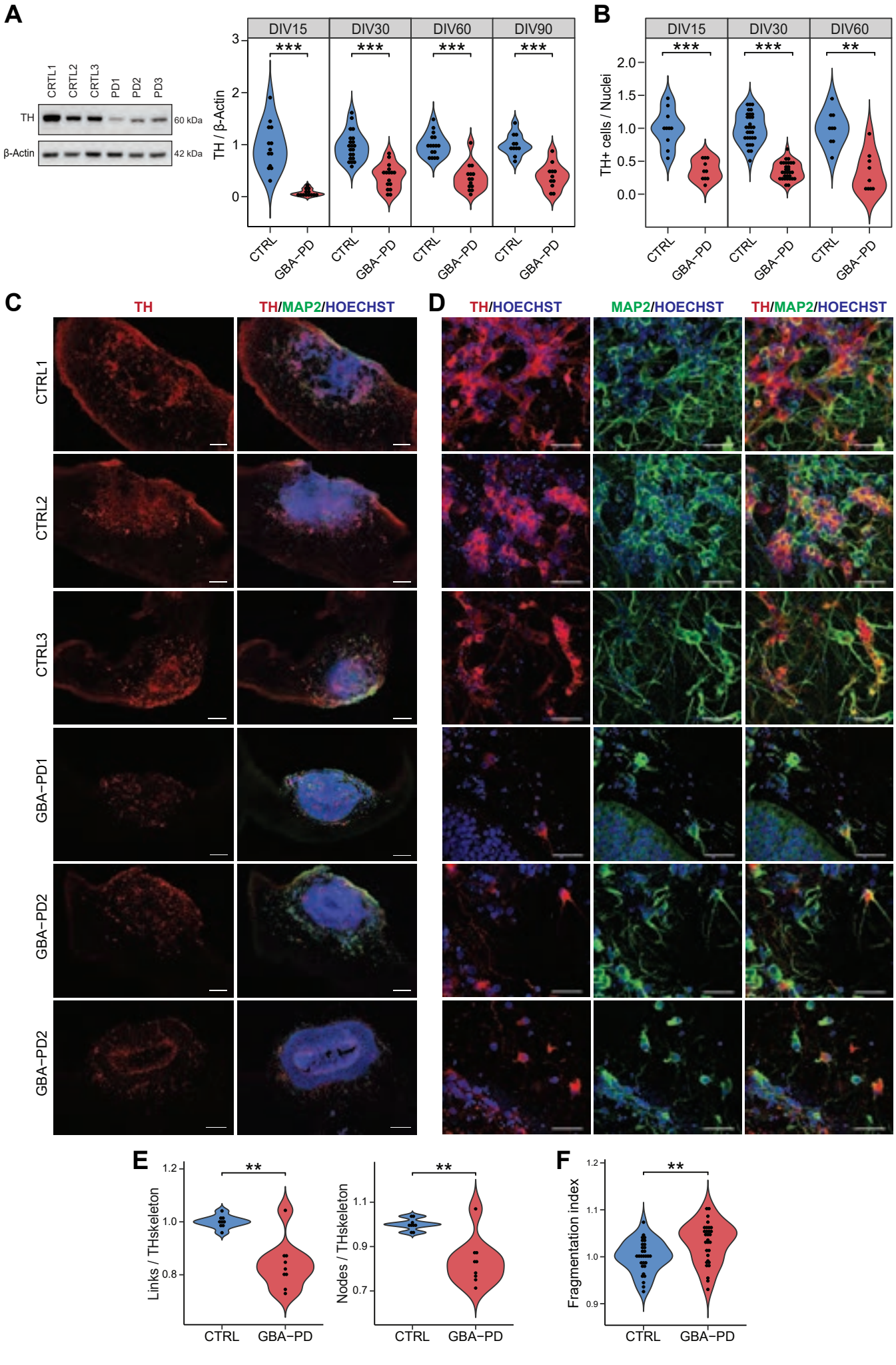
A
CRTL1
CRTL2
CRTL3
PD1
PD2
PD3
TH
60 kDa
β-Actin
42 kDa
TH / β-Actin
DIV15
DIV30
DIV60
DIV90
***
CTRL
GBA−PD
B
TH+ cells / Nuclei
**
C
TH
TH/MAP2/HOECHST
CTRL1
CTRL2
CTRL3
GBA−PD1
GBA−PD2
GBA−PD2
D
TH/HOECHST
MAP2/HOECHST
TH/MAP2/HOECHST
E
Links / THskeleton
Nodes / THskeleton
F
Fragmentation index

Supp Figure 5. Impaired dopaminergic neuronal differentiation

A)-B) Quantification dopaminergic neurons levels at DIV15, DIV30, DIV60 and DIV90 by western blot analysis and automated high content image analysis and representative western blot image at DIV15. Experiments repeated at least three times. Values are normalized to the mean of controls per organoid batch. Wilcoxon T-test.; *p < 0.05, **p < 0.01, ***p < 0.001.

C)-D) Representative images of DIV30 midbrain organoids sections for all six cell lines stained for TH (red), MAP2 (green), nuclei (blue)) acquired at 20x (C) and 40x (D) (scalebar 200 µm and 50 µm, respectively).

E) Differences in neurite branching become more significant at DIV60, measured by the number of nodes (branching points) and links (branches) extracted from the skeletonization of TH mask by the algorithm used for image analysis. Values are normalized to the mean of controls per organoid batch. Wilcoxon T-test.; **p < 0.01.

F) Higher fragmentation of TH+ neurites in organoids from GBA-PD lines. Fragmentation index is calculated by the image analysis script by computing the surface to volume ratio of the TH mask. Values are normalized to the mean of controls per organoid batch. Wilcoxon T-test.; *p < 0.05.

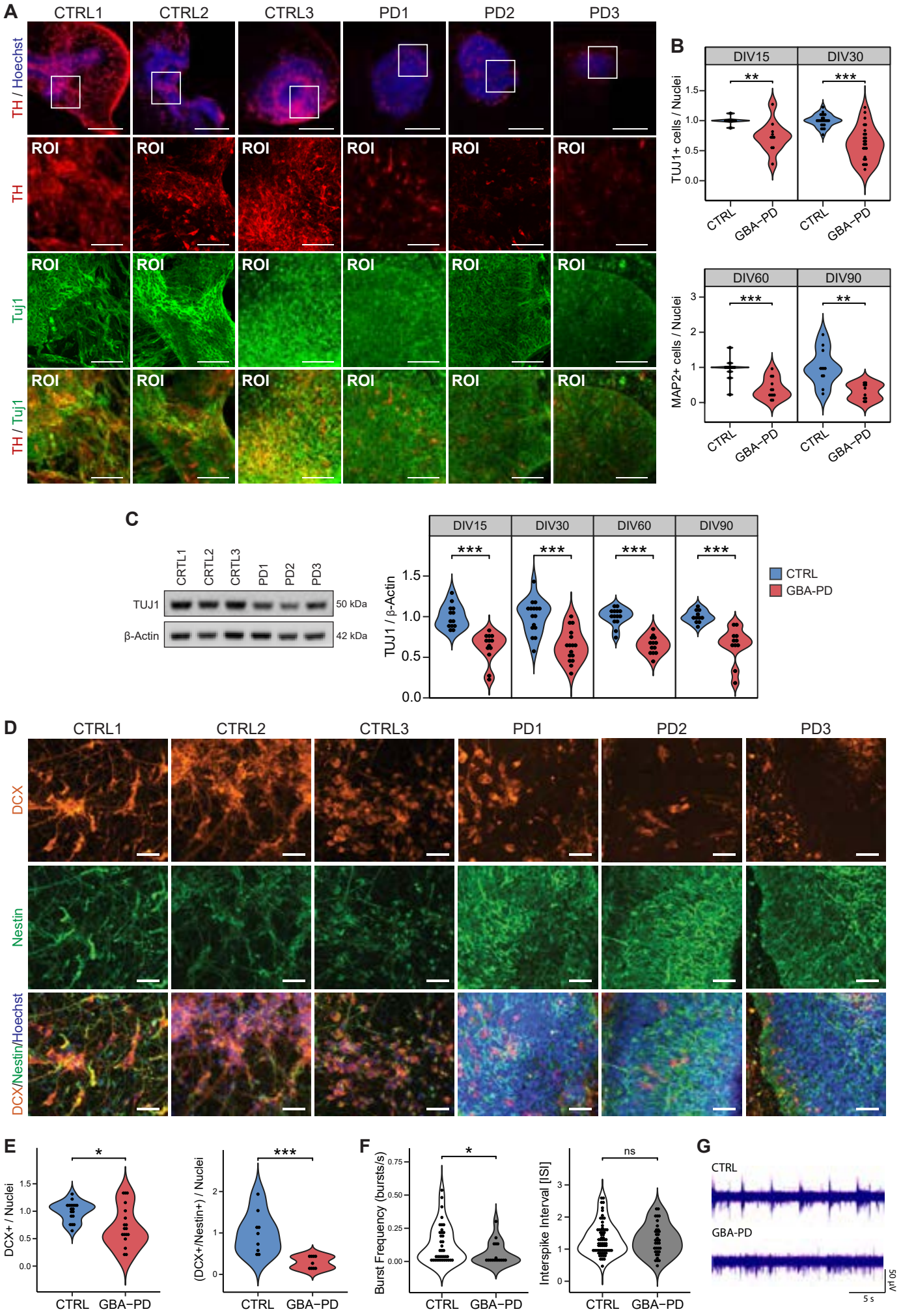
A
CTRL1
CTRL2
CTRL3
PD1
PD2
PD3
TH / Hoechst
TH
Tuj1
TH / Tuj1
ROI
B
DIV15
DIV30
DIV60
DIV90
TUJ1+ cells / Nuclei
MAP2+ cells / Nuclei
**
***
CTRL
GBA-PD
C
CRTL1
CRTL2
CRTL3
PD1
PD2
PD3
TUJ1
β-Actin
50 kDa
42 kDa
TUJ1 / β-Actin
CTRL
GBA-PD
D
DCX
Nestin
DCX/Nestin/Hoechst
E
DCX+ / Nuclei
(DCX+/Nestin+) / Nuclei
*
***
F
Burst Frequency (bursts/s)
Interspike Interval [ISI]
ns
G
CTRL
GBA-PD
50 µV
5 s

Supp Figure 6. Impaired general neurogenesis

A) Representative immunofluorescence images of DIV15 organoids expressing TH (red) and Tuj1 (green) with the respective region of interest (ROI). Nuclei were counterstained with Hoechst (blue) (scalebar 200 µm and 50 µm, respectively).
B) Quantification of neuronal content of midbrain organoids showing decreased general neuronal population at every timepoint, TUJ1 was used as an early neuronal marker at DIV15 and DIV30 (top) and MAP2 was a used as a mature neuronal marker at DIV60 and DIV90 (bottom). Data represent a summary of at least 3 independent organoid differentiations, normalized to the mean of controls per experiment. Wilcoxon T-test.; $^{**}p < 0.01$, $^{***}p < 0.001$.
C) Quantification of the neuronal marker TUJ1 at DIV15, DIV30, DIV60 and DIV90 and representative western blot image at DIV15. The data represent a summary of at least three independent differentiations, normalized to mean of controls per experiment. Wilcoxon T-test.; $^{***}p < 0.001$.
D) Representative images of DIV30 organoid sections stained with the early neuronal marker DCX (orange) and the neural stem cell marker Nestin (green). Nuclei were counterstained with Hoechst (blue) (scalebar 50 µm).
E) Immunofluorescence high content image analysis of DCX (right) at DIV30 normalized to the total amount of cells (nuclei) and the proportion of cells expressing both Nestin and DCX (left), normalized to the total amount of cells (nuclei). The data represent a summary of three independent differentiation experiments per line. Values are normalized to the mean of controls per organoid batch. Wilcoxon T-test.; $^{*}p < 0.05$.
F) MEA measurements of burst frequency and interspike interval at DIV15. Wilcoxon T-test.; $^{*}p < 0.05$.
G) Representative raw recordings traces from individual electrodes showing spontaneous activity of firing neurons in CTRL1 and PD1 organoids at DIV15.

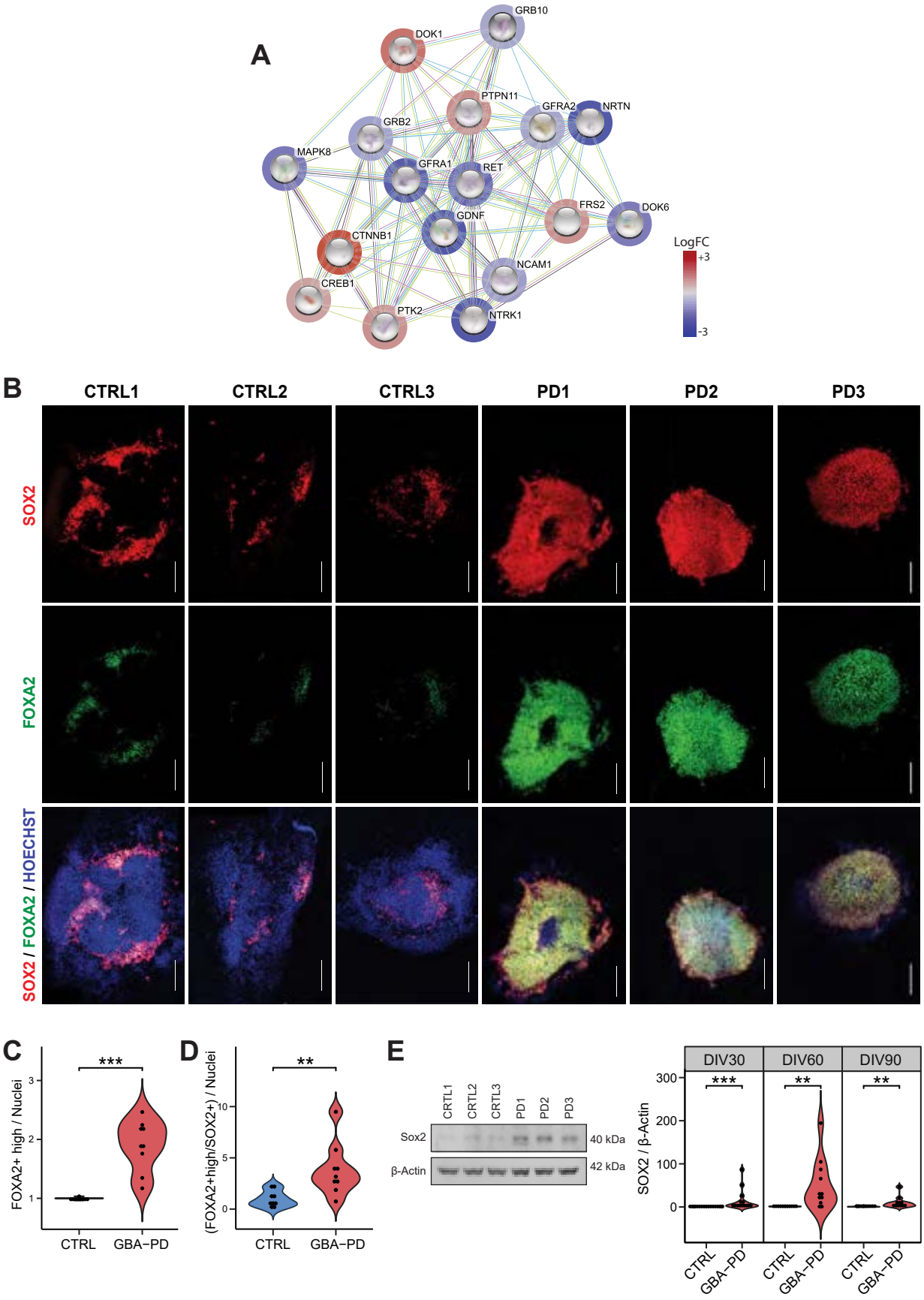
A
GRB10
DOK1
PTPN11
GFRA2
NRTN
GRB2
MAPK8
GFRA1
RET
FRS2
DOK6
GDNF
CTNNB1
NCAM1
CREB1
PTK2
NTRK1
LogFC
+3
-3
B
CTRL1
CTRL2
CTRL3
PD1
PD2
PD3
SOX2
FOXA2
SOX2 / FOXA2 / HOECHST
C
FOXA2+ high / Nuclei
***
CTRL
GBA−PD
D
(FOXA2+high/SOX2+) / Nuclei
**
CTRL
GBA−PD
E
CRTL1
CRTL2
CRTL3
PD1
PD2
PD3
Sox2
40 kDa
β-Actin
42 kDa
SOX2 / β-Actin
DIV30
DIV60
DIV90
***
**
**
CTRL
GBA−PD
CTRL
GBA−PD
CTRL
GBA−PD

Supp Figure 7. Increased proportion of cells expressing neural stem cell markers

A) Downregulation of interactive partners of GDNF (obtained from the STRING database) in GBA-N370S organoids based on the differentially expressed genes.

B) Representative confocal images of SOX2+ (red) and FOXA2+ (green) organoid sections at DIV30 Nuclei were counterstained with Hoechst (blue) (scalebar 200 μm).

C)-D) Automated quantification of cells expressing high levels of FOXA2 (left) and FOXA2+/SOX2+ cells (right) in DIV30 organoids normalized to the total amount of cells (nuclei). The data represent a summary of three independent differentiation experiments per line. Wilcoxon T-test.; ***$p < 0.001$.

E) Higher expression of SOX2 protein at DIV30, DIV60 and DIV90 in mutant organoids compared to controls. Representative western blot image at DIV60. Experiments repeated at least three times. Data is normalized to the mean of controls per experiment. Wilcoxon T-test.; **$p < 0.01$, ***$p < 0.001$.

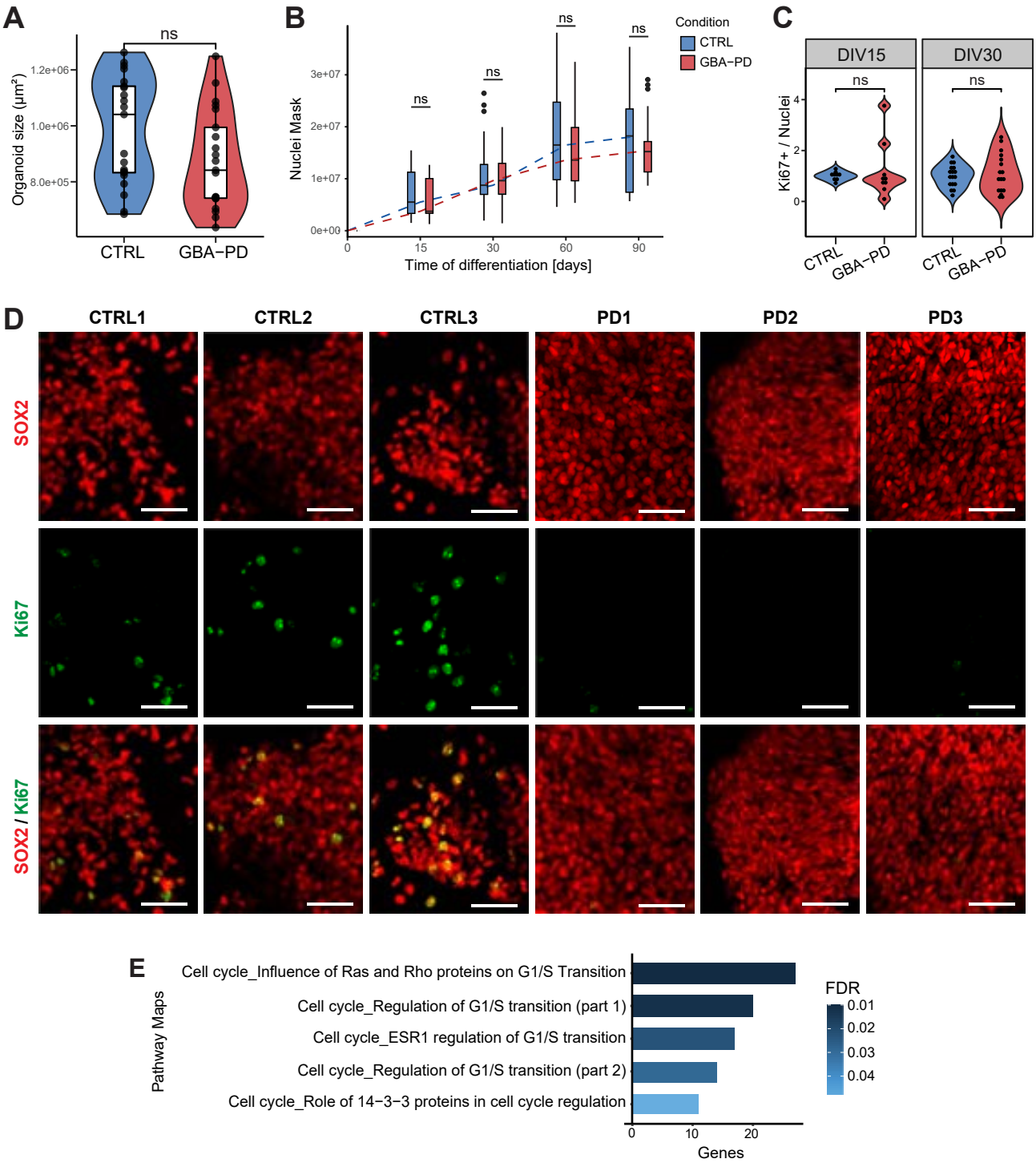
A
ns
Organoid size (µm²)
1.2e+06
1.0e+06
8.0e+05
CTRL
GBA−PD
B
ns
ns
ns
Nuclei Mask
3e+07
2e+07
1e+07
0e+00
0
15
30
60
90
Time of differentiation [days]
Condition
CTRL
GBA−PD
C
DIV15
DIV30
ns
ns
Ki67+ / Nuclei
4
2
0
CTRL
GBA−PD
CTRL
GBA−PD
D
CTRL1
CTRL2
CTRL3
PD1
PD2
PD3
SOX2
Ki67
SOX2 / Ki67
E
Pathway Maps
Cell cycle_Influence of Ras and Rho proteins on G1/S Transition
Cell cycle_Regulation of G1/S transition (part 1)
Cell cycle_ESR1 regulation of G1/S transition
Cell cycle_Regulation of G1/S transition (part 2)
Cell cycle_Role of 14−3−3 proteins in cell cycle regulation
0
10
20
Genes
FDR
0.01
0.02
0.03
0.04

Supp Figure 8. Neural progenitors present lower proliferation capacity in GBA-PD organoids

A) No differences in organoid size (area) between control and patient-derived MOs at DIV30. Data is normalized to the mean of controls per experiment. Wilcoxon T-test, n=7.
B) Organoid size during differentiation, measured by the automated pixel count of the nuclear mask (Hoechst). The data represent a summary of at least three independent differentiation experiments per line. Wilcoxon T-test.
C) Immunofluorescence quantification of cells expressing the proliferative marker Ki67 shows no differences of proliferation between control and mutant conditions at DIV15 and DIV30. Data is normalized to the mean of controls per experiment. Wilcoxon T-test, experiments were repeated at least three times.
D) Representative confocal images of cells expressing SOX2 (red) and Ki67 (green) in DIV30 organoid sections (scalebar 50 μm).
E) Pathway enrichment analysis of differentially expressed genes (DEGs) showing enrichment in pathway maps related to cell cycle regulation (Genego Metacore). Pathways were considered significantly enriched if their P-value adjusted by Benjamini-Hochberg was <0.05.

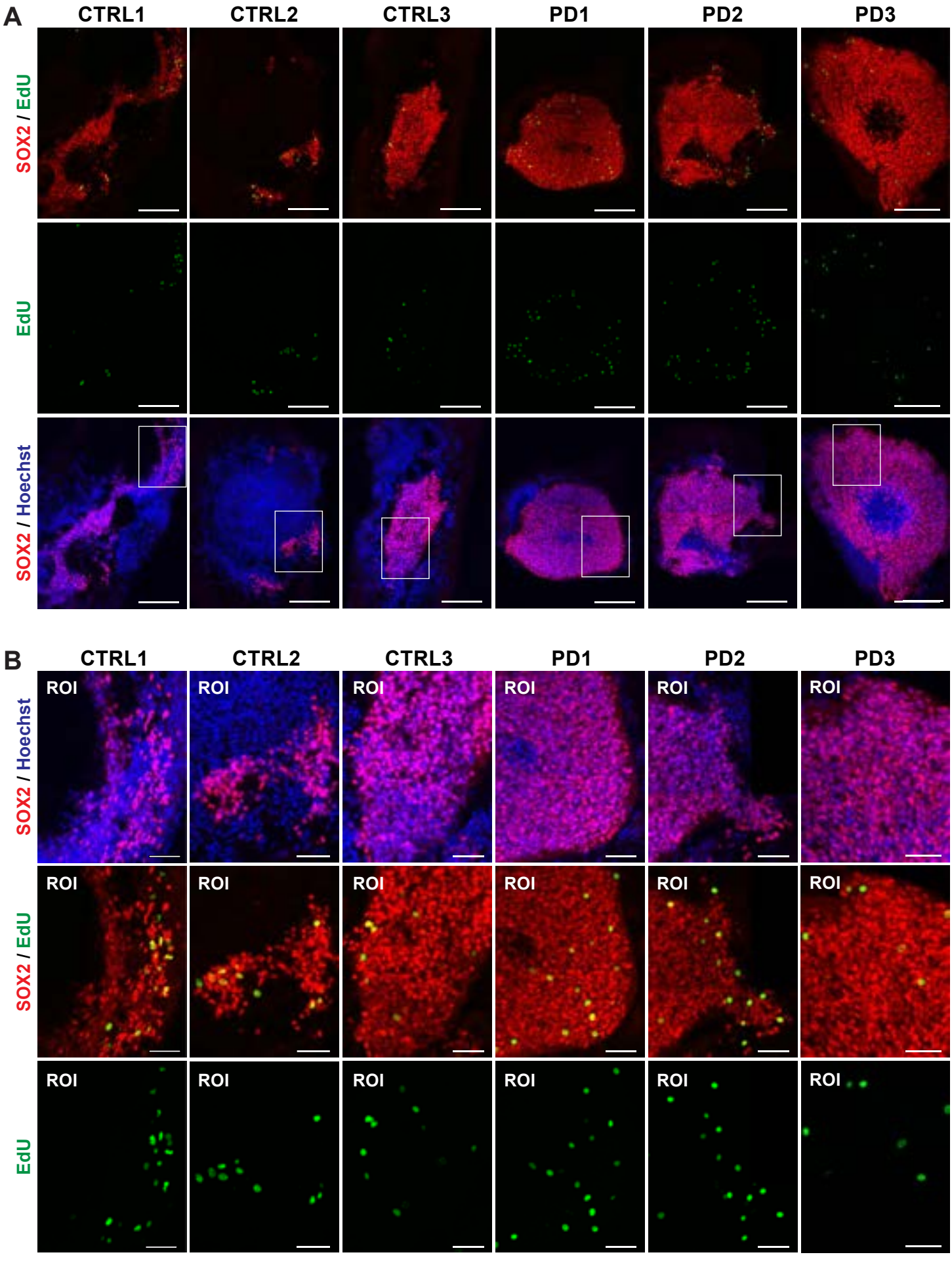
A
CTRL1
CTRL2
CTRL3
PD1
PD2
PD3
SOX2 / EdU
EdU
SOX2 / Hoechst
B
CTRL1
CTRL2
CTRL3
PD1
PD2
PD3
SOX2 / Hoechst
SOX2 / EdU
EdU
ROI

Supp Figure 9. Detection of EdU incorporated into the DNA of after initial pulse.

A) - B) Immunofluorescence detection of Edu incorporation (green) by SOX+ neural progenitors (red) after an 8h pulse (A; scalebar 200 µm) and the respective zoomed region (B; scalebar 50 µm). Sections were counterstained with Hoechst to reveal cellular DNA.

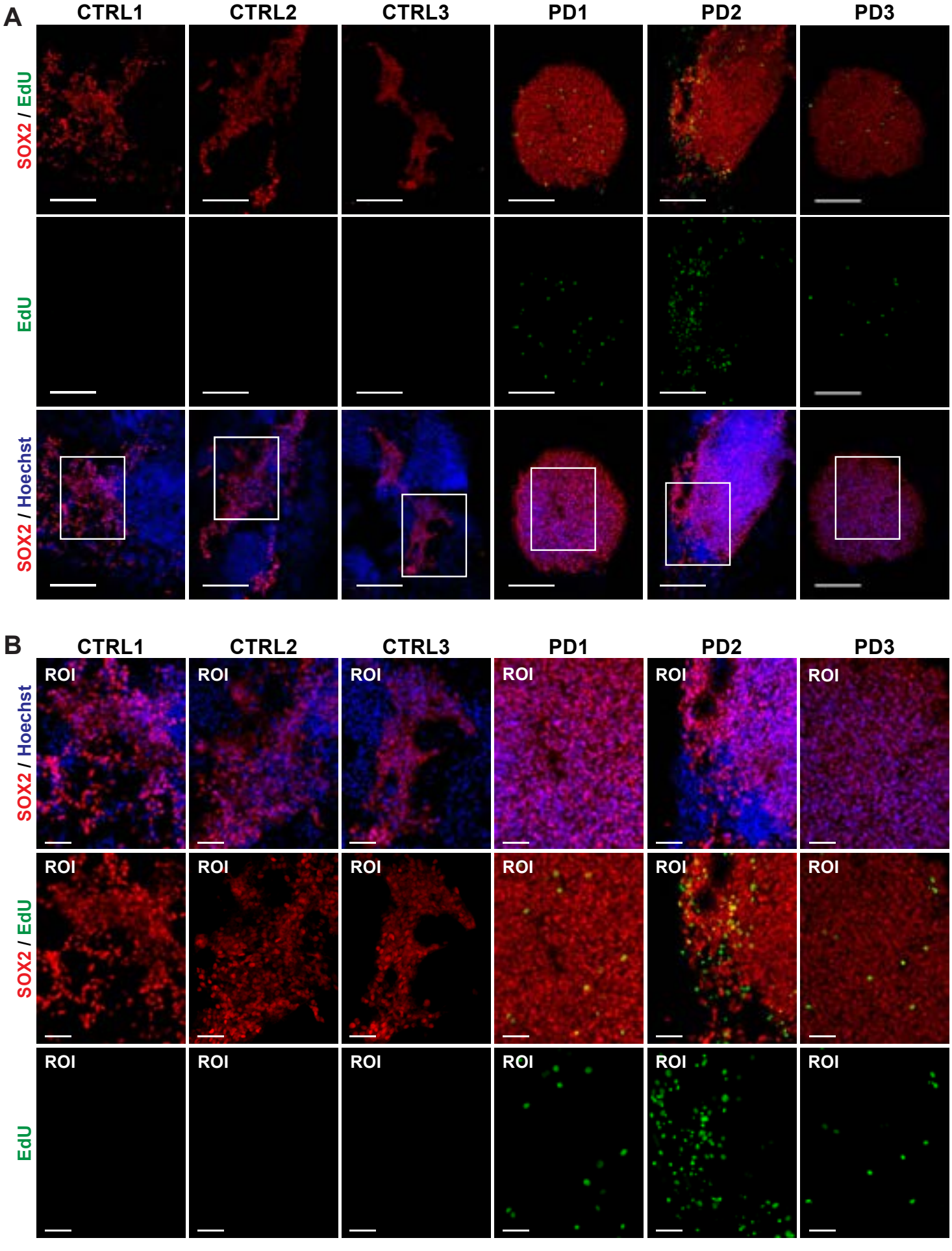
A
CTRL1
CTRL2
CTRL3
PD1
PD2
PD3
SOX2 / EdU
EdU
SOX2 / Hoechst
B
CTRL1
CTRL2
CTRL3
PD1
PD2
PD3
SOX2 / Hoechst
SOX2 / EdU
EdU
ROI

Supp Figure 10. Detection of EdU signal after 7 days from initial pulse.

A) - B) Loss of Edu signal (green) in SOX+ neural progenitors (red) of control MOs after 7 days from the initial pulse (A; scalebar 200 µm) and the respective zoomed region (B; scalebar 50 µm). Sections were counterstained with Hoechst to reveal cellular DNA.

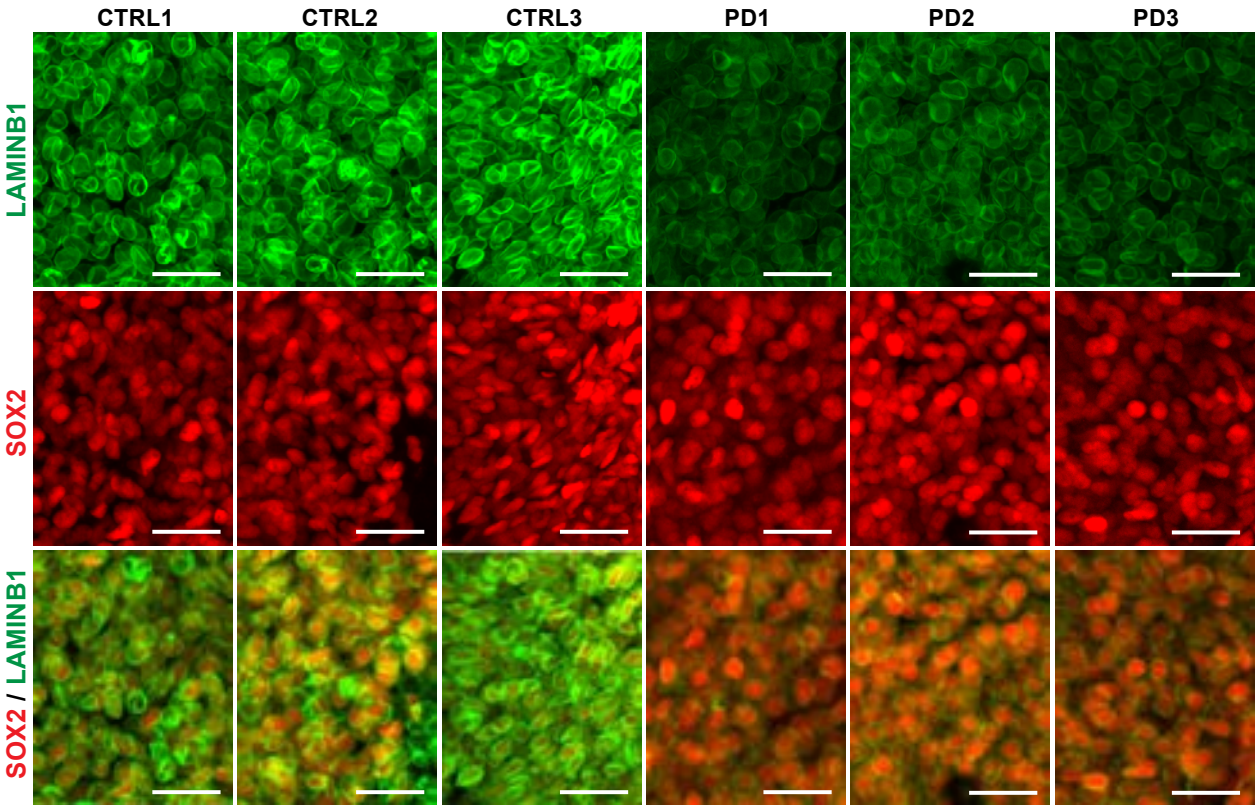
CTRL1
CTRL2
CTRL3
PD1
PD2
PD3
LAMINB1
SOX2
SOX2 / LAMINB1

Supp Figure 11. Expression of senescence-associated markers – LAMINB1

Representative confocal images of cells expressing SOX2 (red) and LAMINB1 (green) in DIV30 organoid sections (scalebar 25 μm).

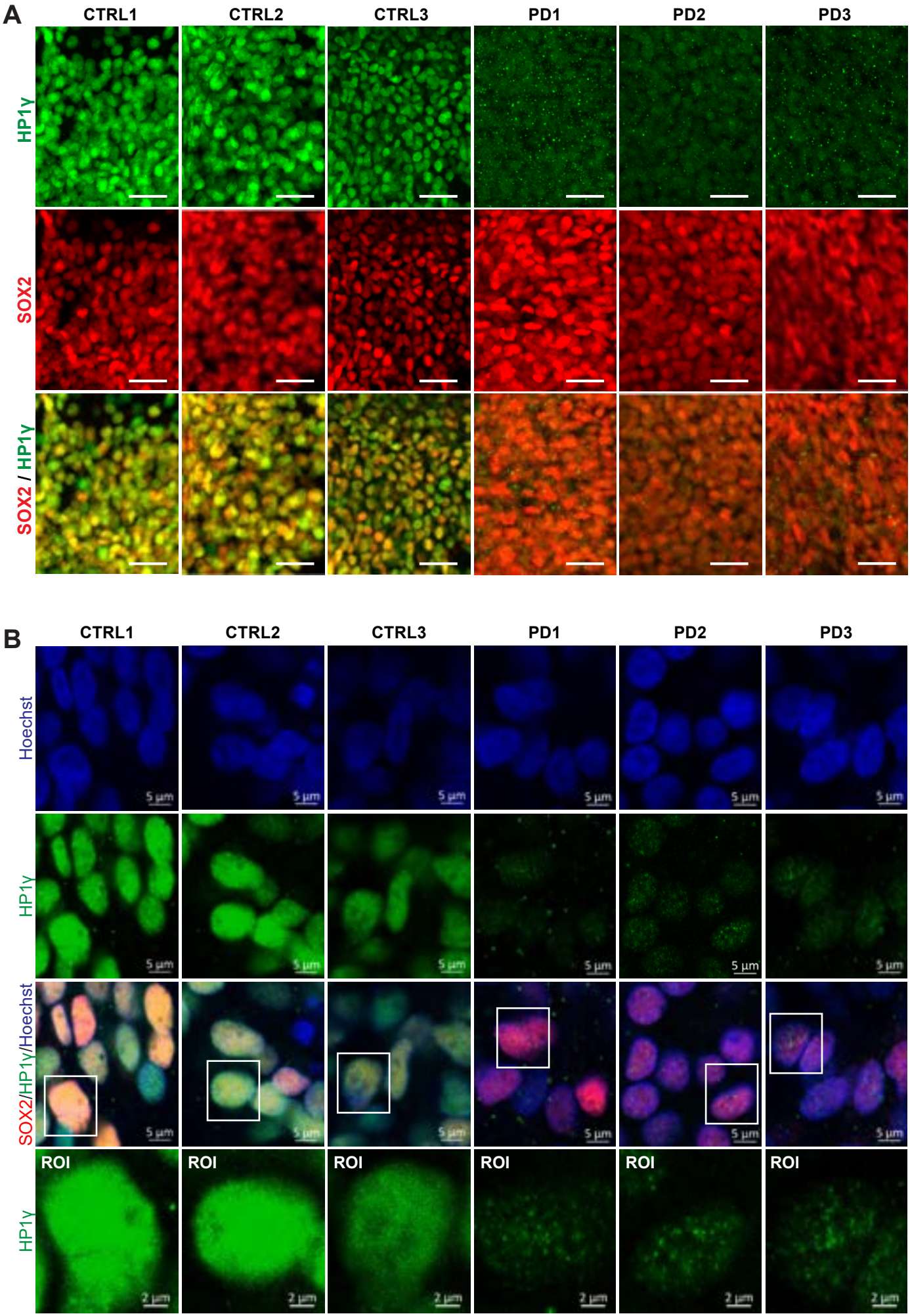
A
CTRL1
CTRL2
CTRL3
PD1
PD2
PD3
HP1γ
SOX2
SOX2 / HP1γ
B
CTRL1
CTRL2
CTRL3
PD1
PD2
PD3
Hoechst
HP1γ
SOX2/HP1γ/Hoechst
ROI
HP1γ
5 µm
2 µm

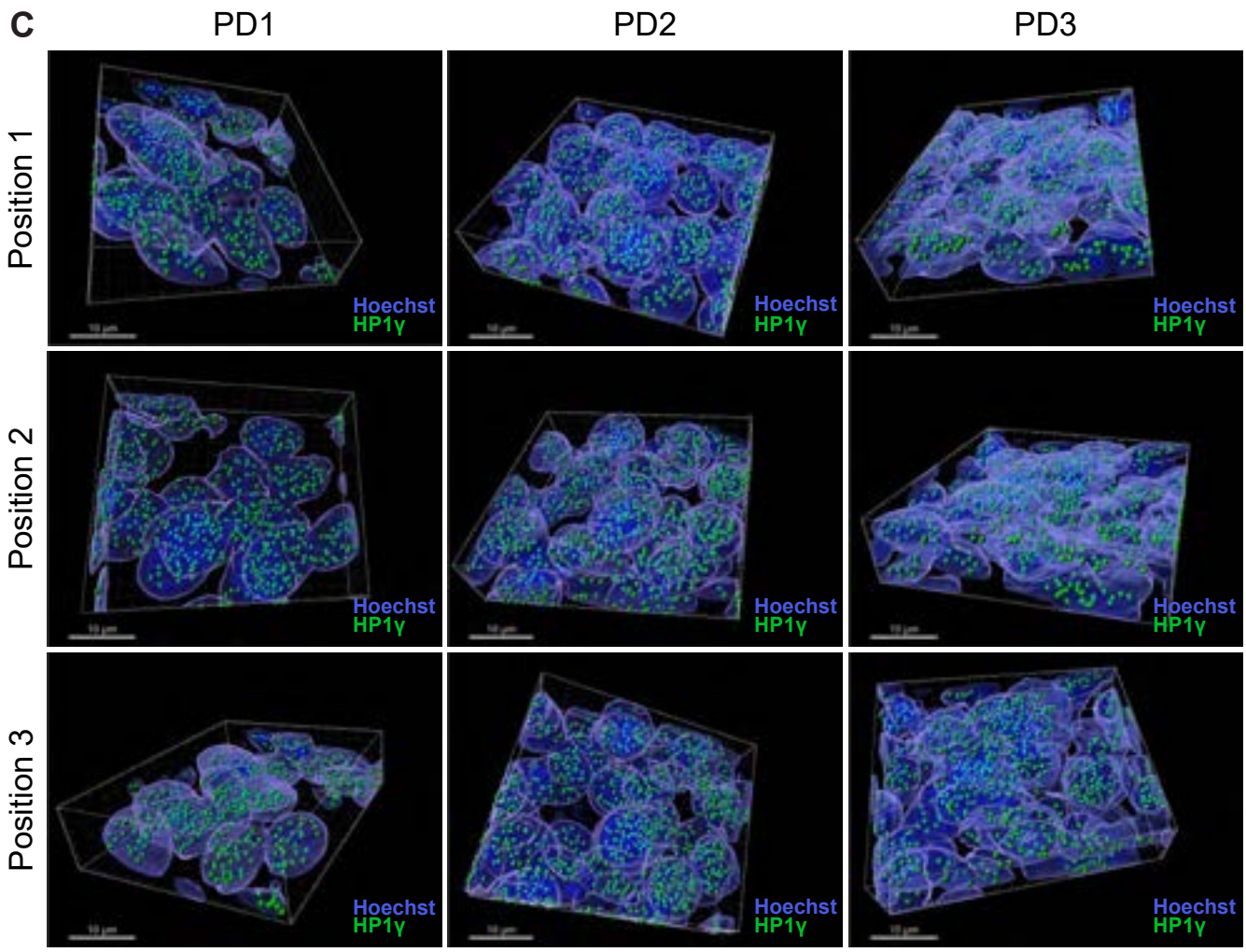
C
PD1
PD2
PD3
Position 1
Position 2
Position 3
Hoechst
HP1γ

Supp Figure 12. Expression of senescence-associated markers – HP1γ

A) Representative confocal images of cells expressing SOX2 (red) and HPIγ (green) in DIV30 organoid sections. Images acquired at 20x magnification (scalebar 25 µm).
B) Presence of dotted pattern of HPIγ (green) in DIV30 GBA-PD organoids. Sox2 (red), Hoechst (blue). Images acquired at 60x magnification with their respective region of interest (ROI) (scalebar 5 µm and 2 µm, respectively).
C) Intranuclear dotted signal of HPIγ (green) in DIV30 GBA-PD organoids identified using the "create spots" algorithm in Imaris. Nuclei were counterstained with Hoechst (blue) and identified using the "surfaces" algorithm (scalebar 10 µm).

Table S1. Human iPSC used in this study

ID	Diagnosis	Genotype	Age of Biopsy	Patient ID	Cell line ID	Source
Control-1	Healthy	wt/wt	68	3012659-MDPD1	278	IBBL / Max Planck Institute
Control-2	Healthy	wt/wt	65	2716623-MDPD1	277	IBBL / Max Planck Institute
Control-3	Healthy	wt/wt	68	-	302	StemBANCC
GBA-PD-1	PD	*GBA*-N370S/wt	69	ND31630 Cl5	309	http://ccr.coriell.org
GBA-PD-2	PD	*GBA*-N370S/wt	55	KTI6	370	University College London
GBA-PD-3	PD	*GBA*-N370S/wt LRRK2-G2019S/wt	75	SGO1	371	University College London

Table S2. Antibodies used in this study

Antibody	Species	Source	Ref.-No.	WB Dilution	IF Dilution
Anti-rabbit	Goat	Cell Signaling	5151S	1:1000	-
Anti-mouse	Goat	Cell Signaling	5470S	1:1000	-
β-Actin	Mouse	Cell Signaling	3700	1:100 000	-
Caspase3	Rabbit	Cell Signaling	9661	-	1:200
DCX	Guinea Pig	Millipore	AB2253	-	1:400
FOXA2	Mouse	Santa Cruz	sc-101060	-	1:250
GBA	Mouse	Abnova	H00002629-M01	-	1:500
GBA	Rabbit	Sigma	G4171	1:500	-
HPIg	Rabbit	Cell Signaling	2619S	-	1:200
Ki67	Mouse	BD Biosciences	550609	-	1:200
LAMP1	Mouse	Abcam	ab25630	-	1:400
LaminB1	Rabbit	Abcam	ab16048		1:200
LC3	Rabbit	MBL	PM036	1:1000	1:1000
MAP2	Rabbit	Abcam	ab32454	-	1:100
MAP2	Mouse	Millipore	MAB3418	-	1:200
MAP2	Chicken	Abcam	ab92434	-	1:1000
Nestin	Mouse	Millipore	MAB5326	-	1:100
OLIG2	Rabbit	Millipore	AB9610	-	1:400
Pax6	Rabbit	Covance	PRB-278P	-	1:300
P62 (SQSTM1)	Mouse	Abcam	ab56416	1:500	-
Sox2	Goat	R&D Systems	AF2018	-	1:100
Sox2	Rabbit	Abcam	ab97959	1:500	-
TH	Rabbit	Santa Cruz	sc-14007	1:1000	-
TH	Rabbit	Abcam	ab112	-	1:1000
Tom20	Mouse	Santa Cruz	sc-17764	1:500	-
TUJ1	Chicken	Millipore	AB9354	-	1:600
TUJ1	Mouse	BioLegend	801201	1: 50 000	-
VDAC	Rabbit	Cell Signaling	4661	1:1000	-

Table S3. Metabolic model composition per cell line

Model	Genes	Reactions	Metabolites
CTRL1	1706	3648	2685
CTRL2	1716	3454	2570
PD1	1635	3990	2917
PD2	1672	4119	2997

Table S4. Reactions related to dopamine metabolism present only in control metabolic models

Reaction ID	Pathway	Reaction
'DOPAENT4tc'	'Transport, extracellular'	'h[e] + dopa[e] <=> h[c] + dopa[c] '
'r2494'	'Transport, extracellular'	'hco3[e] + dopa[c] + HC02199[e] -> hco3[c] + dopa[e] + HC02199[c] '
'r2495'	'Transport, extracellular'	'hco3[e] + dopa[c] + HC02200[e] -> hco3[c] + dopa[e] + HC02200[c] '
'r2496'	'Transport, extracellular'	'hco3[e] + dopa[c] + HC02201[e] -> hco3[c] + dopa[e] + HC02201[c] '

Table S5. Number of reactions per subsystem present only in control models and GBA-PD models, respectively.

Pathway	Reaction number in CTRL models	Pathway	Reaction number in GBA-PD models
Transport, extracellular	116	Transport, extracellular	292
Fatty acid oxidation	75	Exchange/demand reaction	275
Exchange/demand reaction	55	Peptide metabolism	242
Sphingolipid metabolism	26	Fatty acid oxidation	60
Transport, mitochondrial	17	Glycerophospholipid metabolism	19
Valine, leucine, and isoleucine metabolism	9	Nucleotide interconversion	16
Transport, golgi apparatus	9	Transport, mitochondrial	13
Miscellaneous	9	Keratan sulfate degradation	13
Transport, endoplasmic reticular	8	Keratan sulfate synthesis	11
Phosphatidylinositol phosphate metabolism	7	Transport, peroxisomal	9
NAD metabolism	6	Transport, endoplasmic reticular	9
Bile acid synthesis	5	Drug metabolism	7
Glycerophospholipid metabolism	5	Tryptophan metabolism	6
Transport, nuclear	5	Transport, lysosomal	6
Transport, peroxisomal	5	Folate metabolism	6
Glycosphingolipid metabolism	5	Eicosanoid metabolism	5
Folate metabolism	5	Transport, nuclear	4
Tyrosine metabolism	4	Chondroitin sulfate degradation	4
Transport, lysosomal	4	Pentose phosphate pathway	4
Nucleotide interconversion	4	Lysine metabolism	4
Steroid metabolism	4	Phosphatidylinositol phosphate metabolism	4
Urea cycle	4	Glycine, serine, alanine, and threonine metabolism	3
Vitamin B6 metabolism	4	Pyrimidine catabolism	3
C5-branched dibasic acid metabolism	4	O-glycan metabolism	3
Tryptophan metabolism	3	Glycosphingolipid metabolism	3
N-glycan synthesis	3	Inositol phosphate metabolism	3
Fructose and mannose metabolism	3	Bile acid synthesis	3
Glyoxylate and dicarboxylate metabolism	3	Aminosugar metabolism	2
Pentose phosphate pathway	3	Blood group synthesis	2
Phenylalanine metabolism	3	Sphingolipid metabolism	2
Fatty acid synthesis	3	Transport, golgi apparatus	2
Eicosanoid metabolism	3	Pyruvate metabolism	2
Butanoate metabolism	2	Phenylalanine metabolism	2
Propanoate metabolism	2	Purine catabolism	2
Aminosugar metabolism	2	Chondroitin synthesis	2

Cholesterol metabolism	2	Propanoate metabolism	1
Androgen and estrogen synthesis and metabolism	2	Glutathione metabolism	1
N-glycan metabolism	2	ROS detoxification	1
Inositol phosphate metabolism	2	Cholesterol metabolism	1
Purine catabolism	2	Purine synthesis	1
Methionine and cysteine metabolism	2	NAD metabolism	1
Ubiquinone synthesis	1	Pyrimidine synthesis	1
Glycolysis/gluconeogenesis	1	Starch and sucrose metabolism	1
Lysine metabolism	1	Heme degradation	1
Vitamin C metabolism	1	Glycolysis/gluconeogenesis	1
Oxidative phosphorylation	1		
Leukotriene metabolism	1		
Glycine, serine, alanine, and threonine metabolism	1		
Pyrimidine catabolism	1		
Vitamin B2 metabolism	1		
Triacylglycerol synthesis	1		
Chondroitin synthesis	1		
Galactose metabolism	1		

3.3. Manuscript III

Insulin resistance disrupts midbrain metabolic & functional homeostasis and aggravates dopaminergic neuron loss in GBA-PD

Alise Zagare[1,*], Janis Kurlovics[2], Catarina Almeida[1, 3], Daniele Ferrante[1], Daniela Frangenberg[1], Laura Neises[4], Ahmed Hemedan[1], Armelle Vitali[1], Gemma Gomez-Giro[1], Christian Jaeger[1], Paul Antony[1], Rashi Halder[1], Marek Ostaszewski[1], Rejko Krueger[1,4], Enrico Glaab[1], Johannes Meiser[4], Egils Stalidzans[2], Giuseppe Arena[1], Jens C Schwamborn[1,°]

[1]Luxembourg Centre for Systems Biomedicine, University of Luxembourg, 7, Avenue des Hauts-Fourneaux, 4362 Esch-sur-Alzette, Luxembourg

[2]Computational Systems Biology Group, Institute of Microbiology and Biotechnology, University of Latvia, Jelgavas iela 1, Rīga, LV-1004, Latvia

[3]Health Sciences Research Center, Faculty of Health Sciences Research, Faculty of Health Sciences, University of Beira Interior, 6200-506 Covilhã, Portugal

[4]Luxembourg Institute of Health, 1 A-B rue Thomas Edison, L-1445 Strassen, Luxembourg

* First author

° Corresponding author

This article has been submitted to PNAS

3.3.1. Contribution statement

This manuscript is the result of my main PhD project. I generated midbrain organoids from healthy donors and GBA-N370S mutation-carrying PD patient iPSC-derived NESCs. I designed the experiments and from sample preparation to data analysis I carried out Western Blot, high-content imaging, and electrophysiological activity recordings using a multi-electrode array, dopamine ELISA, insulin ELISA, ATP assay, and Seahorse assay. I generated metabolic models and participated in the analysis of the models and visualization of the results. I also analyzed and visualized RNA-sequencing, metabolomics, lipidomics and isotope tracing experiment data after data preprocessing by the collaborators. I prepared all the figures and wrote the original manuscript. The project was supervised by J.C. Schwamborn and guided by J.C. Schwamborn and G.Arena.

3.3.2. Preface

The aim of the manuscript was to investigate how T2D-associated insulin resistance affects healthy midbrain and GBA-N370S mutation-associated PD phenotypes. Additionally, we aimed to explore the potential of antidiabetic drugs in PD therapy.

Both PD and T2D are age-associated diseases which significantly decrease patient life quality and can cause long-term disability. The proposed shared mechanisms between the two diseases are elaborated in section 1.2.2. In this article, we particularly focus on insulin resistance as a common pathophysiological mechanism between PD and T2D. Contrary to previous beliefs that the brain is an insulin-independent organ, insulin has important functions in the CNS, including energy metabolism (elaborated in 1.2.2), therefore insulin resistance in the CNS can have destructive effects. Central insulin resistance can be a result of genetic mutations or induced by peripheral insulin resistance (Hallschmid and Schultes 2009). Moreover, aging, in general, is associated with a decline in many biological processes, including insulin function (Ryan 2000). This means that anyone independently of T2D can potentially develop insulin resistance, which then can trigger other age-associated disease onset, including neurodegenerative diseases. Importantly, T2D-associated insulin resistance can be prevented by increasing physical activity and dietary restrictions, defining T2D as a modifiable risk factor for other disease development.

This article gives insights into molecular mechanisms affected by T2D-associated insulin resistance, particularly in the midbrain, which is the most affected brain region in PD. As discussed in section 1.2.3., cell culture conditions limit the modeling of accurate T2D and physiological conditions long-term. With the given limitations, we focus on hyperinsulinemia which promotes

insulin resistance (standard culture media) and by excluding insulin from one of the neurotrophic supplements, we model more physiological cell conditions in terms of insulin concentration. We observe that the metabolic and functional state of healthy midbrain organoids is affected by insulin resistance predisposing it to PD pathology. Moreover, the utilized GBA-N370S mutation-associated PD organoid model demonstrates insulin signaling dysfunction at the transcriptomic level, implying insulin resistance's role in PD phenotype acceleration. Furthermore, we provide data suggesting that anti-diabetic therapy might be effective in PD treatment.

Insulin resistance disrupts midbrain metabolic & functional homeostasis and aggravates dopaminergic neuron loss in GBA-PD

Alise Zagare[1], Janis Kurlovics[2], Catarina Almeida[1, 3], Daniele Ferrante[1], Daniela Frangenberg[1], Laura Neises[4], Ahmed Hemedan[5], Armelle Vitali[9], Gemma Gomez-Giro[1], Christian Jaeger[6], Paul Antony[7], Rashi Halder[8], Marek Ostaszewski[5], Rejko Krueger[9, 10], Enrico Glaab[11], Johannes Meiser[4], Egils Stalidzans[2], Giuseppe Arena[9], Jens C Schwamborn[1*]

[1]Developmental and Cellular Biology, Luxembourg Centre for Systems Biomedicine (LCSB), University of Luxembourg, 7, Avenue des Hauts-Fourneaux, 4362 Esch-sur-Alzette, Luxembourg

[2]Computational Systems Biology Group, Institute of Microbiology and Biotechnology, University of Latvia, Jelgavas iela 1, Rīga, LV-1004, Latvia

[3]Health Sciences Research Center, Faculty of Health Sciences Research, Faculty of Health Sciences, University of Beira Interior, 6200-506 Covilhã, Portugal

[4]Cancer Metablism, Luxembourg Institute of Health (LIH), 1 A-B rue Thomas Ediison, L-1445 Strassen, Luxembourg

[5]Bioinformatics Core Unit, Luxembourg Centre for Systems Biomedicine (LCSB), University of Luxembourg, 7, Avenue des Hauts-Fourneaux, 4362 Esch-sur-Alzette, Luxembourg

[6]Metablomics Platform, Luxembourg Centre for Systems Biomedicine (LCSB), University of Luxembourg, 7, Avenue des Hauts-Fourneaux, 4362 Esch-sur-Alzette, Luxembourg

[7]Bioimaging Platform, Luxembourg Centre for Systems Biomedicine (LCSB), University of Luxembourg, 7, Avenue des Hauts-Fourneaux, 4362 Esch-sur-Alzette, Luxembourg

[8]Sequencing Platform, Luxembourg Centre for Systems Biomedicine (LCSB), University of Luxembourg, 7, Avenue des Hauts-Fourneaux, 4362 Esch-sur-Alzette, Luxembourg

[9]Translational Neuroscience, Luxembourg Centre for Systems Biomedicine (LCSB), University of Luxembourg, 7, Avenue des Hauts-Fourneaux, 4362 Esch-sur-Alzette, Luxembourg

[10]Transversial Translational Medicine, Luxembourg Institute of Health (LIH), 1 A-B rue Thomas Edison, L-1445 Strassen, Luxembourg

[11]Biomedical Data Science, Luxembourg Centre for Systems Biomedicine (LCSB), University of Luxembourg, 7, Avenue des Hauts-Fourneaux, 4362 Esch-sur-Alzette, Luxembourg

*Lead contact: jens.schwamborn@uni.lu

Abstract

Growing evidence indicates that Type 2 Diabetes (T2D) is associated with an increased risk of developing Parkinson's disease (PD) through shared disease mechanisms. Studies show that insulin resistance, which is the driving pathophysiological mechanism of T2D, plays a major role in neurodegeneration by impairing neuronal functionality, metabolism, and survival. To better understand the importance of insulin signaling in the human midbrain, which is the most affected brain region in PD, we expose induced pluripotent stem cell (iPSC) derived human midbrain organoids from healthy individuals and GBA-N370S mutation-carrying PD patients to either high insulin concentrations, promoting insulin resistance, or to more physiological insulin concentrations restoring normal insulin signaling function. We are able to show that insulin resistance compromises dopaminergic neuron functionality and dopamine levels in the midbrain organoids of healthy donors. Moreover, insulin-resistant organoids display diminished neuronal activity and reduced metabolic efficiency. Furthermore, our findings demonstrate a key role for the gene FOXO1 in insulin resistance-facilitated GBA-PD phenotype severity. We also show the potential beneficial effects of the anti-diabetic drug Pioglitazone in GBA-PD treatment. Overall, our results highlight insulin resistance as a significant target in PD prevention and disease-modifying therapy.

Introduction

Parkinson's disease (PD) is the second most frequent neurodegenerative disease, which affects the motor and cognitive function of patients due to the progressive degeneration of dopaminergic neurons in the *substantia nigra* region of the midbrain (1, 2). Most PD cases are idiopathic with an unknown genetic cause. Along with age as the primary risk factor, also environment, genetic risk factors and comorbidities contribute to the development of idiopathic PD (2). Recent epidemiological studies and meta-analyses show that Type 2 Diabetes (T2D) is associated with a 30 to 40% increased risk of developing PD (3-5). It has also been shown that patients affected by PD and T2D comorbidity, suffer from more severe motor symptoms and cognitive decline (6-9). Moreover, it has been suggested that T2D and PD share underlying pathophysiological mechanisms (5, 10, 11). Along with the dysregulated energy metabolism, aberrant protein aggregation, accumulation of reactive oxygen species and inflammation, insulin resistance seems to play a pivotal role in converging most of these common mechanisms. Insulin receptor presence in the basal ganglia and *substantia nigra* of healthy brains, and their loss in PD brains, suggests

the particular importance of insulin in the regulation of dopaminergic neuron survival, as well as in the maintenance of their functional and metabolic homeostasis (12, 13). In addition, there is evidence showing that insulin resistance can occur in PD brains independently of T2D, highlighting insulin resistance as a potential mediator of PD development or progression (13, 14). Furthermore, several downstream proteins of insulin signaling are shown to be involved in the pathophysiology of PD (15-17). In particular, forkhead box O (FOXO) transcription factors are linked to metabolic alterations, tyrosine hydroxylase (TH) levels (15) and alpha-synuclein (αSyn) accumulation (18). Depending on their expression levels and activity regulated by posttranscriptional modifications, FOXO proteins can be both neuroprotective and neurotoxic (19). Particularly, FOXO1 and genes under its transcriptional regulation have been associated with PD pathology in genome-wide association studies (GWAS) (20). Target genes of FOXO1 are involved in pathways, such as cell cycle, apoptosis, p53 signaling, metabolism and oxidative stress management (20, 21), indicating the importance of FOXO1 functional regulation in health and disease.

Another evidence that T2D and PD are connected, is provided by the beneficial effects of T2D drugs on PD phenotypes (22-25). Gucagon-like peptide-1 (GLP-1) receptor agonists Exenatide and Liraglutide, as well as the thiazolidinedione derivate Pioglitazone, have completed phase 2 of clinical trials (26-28). While GLP-1 agonists showed PD-modifying properties, Pioglitazone clinical trial results were rather inconclusive and controversial to other studies which demonstrate Pioglitazone's association with reduced risk of PD (24, 27, 29). In addition, the antihyperglycemic drug Metformin has been associated with a decreased risk of PD in a dose-dependent manner (25).

In this study, we aimed to evaluate insulin resistance-mediated effects on the healthy and PD-affected midbrain. We used iPSC-derived human midbrain organoids from healthy donors and PD patients, carrying the N370S mutation in the glucocerebrosidase 1 (GBA) gene. We exposed midbrain organoids to a high insulin concentration that promotes insulin resistance, or to a more physiological insulin concentration to retain cells in an insulin-sensitive state. Using a combination of computational and experimental methods we predicted and validated insulin resistance-dependent metabolic alterations and demonstrated a functional decline in insulin-resistant midbrain organoids. We showed that FOXO1 is a potential target in GBA-PD, and its downregulation rescues GBA-PD-associated dopaminergic neuron loss. We also treated GBA-PD midbrain organoids with known anti-diabetic drugs - Pioglitazone and Metformin to explore their potential beneficial effects on GBA-PD. Overall our results demonstrate that insulin resistance is a major factor in determining the severity of PD-associated phenotypes.

Results

Modification of cell culture media activates insulin signaling

Midbrain organoids were generated from four healthy individuals and three GBA-PD patient iPSC-derived neuroepithelial stem cells (NESCs) (Table S1). Prior to organoid generation, the quality of all NESC lines used in the study was confirmed by evaluating the expression of the stem cell marker SOX2, the neural progenitor marker Nestin and the neuroectoderm fate marker PAX6 (Figure S1). Midbrain organoids were cultured in two culture conditions that vary by the concentration of insulin (Figure 1A). First, we determined the insulin concentration in standard basal N2B27 media supplemented with insulin-containing neurotrophic supplements B27 and N2. The insulin concentration in the standard basal media was 393.9 nM, which strongly exceeds the physiological insulin concentration in the CNS, reported to be below 0.1nM (measured in CSF) (30, 31). We hypothesized that this supraphysiological insulin concentration in the standard media might cause insulin resistance (IR) in the organoid culture. We also measured insulin concentration in the supernatant of organoids cultured for three days in the standard media with the high insulin concentration and saw that the insulin concentration remained between 352 nM and 374 nM (Figure 1B). Next, to reduce insulin concentration in the media towards a more physiological one, we prepared a self-made N2 supplement following commercial N2 media formulation, only excluding insulin (see material and methods). Insulin concentration in the N2B27 medium containing self-made N2 was 171.2 nM which is 2.3 times less than in the standard media. After three days of organoid culturing in this reduced insulin media, insulin concentration decreased even more, and was between 103.7 nM and 127.4 nM, suggesting increased usage of insulin by cells (Figure 1B). Further, we confirmed that self-made N2-supplemented media did not affect organoid development and viability (Figure S2) and did not change cellular composition within organoids (Figure S3). Additionally, we validated the self-made N2-supplemented media on iPSC-derived dopaminergic neuron cultures, to verify the effect specifically on the cellular population in which we are the most interested in the context of PD. Self-made N2 media did not cause any changes in dopaminergic neuron differentiation capacity, determined by the similar levels of TH and TUJ1 markers in dopaminergic neurons cultured in standard and self-made N2 supplemented media (Figure S4A). To further confirm that a 2.3 times reduction of the insulin concentration (from 393 nM to 171.2nM) is sufficient to change the activity of insulin signaling, we cultured midbrain organoids in these two insulin conditions from the start of organoid differentiation – day two of organoid culture and maintained until the sample collection – day 30 or day 60 of organoid culture (Figure 1A).

We were able to demonstrate a significant reduction of insulin receptor substrate 1 (IRS1) upstream insulin signaling in organoid samples cultured in the high insulin concentration standard media, confirming insulin signaling dysfunction in these organoids (Figure 1C). Contrary, IRS1 was significantly more abundant in the organoid samples cultured in reduced insulin concentration media, suggesting that this condition promotes cellular insulin sensitivity (IS). Additionally, we looked at the abundance of the central protein of insulin signaling – AKT, which was not changed between organoids cultured in the two insulin conditions (Figure 1D). We triggered acute insulin signaling activation by organoid stimulation with 100nM insulin for two hours and observed that in response to insulin, there was an increase of AKT phosphorylation at Ser473 residue in IS organoids, while IR organoids did not show any change in AKT phosphorylation (Figure 1E-F), further demonstrating loss of insulin sensitivity. Similarly, the acute stimulation of only dopaminergic neurons with increasing concentrations of insulin was able to activate the insulin signaling pathway already at the dose of 10nM, as indicated by the robust increase of AKT phosphorylation (both at Ser473 and Thr308 residues) in dopaminergic neurons cultured in self-made N2-based media. In contrast, even the highest dose of insulin (200nM) was unable to increase phospho-AKT levels in dopaminergic neurons cultured in N2B27 media containing commercial N2, further supporting that insulin concentration change affects the insulin signaling also in dopaminergic neurons (Figure S4B).

To additionally confirm the IR and IS state of midbrain organoids cultured under different insulin concentration media, we measured levels of branched amino acids (BAAs) which are considered biomarkers of insulin resistance and are found in higher levels in the plasma of individuals with changed metabolism and insulin resistance (32, 33). Accordingly, we saw their increased levels in IR organoid-conditioned media (Figure 1G). Furthermore, we observed that most of the metabolites present in the culture media were in significantly lower concentration in the IS organoid spent media after three days of incubation, indicating better metabolite uptake by IS organoids (Figure S5A). These metabolites included glucose, which was also found in significantly decreased levels in IS organoid spent media (Figure 1H). To verify increased glucose uptake by IS organoids, we treated dissociated organoids with a fluorescent glucose analog 2-NBDG, to visualize glucose uptake difference by fluorescence-activated cell sorting (FACS) (Figure S5B). We were able to observe a significantly increased fluorescent signal for IS organoids after acute insulin stimulation, further supporting that they are more insulin responsive than IR organoids. To confirm that glucose uptake in midbrain organoids can be insulin-dependent, we investigated the glucose transporter (GLUT) presence in midbrain organoids. Along with the insulin-independent GLUTs, such as neuron-specific GLUT3 and glia-specific GLUT1, we were able to detect insulin-

dependent GLUT4, which supports insulin's role in glucose uptake and regulation of metabolism in midbrain organoids (Figure S5C). Moreover, we observed that GLUT4 staining overlapped with the neuronal marker MAP2 (Figure S4D) and the glia marker GFAP (Figure S4E), suggesting that GLUT4 is not expressed in a cell type-specific manner. Furthermore, we did not observe a significant difference in SOX2+ stem cells, MAP2+ neurons and the S100b+ glia population in organoids at day 30 nor at day 60 of organoid culture under IS conditions (Figure S3), hence we conclude that here presented metabolic differences are rather insulin concentration-dependent and not the consequence of changes in the major cell type proportions.

Insulin sensitivity increases dopaminergic neuron amount and midbrain organoid functionality

After we confirmed that the reduction of insulin concentration in the cell culture media restores insulin signaling activity in the whole midbrain organoid as well as in the dopaminergic neurons, we wanted to assess whether insulin concentration affects dopaminergic neuron abundance. While at an earlier time point (day 30), there was no significant difference in the amount of TH-positive dopaminergic neurons between the two conditions, we observed a significantly higher number of dopaminergic neurons in IS midbrain organoids at day 60 of organoid culture (Figure 2A-B). Moreover, we confirmed that increased dopaminergic neuron amount in IS organoids is accompanied by a significant increase in dopamine production (Figure 2C). Considering the positive effect of insulin sensitivity on dopaminergic neuron levels and their ability to produce dopamine, we wanted to assess the role of insulin in the electrophysiological activity of the entire midbrain organoid. We measured spontaneous electrophysiological activity in the midbrain organoids by using a multi-electrode array (MEA) system (Figure 2D) and observed that organoids cultured in IS conditions presented a significantly higher mean firing rate (Figure 2E). Furthermore, we confirmed increased electrophysiological activity of IS organoids by recording local field potentials (LFP). Supporting the MEA data, IS organoids demonstrated a significantly higher number of spikes than IR organoids at both time points with an increased spike duration at day 60 of culture (Figure 2F-H). We were also able to detect bursts, which represent synchronized neuronal activity, occurring more often in IS organoids than in IR organoids again at both time points (Figure 2I-K), further confirming that insulin sensitivity promotes neuronal functionality.

Metabolic modeling predicts altered lipid metabolism and decreased glycolysis efficiency under insulin resistance

To further investigate metabolic alterations linked to insulin resistance, we performed metabolic modeling integrating RNA sequencing data of IR and IS midbrain organoids into the Recon3 human metabolic network (34). Gene expression was integrated using the rFASTCORMICS pipeline (35) which builds metabolic models based on gene discretization (Figure S6A-B). We generated IR and IS models from pooled transcriptomic data between three cell lines cultured in the respective conditions. The model composition was not substantially different (Figure S6C). The IR model included 1446 genes, 3620 metabolic reactions and 2632 unique metabolites. While the IS model included 1430 genes, 3470 metabolic reactions and 2521 unique metabolites. Both models were primarily constrained by the N2B27 basis media composition, allowing uptake of only those metabolites that are present in the media. To capture differences in metabolism more accurately, we integrated major metabolic constraints such as glucose uptake and lactate production based on metabolomics results. We also added biomass constraint, as organoid growth between day 16 and day 30 of organoid culture to account for biomass change per unit of time, allowing more precise estimation of required metabolic rates of reactions present in the models.

By model composition analysis we identified the most different pathways by reaction composition between the two models (Figure 3A). The top metabolic pathways included several transport subsystems between cellular compartments and lipid metabolism-associated metabolic subsystems. To confirm that altered lipid metabolism is driven by insulin resistance, we validated our modeling results by lipidomic analysis, which detected an abundance of 18 different lipid classes in midbrain organoid samples. The lipid profile separated IR and IS samples in a principal component analysis (PCA) across the first principal component (11.6%). although the variance between the samples across the second component was higher (63,5%), demonstrating biological variability between the cell lines. We found that seven lipid classes were significantly differentially abundant between IR and IS samples (Figure S7), the most significantly dysregulated class and the major contributor to the IR sample separation were cholesterol esters (Figure 3C,D). Following model predictions that suggested dysregulation in cellular membrane constituents – glycerophospholipids, we verified that one of the most abundant cell membrane phospholipid classes – phosphatidylcholines was significantly increased in IS samples. Additionally, further considering modeling predictions, we investigated lipid species across all measured lipid classes that contained arachidonic acid (C20:4) and its immediate precursor of eicosanoid family – eicosatrienoic acid (C20:3). We found 10 significantly differentially abundant species containing

a 20-carbon backbone across six lipid classes, all being intermediates of glycerophospholipid metabolism, namely – Triacylglycerides (TG), Phosphatidylcholine (PC), 1-alkyl,2-acylphosphatidylethanolamines (PC-O), 1-alkenyl,2-acylphosphatidylethanolamines (PC-P), Lysophosphatidylcholine (LPC), Lysophosphatidylethanolamine (LPE) (Figure S8). The best separation between the IR and IS samples was achieved by major lipid components of the cellular membrane, including PC-Ps, PC-Os and the Phosphatidylcholine*s* derivatives LPCs (Figure 3F). All together these results indicate that insulin resistance is inducing lipid changes that particularly affect the cellular membrane and cholesterol metabolism.

Next, we carried out an *in silico* flux variability analysis (FVA) to predict the differences in metabolic performance of the subsystems of our interest. We included lipid subsystems with high differences in the composition between the models (Figure 3A), and central energy metabolism pathways – glycolysis, TCA and OXPHOS (Figure 3G). We observed higher flux flexibility in glycosphingolipid metabolism in the IS model compared to the IR model, which was in accordance with the differential abundance of several glycosphingolipid classes identified by lipidomics analysis. In contrast, the IR model showed much higher flexibility in fatty acid oxidation than the IS model, suggesting that fatty acid oxidation might contribute to energy generation in insulin-resistant conditions. We wanted to confirm this prediction with the Seahorse metabolic assay, which allows us to evaluate cell dependency from different carbon sources for energy generation. Indeed, we observed that IR organoids are about 10% more dependent on fatty acids than IS organoids (Figure 4H-I). We also performed *in silico* perturbations to determine the importance of glucose uptake and mitochondrial performance for the generation of ATP (Figure 4A). ATP levels were predicted to be slightly higher in the IS model compared to the IR model. We confirmed this by measuring intracellular ATP levels in 30 and 60 days old organoids, demonstrating significantly higher levels of ATP in IS samples at both time points (Figure 4B,C). There was no predicted difference in ATP generation by models after *in silico* blocking mitochondrial complexes I and V. However, the prediction showed that the IS model is unable to generate ATP in case of glucose uptake obstruction (Figure 4A). This suggested that the IS model strongly relies on glucose to produce ATP, while the IR model showed an irrelevant change in ATP levels in case of blocking glucose uptake, thus implying the usage of other carbon sources for energy generation under insulin resistance conditions. We performed glucose C13 labelling to confirm increased glycolytic flux in IS samples. We saw a significant increase in glycolysis intermediates directly derived from labelled glucose – 3-phosphoglycerate (3PG), phosphoenolpyruvate (PEP), pyruvate and lactate in IS samples (Figure 4D). There was no difference in TCA cycle metabolites derived from the

labelled glucose, suggesting no differences in mitochondrial functionality between IR and IS samples. In addition, we observed higher levels of Ribose 5-phosphate and Serine in the IS samples, compared to IR samples, indicating increased activity of glycolysis parallel pathways such as pentose-phosphate pathway and *de novo* serine synthesis respectively (Figure 4E,F). We anticipated that altered metabolism in IR organoids might cause increased oxidative stress which plays an important role in the pathophysiology of both T2D and PD. Indeed, we detected significantly lower levels of NAD+/NADH ratio in IR samples, indicating a changed redox state of IR organoids. In addition, we observed increased cytosolic reactive oxygen species (ROS) levels in IR organoids (Figure 4H, I), further confirming metabolic and redox disbalance in midbrain organoids driven by insulin resistance.

GBA-PD organoids show dopaminergic neuron loss and an altered lipid profile

To assess whether insulin resistance accelerates PD phenotypes, we generated midbrain organoids from three cell lines, derived from PD patients carrying the GBA-N370S mutation (GBA-PD). We cultured GBA-PD organoids under IR and IS conditions following the same strategy as for WT midbrain organoids (Figure 1A). First, we confirmed that GBA-PD (IR,GBA) midbrain organoids exhibit a significant loss of TH-positive dopaminergic neurons and dopamine depletion (Figure 5A-C). However, this phenotype was not affected by reducing insulin concentration in the cell culture media of GBA-PD organoids (IS,GBA) (Figure 5A-C). Nevertheless, IS,GBA organoids showed significantly reduced levels of apoptosis, suggesting a beneficial effect or insulin reduction on the overall cellular viability (Figure 5D-E).

GBA-N307S mutation is associated with lipid changes due to the altered GBA enzymatic activity. Moreover, we observed changed lipid profile in WT-derived midbrain organoids under insulin resistance, suggesting that insulin resistance might amplify GBA-PD associated dyslipidemia Lipidomics profiles of IR,GBA and IS,GBA samples were not clearly separable in PCA (Figure S9A). Nevertheless, IR,GBA samples demonstrated a tendency to cluster more with IR,WT samples, while IS,GBA samples were closer to IS,WT samples, still suggesting insulin role in lipid metabolism. Similarly, to WT organoids, cholesterol esters were the most differentially abundant lipid class between IR,GBA and IS,GBA samples (Figure 5F), implying that cholesterol ester levels depend on the insulin resistance state. Another lipid class that was significantly decreased between WT organoids and IR,GBA organoids and differentially abundant in IS,GBA, were cell membrane phospholipids – PC-Os (Figure 5G), suggesting increased cell membrane damage in IR,GBA organoids. Overall, most of the lipid species in GBA-PD samples were at significantly lower levels compared to WT organoids, suggesting strong GBA mutation-dependent lipid

metabolism alterations (Figure S9B). Although we did not detect GBA mutation-associated accumulation of total ceramides or hexosylceramides in GBA-PD organoids, we observed a significant increase in the relative abundance of those species, derived from myristic (C14) and palmitic acid (C16) compared to other ceramide structures (Figure 5H). Interestingly, ceramide species with a palmitic acid backbone have been considered as a shared biomarker between several neurodegenerative diseases (36). IS,GBA samples showed lower levels of C14 and C16 derived ceramide species, suggesting insulin resistance contribution, particularly to toxic ceramide accumulation. Overall, these results suggest that insulin resistance compromises cell membrane integrity, alters cholesterol metabolism, and accelerates toxic ceramide accumulation.

FOXO1 as a potential drug target in GBA-PD

Next, we investigated whether the insulin signaling transcriptomic profile was different between WT and GBA-PD samples. Based on the expression of insulin signaling-associated genes from the KEGG database (37) we observed that IR,WT and IR,GBA organoid samples cluster separately, suggesting insulin signaling deregulation already at gene epression level in GBA-PD (Figure 6A). Among the major insulin signaling effectors downstream of AKT1, only FOXO1 and FOXO3 genes were significantly differentially expressed between IR,GBA and IS,GBA midbrain organoids (Figure S10A). To assess the potential contribution of the defective insulin signaling in GBA-PD, we compared lists of differentially expressed genes (DEGs) between IR,GBA vs IR,WT; IR,GBA vs IS,WT and IS,GBA vs IS,WT organoid samples. We visualized distinct genes for each comparison (Figure 6B) and performed gene functional enrichment analysis for the DEG clusters of interest (Figure 6C). 366 DEGs that overlapped between all comparisons, representing biological processes dysregulated in GBA-PD independently of IR and IS state, were enriched in developmental processes. 116 DEGs that were distinct to the comparison IS,GBA vs IS,WT, demonstrating biological processes dysregulated in GBA-PD assuming normal insulin signaling function, were enriched in specific plant-derived metabolite catabolic processes with neuroprotective properties (38). Finally, 93 DEGs that were distinct in a comparison IR,GBA vs IS,WT, representing biological processes dysregulated in GBA-PD accelerated by insulin resistance, were enriched in organ development and particularly in neuron developmental processes.

Furthermore, we evaluated the possible role of FOXO1 in governing insulin resistance effects in GBA-PD by exploring the expression of FOXO1 and its targets reported to be highly expressed in PD brains (20). We confirmed significantly increased expression of 9 out of 29 reported FOXO1 target genes in GBA-PD midbrain organoids compared to WT organoids (Figure 6D). Further, we

applied Probabilistic Boolean modelling (PBM) to the transcriptomics data to predict FOXO1-associated phenotypes with simulations reflecting insulin resistance-dependent FOXO1 activity upregulation (AKT1:OFF and FOXO1:ON) in GBA-PD midbrain organoids (Figure 6E). Based on this model, impaired FOXO1 inhibition by AKT1 due to insulin resistance potentially leads to an energy crisis resulting in reduced ATP levels. Consequently, insulin resistance would increase by activation of the feedback loop due to accelerated IRS1 phosphorylation leading to its subsequent degradation. Additionally, model predicted the accumulation of αSyn and neuronal death. Altogether, the transcriptomics data analysis and PBM-derived predictions suggest that multi-faceted assault driven by insulin resistance-dependent FOXO1 overactivation likely contributes to the severity and progression of GBA-PD.

FOXO1 knockout and Pioglitazone rescue GBA-PD associated dopaminergic neuron loss

Given that IS culture conditions were not sufficient to rescue GBA-PD dopaminergic phenotypes most likely due to the underlying transcriptional insulin signalling dysregulation, and potential FOXO1 contribution to the disease progression, we treated GBA-PD midbrain organoids with antisense oligonucleotides (ASOs) designed against FOXO1 (Figure 7A, Figure S10B-G). The efficiency of FOXO1 knock-down by ASOs was confirmed in WT organoids, showing that 28-day-long treatment with ASO downregulates FOXO1 by approximately 25% (Figure S10D,E). To achieve higher knock-down efficiency, we treated GBA-PD organoids for a longer time – until day 60 of organoid culture. We observed that the downregulation of FOXO1 by ASOs, significantly restored dopaminergic neuron numbers and dopamine levels (Figure 7B-D), confirming the role of FOXO1 in GBA-PD. Moreover, FOXO1 downregulation significantly decreased apoptosis in GBA-PD midbrain organoids (Figure 7B,E), further highlighting FOXO1 as a relevant target in PD modifying therapy.

Finally, we treated GBA-PD midbrain organoids with two widely used anti-diabetic drugs – Metformin and Pioglitazone, to evaluate their potential in PD therapy (Figure 7A). We did not observe a significant increase in dopaminergic neuron amount and dopamine levels upon Metformin treatment (Figure 7F,G). Nevertheless, Metformin treatment resulted in a slight reduction of overall cell death in GBA-PD midbrain organoids (Figure 7H). On the other hand, Pioglitazone significantly increased TH-positive dopaminergic neuron numbers and dopamine levels, also reducing cellular death in GBA-PD midbrain organoids (Figure 7I-L). This result demonstrates Pioglitazon's potential in GBA-PD treatment.

Discussion

In this study, we aimed to understand the molecular mechanisms through which T2D contributes to the development of PD and whether it accelerates GBA-PD phenotypes. With a global prevalence of over 10% and a tendency to increase (39, 40), T2D has become a considerable risk factor for many disease development, including neurodegenerative disorders. Thus, there is a need to better understand T2D's contribution to the onset and progression of these diseases. In our study, we focus on insulin resistance, as the driving pathophysiological mechanism of T2D, effects on healthy and GBA-PD midbrain organoid metabolic and functional states.

We demonstrate that under insulin resistance midbrain organoids display reduced spontaneous activity in the form of action potentials and bursts, suggesting decreased neuronal functionality. It has been previously reported that not only T2D but even pre-diabetes with insulin resistance as a common factor, promotes cognitive decline in PD patients (7, 41). Brain energetics is crucial to coordinate electrophysiological activity (42, 43) and since insulin signaling is a major regulator of metabolic processes, it is expected that insulin resistance would affect neuronal signal transmission. Although brain insulin sensitivity is controversial, mouse studies have shown that in some brain regions for rapid glucose uptake neurons are equipped with insulin-dependent glucose transporters in the proximity of synapses (44, 45), supporting insulin's role in controlling brain energy metabolism. Accordingly, we were able to show the presence of insulin-dependent GLUT4 along with the insulin-independent GLUT1 and GLUT3 transporters in midbrain organoids, suggesting at least partial insulin-dependent glucose uptake in the human midbrain.

Further supporting the role of insulin in midbrain metabolism regulation, we show that glycolysis is enhanced in IS organoids. In addition, important intermediates from glycolysis-derived pathways, such as ribose 5-phosphate and serine were also found in increased levels in IS organoids. Both are precursors of nucleotide, lipid and amino acid synthesis, suggesting that IS organoids have a more flexible and sustainable metabolism compared to IR organoids. However, we did not observe any changes in mitochondrial metabolite abundances by C13 glucose tracing, suggesting that IR organoids are still capable of compensating for reduced glycolytic flux with other carbon sources. Supporting this hypothesis, we validated that IR organoids are more dependent on fatty acid oxidation. Overall, these discrepancies in metabolism between IR and IS organoids manifested in an altered redox balance that we confirmed with decreased NAD/NADH ratio and increased cellular ROS levels in IR organoids. Notably, oxidative stress has been suggested as an important disease mediator in both T2D and PD (46, 47).

Altered lipid metabolism seems to present another link between T2D and PD. Mutations in the GBA gene lead to the loss of the enzymatic function of Glucocerebrosidase (GCase), which is crucial in sphingolipid, ceramide and hexosylceramide metabolism. Impaired activity of the GCase is associated with the accumulation of ceramides and hexocylceramides that promotes αSyn pathology (48, 49). It has been reported that particularly short-chain fatty acid ceramides and hexosylceramides are increased in GBA-PD and are also found in lipid extracts from αSyn fibrils (36, 48). Our findings were in line with these previous studies, and demonstrated higher relative levels of C14 and C16 ceramides and hexacylceramides in GBA-PD, while, for instance, C18 species were relatively decreased compared to WT. Ceramides with 18 carbons are the most abundant in the brain and reduction of this ceramide species has been associated with neurodegeneration (50).

Moreover, we showed increased levels of cholesterol esters in IR,WT and IR,GBA samples, which is consistent with previous studies that have reported elevated cholesterol ester levels in neurodegenerative diseases (51-53). In addition, we demonstrated that most of the cellular membrane lipid classes containing arachidonic acid are differentially abundant between IR,WT and IS,WT samples. Arachidonic acid is one the most abundant fatty acids in the brain and it has been associated with prevention of αSyn protein aggregation (54) and neuroprotection in animal models (55). Moreover, it has been reported as a potential biomarker in PD (56), suggesting its relevance in disease progression.

Furthermore, we found that GBA-PD midbrain organoids have different transcriptomic profiles of insulin signaling-associated genes, again indicating that insulin resistance is one of the underlying mechanisms contributing to PD pathology. Particularly, FOXO1 and FOXO3 transcription factors were found to be significantly differentially expressed between WT and GBA-PD midbrain organoids. Moreover, we validated that several genes regulated by FOXO1 according to GWAS (20), were significantly upregulated in GBA-PD midbrain organoids.

To predict FOXO1 overexpression effects in GBA-PD, we performed PBM. The model highlighted that insulin resistance with specific perturbations (AKT1-OFF, FOXO1-ON) is a significant contributing factor to the progression of GBA-PD. The gradual changes in the associated parameters suggested a complex interplay between insulin resistance, altered energy metabolism, and increased cellular death. Furthermore, knockout of FOXO1 by ASOs, increased levels of TH and dopamine, and attenuated cell death in GBA-PD midbrain organoids, providing further evidence of FOXO1 role in GBA-PD phenotype acceleration.

There is a growing amount of studies and clinical trials focused on anti-diabetic medication usage in PD therapy. In this study, we chose to explore Metformin's and Pioglitazone’s effects on GBA-

PD. While Metformin is described to be a mitochondrial complex I inhibitor (57), Pioglitazone increases the activity of insulin signaling by selectively stimulating nuclear receptor peroxisome proliferator-activated receptor gamma (PPAR-γ) (58). There is no significant association between mitochondrial complex I overactivation and GBA-PD, which would explain Metformin's inefficiency in reversing GBA-PD-associated dopaminergic neuron loss in the organoids. On the other hand, our results support Pioglitazone's beneficial effects in GBA-PD, demonstrating increased TH and dopamine levels, and reduced cell death in GBA-PD-treated organoids. Although, clinical trial for Pioglitazone was not extended for phase 3, with the conclusion that it is unlikely to modify PD progression (27), multiple studies, including meta-analysis have reported that Pioglitazone is associated with reduced risk of PD in subgroups of patients (24, 29). This suggests the high importance of therapeutic specificity and a need for a well-stratified approach in PD treatment.

Conclusion

Insulin resistance can potentially predispose the healthy midbrain to PD development by compromising neuronal functionality, dopaminergic neuron amount, dopamine levels and efficiency of metabolism. Observed phenotypes in WT organoids cultured under insulin resistance, were similar to those observed in GBA-PD organoids. Furthermore, insulin dysregulation in GBA-PD aggravates TH loss and cell death, hence insulin resistance represents a relevant target to address neurodegeneration in PD.

Materials and Methods

Data availability

All related data of this study is publicly available at: DOI: https:/doi.org/10.17881/ztcz-2197
RNA sequencing data is available on Gene Expression Omnibus (GEO) under the accession code GSE237116.

Code availability

Matlab and R scripts for data analysis and modeling are available on GitHub at: https://github.com/LCSB-DVB

Ethical approval

The work with iPSCs has been approved by the Ethics Review Panel (ERP) of the University of Luxembourg and the national Luxembourgish research ethics committee (CNER, Comité National d'Ethique de Recherche). CNER No. 201901/01; ivPD

IPSC-derived dopaminergic neuron differentiation and characterization

IPSC from a healthy donor were first converted into neuroepithelial stem cells (NESCs) based on the protocol previously described (59). In brief, the N2B27 medium was used as the basis media for cell culture. N2B27 consists of DMEM-F12 (Thermo Fisher Scientific, cat.no 21331046) and Neurobasal (Thermo Fisher Scientific, cat.no.10888022) 50:50 and is supplemented with 1:200 N2 supplement (Thermo Fisher Scientific cat.no. 17502001), 1:100 B27 supplement w/o Vitamin A (Life Technologies, cat.no. 12587001), 1 % GlutaMAX (Thermo Fisher Scientific, cat.no. 35050061) and 1 % penicillin/streptomycin (Thermo Fisher Scientific, cat.no. 15140122). N2B27 base media was supplemented with 3 µM CHIR-99021 (Axon Medchem, cat.no. CT 99021), 0.75 µM purmorphamine (Enzo Life Science, cat.no. ALX-420-045) and 150 µM ascorbic acid (Sigma, cat.no. A4544). For the generation of midbrain-specific dopaminergic neurons, NESCs were seeded into Geltrex-coated wells in a differentiation medium consisting of N2B27 containing 1 µM PMA, 200 µM ascorbic acid, 10 ng/ml BDNF, 10 ng/ml GDNF, 1 ng/ml TGF-b3 and 500 µM dbcAMP. After six days, differentiating NESCs were shifted to the same medium but without PMA (replaced every two days) and kept until day 30.

The expression of neuronal differentiation markers was assessed by flow cytometry. Briefly, cells were detached with Accutase (Sigma, cat.no. A6964) and then fixed in 4% PFA for 15 minutes. After three washes in FACS buffer (PBS + 5% BSA + 0.1% Sodium Azide), cells were centrifuged

at 700g for 5 minutes and the resulting cell pellet resuspended in Saponin buffer (PBS + 1% BSA + 0.05% Saponin). After 30 minutes of incubation at 4°C, cells were pelleted again and then resuspended in Saponin buffer containing the TH (Millipore, cat.no. AB152) and Tuj1 (Biolegend, cat.no 801201) primary antibodies (1:100 dilution, 30 minutes at 4°C under shaking). Cells were washed three times in FACS buffer, and then incubated for 30 minutes with anti-mouse Alexa 488 (for TUJ1) and anti-rabbit Alexa 568 (for TH) secondary antibodies (at 4°C in the dark). After two washes in the FACS buffer, cells were pelleted and finally resuspended in PBS. Cells were analyzed with the BD LSRFortessa flow cytometer and the mean fluorescence intensity of each dye was assessed on at least 10,000 single cells using the FlowJo software (v.10.7.2.).

Midbrain organoid culture

Cell lines used in this study are summarised in Table S1. As starting population for midbrain organoid generation, we used NESCs described in Reinhardt et al., 2013 (59). NESCs were cultured as described in paragraph *iPSC-derived dopaminergic neuron differentiation and characterization*. Midbrain organoids were generated as described in Monzel et al.,2017 (60) and Nickels et al., 2020 (61). For organoid generation, at 80% of confluency, NESCs were detached using Accutase (Sigma, cat.no. A6964) and viable cells were counted using Trypan Blue. $9x10^5$ cells were transferred into 15ml of N2B27 maintenance media for seeding in 96-well ultra-low attachment plates (faCellitate, cat.no. F202003). In each well 150µl with 9000 cells were distributed. Plates were centrifuged at 300 g for one minute to facilitate colony formation at the bottom of the well. On the 2nd day of organoid culture, media was changed to N2B27 pattering media, which is N2B27 base media supplemented with 10 ng/ml hBDNF (Peprotech, cat.no. 450-02-1mg), 10 ng/ml hGDNF (Peprotech, cat.no. 450-10-1mg), 500 µM dbcAMP (STEMCELL Technologies, cat.no.100-0244), 200 µM ascorbic acid (Sigma), 1 ng/ml TGF-β3 (Peprotech cat.no. 100-36E) and 1 µM purmorphamine (Enzo Life Science, cat.no ALX-420-045). Media was next changed on the 5th day of organoid culture. On day 8 of organoid culture, organoids for high-content imaging were embedded in extracellular matrix-like Gelltrex (Thermo Fisher Scientific, cat.no. A1413302) droplets as described in Zagare & Gobin, et al., 2021 (62) to support the outgrowth of neurites. Embedded organoids were kept in dynamic conditions on an orbital shaker (IKA), rotating at 80 rpm until the collection day. From day 8 of organoid culture organoids were kept in N2B27 differentiation media which only differs from the pattering media by lack of purmorphamine. Media changes were done every 3-4 days for embedded and non-embedded organoids until the day of sample collection – day 30 or day 60 of organoid culture. For organoid cultures with reduced insulin concentration in media, commercial N2 supplement was substituted

by self-made N2 supplement w/o insulin starting from day 2 of organoid culture. Self-made N2 was prepared as described in Harrison et al. (63), adding human Apo-transferrin (Sigma, cat.no.T1147), Putrescine dihydrochloride powder, cell-culture tested (Sigma, cat. no. P5780), Sodium selenite powder, cell-culture tested (Sigma, cat. no. S5261), Progesterone powder, cell-culture tested (Sigma, cat. no. P8783) in cell media in the same concentrations as in the commercial N2 supplement (Table S2).
All cell cultures were tested for mycoplasma contamination once per month using LookOut® Mycoplasma PCR Detection Kit (Sigma, cat.no. MP0035-1KT).

Organoid treatment with anti-diabetic drugs and ASOs

Organoids were treated with 500µM of Metformin (STEMCELL technologies, cat.no.73252) diluted in DPBS (Thermo Fisher Scientific, cat.no. 14190250) and 10µM of Pioglitazone hydrochloride (Sigma, cat.no. E6910-10MG) diluted in DMSO (Sigma, cat.no. D2650-100ml) starting from day 2 of organoid culture. Additionally, organoids were treated with the respective solvents in the same volume and frequency as Metformin and Pioglitazone.
For a targeted FOXO1 knockdown, four LNA-enhanced antisense oligonucleotides (ASOs) were designed. Their efficiency was tested for seven days by treating NESCs with 100nM of ASOs, changing media every two days. The most efficient ASO was also tested in organoids, treating non-embedded organoids for 30 days, and changing media every 3-4 days.
Scrambled non-human RNA sequence – Negative control B (Qiagen, cat no.339515) was used as a negative control for the ASOS treatment in the same concentration and frequency.

Insulin ELISA

Insulin in fresh cell culture media and organoid supernatant was measured with Insulin ELISA (Mercodia, cat.no. 10-1113-01) following the manufacturer's instructions. The supernatant was collected after 2 hours of incubation with cells. Before the essay media and supernatant were diluted in DMEM-F12 (Thermo Fisher Scientific, cat.no 21331046) 1:500 to ensure that insulin concentration do not exceed the measurement range of the kit. DMEM-F12 was used as a negative control for the assay as it does not contain any insulin. All samples were measured in duplicates from which the average was calculated.

Western Blot

IPSC-derived dopaminergic neurons were lysed in 1% SDS supplemented with protease inhibitors (Roche, cat no. 11697498001) and immediately boiled at 95°C for 5 minutes. Cell extracts were then sonicated at 4°C for 5 cycles (30 seconds on / 30 seconds off) with the Bioruptor Pico (Diagenode), prior to proceeding with protein quantification using the Pierce™ BCA Protein Assay Kit (Thermo Fisher Scientific, cat. no. 23225). 10µg of proteins were resolved using SDS-PAGE (4-12% Bis-Tris precast gels in buffer MES), followed by transfer on nitrocellulose membrane in Tris-Glycine buffer containing 20% ethanol (1h15 at 400mA). Membranes were blocked for 1h in TBS buffer containing 0.2% Tween (TBS-T) and 5% BSA, and then incubated overnight at 4°C with the primary antibodies (see Table S2). Membranes were then washed in TBS-T for 30 minutes, followed by 1h incubation at RT with the corresponding HRP-linked anti-rabbit or anti-mouse secondary antibodies. After additional washes in TBS-T for 30 minutes, proteins were revealed using the ECL prime and images acquired with the STELLA 8300 imaging system (Raytest).

For the analysis of midbrain organoids, eight non-embedded organoids were pulled together from three independent organoid generation rounds and lysed using RIPA buffer (Abcam, cat no. ab156034) supplemented with cOmplete™ Protease Inhibitor Cocktail (Roche, cat no. 11697498001) and Phosphatase Inhibitor Cocktail Set V (Merck, cat..no. 524629) for 20 minutes on ice. To disrupt DNA, protein lysates were sonicated for 10 cycles (30 seconds on / 30 seconds off) using the Bioruptor Pico (Diagenode). Samples were centrifuged at 4°C for 30 minutes at 14,000g. Protein concentration was determined using the Pierce™ BCA Protein Assay Kit (Thermo Fisher Scientific, cat. no. 23225). The concentration of samples was adjusted by dilution with RIPA buffer. Samples were then boiled at 95°C for five minutes in denaturalizing loading buffer. 20µg of protein of each sample was used for protein detection. Proteins were separated using SDS polyacrylamide gel electrophoresis (Bolt™ 4-12% Bis-Tris Plus Gel, Thermo Fisher Scientific) and further transferred onto a PVDF membrane (Thermo Fisher Scientific) using iBlot™ 2 Gel Transfer Device (Thermo Fisher Scientific). For IRS1 protein, protein separation was achieved using NuPAGE™ 3 to 8%, Tris-Acetate gel (Thermo Fisher Scientific). After transfer, membranes were fixed in 0.4% paraformaldehyde (PFA) in PBS for 30 minutes at room temperature (RT) and then washed twice with PBS for 10 minutes. Membranes then were blocked for one hour at RT in 5% skimmed milk powder or 5% BSA (for phosphorylated proteins) and 0.2% Tween in PBS following overnight incubation at 4°C with the primary antibodies prepared in 5% skimmed milk powder or 5% BSA (for phosphorylated proteins) and 0.2% Tween in PBS. A list of primary antibodies see in Table S2. After incubation with primary antibodies, membranes

were washed three times for five minutes with 0.02% Tween in PBS and incubated for one hour at RT with HRP-linked antibodies – anti-rabbit (VWR, cat.no. NA934) or anti-mouse (VWR, cat.no. NA931). Membranes were then washed three times for ten minutes with 0.02% Tween in PBS. The signal was developed using a chemiluminescent substrate (Life Technologies, cat.no. 34580) and imaged with STELLA 8300 imaging system (Raytest). After developing phospho-AKT and phosphor-FOXO1 protein signal, membranes were stripped using Restore™ Western Blot Stripping Buffer (Thermo Fisher Scientific, cat.no. 21063) for 15 minutes at 37°C, and then washed twice for 10 min with 0.2% Tween in PBS at RT. Membranes were blocked again for one hour before overnight incubation with the AKT pan or FOXO1 pan antibody respectively.
Band intensity was quantified using ImageJ software. Phosphorylated protein relative abundance was determined in comparison to the total protein. For all other proteins, relative abundance was determined in comparison to the housekeeping protein β-Actin. Results were batch normalized to the mean intensity of all samples.

Extracellular metabolite detection with GC-MS

Spent medium pooled from five embedded organoids from each cell line and condition in triplicates were collected 72 hours after the last media change. Extracellular metabolite extraction and subsequent GC-MS analysis were performed as previously described (64).
Metabolite derivatisation was performed using a multi-purpose sampler (Gerstel). Dried polar sample extracts were dissolved in 20 µL pyridine, containing 20 mg/mL of methoxyamine hydrochloride (Sigma-Aldrich), and incubated under shaking for 120 min at 45 °C. After adding 20 µL N-methyl-N-trimethylsilyl-trifluoroacetamide (MSTFA; Macherey-Nagel), samples were incubated for an additional 30 min at 45 °C under continuous shaking.
GC-MS analysis was performed using an Agilent 7890B GC – 5977A MS instrument (Agilent Technologies). A sample volume of 1 µL was injected into a Split/Splitless inlet, operating in split mode (10:1) at 270 °C. The gas chromatograph was equipped with a 5 m guard column + 30 m (I.D. 250 µm, film 0.25 µm) DB-35MS capillary column (Agilent J&W GC Column). Helium was used as the carrier gas with a constant flow rate of 1.2 mL/min.
The GC oven temperature was held at 90 °C for 1 min and increased to 270 °C at 9 °C/min. Then, the temperature was increased to 320 °C at 25 °C/min and held for 7 min. The total run time was 30 min. The transfer line temperature was set constantly to 280 °C. The mass selective detector (MSD) was operating under electron ionisation at 70 eV. The MS source was held at 230 °C and the quadrupole at 150 °C. Mass spectrometric data were acquired in full scan mode (m/z 70 to 700).

All GC-MS chromatograms were processed using MetaboliteDetector (v3.2.20190704) (65). Compounds were annotated by retention index and mass spectrum using an in-house mass spectral library. The following deconvolution settings were applied: Peak threshold: 10; Minimum peak height: 10; Bins per scan: 10; Deconvolution width: 5 scans; No baseline adjustment; Minimum 15 peaks per spectrum; No minimum required base peak intensity. The dataset was normalized by using the response ratio of the integrated peak area of the analyte and the integrated peak area of the internal standard. Final metabolite relative abundance was normalized to the total area of organoids from each cell line and condition from the respective batch.

Multielectrode array

Multielectrode array (MEA) recordings were performed using the Maestro system from Axion BioSystems. Firing activity was recorded for midbrain organoids at day 30 and day 60 of organoid culture from three independent organoid generations for both time points. Three days before recording non-embedded organoids were placed into CytoView MEA 48-Black (Axion, cat.no. M768-tMEA-48B-5) plate precoated with 0.1 mg/ml poly-D-lysine hydrobromide (Sigma, cat.no.P7886) for 24 hours following 10 µg/ml laminin (Sigma, cat.no.L2020) coating for another 24 hours. Organoids were positioned at the centre of the well and covered with a droplet (20µ) of geltrex (Invitrogen, cat.no.A1413302) to secure organoid attachment. Recorded firing activity was exported using AxIS software (v.2.1. Axion) and analyzed with R (version 4.2.2). The organoid activity was analyzed from the active electrodes. Electrodes that did not record any activity or recorded three or fewer spikes in five minutes were excluded from the analysis. Statistical analysis was determined with Wilcoxon signed-rank test. Outliers were excluded using interquartile range (IQR) 1.5 method based on 25^{th} and 75^{th} percentiles. Data was batch normalized by the average value of the batch in each time point.

Local field-potential recording

Individual organoids were randomly selected from three different organoid generation batches and recorded between day 30 and day 33 or day 60 and day 63. For each organoid recordings were performed in multiple local fields. Each measurement is depicted as a separate data point. Live organoids were stuck on the bottom of the slice recording chamber using a customised platinum anchor and were perfused with a fast-flow rate (8-10 ml/min) warmed (37°C) extracellular solution containing (in mM): 140 NaCl, 2 CaCl2, 1 MgCl2, 4 KCl, 10 glucose, and 10 HEPES (pH 7.3 with NaOH), bubbled with an air pump at room atmospherically condition. Solution temperature was controlled by Perfusion Temperature Controller (Scientifica). To avoid bubbles

in the recording chamber, a bubble trap was employed in the inlet line, perfused by gravity drip. Local field-potential (LFP) activity was recorded using a patch pipette prepared from thin-borosilicate glass (1.5mmOD, 0.84mmID, World Precision Instruments, cat.no. 1B150F-4) pulled and fire-polished on a Flaming/Brown micropipette puller (Sutter Instrument, Model P-1000) to a final resistance of 1,5-2,5 MΩ when filled with standard extracellular solution. LFP recordings were performed with a Multiclamp 700B/Digidata1550 system (MolecularDevices) in a current-clamp configuration on a visually identified zone of healthy neurons on the organoid using a slice scope upright microscope (Scientifica). The patch pipette was pushed against the organoid for a depth of 40-60 µm until a small increase in the standard deviation of the recorded voltage was seen.

Data were acquired with Clampex software (v.11.2, MolecularDevices) at 3 kHz sample frequency and filtered at 3 kHz with a low-pass Bessel filter and 1Hz with a high-pass filter. All data were analyzed offline with Clampex software (v.11.2, MolecularDevices). The detection of LFP was done in 5-minute temporary windows recording with the threshold search function that recognizes only spikes over 6X standard deviation. Bursts with a minimum of 3 spikes and an inter-spike interval of ≤150 msec were detected and considered for analysis.

Immunofluorescence staining for NESC characterization

For immunofluorescent characterization, NESCs were seeded on geltrex-coated coverslips placed in a 24-well cell culture plate. At 60-70% of confluency, NESCs were fixed for 15 min at RT with 4% Paraformaldehyde (PFA). Then cells were washed 3x for 5 min with PBS, which was followed by cell permeabilization with 0.3% Triton X-100 in PBS for 15 min at RT. Afterwards, cells were washed 3x for 5 min with PBS and then blocked with 10% fetal bovine serum (FBS) in PBS for 1h at RT. Incubation with primary antibodies (Table S3) was done overnight at 4°C. Antibodies were diluted in 3% FBS in PBS. After overnight incubation, cells were washed 3x for 5 min with PBS and incubated for 1h at RT with Alexa Fluor® conjugated secondary antibodies (Table S3) and nuclei stain Hoechst 33342 (Invitrogen cat.no. 62249). After 3x washes for 5 min with PBS, coverslips were mounted on a glass slide for image acquisition.

Immunofluorescence staining of organoid sections

Organoids were fixed with 4% PFA for six hours at RT and then washed three times with PBS for 15 minutes. Individual organoids were embedded in 3% low-melting point agarose (Biozym Scientific GmbH, cat.no. 840100). Using a vibrating blade microtome (Leica VT1000s), organoids were sliced into 70 µm sections. Sections were permeabilized with 0.5% Triton X-100 for 30

minutes at RT and then blocked with blocking buffer (2.5% normal donkey serum, 2.5 % BSA, 0.01% Triton X-100 and 0.1 % sodium azide). Sections were incubated with primary antibodies diluted in a blocking buffer for 48 hours at 4 °C on an orbital shaker. Primary antibodies are listed in Table S4. After incubation with primary antibodies, sections were washed three times for 5 minutes with 0.01% Triton X-100 in PBS. Then sections were incubated with nuclei stain Hoechst 33342 (Invitrogen cat.no.62249) in dilution of 1:10 000 and The Alexa Fluor® conjugated secondary antibodies (Table S3) for two hours at RT on an orbital shaker. Sections were washed twice for 5 minutes with 0.01% Triton X-100 in PBS and once with MiliQ. Sections were mounted on slides (De Beer Medicals, cat.no.BM-9244) and covered with mounting media Fluoromount-G® (SouthernBiotech, cat.no.0100-01).

Apoptotic cells were stained using Tunel In Situ Cell Death Detection Kit, Fluorescein (Merck, cat.no. 11684795910). Kit components were integrated into the staining procedure. Staining with primary antibodies was done as described above. Secondary antibodies and Hoechst were diluted in the Tunel kit buffer. Sections were incubated for one hour at RT on an orbital shaker following washing and mounting steps as described above.

Image acquisition and analysis

High-content imaging was performed using the Yokogawa CV8000 high-content screening microscope with a 20x objective. One to three sections from at least three independent organoid generation rounds were analyzed per cell line and condition for each staining combination. Acquired images were analyzed with a customized pipeline using Matlab (v.2021a) as described in Bolognin et al, 2018 (66) and Monel et al, 2020 (67). Sections with non-optimal mask for a target protein or out of focus were excluded from further analysis. Data was batch normalized by the average value of the batch per feature and per time point. Outliers were excluded using interquartile range (IQR) 1.5 method based on 25^{th} and 75^{th} percentiles. Qualitative images were acquired using a confocal laser scanning microscope (Zeiss LSM 710) with either a 20x, 40x or 60x objective and processed with Zen Software (Zeiss)

RNA sequencing and analysis

The total RNA was extracted from 12 embedded organoids, which were pulled from three independent organoid generations (four organoids from each generation per cell line and per condition). RNA isolation was achieved using Trizol reagent (Thermo Fisher Scientific, cat. no. 15596026) following the manufacturer's protocol. Library preparation was done using TruSeq

stranded mRNA library preparation kit (cat. no. 20020594, Illumina) and sequenced on NextSeq2000.

The raw RNA-seq data were pre-processed using the software package "Rsubread" (version 1.34.7) (68). Gene-level differential expression analysis was conducted in the R statistical programming software (v. 3.6.0) using the software package "DESeq2" (version 2_1.26.0) (69) and filtering out genes with low expression counts using the filterByExpr-function with default parameters from the package edgeR (70). P-value significance scores for differential expression were adjusted for multiple hypothesis testing according to the Benjamini and Hochberg method (71). Pathway enrichment analyses were implemented in the GeneGo MetaCore™ software (https://portal.genego.com) using the gene-level differential expression analysis results obtained with DESeq2 as input for the standard enrichment analysis workflow. The pathway over-representation analysis statistics, including false-discovery rate (FDR) scores according to the method by Benjamini and Hochberg, were determined for the GeneGo collections of cellular pathway maps, process networks and Gene Ontology gene set terms. UpSet plot (72) was used to visualize differentially expressed gene intersections between the groups.

Metabolic modeling

Gene expression from RNA sequencing was normalized to the transcripts per kilobase million (TPM) reads. The Median of TPM expression was calculated between the three cell lines per IR and IS condition to enable the generation of one context-specific model per condition. Gene EntrezID as required input in the modeling pipeline was mapped using the clusterProfiler package (version 3.9) (73) in R (version 3.6.2). Context-specific models were reconstructed from the stoichiometrically and flux-consistent subset of the human genome-scale metabolic network Recon3 (34) using the rFASTCORMICS pipeline (35). Additionally, models were constrained by the cell culture media composition, allowing uptake of only those metabolites present in the media. Models were analyzed in Matlab (v.2019b) using the COBRA toolbox (74).

Models were compared by reaction composition, using the setdiff function in Matlab. Reactions that were unique for one of the models, were assigned to the subsystem. Subsystems with more than eight reactions unique for one of the models were selected for further analysis. For selected subsystems, the number of unique reactions was expressed as a percentage of the total number of reactions in the respective subsystem in Recon3.

Flux of the ATP demand/generation ‘DM_atp_c_ ’reaction in each model was estimated by the addition of qualitative constraints of glucose uptake ‘EX_glc_D[e]’, lactate secretion ‘EX_lac_L[e]’ and biomass reaction. Biomass increase per hour was calculated based on embedded organoid

area increase between day 16 and day 30 of organoid culture. Dry weight (DW) for a single cell was calculated considering that the total protein fraction within the DA neurons is 55.93% (75). Glucose uptake and lactate secretion were calculated as mmol/gDW*h. The concentration change of glucose and lactate within 72 hours for DW was estimated by comparing the relative abundance determined with LC-MS to metabolite concentration in the commercial media. Glucose and lactate relative abundance for each model was calculated as a median between the samples, after averaging values between technical replicates. The lower and upper bounds for glucose uptake and lactate secretion were set as +/- 10% of the calculated flux, while the lower and upper bounds for biomass were kept exact. Next, estimated ATP demand for each model was used as an objective function set as the lower bound for the 'DM_atp_c_' reaction. Further, FVA using IBM_CPLEX solver (version 12.10) was performed for shared reactions between the two models for the subsystems of interest – all subsystems determined to have the largest differences in reaction composition with the addition of glycolysis, TCA and OXPHOS. An average of min and max fluxes was calculated for visualization of flux variability between the two models. ATP perturbations were performed by setting the upper bound of reactions of interest to 0 and re-estimating ATP demand flux.

Probabilistic Boolean modeling

PyMaBoSS (76), Python API for MaBoSS software, was used to perform an in-depth stochastic simulation of the Wnt-PI3K/AKT model. The analysis was performed based on transcriptomic data, incorporating a probabilistic Boolean modeling (PBM) approach to understand the complex dynamics of the model (77). The perturbations within the model were defined as a knockout of AKT1 (represented as "Zero") and overexpression of FOXO1 (represented as "One"). We simulated the downstream signaling effects of these perturbations, which included insulin resistance states and SNCA accumulation, crucial components in the context of PD progression. Further, we identified the activity of intermediary molecules including ATP, IRS1, IRSIP, and the active form of TFEB (TFEB- SNCA complex).

The PBM approach identified a series of random walks to determine the probability of components within the model (78). The PBM combined the qualities of both discrete and continuous Markov processes, within a Monte Carlo framework (79). The goal was to accurately predict the temporal fluctuations in the model. In addition, we used the multiple change-point regression algorithm to detect inflexion points throughout the iterative steps. This helped to identify the significant alterations within the model's behaviour during the simulation (77).

Intracellular ATP assay

Intracellular ATP was measured using luminescence-based CellTiter-Glo® 3D Cell Viability Assay (Promega, cat.no. G9681) following the manufacturer's instructions. Three organoids per cell line and per condition were transferred into the imaging plate (PerkinElmer, cat.no.6055300)– one organoid per well. Media leftovers were aspirated and 50 µl of CellTiter-Glo® reagent was added to each well. The plate was incubated for 30min on a shaker at RT. Luminescence was measured using a Cytation5 M cell imaging reader. The experiment was repeated for five independent organoid generation rounds at day 30 and day 60 of organoid generation. The luminescence readout per sample of each batch was normalized to the mean luminescence of the batch. A median of three organoids of each cell line and conditions was calculated and normalized to the size factor. The size factor for each cell line and condition was determined as a mean of random 20 organoids at day 30 and 10 organoids at day 60 from five independent organoid generation rounds. The area of organoids was measured using the Cytation5M cell imaging reader.

Fatty acid dependency assay (Seahorse XF Mito fuel flex test)

The rate of fatty acids oxidation was determined in 30 days old midbrain organoids following Seahorse XF Mito fuel flex test protocol (Agilent) and using Seahorse XFe96 Spheroid FluxPak (Agilent, cat.no. 102905-100). The utility plate was coated with Corning® Cell-Tak™ Cell and Tissue Adhesive (Corning, cat.no. 354241) and for one hour incubated at 37^0C before organoid seeding in the plate. Organoids were incubated for one hour in Seahorse XF DMEM medium, pH 7.4 (Agilent, cat.n.103575-100) supplemented with 1 mM pyruvate, 2 mM glutamine, and 10 mM glucose at 37^0C in the non-CO2 incubator. Assay was performed for five independent organoid generation rounds, using 6-8 organoids per cell line and condition in each assay run. Results were normalized to the size factor. The size factor for day 30-old organoids for each cell line and condition was determined as a mean of random 20 organoids from five independent organoid generation rounds. The area of organoids was measured using the Cytation5M cell imaging reader. Data were analyzed with the Seahorse Wave Desktop software (Agilent). Wells with aberrant OCR patterns were excluded from each of the individual experiments.

Stable isotope tracing

Cell culture media was prepared in DMEM w/o glucose (Themor Fisher Scientific, cat.no. A1443001) and Neuobasal A w/o glucose (Thermo Fisher Scientific, cat.no. A2477501). Glucose ^{13}C stable isotope tracer (Eurisotop, cat.no.CLM-1396) was added to the media to a final concentration of 21.25mM. 30 days old, non-embedded organoids were incubated in a tracer

medium for 24h. Eight organoids per cell line and condition were pulled to perform metabolite extraction. Collected samples were first washed with DPBS and then resuspended in ice-cold extraction solvent (50% MeOH, 30% ACN, 20% H2O). Samples were incubated in a thermo shaker at 4°C for 5 min and then centrifuged at full speed at 4°C for 10 min. 70µl of supernatant was transferred into LC-MS vials and stored at -80°C until the analysis.

Reactive oxygen species detection with fluorescence-activated cell sorting

To quantitatively determine cytoplasmic ROS levels in live cells, 4-5 non-embedded organoids at day 30 of organoid culture were pulled per sample and dissociated using Accuatse (Sigma, cat.no. A6964). Samples were first incubated with Accutase for one hour at 37^0C under dynamic conditions, following trituration with a 1000 or 200 µl pipette (depending on organoid size) to support organoid dissociation into single cells. Reducing incubation time to 30 min, these steps were repeated until organoids were fully dissociated. Each sample then was split into two 2ml Eppendorf tubes as technical replicates for the assay. Samples were centrifuged for 3 min at 500 g and Accutase was replaced with 500ul assay medium containing 2µM 2',7' –dichlorofluorescein diacetate (DCFDA) (Thermo Fisher Scientific, cat.no. D399) and 1:1000 live-dead stain Zombie NIR (Biolegend, cat.no. 423106) in DPBS (Thermo Fisher Scientific, cat.no. 14190250). Cells were incubated with the assay media containing the fluorescent dyes for 20 min at 37^0C. Samples were then run on BD LSRFortessa flow cytometer, acquiring 10,000 single-cell events (DCFDA+, live cells) per sample. Fluorescence intensity was analyzed with FlowJo software (v.10.7.2). Data of two technical replicates per sample were averaged and the percentage of positive cells to the DCFDA staining was batch normalized to the mean percentage of the batch.

FACS-based glucose uptake assay using a 2-NBDG probe

Glucose uptake was measured using fluorescently tagged, non-metabolizable glucose analogue 2-(N-(7-nitrobenz-2-oxa-1,3-diazol-4-yl) amino)-2-deoxyglucose (2-NBDG) (Thermo Fisher Scientific, cat.no. 11569116). Samples were prepared as described in the section: *Reactive oxygen species (ROS) detection with fluorescence-activated cell sorting (FACS).* Cells were incubated for 30 min at 37^0C with 1:500 2-NBDG and 1:1000 live-dead stain Zombie NIR (Biolegend, cat.no. 423106) in cell culture media with either high or low insulin concentration. Samples were run on BD LSRFortessa flow cytometer, acquiring 10,000 single-cell events (2-NBDG+, live cells) per sample. Fluorescence intensity was analyzed with FlowJo software (v.10.7.2). Data of two technical replicates per sample were averaged and the fluorescence intensity was batch normalized to the IR condition.

Lipidomics

Lipidomics analysis was performed by Lipometrix (http://www.lipometrix.be) using HILIC LC-MS/MS. Samples were prepared as a pool of eight non-embedded organoids per cell and per condition from four independent organoid generation rounds. Samples were collected on day 30 of organoid culture, washed once with ice-cold PBS, snap-frozen with liquid nitrogen and stored at -80°C until the analysis. The concentration of detected lipid species was normalized to DNA content. Statistical significance for lipids of interest was determined using paired Wilcoxon signed-rank, two-sided test. Principal component analysis was performed using the factoextra package (v.1.0.7) in R (v.4.2.2).

Dopamine ELISA

Extracellular dopamine concentration was measured with Dopamine ELISA (Immusmol, cat no. BA-E-5300R) following the manufacturer's instructions. Dopamine ELISA was performed using a 750 µl volume of a sample. Each sample was a pull of 400 µl of supernatant from three embedded midbrain organoids, collected at day 60 of organoid culture, 72 hours after the last media change. Samples were collected from three independent organoid generation rounds. Final dopamine concentration (nmol/l) was normalized to the mean nuclei count determined during the high-content imaging workflow from randomly selected three organoid sections per cell line and condition. Normalized results were batch-corrected against WT organoid mean values.

Data analysis and statistics

If not stated otherwise, data were analyzed and visualized in GraphPad Prism (v.9.5.1) or R software (v.4.2.2). All data were batch normalized for every experiment. For comparisons between IR and IS samples, for data not normally distributed, statistical significance was tested with a non-parametric, two-tailed Wilcoxon matched-pairs signed rank test. For normally distributed data, statistical significance was tested with tested using a two-tailed, paired t-test. Data normality was tested with the Shapiro-Wilk normality test. For samples comparing multiple groups, statistical significance was determined using the Kruskal-Wallis test. Significance asterisks represent $P<0.05$ *, $P<0.01$ **, $P<0.001$ ***, $P<0.0001$ ****. Error bars represent mean + SD.

Acknowledgements

This work was mainly supported by the internal flagship project at the Luxembourg Centre for Systems Biomedicine and by the Luxembourg National Research Fund CORE grant to GA (C21/BM/15850547/PINK1-DiaPDs). Further, we acknowledge support from the National Centre of Excellence in Research on Parkinson's Disease (NCER-PD) which is funded by the Luxembourg National Research Fund (FNR/NCER13/BM/11264123). We thank Dr. Sarah Nickels and Dr. Isabel Rosety for the characterization of iPSCs and the derivation of NESCs. Also, we would like to thank Prof. Dr. Rudi Balling for the valuable ideas, which inspired this project.

Author Contributions

A.Z. designed experiments, analyzed and interpreted data, prepared figures, and wrote the original draft. J.K. analyzed metabolic models. C.A. and A.V. carried out Western Blot experiments. D.F. carried out the mounting of stained organoid sections. D.F. performed local field potential recordings and data analysis. G.A. and G.G.G. designed experiments, reviewed, and edited the manuscript. C.J. performed a GC-MS metabolomics experiment. L.N. and M.J. supervised the C13 glucose tracing experiment and performed data processing and analysis. P.A. supervised high-content imaging workflow. R.H. performed RNA sequencing. E.G. performed RNA sequencing data processing and analysis. E.S. supervised the metabolic modeling part, reviewed, and edited the manuscript. A.H. and M.O. performed PBM. R.K. reviewed and edited the manuscript. J.C.S. conceived and supervised the project and edited the manuscript.

Declaration of Interests

JCS is a co-inventor on a patent covering the generation of the here-described midbrain organoids (WO2017060884A1). Furthermore, JCS is a co-founder and shareholder of the company OrganoTherapeutics which makes use of midbrain organoid technology.
The other authors declare no competing interests.

References

1. Z. Ou *et al.*, Global Trends in the Incidence, Prevalence, and Years Lived With Disability of Parkinson's Disease in 204 Countries/Territories From 1990 to 2019. *Front Public Health* **9**, 776847 (2021).
2. D. K. Simon, C. M. Tanner, P. Brundin, Parkinson Disease Epidemiology, Pathology, Genetics, and Pathophysiology. *Clin Geriatr Med* **36**, 1-12 (2020).
3. X. Yue *et al.*, Risk of Parkinson Disease in Diabetes Mellitus: An Updated Meta-Analysis of Population-Based Cohort Studies. *Medicine (Baltimore)* **95**, e3549 (2016).
4. E. De Pablo-Fernandez, R. Goldacre, J. Pakpoor, A. J. Noyce, T. T. Warner, Association between diabetes and subsequent Parkinson disease: A record-linkage cohort study. *Neurology* **91**, e139-e142 (2018).
5. J. L. Y. Cheong, E. de Pablo-Fernandez, T. Foltynie, A. J. Noyce, The Association Between Type 2 Diabetes Mellitus and Parkinson's Disease. *J Parkinsons Dis* **10**, 775-789 (2020).
6. D. Athauda *et al.*, The Impact of Type 2 Diabetes in Parkinson's Disease. *Mov Disord* **37**, 1612-1623 (2022).
7. J. Park, S. Choi, R. Kim, Association between prediabetes and cognitive function in Parkinson's disease. *Brain Behav* **13**, e2838 (2023).
8. J. D. Barter *et al.*, Parkinson's Disease and Diabetes Mellitus: Individual and Combined Effects on Motor, Cognitive, and Psychosocial Functions. *Healthcare (Basel)* **11** (2023).
9. N. I. Bohnen *et al.*, Diabetes mellitus is independently associated with more severe cognitive impairment in Parkinson disease. *Parkinsonism Relat Disord* **20**, 1394-1398 (2014).
10. C. M. Labandeira *et al.*, Parkinson's disease and diabetes mellitus: common mechanisms and treatment repurposing. *Neural Regen Res* **17**, 1652-1658 (2022).
11. S. S. Sabari *et al.*, Type 2 Diabetes (T2DM) and Parkinson's Disease (PD): a Mechanistic Approach. *Mol Neurobiol* 10.1007/s12035-023-03359-y, 1-27 (2023).
12. B. Knusel, P. P. Michel, J. S. Schwaber, F. Hefti, Selective and nonselective stimulation of central cholinergic and dopaminergic development in vitro by nerve growth factor, basic fibroblast growth factor, epidermal growth factor, insulin and the insulin-like growth factors I and II. *J Neurosci* **10**, 558-570 (1990).
13. R. J. Schulingkamp, T. C. Pagano, D. Hung, R. B. Raffa, Insulin receptors and insulin action in the brain: review and clinical implications. *Neurosci Biobehav Rev* **24**, 855-872 (2000).
14. E. Hogg *et al.*, High Prevalence of Undiagnosed Insulin Resistance in Non-Diabetic Subjects with Parkinson's Disease. *J Parkinsons Dis* **8**, 259-265 (2018).
15. K. V. Doan *et al.*, FoxO1 in dopaminergic neurons regulates energy homeostasis and targets tyrosine hydroxylase. *Nat Commun* **7**, 12733 (2016).
16. A. J. Garcia-Yague, I. Lastres-Becker, L. Stefanis, D. K. Vassilatis, A. Cuadrado, alpha-Synuclein Induces the GSK-3-Mediated Phosphorylation and Degradation of NURR1 and Loss of Dopaminergic Hallmarks. *Mol Neurobiol* **58**, 6697-6711 (2021).
17. J. Su *et al.*, PI3K polymorphism in patients with sporadic Parkinson's disease. *Medicine (Baltimore)* **101**, e32349 (2022).

18. E. Pino *et al.*, FOXO3 determines the accumulation of alpha-synuclein and controls the fate of dopaminergic neurons in the substantia nigra. *Hum Mol Genet* **23**, 1435-1452 (2014).
19. V. Oli, R. Gupta, P. Kumar, FOXO and related transcription factors binding elements in the regulation of neurodegenerative disorders. *J Chem Neuroanat* **116**, 102012 (2021).
20. A. Dumitriu *et al.*, Gene expression profiles in Parkinson disease prefrontal cortex implicate FOXO1 and genes under its transcriptional regulation. *PLoS Genet* **8**, e1002794 (2012).
21. A. E. Webb, A. Kundaje, A. Brunet, Characterization of the direct targets of FOXO transcription factors throughout evolution. *Aging Cell* **15**, 673-685 (2016).
22. R. Brauer *et al.*, Diabetes medications and risk of Parkinson's disease: a cohort study of patients with diabetes. *Brain* **143**, 3067-3076 (2020).
23. X. Qin *et al.*, Association Between Diabetes Medications and the Risk of Parkinson's Disease: A Systematic Review and Meta-Analysis. *Front Neurol* **12**, 678649 (2021).
24. H. Zhao *et al.*, Thiazolidinedione use and risk of Parkinson's disease in patients with type 2 diabetes mellitus. *NPJ Parkinsons Dis* **8**, 138 (2022).
25. K. H. Huang, Y. L. Chang, S. Y. Gau, T. H. Tsai, C. Y. Lee, Dose-Response Association of Metformin with Parkinson's Disease Odds in Type 2 Diabetes Mellitus. *Pharmaceutics* **14** (2022).
26. D. Athauda *et al.*, Exenatide once weekly versus placebo in Parkinson's disease: a randomised, double-blind, placebo-controlled trial. *Lancet* **390**, 1664-1675 (2017).
27. N. E. T. i. P. D. F.-Z. Investigators, Pioglitazone in early Parkinson's disease: a phase 2, multicentre, double-blind, randomised trial. *Lancet Neurol* **14**, 795-803 (2015).
28. Anonymous, <SSRN-id4212371.pdf>.
29. L. Chen, Y. Tao, J. Li, M. Kang, Pioglitazone use is associated with reduced risk of Parkinson's disease in patients with diabetes: A systematic review and meta-analysis. *J Clin Neurosci* **106**, 154-158 (2022).
30. Anonymous, <wallum1987.pdf>.
31. S. L. C. Geijselaers *et al.*, Association of Cerebrospinal Fluid (CSF) Insulin with Cognitive Performance and CSF Biomarkers of Alzheimer's Disease. *J Alzheimers Dis* **61**, 309-320 (2018).
32. C. B. Newgard *et al.*, A branched-chain amino acid-related metabolic signature that differentiates obese and lean humans and contributes to insulin resistance. *Cell Metab* **9**, 311-326 (2009).
33. B. C. Batch *et al.*, Branched chain amino acids are novel biomarkers for discrimination of metabolic wellness. *Metabolism* **62**, 961-969 (2013).
34. E. Brunk *et al.*, Recon3D enables a three-dimensional view of gene variation in human metabolism. *Nat Biotechnol* **36**, 272-281 (2018).
35. M. P. Pacheco *et al.*, Identifying and targeting cancer-specific metabolism with network-based drug target prediction. *EBioMedicine* **43**, 98-106 (2019).
36. D. C. Pant, S. Aguilera-Albesa, A. Pujol, Ceramide signalling in inherited and multifactorial brain metabolic diseases. *Neurobiol Dis* **143**, 105014 (2020).
37. M. Kanehisa, Y. Sato, M. Kawashima, M. Furumichi, M. Tanabe, KEGG as a reference resource for gene and protein annotation. *Nucleic Acids Res* **44**, D457-462 (2016).
38. A. Jo *et al.*, PARIS farnesylation prevents neurodegeneration in models of Parkinson's disease. *Sci Transl Med* **13** (2021).

39. M. A. B. Khan *et al.*, Epidemiology of Type 2 Diabetes - Global Burden of Disease and Forecasted Trends. *J Epidemiol Glob Health* **10**, 107-111 (2020).
40. H. Sun *et al.*, IDF Diabetes Atlas: Global, regional and country-level diabetes prevalence estimates for 2021 and projections for 2045. *Diabetes Res Clin Pract* **183**, 109119 (2022).
41. E. C. McNay, A. K. Recknagel, Brain insulin signaling: a key component of cognitive processes and a potential basis for cognitive impairment in type 2 diabetes. *Neurobiol Learn Mem* **96**, 432-442 (2011).
42. G. Capo Rangel, J. Prezioso, L. Gerardo-Giorda, E. Somersalo, D. Calvetti, Brain energetics plays a key role in the coordination of electrophysiology, metabolism and hemodynamics: Evidence from an integrated computational model. *J Theor Biol* **478**, 26-39 (2019).
43. C. M. Diaz-Garcia *et al.*, The distinct roles of calcium in rapid control of neuronal glycolysis and the tricarboxylic acid cycle. *Elife* **10** (2021).
44. G. Ashrafi, Z. Wu, R. J. Farrell, T. A. Ryan, GLUT4 Mobilization Supports Energetic Demands of Active Synapses. *Neuron* **93**, 606-615 e603 (2017).
45. S. El Messari *et al.*, Immunocytochemical localization of the insulin-responsive glucose transporter 4 (Glut4) in the rat central nervous system. *J Comp Neurol* **399**, 492-512 (1998).
46. A. P. Gomes *et al.*, Declining NAD(+) induces a pseudohypoxic state disrupting nuclear-mitochondrial communication during aging. *Cell* **155**, 1624-1638 (2013).
47. A. O. Odegaard *et al.*, Oxidative stress, inflammation, endothelial dysfunction and incidence of type 2 diabetes. *Cardiovasc Diabetol* **15**, 51 (2016).
48. C. Galvagnion *et al.*, Sphingolipid changes in Parkinson L444P GBA mutation fibroblasts promote alpha-synuclein aggregation. *Brain* **145**, 1038-1051 (2022).
49. A. Navarro-Romero *et al.*, Lysosomal lipid alterations caused by glucocerebrosidase deficiency promote lysosomal dysfunction, chaperone-mediated-autophagy deficiency, and alpha-synuclein pathology. *NPJ Parkinsons Dis* **8**, 126 (2022).
50. S. D. Spassieva *et al.*, Ectopic expression of ceramide synthase 2 in neurons suppresses neurodegeneration induced by ceramide synthase 1 deficiency. *Proc Natl Acad Sci U S A* **113**, 5928-5933 (2016).
51. G. R. Phillips *et al.*, Cholesteryl ester levels are elevated in the caudate and putamen of Huntington's disease patients. *Sci Rep* **10**, 20314 (2020).
52. R. van der Kant *et al.*, Cholesterol Metabolism Is a Druggable Axis that Independently Regulates Tau and Amyloid-beta in iPSC-Derived Alzheimer's Disease Neurons. *Cell Stem Cell* **24**, 363-375 e369 (2019).
53. P. Garcia-Sanz *et al.*, N370S-GBA1 mutation causes lysosomal cholesterol accumulation in Parkinson's disease. *Mov Disord* **32**, 1409-1422 (2017).
54. M. Iljina *et al.*, Arachidonic acid mediates the formation of abundant alpha-helical multimers of alpha-synuclein. *Sci Rep* **6**, 33928 (2016).
55. Y. Qu, H. L. Zhang, X. P. Zhang, H. L. Jiang, Arachidonic acid attenuates brain damage in a rat model of ischemia/reperfusion by inhibiting inflammatory response and oxidative stress. *Hum Exp Toxicol* **37**, 135-141 (2018).
56. J. Zhang *et al.*, Targeted fatty acid metabolomics to discover Parkinson's disease associated metabolic alteration. *J Mass Spectrom* **56**, e4781 (2021).
57. I. Pernicova, M. Korbonits, Metformin--mode of action and clinical implications for diabetes and cancer. *Nat Rev Endocrinol* **10**, 143-156 (2014).

58. M. J. Reginato, M. A. Lazar, Mechanisms by which Thiazolidinediones Enhance Insulin Action. *Trends Endocrinol Metab* **10**, 9-13 (1999).
59. P. Reinhardt *et al.*, Derivation and expansion using only small molecules of human neural progenitors for neurodegenerative disease modeling. *PLoS One* **8**, e59252 (2013).
60. A. S. Monzel *et al.*, Derivation of Human Midbrain-Specific Organoids from Neuroepithelial Stem Cells. *Stem Cell Reports* **8**, 1144-1154 (2017).
61. S. L. Nickels *et al.*, Reproducible generation of human midbrain organoids for in vitro modeling of Parkinson's disease. *Stem Cell Res* **46**, 101870 (2020).
62. A. Zagare, M. Gobin, A. S. Monzel, J. C. Schwamborn, A robust protocol for the generation of human midbrain organoids. *STAR Protoc* **2**, 100524 (2021).
63. S. E. Harrison, B. Sozen, M. Zernicka-Goetz, In vitro generation of mouse polarized embryo-like structures from embryonic and trophoblast stem cells. *Nat Protoc* **13**, 1586-1602 (2018).
64. J. Modamio *et al.*, 10.1101/2021.07.15.452499 (2021).
65. K. Hiller *et al.*, MetaboliteDetector: comprehensive analysis tool for targeted and nontargeted GC/MS based metabolome analysis. *Anal Chem* **81**, 3429-3439 (2009).
66. S. Bolognin *et al.*, 3D Cultures of Parkinson's Disease-Specific Dopaminergic Neurons for High Content Phenotyping and Drug Testing. *Adv Sci (Weinh)* **6**, 1800927 (2019).
67. A. S. Monzel *et al.*, Machine learning-assisted neurotoxicity prediction in human midbrain organoids. *Parkinsonism Relat Disord* **75**, 105-109 (2020).
68. Y. Liao, G. K. Smyth, W. Shi, The R package Rsubread is easier, faster, cheaper and better for alignment and quantification of RNA sequencing reads. *Nucleic Acids Res* **47**, e47 (2019).
69. M. I. Love, W. Huber, S. Anders, Moderated estimation of fold change and dispersion for RNA-seq data with DESeq2. *Genome Biol* **15**, 550 (2014).
70. M. D. Robinson, D. J. McCarthy, G. K. Smyth, edgeR: a Bioconductor package for differential expression analysis of digital gene expression data. *Bioinformatics* **26**, 139-140 (2010).
71. Anonymous, <benjamini1995.pdf>.
72. J. R. Conway, A. Lex, N. Gehlenborg, UpSetR: an R package for the visualization of intersecting sets and their properties. *Bioinformatics* **33**, 2938-2940 (2017).
73. G. Yu, L. G. Wang, Y. Han, Q. Y. He, clusterProfiler: an R package for comparing biological themes among gene clusters. *OMICS* **16**, 284-287 (2012).
74. L. Heirendt *et al.*, Creation and analysis of biochemical constraint-based models using the COBRA Toolbox v.3.0. *Nat Protoc* **14**, 639-702 (2019).
75. W. T. Norton, T. Abe, S. E. Poduslo, G. H. DeVries, The lipid composition of isolated brain cells and axons. *J Neurosci Res* **1**, 57-75 (1975).
76. G. Stoll *et al.*, MaBoSS 2.0: an environment for stochastic Boolean modeling. *Bioinformatics* **33**, 2226-2228 (2017).
77. A. A. Hemedan, R. Schneider, M. Ostaszewski, Applications of Boolean modeling to study the dynamics of a complex disease and therapeutics responses. *Front Bioinform* **3**, 1189723 (2023).
78. A. A. Hemedan, A. Niarakis, R. Schneider, M. Ostaszewski, Boolean modelling as a logic-based dynamic approach in systems medicine. *Comput Struct Biotechnol J* **20**, 3161-3172 (2022).

79. A. Montagud *et al.*, Patient-specific Boolean models of signaling networks guide personalised treatments. *Elife* **11** (2022).

Figure Legends

Figure 1. Modification of cell culture media activates insulin signaling

A) Representative image of midbrain organoid generation and cell culture media conditions.

B) Insulin concentration in standard media and self-made N2 media measured in fresh media (0h) and after three days of incubation with cells (72h). Scale bars 200µm.

C) Representative image of WB and quantification of IRS1 levels relative to the housekeeping β-actin. Statistical significance was determined with two-tailed, match-pairs signed ranked Wilcoxon test (*P*<0.05 *, *P* <0.01 **, *P* <0.001 ***, *P* <0.0001 ****). Error bars represent mean + SD. n (IR) =9, n (IS) =9

D) Representative image of WB and quantification of AKT1 levels relative to the housekeeping β-actin. Statistical significance was determined with two-tailed, match-pairs signed ranked Wilcoxon test (*P*<0.05 *, *P* <0.01 **, *P* <0.001 ***, *P* <0.0001 ****). Error bars represent mean + SD. n (IR) =9, n (IS) =9

E) Representative image of WB and quantification of AKT1 pSer73 levels after acute stimulation with 100nM of insulin in IR samples, relative to the total AKT levels. Statistical significance was determined with two-tailed, match-pairs signed ranked Wilcoxon test (*P*<0.05 *, *P* <0.01 **, *P* <0.001 ***, *P* <0.0001 ****). Error bars represent mean + SD. n (IR) =9, n (IS) =9

F) Representative image of WB and quantification of AKT1 pSer73 after acute stimulation with 100nM of insulin in IS samples, relative to the total AKT levels. Statistical significance was determined with two-tailed, match-pairs signed ranked Wilcoxon test (*P*<0.05 *, *P* <0.01 **, *P* <0.001 ***, *P* <0.0001 ****). Error bars represent mean + SD. n (IR) =9, n (IS) =9

G) Relative abundance of branched amino acids – Valine, Leucine, and Isoleucine, detected by LC-MS in midbrain organoid supernatant after 72h incubation with organoid. Statistical significance was determined with a two-tailed, paired t-test (*P*<0.05 *, *P* <0.01 **, *P* <0.001 ***, *P* <0.0001 ****). n (IR) =9, n (IS) =9

H) Relative abundance of glucose, detected by LC-MS in midbrain organoid supernatant after 72h incubation with organoid. Statistical significance was determined with a two-tailed, paired t-test (*P*<0.05 *, *P* <0.01 **, *P* <0.001 ***, *P* <0.0001 ****). n (IR) =9, n (IS) =9

Figure 2. Insulin sensitivity increases dopaminergic neuron amount and midbrain organoid functionality

A) Representative immunofluorescent images of TH and MAP2 staining of 60 days old midbrain organoids. Scale bars 100µm.

B) Quantification of TH positive area normalized to the Hoechst area in immunofluorescent stainings of 30 and 60 days old midbrain organoids. Statistical significance was determined with a two-tailed Wilcoxon test (*P*<0.05 *, *P* <0.01 **, *P* <0.001 ***, *P* <0.0001 ****). D30: n (IR) =28, n (IS) =27; D60: n (IR) =29, n (IS) =29

C) Extracellular dopamine levels measured in spent media of 60 days old midbrain organoids. Statistical significance was determined with a two-tailed Wilcoxon test (*P*<0.05 *, *P* <0.01 **, *P* <0.001 ***, *P* <0.0001 ****). n (IR) =12, n (IS) =12

D) Representative image of organoid placed on electrodes in a well of the multielectrode plate. Scale bar 200µm.

E) Mean firing rate of 30 and 60 days old midbrain organoids Recording time-5min. Statistical significance was determined with a two-tailed Wilcoxon test (*P*<0.05 *, *P* <0.01 **, *P* <0.001 ***, *P* <0.0001 ****). D30: n (IR) =7, n (IS) =11; D60: n (IR) =9, n (IS) =12

F) Representative image of local field potential recording of spontaneous firing in midbrain organoids at day 30.

G) Quantification of spikes per time of recording (5min) for day 30 and day 60 old organoids. statistical significance was determined with Mann–Whitney t-test (*P*<0.05 *, *P* <0.01 **, *P* <0.001 ***, *P* <0.0001 ****). Error bars represent mean + SD. D30: n (IR) =40, n (IS) =46; D60: n (IR) =34, n (IS) =33

H) Quantification of spikes duration in seconds for day 30 and day 60 old organoids. statistical significance was determined with Mann–Whitney t-test (*P*<0.05 *, *P* <0.01 **, *P* <0.001 ***, *P* <0.0001 ****). Error bars represent mean + SD. D30: n (IR) =40, n (IS) =46; D60: n (IR) =34, n (IS) =33

I) Representative image of local field potential recording of burst firing in midbrain organoids at day 60.

J) Quantification of bursts per time of recording (5min) for day 30 and day 60 old organoids. statistical significance was determined with Mann–Whitney t-test (*P*<0.05 *, *P* <0.01 **, *P* <0.001 ***, *P* <0.0001 ****). Error bars represent mean + SD. D30: n (IR) =32, n (IS) =38; D60: n (IR) =31, n (IS) =30

K) Quantification of inter-burst interval in seconds for day 30 and day 60 old organoids. statistical significance was determined with Mann–Whitney t-test (P<0.05 *, P <0.01 **, P <0.001 ***, P <0.0001 ****). Error bars represent mean + SD. D30: n (IR) =31, n (IS) =38; D60: n (IR) =31, n (IS) =30

Figure 3. Insulin resistance-mediated lipid alterations

A) Prediction of the most dysregulated metabolic pathways in the IR model based on model composition analysis. The size of a dot represents the number of reactions different between models. The location on the x-axis represents the percentage of reactions different from the total reaction number per subsystem in Recon3. Highlighted subsystems belong to lipid metabolism.

B) PCA scores plot of lipidomics analysis, demonstrating the percentage of variation between IR and IS sample lipidomic profiles, explained by the first and second components.

C) Correlation plot, demonstrating feature (individual lipid class) correlation across the samples and contribution to the variance between the conditions.

D) Quantification of Cholesterol esters. Concentration normalized to the mgDNA. Statistical significance was determined with two-tailed, match-pairs signed ranked Wilcoxon test (P<0.05 *, P <0.01 **, P <0.001 ***, P <0.0001 ****). n (IR) =12, n (IS) =12

E) Quantification of 1-alkenyl,2-acylphospatidylcholine. Concentration normalized to the mgDNA. Statistical significance was determined with two-tailed, match-pairs signed ranked Wilcoxon test (P<0.05 *, P <0.01 **, P <0.001 ***, P <0.0001 ****). n (IR) =12, n (IS) =12

F) Unsupervised clustering of the most significantly differentially abundant lipid species derived from 20-carbon arachidonic or eicosanoid acid.

G) Prediction of metabolic pathway performance by flux variability analysis (FVA).

H) Fatty acid dependency measurements obtained using Seahorse assay.

I) Quantification of the percentage of fatty acid oxidation from the total fuel oxidation. Results normalized to the size of organoids. Statistical significance was tested using paired two-tailed t-test. Error bars represent mean + SD. n (IR) =4, n (IS) =4

Figure 4. Insulin resistance compromises ATP levels and glycolysis efficiency

A) Prediction of ATP production by IR and IS model following *in silico* inhibition of mitochondrial complexes present in the model and glucose uptake inhibition.

B) Intracellular ATP measurement for organoids at day 30 of organoid culture. Statistical significance was determined with a two-tailed, match-pairs signed ranked Wilcoxon test (*P*<0.05 *, *P* <0.01 **, *P* <0.001 ***, *P* <0.0001 ****). Error bars represent mean + SD. n (IR) =15, n (IS) =15

C) Intracellular ATP measurement for organoids at day 60 of organoid culture. Statistical significance was determined with a two-tailed, match-pairs signed ranked Wilcoxon test (*P*<0.05 *, *P* <0.01 **, *P* <0.001 ***, *P* <0.0001 ****). Error bars represent mean + SD. n (IR) =15, n (IS) =15

D) Fractional abundance of glycolysis and TCA metabolites derived from 13C labelled glucose. Statistical significance was determined with a two-tailed, match-pairs signed ranked Wilcoxon test (*P*<0.05 *, *P* <0.01 **, *P* <0.001 ***, *P* <0.0001 ****). Error bars represent mean + SD. n (IR) =6, n (IS) =6

E) Quantification of Serine derived from 13C labelled glucose. Statistical significance was determined with a two-tailed, paired t-test (*P*<0.05 *, *P* <0.01 **, *P* <0.001 ***, *P* <0.0001 ****). Error bars represent mean + SD. n (IR) =6, n (IS) =6

F) Quantification of Ribose 5-phosphate derived from 13C labelled glucose. Statistical significance was determined with a two-tailed, paired t-test (*P*<0.05 *, *P* <0.01 **, *P* <0.001 ***, *P* <0.0001 ****). Error bars represent mean + SD. n (IR) =6, n (IS) =6

G) The ratio of total and reduced NAD. Statistical significance was determined with a two-tailed, paired t-test (*P*<0.05 *, *P* <0.01 **, *P* <0.001 ***, *P* <0.0001 ****). Error bars represent mean + SD. n (IR) =6, n (IS) =6

H) Flow cytometry representative histograms, showing DCFDA positive (FITC-A+) fraction of cells in IR and IS condition.

I) Quantification of live cells positive to DCFDA (FITC-A) fluorescent signal. Statistical significance was determined with a two-tailed, paired t-test (*P*<0.05 *, *P* <0.01 **, *P* <0.001 ***, *P* <0.0001 ****). Error bars represent mean + SD. n (IR) =9, n (IS) =9

Figure 5. GBA-PD organoids show dopaminergic neuron loss and altered lipid profile

A) Representative immunofluorescent images of MAP2 and TH staining in 60 days old midbrain organoids. Scale bars: 100µm.

B) Quantification of TH positive area normalized to the Hoechst area in immunofluorescent stainings of 60 days old midbrain organoids. Statistical significance was determined with the

Kruskal-Wallis test (*P*<0.05 *, *P* <0.01 **, *P* <0.001 ***, *P* <0.0001 ****). n (IR,WT) = 22; n (IR,GBA) = 27; n (IS,GBA) = 26

C) Extracellular dopamine levels measured in spent media of 60 days old midbrain organoids. Statistical significance was determined with the Kruskal-Wallis test (*P*<0.05 *, *P* <0.01 **, *P* <0.001 ***, *P* <0.0001 ****). Error bars represent mean + SD. n (IR,WT) = 12; n (IR,GBA) = 9; n (IS,GBA) = 9

D) Representative immunofluorescent images of Tunel staining in 60 days old midbrain organoids. Scale bars: 100µm.

E) Quantification of Tunel positive area normalized to the Hoechst area in immunofluorescent stainings of 60 days old midbrain organoids. Statistical significance was determined with the Kruskal-Wallis test (*P*<0.05 *, *P* <0.01 **, *P* <0.001 ***, *P* <0.0001 ****). n (IR,WT) = 23; n (IR,GBA) = 27; n (IS,GBA) = 27

F) Quantification of Cholesterol esters. Concentration normalized to the mgDNA. Statistical significance was determined with the Kruskal-Wallis test (*P*<0.05 *, *P* <0.01 **, *P* <0.001 ***, *P* <0.0001 ****). n (IR,WT) = 12; n (IS,WT) = 12; n (IR,GBA) = 9; n (IS,GBA) = 9

G) Quantification of 1-alkenyl,2-acylphosphatidylcholine. Concentration normalized to the mgDNA. Statistical significance was determined with the Kruskal-Wallis test (*P*<0.05 *, *P* <0.01 **, *P* <0.001 ***, *P* <0.0001 ****). n (IR,WT) = 12; n (IS,WT) = 12; n (IR,GBA) = 9; n (IS,GBA) = 9

H) The relative concentration of the sum of Ceramide and Hexosylceramide species sharing the same carbon number expressed as log2 fold change (FC) in GBA-PD samples against IR,WT samples. n (IR,WT) = 12; n (IS,WT) = 12; n (IR,GBA) = 9; n (IS,GBA) = 9

Figure 6. Transcriptome analysis of GBA-PD midbrain organoids

A) Unsupervised clustering of insulin signaling genes between IR,GBA and IR,WT midbrain organoids. Gene expression normalized using Z-score transformation.

B) UpSet plot demonstrating the number of unique differentially expressed genes (p.adjust<0.05) found in each comparison.

C) Gene enrichment analysis of the selected specific genes.

D) Volcano plot of a set of FOXO1 target gene expression in IR,GBA vs IR,WT midbrain organoids.

E) A probabilistic Boolean model with defined perturbations: AKT off and FOXO1 on, demonstrating dynamic behaviour of downstream effects associated with PD (axis-Y) over the number of iterations (axis-X).

Figure 7. Rescue experiments of GBA-PD associated phenotypes using anti-diabetic drugs

A) Representative image of organoid treatment strategy with ASOs, Pioglitazone and Metformin.

B) Representative immunofluorescent images of MAP2, TH and Tunel staining in 60 days old GBA-PD midbrain organoids treated with negative control (NC), and ASO targeting FOXO1 transcript (FOXO1-ASO). Scale bars: 100µm.

C) Quantification of TH positive area normalized to the Hoechst area in immunofluorescent stainings of 60 days old GBA-PD midbrain organoids treated with negative control (NC), and ASO targeting FOXO1 transcript. n (IR,WT) = 22; n (IR,GBA) = 27; n (NC,GBA) = 20; n (ASO,GBA) = 29

D) Extracellular dopamine levels measured in spent media of 60 days old GBA-PD midbrain organoids treated with negative control (NC), and ASO targeting FOXO1 transcript. n (IR,WT) = 12; n (IR,GBA) = 9; n (NC,GBA) = 9; n (ASO,GBA) = 9

E) Quantification of Tunel positive area normalized to the Hoechst area in immunofluorescent stainings of 60 days old GBA-PD midbrain organoids treated with negative control (NC), and ASO targeting FOXO1 transcript. n (IR,WT) = 23; n (IR,GBA) = 27; n (NC,GBA) = 21; n (ASO,GBA) = 26

F) Quantification of TH positive area normalized to the Hoechst area in immunofluorescent stainings of 60 days old GBA-PD midbrain organoids treated with vehicle (DMSO), and Pioglitazone (Piogl). n (IR,WT) = 22; n (IR,GBA) = 27; n (DMSO,GBA) = 22; n (Piogl,GBA) = 23

G) Extracellular dopamine levels measured in spent media of 60 days old GBA-PD midbrain organoids treated with vehicle (DMSO), and Pioglitazone (Piogl). n (IR,WT) = 12; n (IR,GBA) = 9; n (DMSO,GBA) = 9; n (Piogl,GBA) = 9

H) Quantification of Tunel positive area normalized to the Hoechst area in immunofluorescent stainings of 60 days old GBA-PD midbrain organoids treated with vehicle (DMSO), and Pioglitazone (Piogl). n (IR,WT) = 23; n (IR,GBA) = 27; n (DMSO,GBA) = 25; n (Piogl,GBA) = 23

I) Quantification of TH positive area normalized to the Hoechst area in immunofluorescent stainings of 60 days old GBA-PD midbrain organoids treated with vehicle (PBS), and Metformin (Metfl). n (IR,WT) = 22; n (IR,GBA) = 27; n (PBS,GBA) = 20; n (Metf,GBA) = 32

J) Extracellular dopamine levels measured in spent media of 60 days old GBA-PD midbrain organoids treated with vehicle (PBS), and Metformin (Metf). n (IR,WT) = 12; n (IR,GBA) = 9; n (PBS,GBA) = 9; n (Metf,GBA) = 9

K) Quantification of Tunel positive area normalized to the Hoechst area in immunofluorescent stainings of 60 days old GBA-PD midbrain organoids treated with vehicle (PBS), and Metformin (Metfl). n (IR,WT) = 23; n (IR,GBA) = 27; n (PBS,GBA) = 22; n (Metf,GBA) = 32

For panels C-K, statistical significance was determined with the Kruskal-Wallis test (*P*<0.05 *, *P* <0.01 **, *P* <0.001 ***, *P* <0.0001 ****). Error bars represent mean + SD.

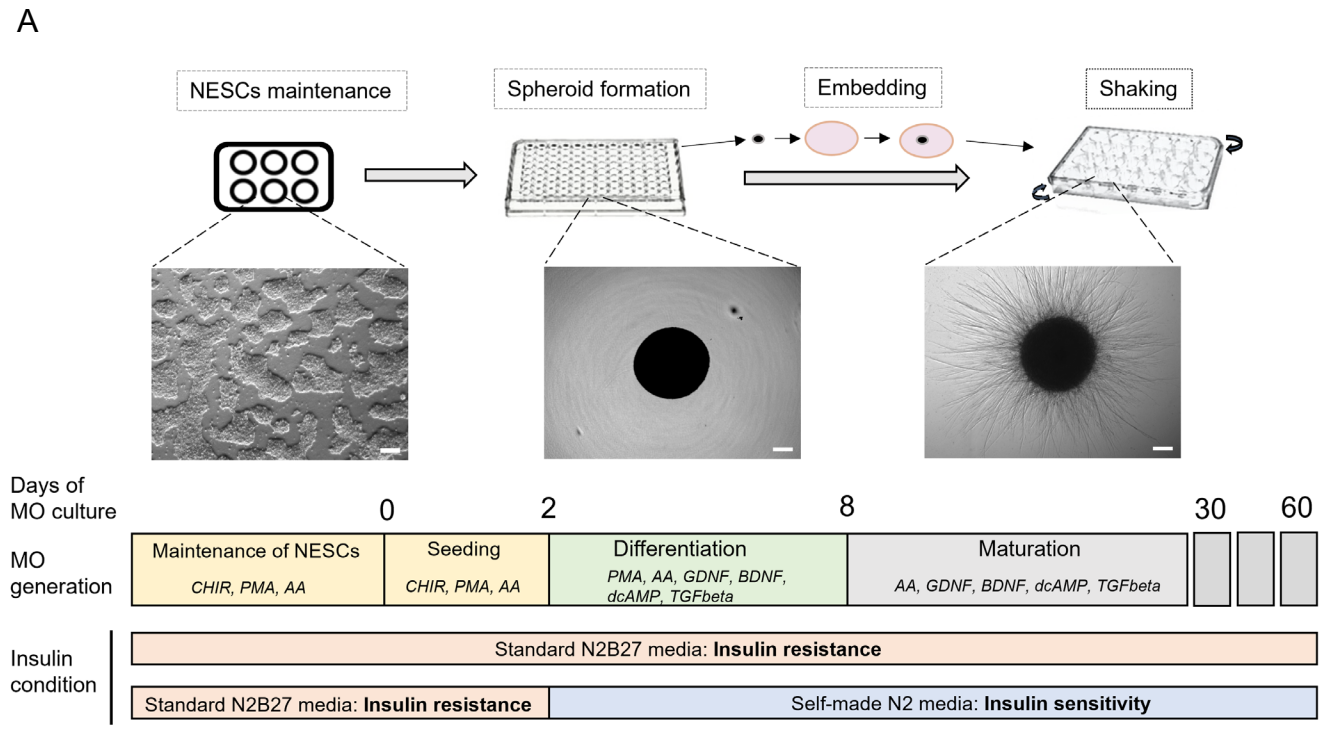
A
NESCs maintenance
Spheroid formation
Embedding
Shaking
Days of MO culture
0
2
8
30
60
MO generation
Maintenance of NESCs
CHIR, PMA, AA
Seeding
CHIR, PMA, AA
Differentiation
PMA, AA, GDNF, BDNF, dcAMP, TGFbeta
Maturation
AA, GDNF, BDNF, dcAMP, TGFbeta
Insulin condition
Standard N2B27 media: Insulin resistance
Standard N2B27 media: Insulin resistance
Self-made N2 media: Insulin sensitivity

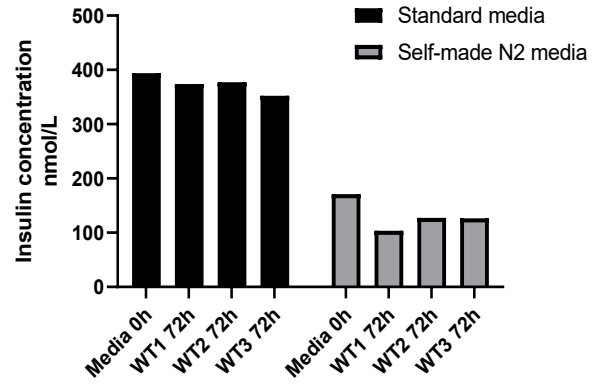
B
Insulin concentration nmol/L
Standard media
Self-made N2 media
Media 0h
WT1 72h
WT2 72h
WT3 72h
Media 0h
WT1 72h
WT2 72h
WT3 72h

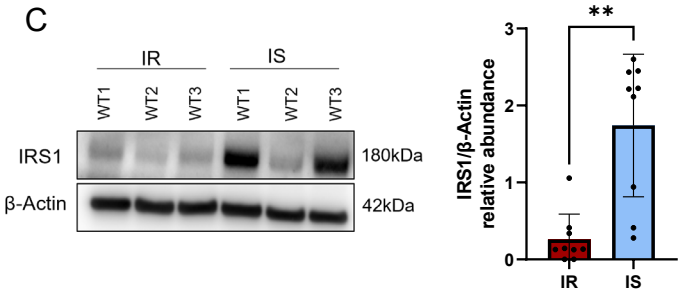
C
IR
IS
WT1
WT2
WT3
IRS1
180kDa
β-Actin
42kDa
IRS1/β-Actin relative abundance
**
IR
IS

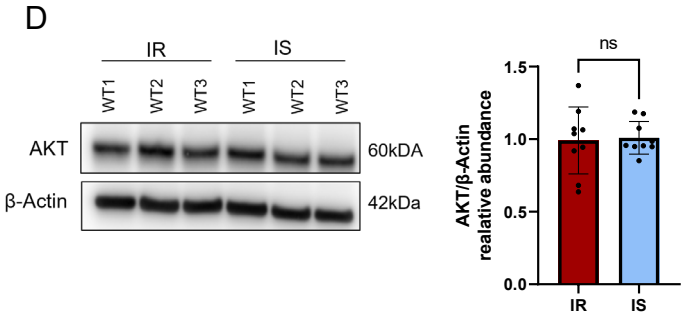
D
IR
IS
WT1
WT2
WT3
AKT
60kDA
β-Actin
42kDa
AKT/β-Actin relative abundance
ns
IR
IS

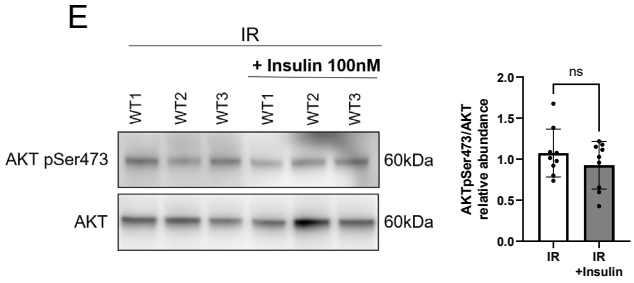
E
IR
+ Insulin 100nM
WT1
WT2
WT3
AKT pSer473
60kDa
AKT
60kDa
AKTpSer473/AKT relative abundance
ns
IR
IR +Insulin

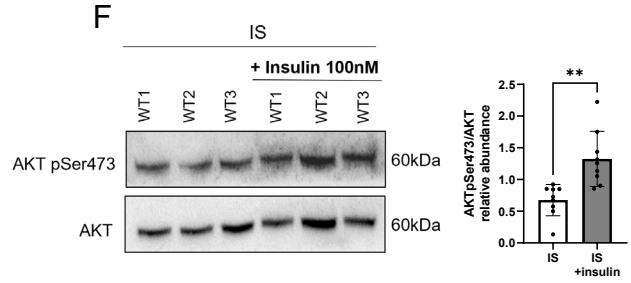
F
IS
+ Insulin 100nM
WT1
WT2
WT3
AKT pSer473
60kDa
AKT
60kDa
AKTpSer473/AKT relative abundance
**
IS
IS +insulin

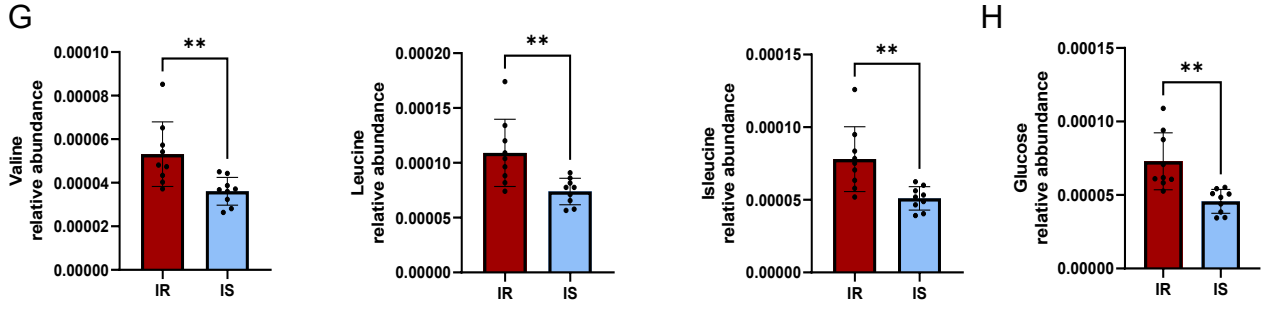
G
Valine relative abundance
Leucine relative abundance
Isleucine relative abundance
H
Glucose relative abbundance
**
IR
IS

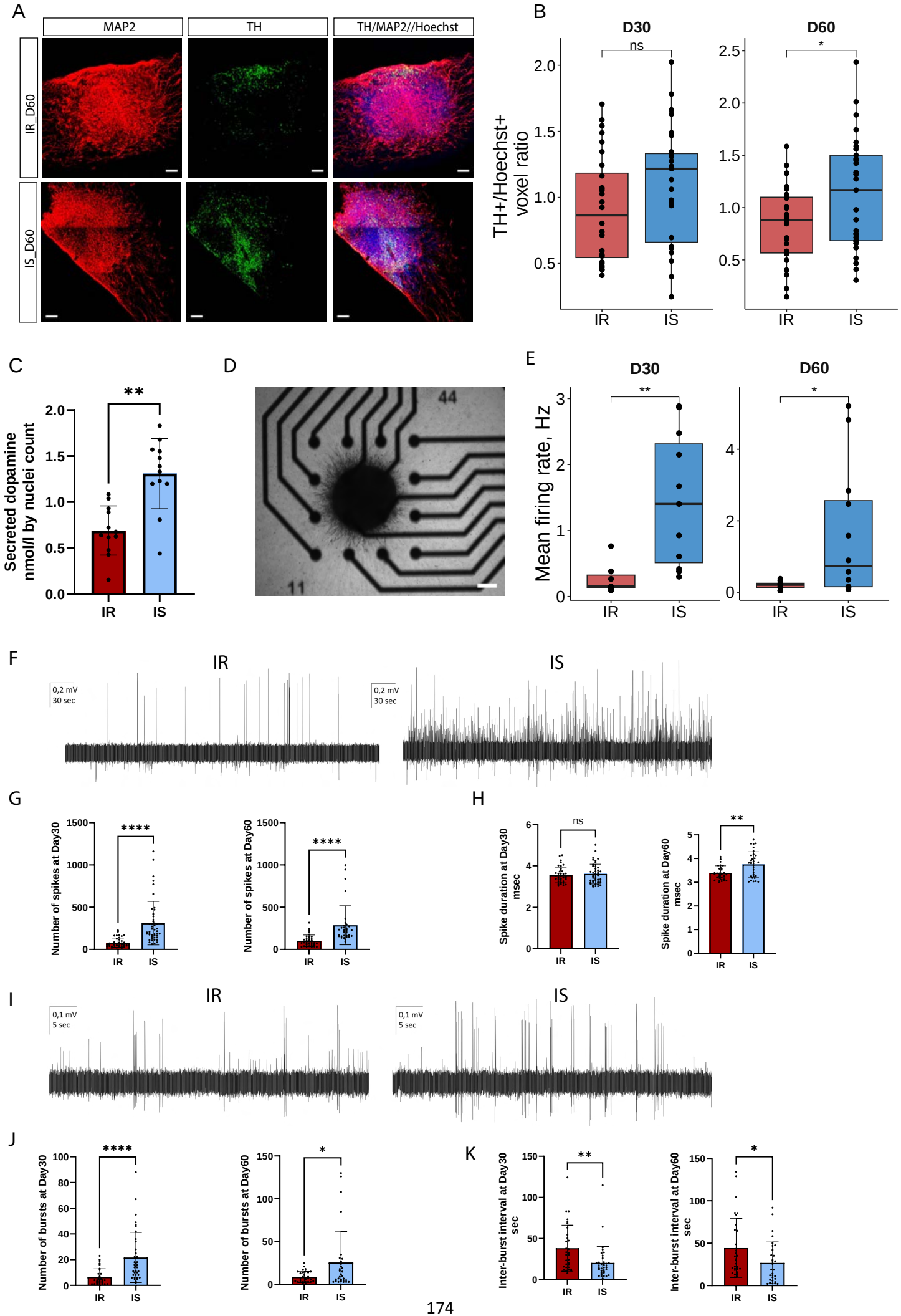
A
MAP2
TH
TH/MAP2//Hoechst
IR_D60
IS_D60
B
D30
D60
ns
*
TH+/Hoechst+ voxel ratio
IR
IS
C
**
Secreted dopamine nmol/l by nuclei count
IR
IS
D
44
11
E
D30
D60
**
*
Mean firing rate, Hz
IR
IS
F
IR
IS
0,2 mV
30 sec
G
****
Number of spikes at Day30
Number of spikes at Day60
H
ns
**
Spike duration at Day30 msec
Spike duration at Day60 msec
I
IR
IS
0,1 mV
5 sec
J
****
*
Number of bursts at Day30
Number of bursts at Day60
K
**
*
Inter-burst interval at Day30 sec
Inter-burst interval at Day60 sec

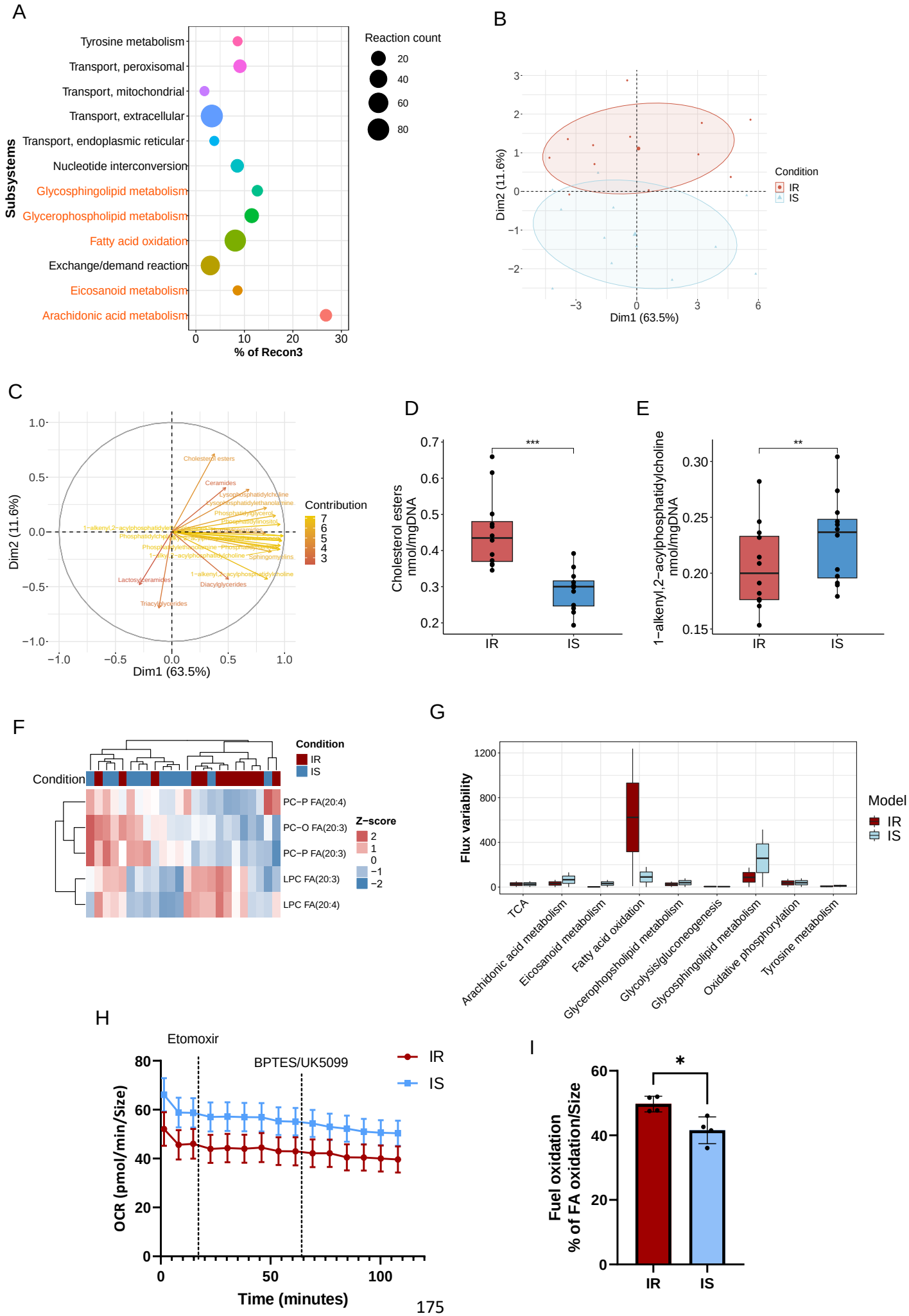
A
Tyrosine metabolism
Transport, peroxisomal
Transport, mitochondrial
Transport, extracellular
Transport, endoplasmic reticular
Nucleotide interconversion
Glycosphingolipid metabolism
Glycerophospholipid metabolism
Fatty acid oxidation
Exchange/demand reaction
Eicosanoid metabolism
Arachidonic acid metabolism
Subsystems
Reaction count
20
40
60
80
% of Recon3
B
Dim2 (11.6%)
Dim1 (63.5%)
Condition
IR
IS
C
Contribution
Dim2 (11.6%)
Dim1 (63.5%)
Cholesterol esters
Ceramides
Lysophosphatidylcholine
Lysophosphatidylethanolamine
Phosphatidylglycerol
Phosphatidylinositol
Phosphatidylcholine
Phosphatidylethanolamine
Sphingomyelins
Lactosylceramides
Diacylglycerides
Triacylglycerides
D
Cholesterol esters nmol/mgDNA
***
IR
IS
E
1−alkenyl,2−acylphosphatidylcholine nmol/mgDNA
**
IR
IS
F
Condition
IR
IS
Z-score
PC−P FA(20:4)
PC−O FA(20:3)
PC−P FA(20:3)
LPC FA(20:3)
LPC FA(20:4)
G
Flux variability
Model
IR
IS
TCA
Arachidonic acid metabolism
Eicosanoid metabolism
Fatty acid oxidation
Glycerophospholipid metabolism
Glycolysis/gluconeogenesis
Glycosphingolipid metabolism
Oxidative phosphorylation
Tyrosine metabolism
H
Etomoxir
BPTES/UK5099
IR
IS
OCR (pmol/min/Size)
Time (minutes)
I
Fuel oxidation % of FA oxidation/Size
*
IR
IS

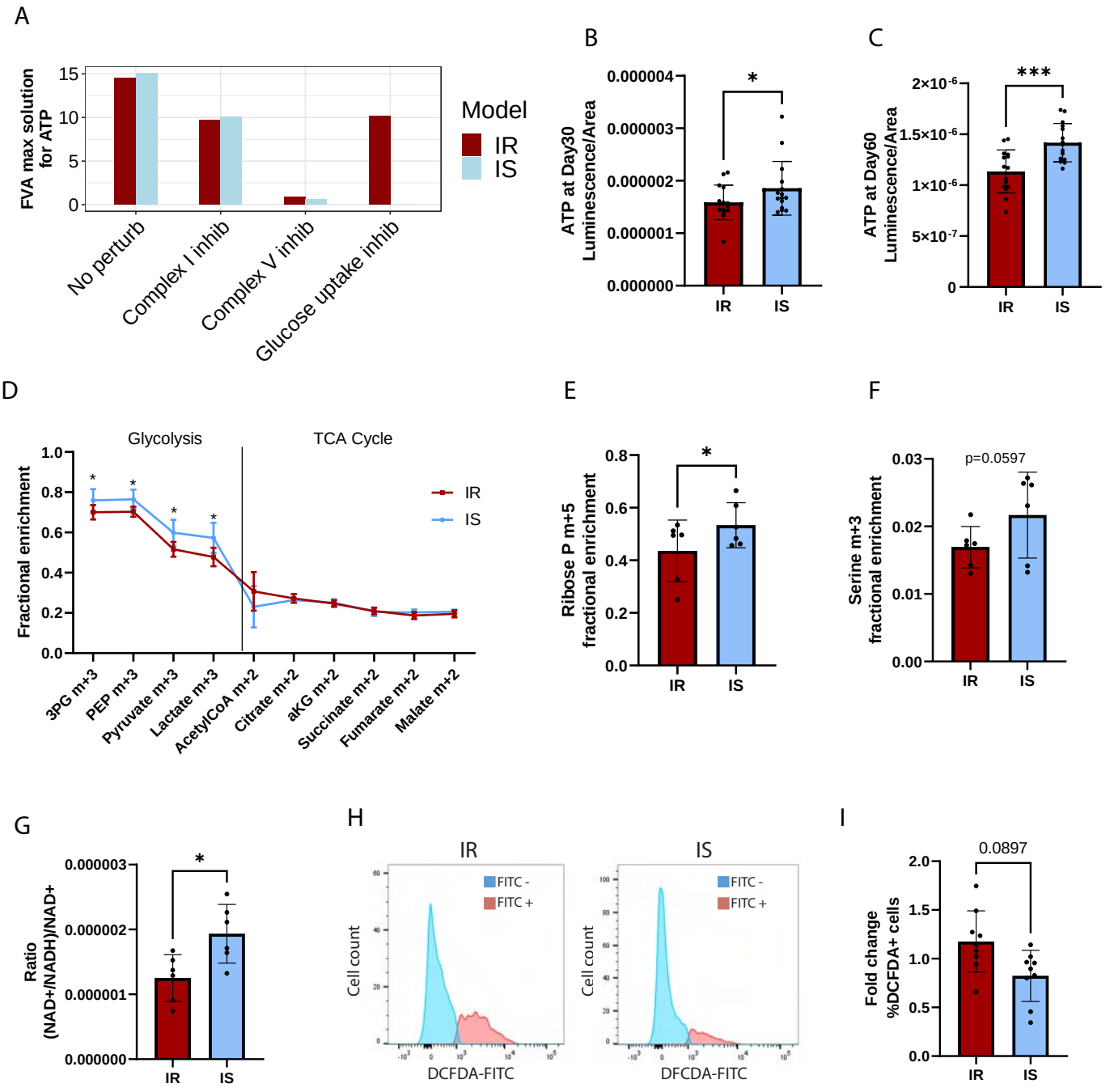
A
FVA max solution for ATP
15
10
5
0
No perturb
Complex I inhib
Complex V inhib
Glucose uptake inhib
Model
IR
IS
B
ATP at Day30 Luminescence/Area
0.000004
0.000003
0.000002
0.000001
0.000000
*
IR
IS
C
ATP at Day60 Luminescence/Area
2×10-6
1.5×10-6
1×10-6
5×10-7
0
***
IR
IS
D
Glycolysis
TCA Cycle
Fractional enrichment
1.0
0.8
0.6
0.4
0.2
0.0
IR
IS
3PG m+3
PEP m+3
Pyruvate m+3
Lactate m+3
AcetylCoA m+2
Citrate m+2
aKG m+2
Succinate m+2
Fumarate m+2
Malate m+2
E
Ribose P m+5 fractional enrichment
0.8
0.6
0.4
0.2
0.0
*
IR
IS
F
Serine m+3 fractional enrichment
0.03
0.02
0.01
0.00
p=0.0597
IR
IS
G
Ratio (NAD+/NADH)/NAD+
0.000003
0.000002
0.000001
0.000000
*
IR
IS
H
IR
IS
FITC -
FITC +
Cell count
DCFDA-FITC
DFCDA-FITC
I
Fold change %DCFDA+ cells
2.0
1.5
1.0
0.5
0.0
0.0897
IR
IS

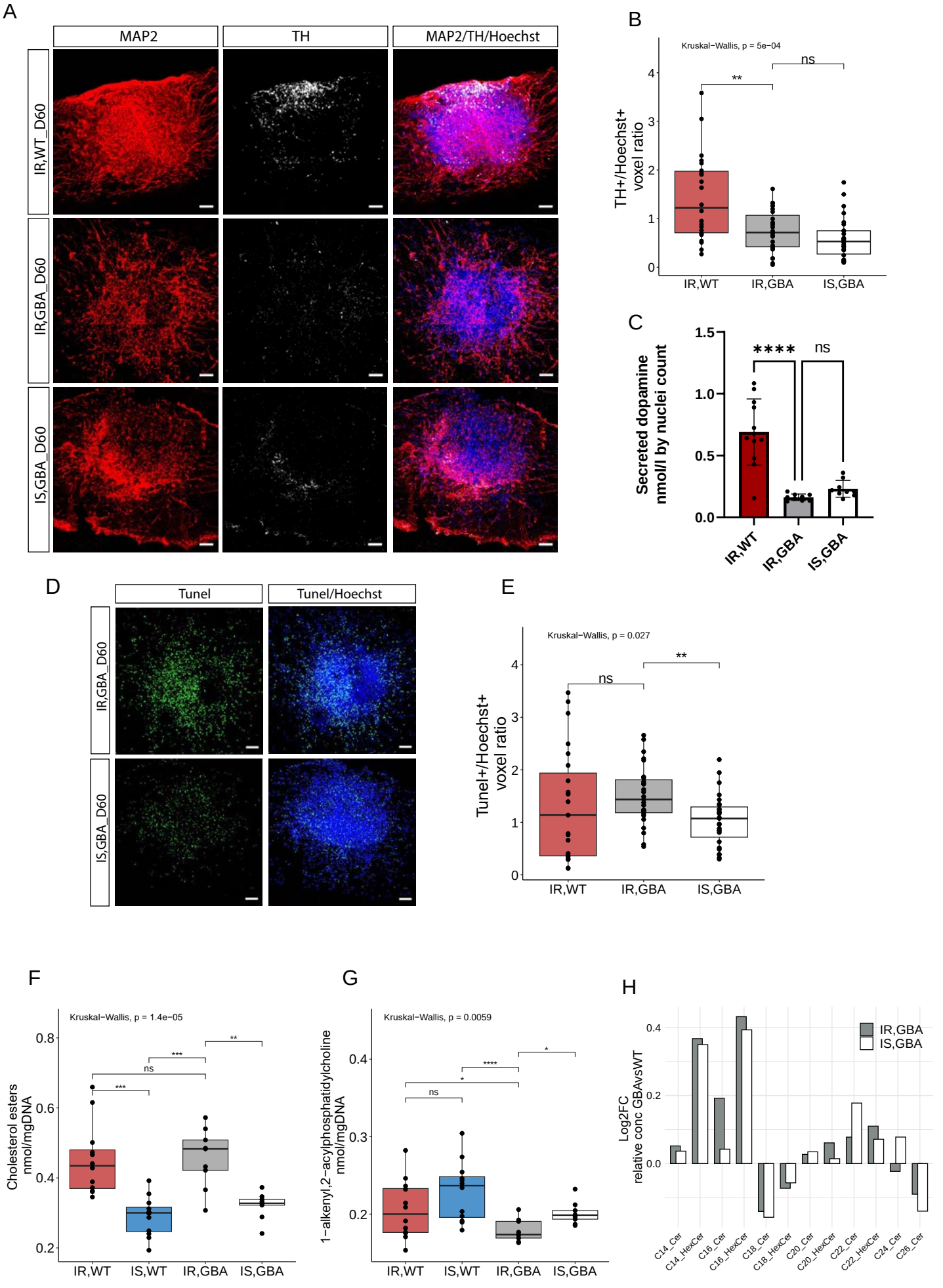
A
MAP2
TH
MAP2/TH/Hoechst
IR,WT_D60
IR,GBA_D60
IS,GBA_D60
B
Kruskal−Wallis, p = 5e−04
ns
**
TH+/Hoechst+ voxel ratio
IR,WT
IR,GBA
IS,GBA
C
****
ns
Secreted dopamine nmol/l by nuclei count
IR,WT
IR,GBA
IS,GBA
D
Tunel
Tunel/Hoechst
IR,GBA_D60
IS,GBA_D60
E
Kruskal−Wallis, p = 0.027
ns
**
Tunel+/Hoechst+ voxel ratio
IR,WT
IR,GBA
IS,GBA
F
Kruskal−Wallis, p = 1.4e−05
Cholesterol esters nmol/mgDNA
IR,WT
IS,WT
IR,GBA
IS,GBA
G
Kruskal−Wallis, p = 0.0059
1−alkenyl,2−acylphosphatidylcholine nmol/mgDNA
IR,WT
IS,WT
IR,GBA
IS,GBA
H
IR,GBA
IS,GBA
Log2FC relative conc GBAvsWT
C14_Cer
C14_HexCer
C16_Cer
C16_HexCer
C18_Cer
C18_HexCer
C20_Cer
C20_HexCer
C22_Cer
C22_HexCer
C24_Cer
C26_Cer

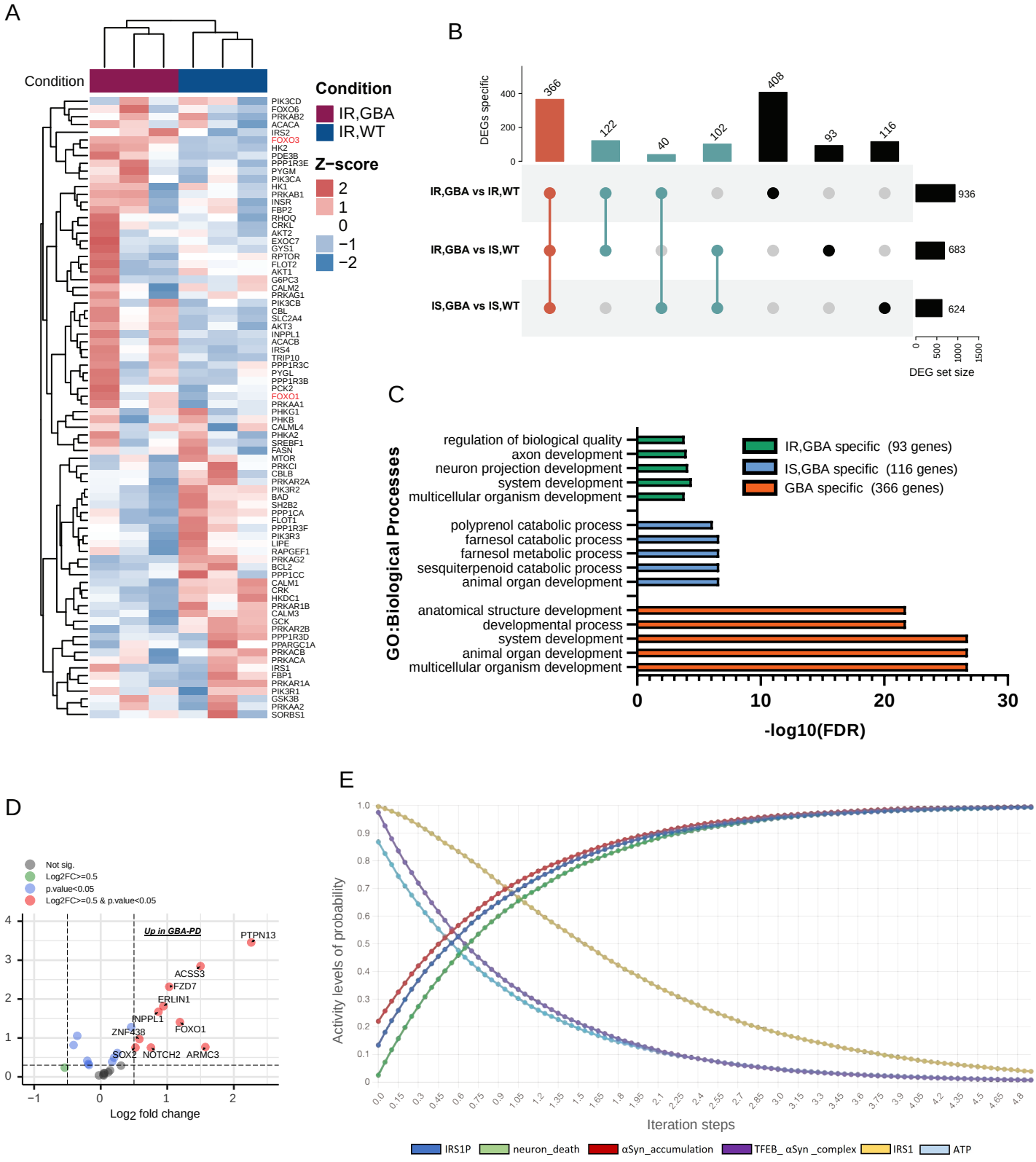
A
Condition
Condition
IR,GBA
IR,WT
Z−score
2
1
0
−1
−2
B
DEGs specific
366
122
40
102
408
93
116
IR,GBA vs IR,WT
IR,GBA vs IS,WT
IS,GBA vs IS,WT
936
683
624
DEG set size
C
GO:Biological Processes
regulation of biological quality
axon development
neuron projection development
system development
multicellular organism development
polyprenol catabolic process
farnesol catabolic process
farnesol metabolic process
sesquiterpenoid catabolic process
animal organ development
anatomical structure development
developmental process
system development
animal organ development
multicellular organism development
IR,GBA specific (93 genes)
IS,GBA specific (116 genes)
GBA specific (366 genes)
-log10(FDR)
D
Not sig.
Log2FC>=0.5
p.value<0.05
Log2FC>=0.5 & p.value<0.05
Up in GBA-PD
PTPN13
ACSS3
FZD7
ERLIN1
INPPL1
FOXO1
ZNF438
SOX2
NOTCH2
ARMC3
−Log10 P
Log2 fold change
E
Activity levels of probability
Iteration steps
IRS1P
neuron_death
αSyn_accumulation
TFEB_ αSyn _complex
IRS1
ATP

Figure 7

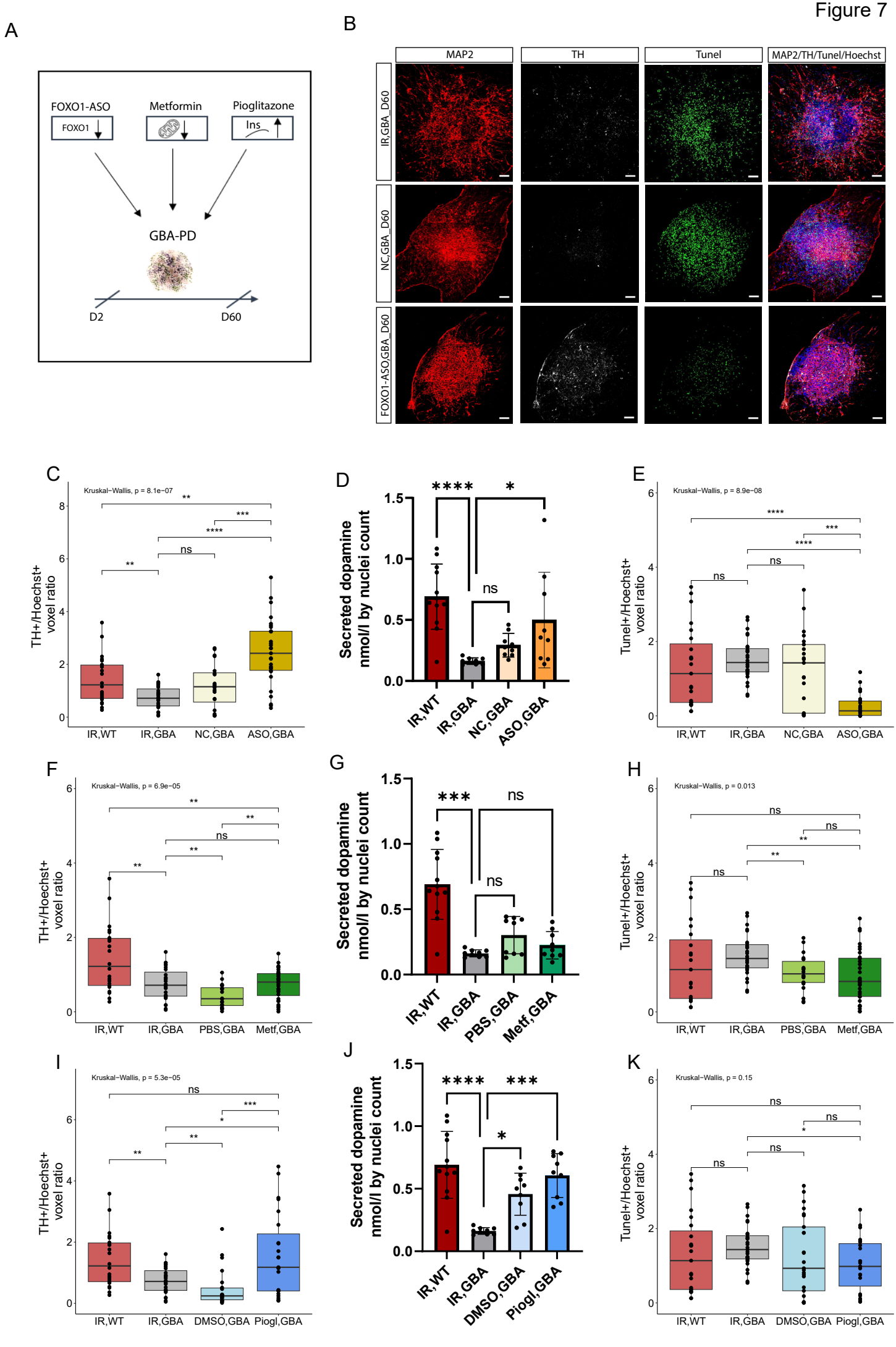
A
FOXO1-ASO
FOXO1
Metformin
Pioglitazone
Ins
GBA-PD
D2
D60
B
MAP2
TH
Tunel
MAP2/TH/Tunel/Hoechst
IR,GBA_D60
NC,GBA_D60
FOXO1-ASO,GBA_D60
C
Kruskal−Wallis, p = 8.1e−07
TH+/Hoechst+ voxel ratio
IR,WT
IR,GBA
NC,GBA
ASO,GBA
D
Secreted dopamine nmol/l by nuclei count
E
Kruskal−Wallis, p = 8.9e−08
Tunel+/Hoechst+ voxel ratio
F
Kruskal−Wallis, p = 6.9e−05
PBS,GBA
Metf,GBA
G
H
Kruskal−Wallis, p = 0.013
I
Kruskal−Wallis, p = 5.3e−05
DMSO,GBA
Piogl,GBA
J
K
Kruskal−Wallis, p = 0.15

Supplementary Figures

Insulin resistance disrupts midbrain metabolic & functional homeostasis and aggravates dopaminergic neuron loss in GBA-PD

Alise Zagare[1], Janis Kurlovics[2], Catarina Almeida[1, 3], Daniele Ferrante[1], Daniela Frangenberg[1], Laura Neises[4], Ahmed Hemedan[5], Armelle Vitali[9], Gemma Gomez-Giro[1], Christian Jaeger[6], Paul Antony[7], Rashi Halder[8], Marek Ostaszewski[5], Rejko Krueger[9, 10], Enrico Glaab[11], Johannes Meiser[4], Egils Stalidzans[2], Giuseppe Arena[9], Jens C Schwamborn[1*]

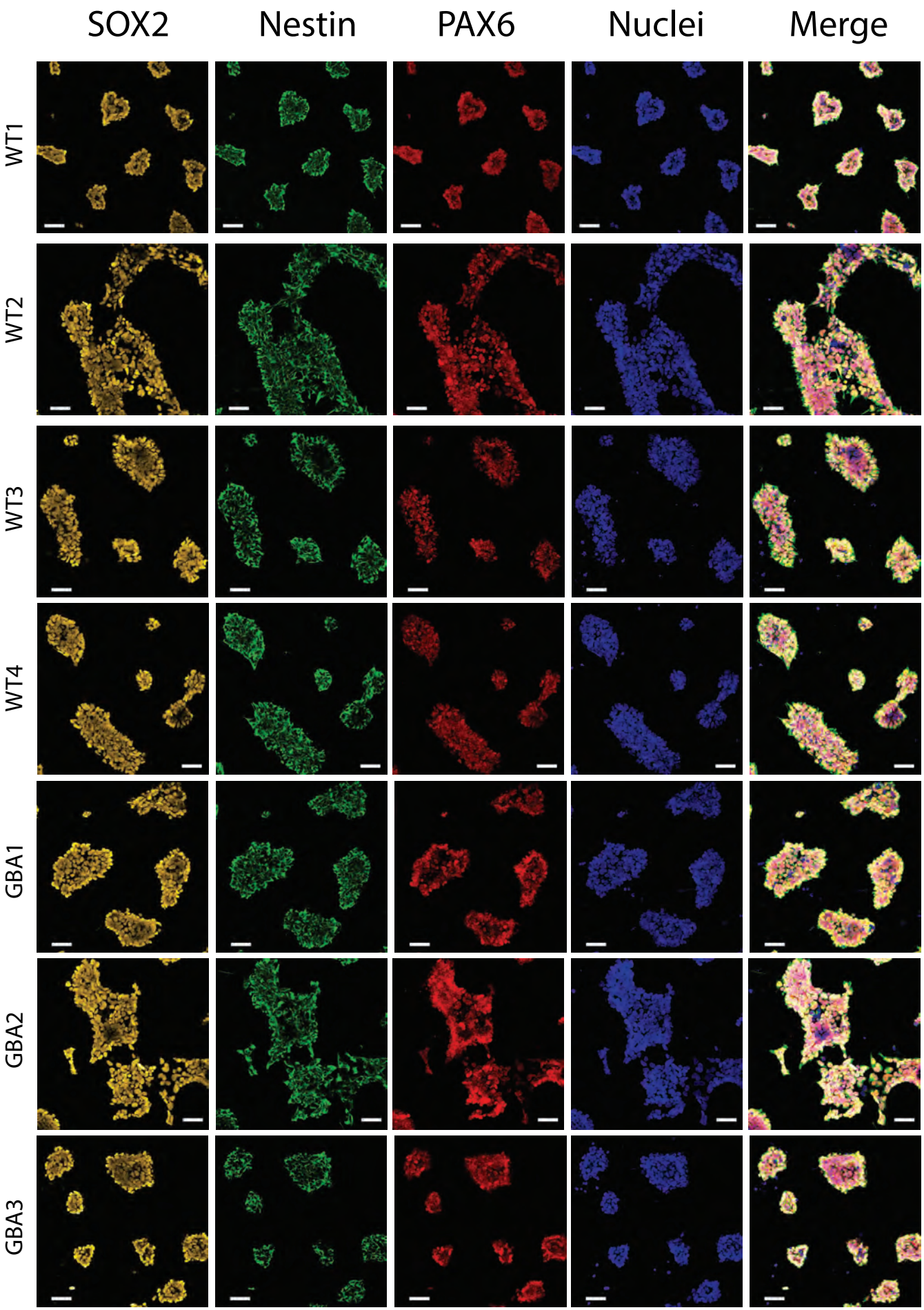

Figure S1. NESC characterization. Immunofluorescent images of neuronal stem cell typical markers-SOX2 and Nestin, and neuroectoderm marker PAX6. Scale bars 50µm.

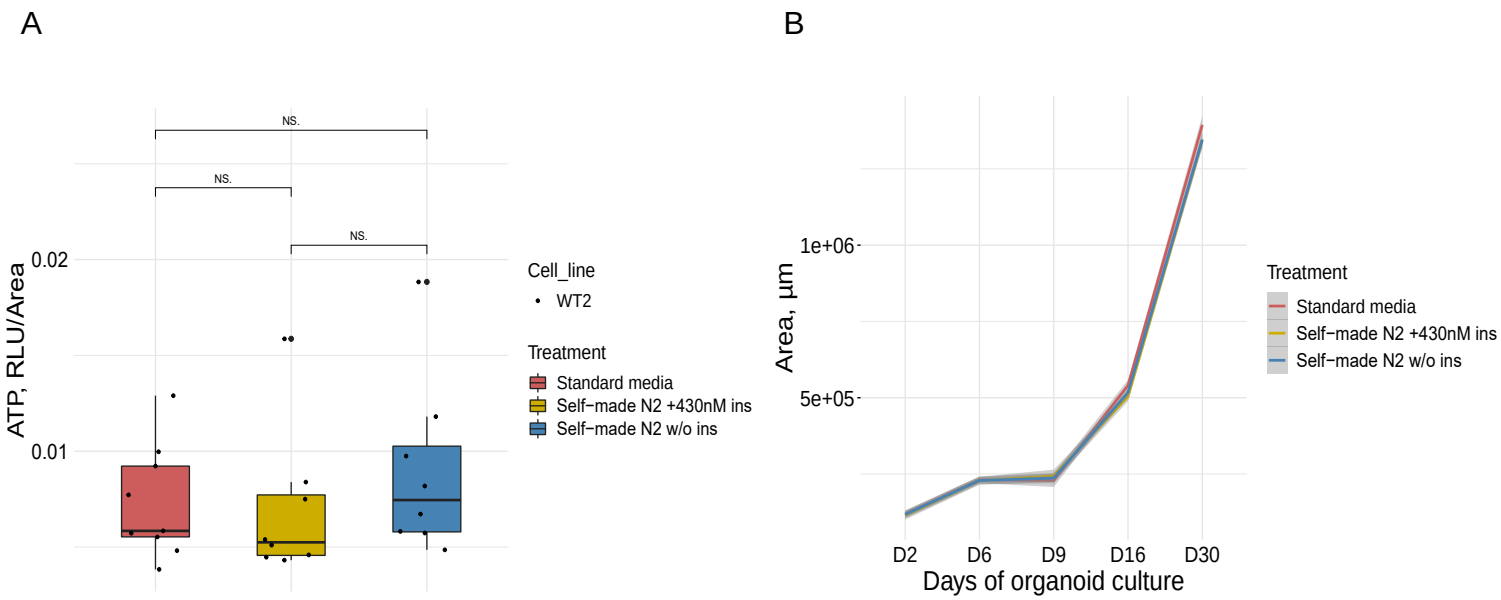

Figure S2. Self-made N2 supplement validation in midbrain organoid culture. Midbrain organoids cultured until day 30 in standard media (high insulin), self-made N2 media + 430nM insulin (to mimic theorethical insulin concentration in standard media), and self-made N2 media w/o insulin. A) Intracellular ATP measurment at day 30 representing organoid viability. B) Area measurment of midbrain organoids over the differentiation time.

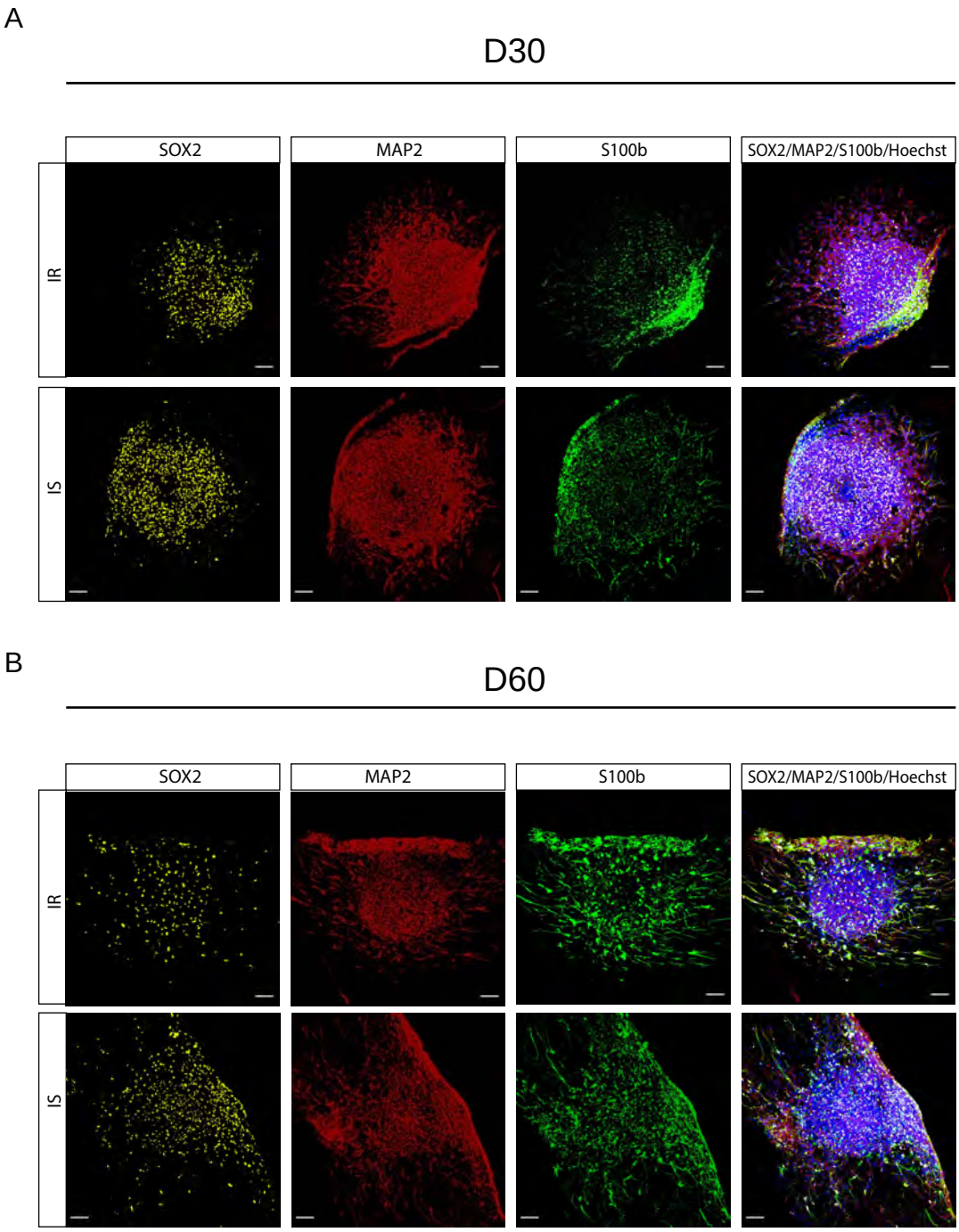

C

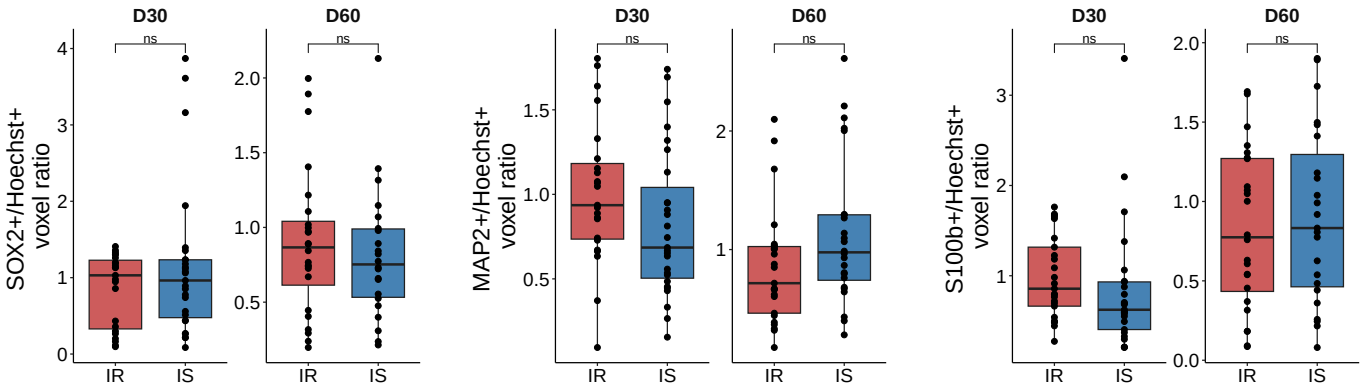

Figure S3. Cell types in midbrain organoids.
Representative immunofluorescent images of SOX2, MAP2 and S100b staining in insulin resistant (IR) and insulin sensitive (IS) midbrain organoids at A) day D30 and B) day 60. Scale bars: 100µm. C) Quantification of SOX2, MAP2 and S100b positive area over Nuclei (Hoechst) area.

A

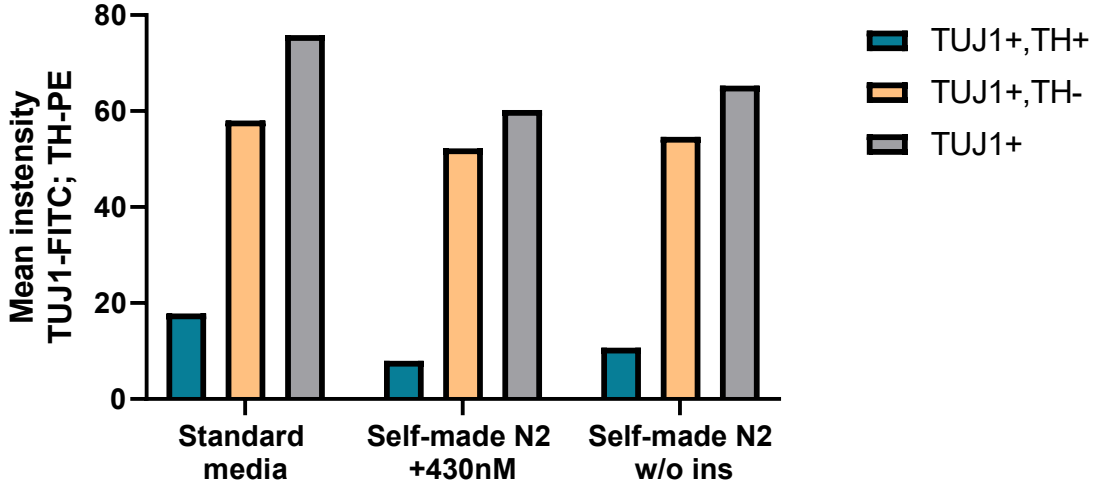

B

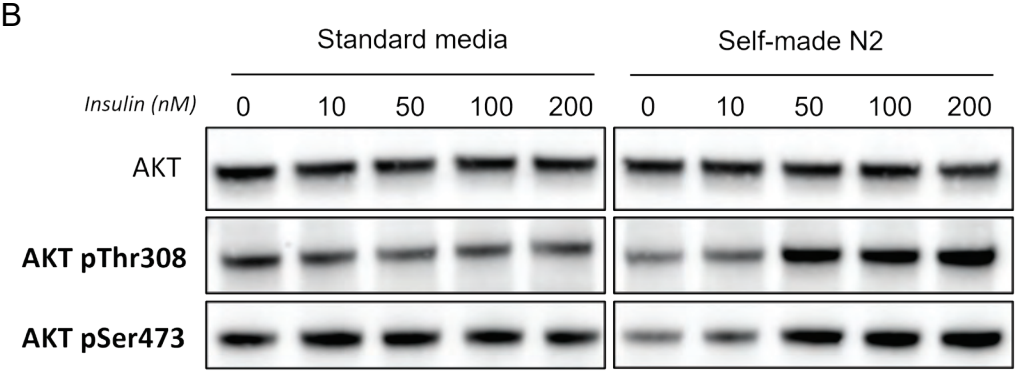

Figure S4. Self-made N2 supplement validation in 2D IPSC-derived dopaminergic neurons. Dopaminergic neurons were cultured in Standard media, self-made N2 media + 430nM insulin (to mimic theoretical insulin concentration in standard media), and self-made N2 media w/o insulin until day 30 of differentiation. A) Percentage of cells quantified by FACS, expressing the indicated neuronal differentiation markers at day 30 of differentiation. B) Activation of AKT signaling pathway was evaluated after 30 days of NESC differentiation in the two media (standard vs self-made N2), upon acute stimulation with increasing insulin doses (from 10 to 200nM) for 30 minutes. AKT phosphorylation at both T308 and S473 residues was assessed by immunoblotting and normalized against total AKT levels.

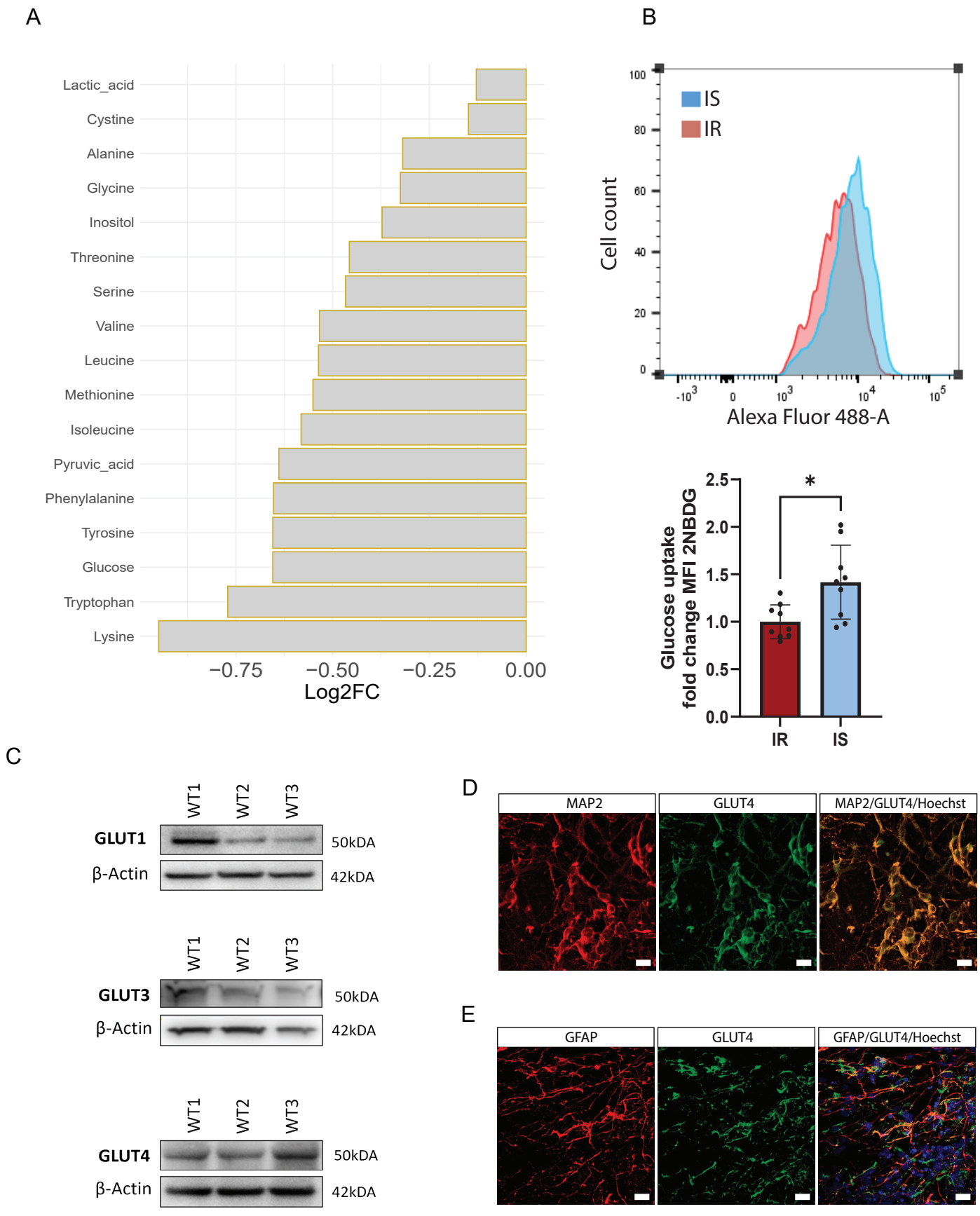

Figure S5. Insulin-dependent metabolic changes and glucose transporter presence in midbrain organoids. A) GC-MS detected metabolite relative concentration in IS organoid spent media demonstrated as log2 fold change (FC) against IR samples. Metabolite relative abundance normalised to the organoid area. B) Representative histogram of cells positive to the Alexa-Fluor 488 signal demonstrating uptake of fluorescent glucose analog - 2NBDG. Measurement performed after 30 min incubation of high (standard media) or reduced (self-made N2 media) insulin concentration after organoid dissociation. Statistical significance tested with paired t-test. C) Representative images of Western Blots showing GLUT1, GLUT3 and GLUT4 presence in midbrain organoids. D) Representative immunofluorescent staining of MAP2 and GLUT4 at day 30 of organoid culture. Scale bars:20µm. E) Representative immunofluorescent staining of GFAP and GLUT4 at day 60 of organoid culture. Scale bars:20µm.

A

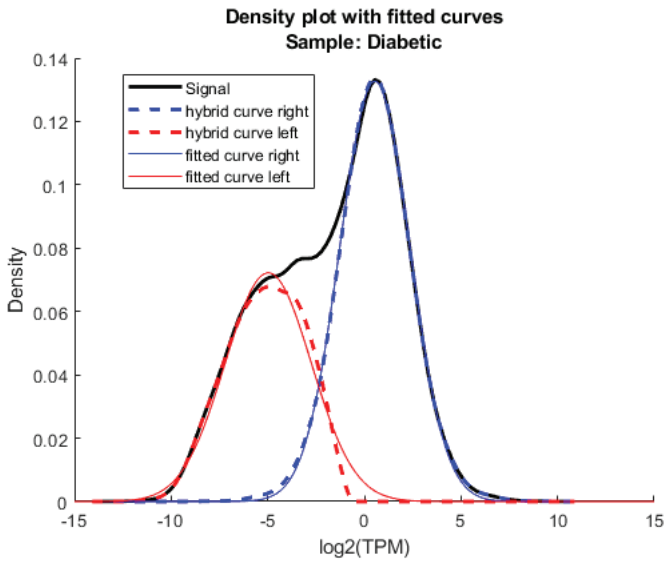

B

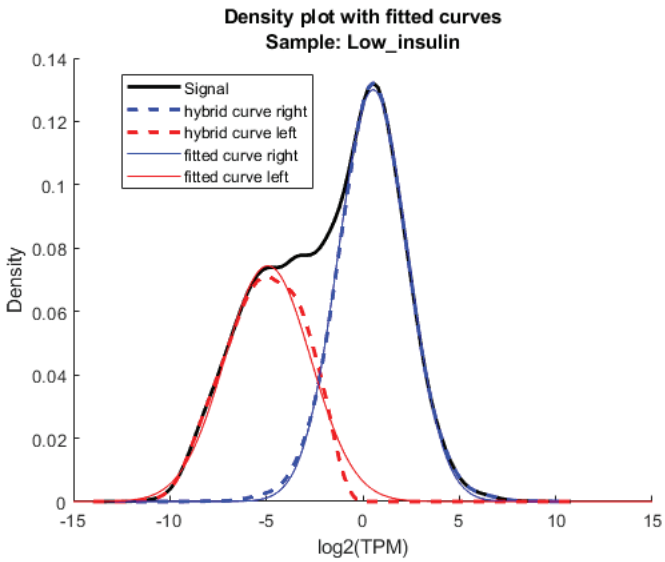

C

Model	Genes	Rxns	Mets
IR	1446	3620	2632
IS	1430	3470	2521

Figure S6. Generation of context-specific metabolic models.

Representative histogram of gene discretization based on their expression levels of pulled data of A) IR samples (Diabetic) and B) IS samples (Low_insulin). C) Generated model composition regarding the number of genes, reactions (Rxns) and metabolites (Mets) in each model.

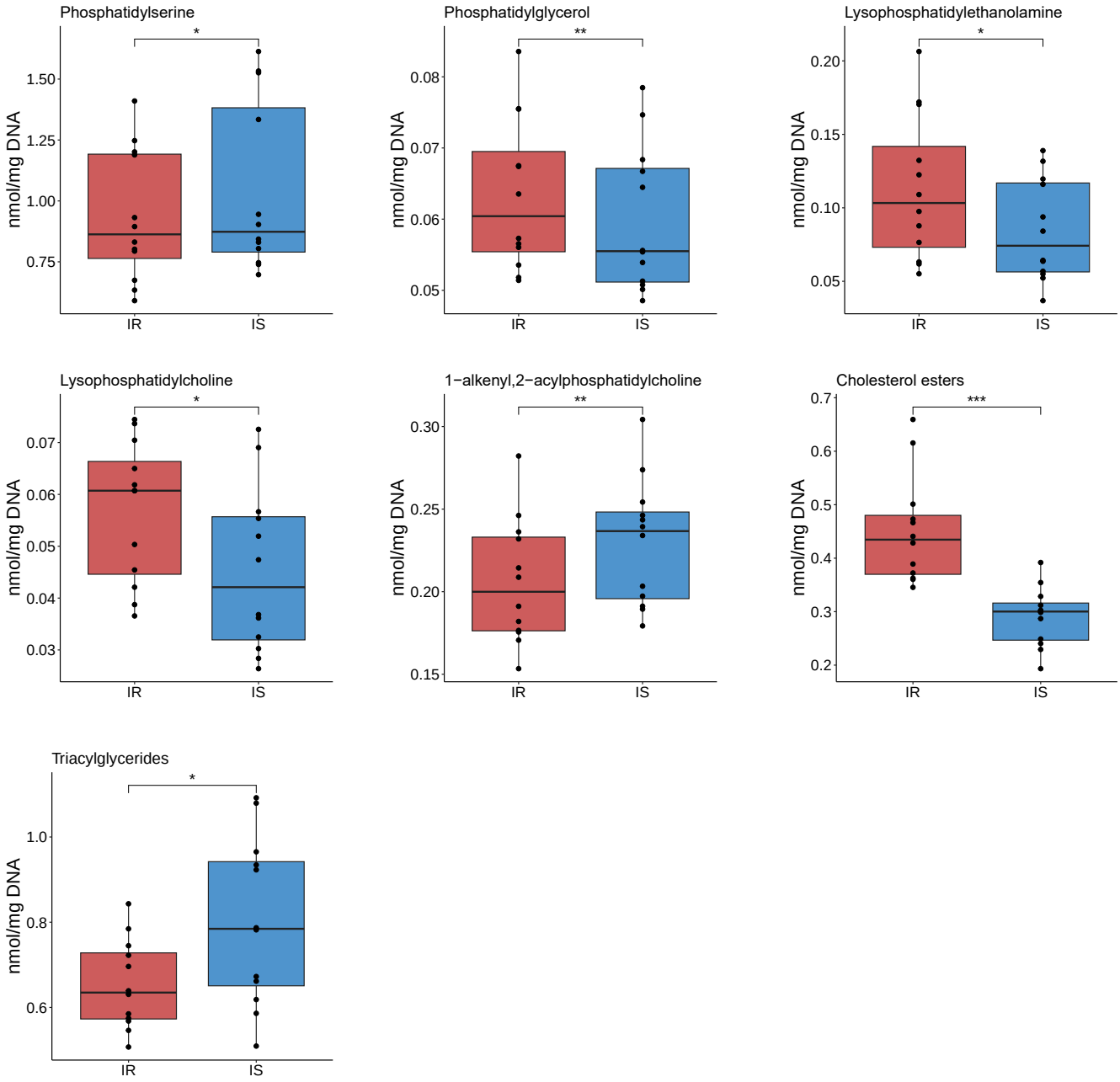

Figure S7. Significantly differentially abundant lipid classes.
Lipids measured by LC-MS. Final concentration normalized to the DNA content of each samples. Statistical significnace tested with two-sided, paired Wilcoxon test (P<0.05 *, P <0.01 **, P <0.001 ***).

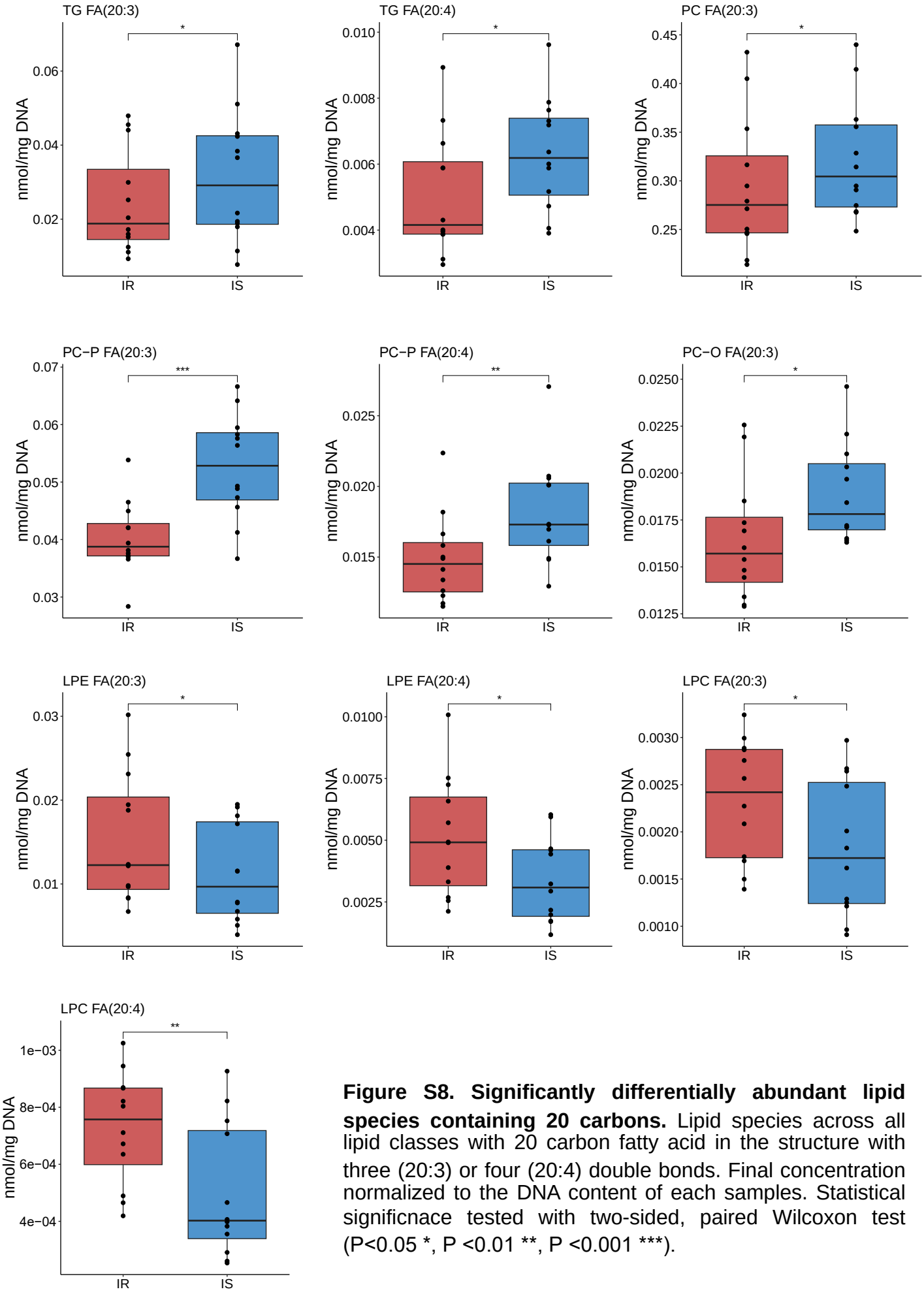

Figure S8. Significantly differentially abundant lipid species containing 20 carbons. Lipid species across all lipid classes with 20 carbon fatty acid in the structure with three (20:3) or four (20:4) double bonds. Final concentration normalized to the DNA content of each samples. Statistical significnace tested with two-sided, paired Wilcoxon test (P<0.05 *, P <0.01 **, P <0.001 ***).

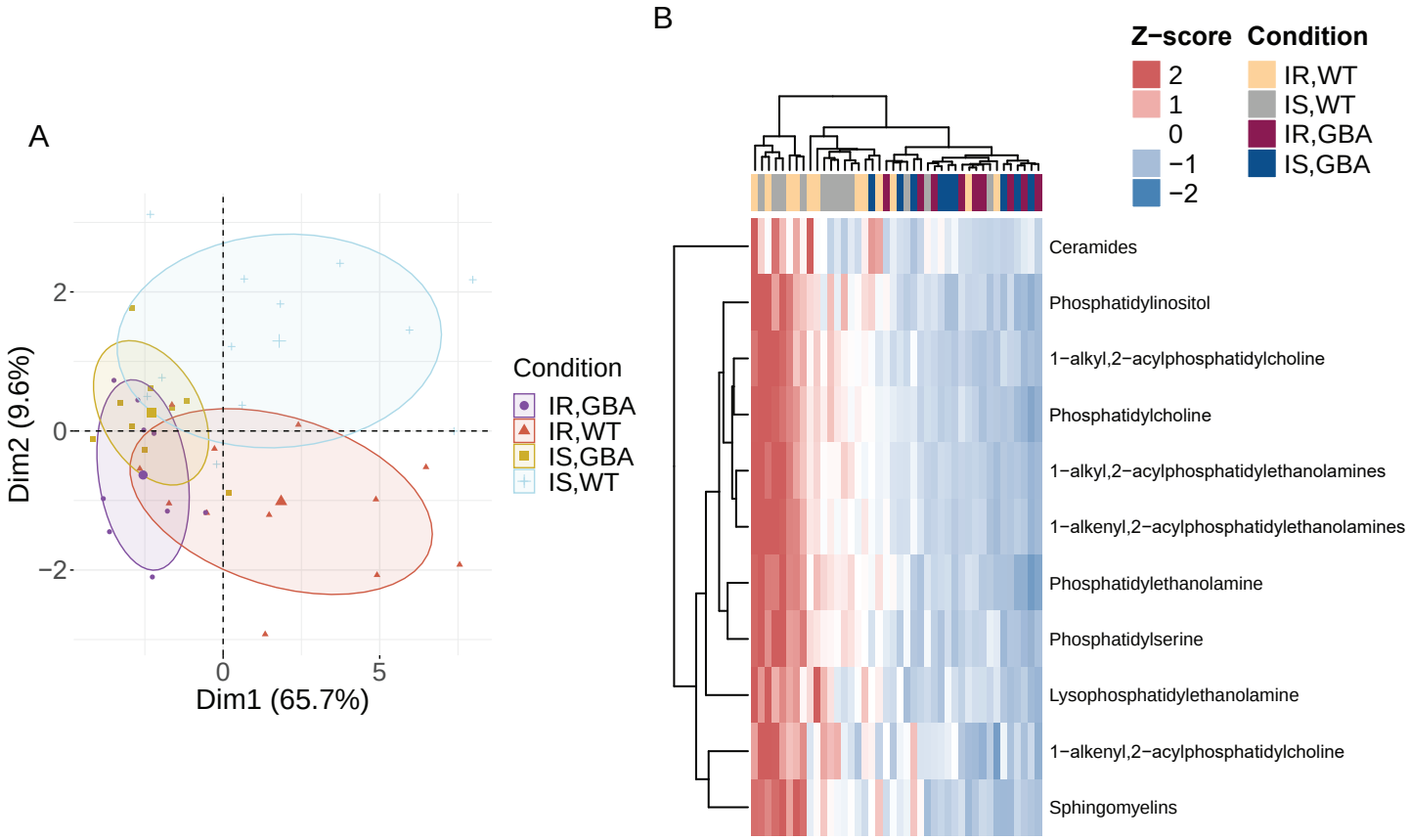

Figure S9. Lipid profile in WT and GBA-PD samples.
A) PCA scores plot, demonstrating sample clustering according to lipid abundance.
B) Heatmap demonstrating sample clustering and lipid class abundnace after Z-score transformation.

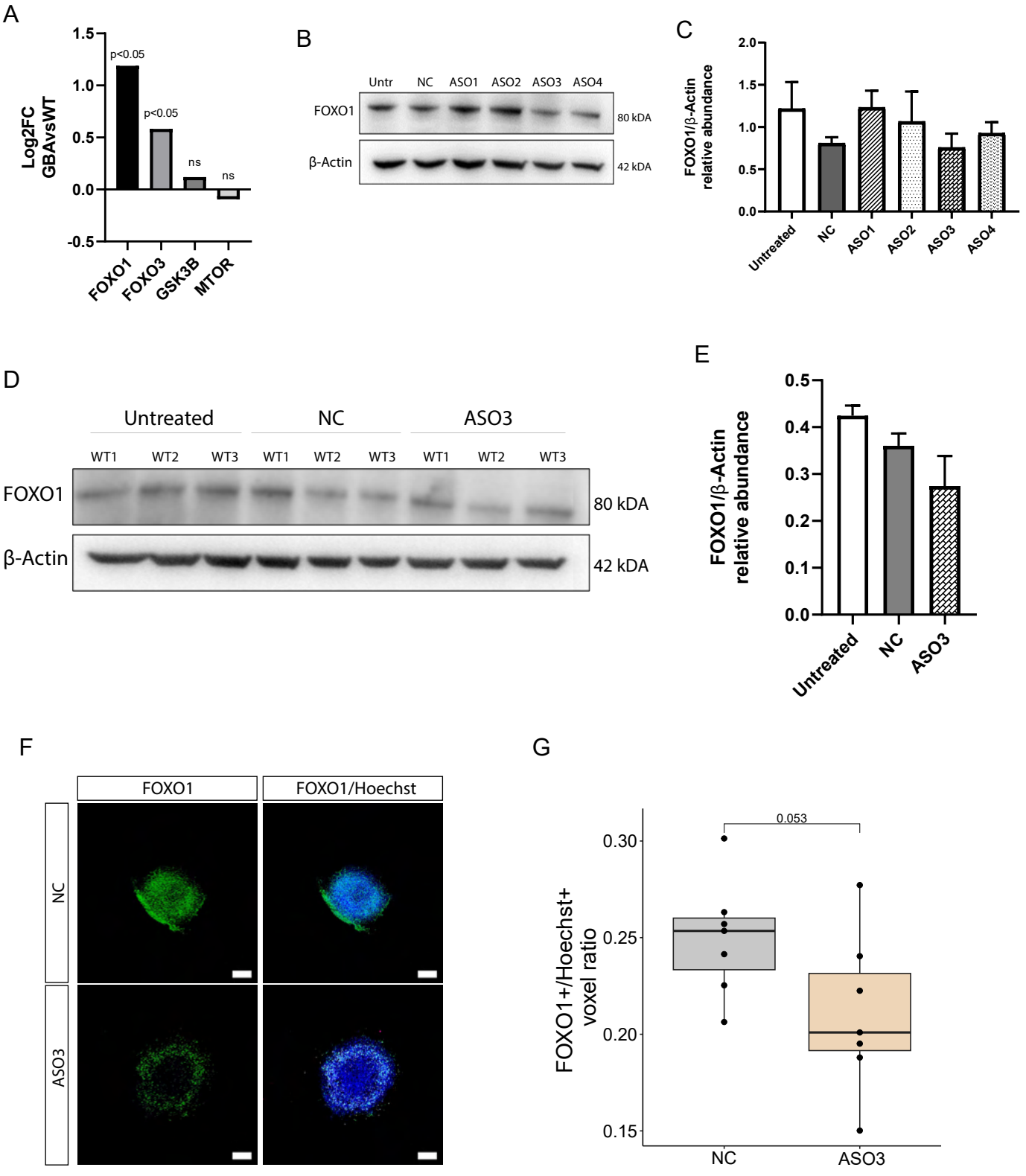

Figure S10. FOXO1 downregulation with ASO.

A) Log2 fold change (FC) of gene expression downstream AKT1 in GBA-PD samples against WT. B) Representative Western Blot (WB) image showing FOXO1 protein levels after NESC treatment with customised ASOs and negative control (NC). C) Quantification of FOXO1 protein levels relative to the β-Actin in NESC samples. D) Representative WB image showing FOXO1 protein levels after midbrain organoid treatment for 28 days with ASO3 and NC. E) Quantification of FOXO1 protein levels relative to the β-Actin in midbrain organoid samples. F) Immunofluorescent staining of FOXO1 in midbrain organoids after 28 days of treatment with ASO3 and NC. G) Quantification of FOXO1 positive pixel area normalized to the Hoechst pixel area.

Table S1. Cell lines used in this study

Sample ID	Diagnosis	Genotype	Age of sampling	IPSC ID	Source of IPSC
WT1	Healthy	wt/wt	68	2.0.0.71.1.0	IBBL / Max Planck Institute
WT2	Healthy	wt/wt	68	2.0.0.77.0.0	STEMBANCC
WT3	Healthy	wt/wt	55	2.0.0.27.0.0	Coriell
WT4	Healthy	wt/wt	63	2.0.0.72.1.0	IBBL / Max Planck Institute
GBA1	PD	GBA-N370S/wt	81	2.1.5.153.2.0	European Bank for induced pluripotent stem cells
GBA2	PD	GBA-N370S/wt	55	2.1.33.167.0.0	University College London
GBA3	PD	GBA-N370S/wt	66	2.1.5.28.5.3	Coriell

Table S2. Primary antibodies used for WB

Antibody	Source	Cat.no.	RRID	Species	Dilution
Phospho-Akt (Ser473)	Cell Signaling	4060T	*AB_2315049*	Rabbit	1:300 (organoids) 1:1000 (dopaminergic neurons)
Phospho-Akt (Thr308)	Cell Signaling	13038T	*AB_2629447*	Rabbit	1:1000 (dopaminergic neurons)
AKT pan	Cell Signaling	4691T	*AB_915783*	Rabbit	1:500 (organoids) 1:2000 (dopaminergic neurons)
IRS1	Cell Signaling	2382	*AB_330333*	Rabbit	1:300
Phospho-FOXO1 (Thr24)	Millipore	07-2126	*AB_11204867*	Rabbit	1:300
FoxO1	Cell Signalling	2880S	*AB_2106495*	Rabbit	1:500
GLUT1	Proteintech	21829-1-AP	*AB_10837075*	Rabbit	1:300
GLUT3	Proteintech	20403-1-AP	*AB_10694437*	Rabbit	1:300
GLUT4	Proteintech	66846-1-Ig	*AB_2882186*	Mouse	1:300
Beta-Actin	Cell Signaling	3700S	*AB_2242334*	Mouse	1:10 000

Table S3. Primary and secondary antibodies used for immunofluorescence stainings

Antibody	Source	Cat.no.	RRID	Species	Dilution
Nestin	BD Bioscience	611659	*AB_399177*	Mouse	1:200
PAX6	Biolegend	901302	*AB_2749901*	Rabbit	1:300
TH	Abcam	ab112	*AB_297840*	Rabbit	1:1000
TH	Sigma	T2928	*AB_477569*	Mouse	1:200
MAP2	Abcam	ab92434	*AB_2138147*	Chicken	1:1000
GLUT4	Proteintech	66846-1-Ig	*AB_2882186*	Mouse	1:500
GFAP	Millipore	AB5541	*AB_177521*	Chicken	1:1000
S100b	Sigma	S2532	*AB_477499*	Mouse	1:500
SOX2	R&D Systems	AF2018	*AB_355110*	Goat	1:200
FOXO1	Proteintech	66457-1-Ig	*AB_2881826*	Mouse	1:200
Phospho-FOXO1 (Thr24)	Millipore	07-2126	*AB_11204867*	Rabbit	1:200
Anti-chicken 647	Jackson Immuno Research	703-605-155	*AB_2340379*	Donkey	1:1000
Anti-rabbit 488	Invitrogen	A21206	*AB_2535792*	Donkey	1:1000
Anti-rabbit 568	Invitrogen	A10042	*AB_2534017*	Donkey	1:1000
Anti-goat 568	Invitrogen	A11057	*AB_2534104*	Donkey	1:1000
Anti-mouse 488	Invitrogen	A21202	*AB_141607*	Donkey	1:1000
Anti-mouse 568	Invitrogen	A10037	*AB_2534013*	Donkey	1:1000
Anti-goat 647	Invitrogen	A21447	*AB_2535864*	Donkey	1:1000

CHAPTER 4

Conclusions and Perspectives

By combining experimental and computational methods, this thesis provides insights into dysregulated mechanisms by LRRK2-G2019S, GBA-N370S and T2D-associated insulin resistance that contribute to the development of PD. Altogether, these results show that PD is a highly complex disease, and midbrain dopaminergic neuron loss most likely is a result of multiple pathogenic mechanism interactions. Moreover, predisposition to PD might be already determined at the neurodevelopmental stage by genetic risk factors and further accelerated by other factors, such as T2D.

Importantly, to investigate the complex pathogenesis of PD, a relevant model that represents the human brain complexity and recapitulates the most important PD aspects is crucial. iPSC technology allows disease modeling and drug screening using patient-specific cells, thus enabling disease research on the patient genetic background, and bringing us closer to personalized medicine. Moreover, more advanced iPCS-derived *in vitro* models like organoids provide organotypic structure and organization of tissue, enabling the investigation of different cell type interactions, which is crucial since usually not an isolated cell type is affected by the disease. Midbrain organoids represent great potential in PD modeling by possessing human midbrain identity and comprising multiple midbrain-specific cell types, including glial cells, perivascular cells, dopaminergic neurons – a cell population specifically affected in PD, and other types of neurons as demonstrated in Manuscript I. Furthermore, in this thesis, we confirm that midbrain organoids closely mimic human embryonic development, which allows us to study neurodevelopmental defects in PD. Regardless of all the advantages of the organoid model, there are still some limitations. The organoid model does not fully recapitulate aging phenotypes since the patient somatic cell reprogramming to iPSCs is reversing age-associated molecular changes (Puri and Wagner 2023). However, aging is a primary risk factor for the development of many diseases, including PD, therefore, efforts have been done to introduce aging in iPSC-derived models, such as prolonged iPCS culturing (Lo Sardo et al. 2017), telomerase inhibition (Vera, Bosco, and Studer 2016) and expression of progerin (Miller et al. 2013). Another limitation of the midbrain organoid model is that we lack microglia and vasculature cells, which originate from a different germ layer, and therefore cannot simultaneously be differentiated along with the neuronal cells. Also, in regard to this, recent efforts of our group have been successful in

introducing microglia in the midbrain organoid model (Sabate-Soler et al. 2022). In addition, further improvements in advancing organoid model complexity might be achieved by merging different brain region organoids, for example, midbrain and striatum, recapitulating the nigrostriatal pathway.

In this thesis, we also show that the two most common mutations associated with PD – LRRK2-G2019S and GBA-N370S are affecting neurodevelopment. Generally, PD is associated with age - related neurodegeneration and the neurodevelopmental aspect of PD is a relatively new theory that suggests a less mature and more vulnerable dopaminergic neuron population prone to degeneration (Schwamborn 2018). In fact, in neither of the Manuscripts, we observed progressive dopaminergic neuron degeneration as an isolated phenotype. The reduced levels of dopaminergic neurons in midbrain organoids from GBA-N370 mutation-carrying patients were primarily caused by impaired neurogenesis, suggesting that dopaminergic neurons in these patients might never reach the same abundance as in individuals without GBA mutation. Contrary, the number of dopaminergic neurons was not reduced in LRRK2-G2019S mutant midbrain organoids compared to the WT organoids at any analyzed time point, although the pseudotime analysis revealed impaired differentiation capability of mutant organoid dopaminergic neurons. In this case, it would be interesting to prolong the LRRK2-G2019S mutant organoid cultures to investigate the potential neurodegeneration of less mature dopaminergic neurons. Another explanation might be that the LRRK2-G2019S mutation was introduced in the cell line of a healthy donor. A healthy genetic background could also play a role in mitigation of neurodegenerative phenotype. It would be crucial to conduct experiments using samples derived from LRRK2-G2019S patients to evaluate the neurodegeneration aspect linked to LRRK2-G2019S. Overall, although LRRK2-G2019S and GBA-N370S seem to cause profound neurodevelopmental defects, not all people carrying these mutations develop PD. This strongly suggests that other factors including environment, lifestyle and essentially aging have a critical role in PD development. Apart from aging, other factors are modifiable and can be considered in PD prevention.

T2D is one of the factors that can be prevented in most cases (Galaviz et al. 2018), therefore it can be considered as a modifiable risk factor. In Manuscript III we demonstrate T2D-associated insulin resistance effects on PD development and progression. We show that insulin resistance alters neural activity and metabolism. Interestingly, the most affected metabolic pathways by insulin resistance in non-PD midbrain organoids are the same as the ones in GBA-N370S mutant midbrain organoids, suggesting that T2D might significantly amplify the PD phenotypes for GBA mutation-carrying individuals. Accordingly, healthier cell culture conditions improved GBA-N370S mutant

organoid viability and lipid profile. Additionally, we found that insulin signaling is already altered at the transcriptomic level in GBA-N370S mutant organoids, highlighting FOXO1 as a potential mediator of insulin signaling impairment-associated pathogenesis. Importantly, we were able to demonstrate that the downregulation of FOXO1, significantly increased dopaminergic neuron amount in GBA-N370S mutant midbrain organoids, suggesting that FOXO1 plays an important role in the regulation of dopaminergic neuron development. Additionally, based on the growing evidence of antidiabetic drug neuroprotective and neurorestorative potential in PD, we tested two antidiabetic drugs – Metformin and Pioglitazone on GBA-N370S mutant midbrain organoids. While both drugs increased cellular viability, only Pioglitazone rescued dopaminergic neuron loss and secreted dopamine levels in GBA-N370S patient-derived midbrain organoids. However, we did not investigate whether Pioglitazone treatment affected FOXO1 gene levels, which could be an additional confirmation of FOXO1 role in GBA-PD. In general, there are many anti-diabetic drugs available, each characterized by distinct mechanisms of action. Although anti-diabetic treatments hold promise in PD therapy, the most effective molecule could vary for each specific PD subgroup. To address this hypothesis, the next step could be to design a larger screening experiment using multiple different antidiabetic molecules to treat midbrain organoids derived from PD patients carrying other PD-associated mutations or from idiopathic PD patients. Additionally, it would be interesting to investigate the role of T2D on aSyn aggregation, which is not covered in this thesis but is an important element of PD pathogenesis. However, sample size and culture conditions are two critical aspects that must be further considered. The limited availability of iPSC lines from PD patients as well as from healthy individuals is a significant challenge and is usually a cause of insufficient sample size in iPSC-related studies. Moreover, culture conditions have to be optimized and defined as close to the physiological cellular environment as possible to be able to produce accurate and robust results that can be further translated into clinics.

In summary, this thesis supports the idea that PD has a neurodevelopmental component, which affects neural sustainability and increases cell vulnerability to insults, which eventually can lead to neurodegeneration. However, this presents a large time window for preventative actions or treatments to delay PD onset. T2D is one of the modifiable risk factors, and in the case, that it is not prevented, it can predispose to PD pathology by compromising cellular metabolic functions and neural functionality. Moreover, insulin signaling impairment affects GBA-N370S-associated PD phenotypes. A promising aspect is that shared pathophysiology between PD and T2D also implies possible shared therapeutic strategies, which ultimately opens new avenues to develop efficient PD treatments.

Bibliography

Alcalay, R. N., O. A. Levy, C. C. Waters, S. Fahn, B. Ford, S. H. Kuo, P. Mazzoni, M. W. Pauciulo, W. C. Nichols, Z. Gan-Or, G. A. Rouleau, W. K. Chung, P. Wolf, P. Oliva, J. Keutzer, K. Marder, and X. Zhang. 2015. "Glucocerebrosidase activity in Parkinson's disease with and without GBA mutations." *Brain* 138 (Pt 9):2648-58. doi: 10.1093/brain/awv179.

Almeida Mdo, R. 2012. "Glucocerebrosidase involvement in Parkinson disease and other synucleinopathies." *Front Neurol* 3:65. doi: 10.3389/fneur.2012.00065.

Andersen, M. S., S. Bandres-Ciga, R. H. Reynolds, J. Hardy, M. Ryten, L. Krohn, Z. Gan-Or, I. R. Holtman, L. Pihlstrom, and Consortium International Parkinson's Disease Genomics. 2021. "Heritability Enrichment Implicates Microglia in Parkinson's Disease Pathogenesis." *Ann Neurol* 89 (5):942-951. doi: 10.1002/ana.26032.

Arenas, E. 2014. "Wnt signaling in midbrain dopaminergic neuron development and regenerative medicine for Parkinson's disease." *J Mol Cell Biol* 6 (1):42-53. doi: 10.1093/jmcb/mju001.

Arenas, E., M. Denham, and J. C. Villaescusa. 2015. "How to make a midbrain dopaminergic neuron." *Development* 142 (11):1918-36. doi: 10.1242/dev.097394.

Athauda, D., J. Evans, A. Wernick, G. Virdi, M. L. Choi, M. Lawton, N. Vijiaratnam, C. Girges, Y. Ben-Shlomo, K. Ismail, H. Morris, D. Grosset, T. Foltynie, and S. Gandhi. 2022. "The Impact of Type 2 Diabetes in Parkinson's Disease." *Mov Disord* 37 (8):1612-1623. doi: 10.1002/mds.29122.

Auburger, G., M. Klinkenberg, J. Drost, K. Marcus, B. Morales-Gordo, W. S. Kunz, U. Brandt, V. Broccoli, H. Reichmann, S. Gispert, and M. Jendrach. 2012. "Primary skin fibroblasts as a model of Parkinson's disease." *Mol Neurobiol* 46 (1):20-7. doi: 10.1007/s12035-012-8245-1.

Aune, D., S. Schlesinger, Y. Mahamat-Saleh, B. Zheng, C. T. Udeh-Momoh, and L. T. Middleton. 2023. "Diabetes mellitus, prediabetes and the risk of Parkinson's disease: a systematic review and meta-analysis of 15 cohort studies with 29.9 million participants and 86,345 cases." *Eur J Epidemiol* 38 (6):591-604. doi: 10.1007/s10654-023-00970-0.

Avazzadeh, S., J. M. Baena, C. Keighron, Y. Feller-Sanchez, and L. R. Quinlan. 2021. "Modelling Parkinson's Disease: iPSCs towards Better Understanding of Human Pathology." *Brain Sci* 11 (3). doi: 10.3390/brainsci11030373.

Awad, O., L. M. Panicker, R. M. Deranieh, M. P. Srikanth, R. A. Brown, A. Voit, T. Peesay, T. S. Park, E. T. Zambidis, and R. A. Feldman. 2017. "Altered Differentiation Potential of Gaucher's Disease iPSC Neuronal Progenitors due to Wnt/beta-Catenin Downregulation." *Stem Cell Reports* 9 (6):1853-1867. doi: 10.1016/j.stemcr.2017.10.029.

Ayala, A., M. F. Munoz, and S. Arguelles. 2014. "Lipid peroxidation: production, metabolism, and signaling mechanisms of malondialdehyde and 4-hydroxy-2-nonenal." *Oxid Med Cell Longev* 2014:360438. doi: 10.1155/2014/360438.

Baldereschi, M., A. Di Carlo, W. A. Rocca, P. Vanni, S. Maggi, E. Perissinotto, F. Grigoletto, L. Amaducci, and D. Inzitari. 2000. "Parkinson's disease and parkinsonism in a longitudinal study: two-fold higher incidence in men. ILSA Working Group. Italian Longitudinal Study on Aging." *Neurology* 55 (9):1358-63. doi: 10.1212/wnl.55.9.1358.

Barbagallo, M., and L. J. Dominguez. 2014. "Type 2 diabetes mellitus and Alzheimer's disease." *World J Diabetes* 5 (6):889-93. doi: 10.4239/wjd.v5.i6.889.

Bardy, C., M. van den Hurk, T. Eames, C. Marchand, R. V. Hernandez, M. Kellogg, M. Gorris, B. Galet, V. Palomares, J. Brown, A. G. Bang, J. Mertens, L. Bohnke, L. Boyer, S. Simon, and F. H. Gage. 2015. "Neuronal medium that supports basic synaptic functions and activity of human neurons in vitro." *Proc Natl Acad Sci U S A* 112 (20):E2725-34. doi: 10.1073/pnas.1504393112.

Bassil, F., A. Delamarre, M. H. Canron, N. Dutheil, A. Vital, M. L. Negrier-Leibreich, E. Bezard, P. O. Fernagut, and W. G. Meissner. 2022. "Impaired brain insulin signalling in Parkinson's disease." *Neuropathol Appl Neurobiol* 48 (1):e12760. doi: 10.1111/nan.12760.

Batista, T. M., N. Haider, and C. R. Kahn. 2022. "Correction to: Defining the underlying defect in insulin action in type 2 diabetes." *Diabetologia* 65 (6):1064. doi: 10.1007/s00125-022-05684-8.

Bergman, M., M. Buysschaert, P. E. Schwarz, A. Albright, K. V. Narayan, and D. Yach. 2012. "Diabetes prevention: global health policy and perspectives from the ground." *Diabetes Manag (Lond)* 2 (4):309-321. doi: 10.2217/dmt.12.34.

Billingsley, K. J., I. A. Barbosa, S. Bandres-Ciga, J. P. Quinn, V. J. Bubb, C. Deshpande, J. A. Botia, R. H. Reynolds, D. Zhang, M. A. Simpson, C. Blauwendraat, Z. Gan-Or, J. R. Gibbs, M. A. Nalls, A. Singleton, Consortium International Parkinson's Disease Genomics, M. Ryten, and S. Koks. 2019. "Mitochondria function associated genes contribute to Parkinson's Disease risk and later age at onset." *NPJ Parkinsons Dis* 5:8. doi: 10.1038/s41531-019-0080-x.

Biskup, S., and A. B. West. 2009. "Zeroing in on LRRK2-linked pathogenic mechanisms in Parkinson's disease." *Biochim Biophys Acta* 1792 (7):625-33. doi: 10.1016/j.bbadis.2008.09.015.

Bjorkhem, I., and S. Meaney. 2004. "Brain cholesterol: long secret life behind a barrier." *Arterioscler Thromb Vasc Biol* 24 (5):806-15. doi: 10.1161/01.ATV.0000120374.59826.1b.

Blauwendraat, C., X. Reed, L. Krohn, K. Heilbron, S. Bandres-Ciga, M. Tan, J. R. Gibbs, D. G. Hernandez, R. Kumaran, R. Langston, L. Bonet-Ponce, R. N. Alcalay, S. Hassin-Baer, L. Greenbaum, H. Iwaki, H. L. Leonard, F. P. Grenn, J. A. Ruskey, M. Sabir, S. Ahmed, M. B. Makarious, L. Pihlstrom, M. Toft, J. J. van Hilten, J. Marinus, C. Schulte, K. Brockmann, M. Sharma, A. Siitonen, K. Majamaa, J. Eerola-Rautio, P. J. Tienari, Team andMe Research, A. Pantelyat, A. E. Hillis, T. M. Dawson, L. S. Rosenthal, M. S. Albert, S. M. Resnick, L. Ferrucci, C. M. Morris, O. Pletnikova, J. Troncoso, D. Grosset, S. Lesage, J. C. Corvol, A. Brice, A. J. Noyce, E. Masliah, N. Wood, J. Hardy, L. M. Shulman, J. Jankovic, J. M. Shulman, P. Heutink, T. Gasser, P. Cannon, S. W. Scholz, H. Morris, M. R. Cookson, M. A. Nalls, Z. Gan-Or, and A. B. Singleton. 2020. "Genetic modifiers of risk and age at onset in GBA associated Parkinson's disease and Lewy body dementia." *Brain* 143 (1):234-248. doi: 10.1093/brain/awz350.

Boden, G. 2003. "Effects of free fatty acids (FFA) on glucose metabolism: significance for insulin resistance and type 2 diabetes." *Exp Clin Endocrinol Diabetes* 111 (3):121-4. doi: 10.1055/s-2003-39781.

Bohnen, N. I., V. Kotagal, M. L. Muller, R. A. Koeppe, P. J. Scott, R. L. Albin, K. A. Frey, and M. Petrou. 2014. "Diabetes mellitus is independently associated with more severe cognitive impairment in Parkinson disease." *Parkinsonism Relat Disord* 20 (12):1394-8. doi: 10.1016/j.parkreldis.2014.10.008.

Bolam, J. P., and E. K. Pissadaki. 2012. "Living on the edge with too many mouths to feed: why dopamine neurons die." *Mov Disord* 27 (12):1478-83. doi: 10.1002/mds.25135.

Booth, H. D. E., W. D. Hirst, and R. Wade-Martins. 2017. "The Role of Astrocyte Dysfunction in Parkinson's Disease Pathogenesis." *Trends Neurosci* 40 (6):358-370. doi: 10.1016/j.tins.2017.04.001.

Bose, A., and M. F. Beal. 2016. "Mitochondrial dysfunction in Parkinson's disease." *J Neurochem* 139 Suppl 1:216-231. doi: 10.1111/jnc.13731.

Braak, H., and K. Del Tredici. 2004. "Poor and protracted myelination as a contributory factor to neurodegenerative disorders." *Neurobiol Aging* 25 (1):19-23. doi: 10.1016/j.neurobiolaging.2003.04.001.

Braak, H., E. Ghebremedhin, U. Rub, H. Bratzke, and K. Del Tredici. 2004. "Stages in the development of Parkinson's disease-related pathology." *Cell Tissue Res* 318 (1):121-34. doi: 10.1007/s00441-004-0956-9.

Braak, H., D. Sandmann-Keil, W. Gai, and E. Braak. 1999. "Extensive axonal Lewy neurites in Parkinson's disease: a novel pathological feature revealed by alpha-synuclein immunocytochemistry." *Neurosci Lett* 265 (1):67-9. doi: 10.1016/s0304-3940(99)00208-6.

Brand, M. D., A. L. Orr, I. V. Perevoshchikova, and C. L. Quinlan. 2013. "The role of mitochondrial function and cellular bioenergetics in ageing and disease." *Br J Dermatol* 169 Suppl 2 (0 2):1-8. doi: 10.1111/bjd.12208.

Brauer, R., L. Wei, T. Ma, D. Athauda, C. Girges, N. Vijiaratnam, G. Auld, C. Whittlesea, I. Wong, and T. Foltynie. 2020. "Diabetes medications and risk of Parkinson's disease: a cohort study of patients with diabetes." *Brain* 143 (10):3067-3076. doi: 10.1093/brain/awaa262.

Brunk, E., S. Sahoo, D. C. Zielinski, A. Altunkaya, A. Drager, N. Mih, F. Gatto, A. Nilsson, G. A. Preciat Gonzalez, M. K. Aurich, A. Prlic, A. Sastry, A. D. Danielsdottir, A. Heinken, A. Noronha, P. W. Rose, S. K. Burley, R. M. T. Fleming, J. Nielsen, I. Thiele, and B. O. Palsson. 2018. "Recon3D enables a three-dimensional view of gene variation in human metabolism." *Nat Biotechnol* 36 (3):272-281. doi: 10.1038/nbt.4072.

Cascella, R., S. W. Chen, A. Bigi, J. D. Camino, C. K. Xu, C. M. Dobson, F. Chiti, N. Cremades, and C. Cecchi. 2021. "The release of toxic oligomers from alpha-synuclein fibrils induces dysfunction in neuronal cells." *Nat Commun* 12 (1):1814. doi: 10.1038/s41467-021-21937-3.

Cathery, W., A. Faulkner, D. Maselli, and P. Madeddu. 2018. "Concise Review: The Regenerative Journey of Pericytes Toward Clinical Translation." *Stem Cells* 36 (9):1295-1310. doi: 10.1002/stem.2846.

Caudle, W. M., T. S. Guillot, C. R. Lazo, and G. W. Miller. 2012. "Industrial toxicants and Parkinson's disease." *Neurotoxicology* 33 (2):178-88. doi: 10.1016/j.neuro.2012.01.010.

Cerf, M. E. 2013. "Beta cell dysfunction and insulin resistance." *Front Endocrinol (Lausanne)* 4:37. doi: 10.3389/fendo.2013.00037.

Chambers, S. M., C. A. Fasano, E. P. Papapetrou, M. Tomishima, M. Sadelain, and L. Studer. 2009. "Highly efficient neural conversion of human ES and iPS cells by dual inhibition of SMAD signaling." *Nat Biotechnol* 27 (3):275-80. doi: 10.1038/nbt.1529.

Chandler, R. J., S. Cogo, P. A. Lewis, and E. Kevei. 2021. "Modelling the functional genomics of Parkinson's disease in Caenorhabditis elegans: LRRK2 and beyond." *Biosci Rep* 41 (9). doi: 10.1042/BSR20203672.

Chartier-Harlin, M. C., J. Kachergus, C. Roumier, V. Mouroux, X. Douay, S. Lincoln, C. Levecque, L. Larvor, J. Andrieux, M. Hulihan, N. Waucquier, L. Defebvre, P. Amouyel, M. Farrer, and A. Destee. 2004. "Alpha-synuclein locus duplication as a cause of familial Parkinson's disease." *Lancet* 364 (9440):1167-9. doi: 10.1016/S0140-6736(04)17103-1.

Chaudhary, H., A. N. Stefanovic, V. Subramaniam, and M. M. Claessens. 2014. "Membrane interactions and fibrillization of alpha-synuclein play an essential role in membrane disruption." *FEBS Lett* 588 (23):4457-63. doi: 10.1016/j.febslet.2014.10.016.

Chavez, J. A., M. M. Siddique, S. T. Wang, J. Ching, J. A. Shayman, and S. A. Summers. 2014. "Ceramides and glucosylceramides are independent antagonists of insulin signaling." *J Biol Chem* 289 (2):723-34. doi: 10.1074/jbc.M113.522847.

Cheng, K., L. Martin-Sancho, L. R. Pal, Y. Pu, L. Riva, X. Yin, S. Sinha, N. U. Nair, S. K. Chanda, and E. Ruppin. 2021. "Genome-scale metabolic modeling reveals SARS-CoV-2-induced metabolic changes and antiviral targets." *Mol Syst Biol* 17 (11):e10260. doi: 10.15252/msb.202110260.

Chohan, H., K. Senkevich, R. K. Patel, J. P. Bestwick, B. M. Jacobs, S. Bandres Ciga, Z. Gan-Or, and A. J. Noyce. 2021. "Type 2 Diabetes as a Determinant of Parkinson's Disease Risk and Progression." *Mov Disord* 36 (6):1420-1429. doi: 10.1002/mds.28551.

Collaborators, G. B. D. Parkinson's Disease. 2018. "Global, regional, and national burden of Parkinson's disease, 1990-2016: a systematic analysis for the Global Burden of Disease Study 2016." *Lancet Neurol* 17 (11):939-953. doi: 10.1016/S1474-4422(18)30295-3.

Correia Guedes, L., J. J. Ferreira, M. M. Rosa, M. Coelho, V. Bonifati, and C. Sampaio. 2010. "Worldwide frequency of G2019S LRRK2 mutation in Parkinson's disease: a systematic review." *Parkinsonism Relat Disord* 16 (4):237-42. doi: 10.1016/j.parkreldis.2009.11.004.

Dakic, T., T. Jevdjovic, I. Lakic, A. Ruzicic, N. Jasnic, S. Djurasevic, J. Djordjevic, and P. Vujovic. 2023. "The Expression of Insulin in the Central Nervous System: What Have We Learned So Far?" *Int J Mol Sci* 24 (7). doi: 10.3390/ijms24076586.

Damier, P., E. C. Hirsch, Y. Agid, and A. M. Graybiel. 1999. "The substantia nigra of the human brain. II. Patterns of loss of dopamine-containing neurons in Parkinson's disease." *Brain* 122 (Pt 8):1437-48. doi: 10.1093/brain/122.8.1437.

Day, J. O., and S. Mullin. 2021. "The Genetics of Parkinson's Disease and Implications for Clinical Practice." *Genes (Basel)* 12 (7). doi: 10.3390/genes12071006.

de la Mata, M., D. Cotan, M. Oropesa-Avila, J. Garrido-Maraver, M. D. Cordero, M. Villanueva Paz, A. Delgado Pavon, E. Alcocer-Gomez, I. de Lavera, P. Ybot-Gonzalez, A. Paula Zaderenko, C. Ortiz Mellet, J. M. Garcia Fernandez, and J. A. Sanchez-Alcazar. 2015. "Pharmacological Chaperones and Coenzyme Q10 Treatment Improves Mutant beta-Glucocerebrosidase Activity and Mitochondrial Function in Neuronopathic Forms of Gaucher Disease." *Sci Rep* 5:10903. doi: 10.1038/srep10903.

De Meyts, P. 2000. "The Insulin Receptor and Its Signal Transduction Network." In *Endotext*, edited by K. R. Feingold, B. Anawalt, M. R. Blackman, A. Boyce, G. Chrousos, E. Corpas, W. W. de Herder, K. Dhatariya, K. Dungan, J. Hofland, S. Kalra, G. Kaltsas, N. Kapoor, C. Koch, P. Kopp, M. Korbonits, C. S. Kovacs, W. Kuohung, B. Laferrere, M. Levy, E. A. McGee, R. McLachlan, M. New, J. Purnell, R. Sahay, A. S. Shah, F. Singer, M. A. Sperling, C. A. Stratakis, D. L. Trence and D. P. Wilson. South Dartmouth (MA).

De Pablo-Fernandez, E., R. Goldacre, J. Pakpoor, A. J. Noyce, and T. T. Warner. 2018. "Association between diabetes and subsequent Parkinson disease: A record-linkage cohort study." *Neurology* 91 (2):e139-e142. doi: 10.1212/WNL.0000000000005771.

de Rus Jacquet, A., M. Alpaugh, H. L. Denis, J. L. Tancredi, M. Boutin, J. Decaestecker, C. Beauparlant, L. Herrmann, M. Saint-Pierre, M. Parent, A. Droit, S. Breton, and F. Cicchetti. 2023. "The contribution

of inflammatory astrocytes to BBB impairments in a brain-chip model of Parkinson's disease." *Nat Commun* 14 (1):3651. doi: 10.1038/s41467-023-39038-8.

DeBose-Boyd, R. A., and J. Ye. 2018. "SREBPs in Lipid Metabolism, Insulin Signaling, and Beyond." *Trends Biochem Sci* 43 (5):358-368. doi: 10.1016/j.tibs.2018.01.005.

Delic, V., K. D. Beck, K. C. H. Pang, and B. A. Citron. 2020. "Biological links between traumatic brain injury and Parkinson's disease." *Acta Neuropathol Commun* 8 (1):45. doi: 10.1186/s40478-020-00924-7.

Do, J., C. McKinney, P. Sharma, and E. Sidransky. 2019. "Glucocerebrosidase and its relevance to Parkinson disease." *Mol Neurodegener* 14 (1):36. doi: 10.1186/s13024-019-0336-2.

Doege, H., A. Schurmann, G. Bahrenberg, A. Brauers, and H. G. Joost. 2000. "GLUT8, a novel member of the sugar transport facilitator family with glucose transport activity." *J Biol Chem* 275 (21):16275-80. doi: 10.1074/jbc.275.21.16275.

Doorn, K. J., T. Moors, B. Drukarch, WDj van de Berg, P. J. Lucassen, and A. M. van Dam. 2014. "Microglial phenotypes and toll-like receptor 2 in the substantia nigra and hippocampus of incidental Lewy body disease cases and Parkinson's disease patients." *Acta Neuropathol Commun* 2:90. doi: 10.1186/s40478-014-0090-1.

Dorn, A., A. Rinne, H. G. Bernstein, H. J. Hahn, and M. Ziegler. 1983. "Insulin and C-peptide in human brain neurons (insulin/C-peptide/brain peptides/immunohistochemistry/radioimmunoassay)." *J Hirnforsch* 24 (5):495-9.

Duarte, A. I., P. I. Moreira, and C. R. Oliveira. 2012. "Insulin in central nervous system: more than just a peripheral hormone." *J Aging Res* 2012:384017. doi: 10.1155/2012/384017.

Eagle, H. 1959. "Amino acid metabolism in mammalian cell cultures." *Science* 130 (3373):432-7. doi: 10.1126/science.130.3373.432.

Ebrahimi-Fakhari, D., L. Wahlster, and P. J. McLean. 2012. "Protein degradation pathways in Parkinson's disease: curse or blessing." *Acta Neuropathol* 124 (2):153-72. doi: 10.1007/s00401-012-1004-6.

El Messari, S., C. Leloup, M. Quignon, M. J. Brisorgueil, L. Penicaud, and M. Arluison. 1998. "Immunocytochemical localization of the insulin-responsive glucose transporter 4 (Glut4) in the rat central nervous system." *J Comp Neurol* 399 (4):492-512. doi: 10.1002/(sici)1096-9861(19981005)399:4<492::aid-cne4>3.0.co;2-x.

Emmanuel, Y., L. E. Cochlin, D. J. Tyler, C. A. de Jager, A. D. Smith, and K. Clarke. 2013. "Human hippocampal energy metabolism is impaired during cognitive activity in a lipid infusion model of insulin resistance." *Brain Behav* 3 (2):134-44. doi: 10.1002/brb3.124.

Evans, J. L., B. A. Maddux, and I. D. Goldfine. 2005. "The molecular basis for oxidative stress-induced insulin resistance." *Antioxid Redox Signal* 7 (7-8):1040-52. doi: 10.1089/ars.2005.7.1040.

Falkenburger, B. H., T. Saridaki, and E. Dinter. 2016. "Cellular models for Parkinson's disease." *J Neurochem* 139 Suppl 1:121-130. doi: 10.1111/jnc.13618.

Fearnley, J. M., and A. J. Lees. 1991. "Ageing and Parkinson's disease: substantia nigra regional selectivity." *Brain* 114 (Pt 5):2283-301. doi: 10.1093/brain/114.5.2283.

Fernandes, H. J., E. M. Hartfield, H. C. Christian, E. Emmanoulidou, Y. Zheng, H. Booth, H. Bogetofte, C. Lang, B. J. Ryan, S. P. Sardi, J. Badger, J. Vowles, S. Evetts, G. K. Tofaris, K. Vekrellis, K. Talbot, M. T. Hu, W. James, S. A. Cowley, and R. Wade-Martins. 2016. "ER Stress and Autophagic Perturbations Lead to Elevated Extracellular alpha-Synuclein in GBA-N370S Parkinson's iPSC-Derived Dopamine Neurons." *Stem Cell Reports* 6 (3):342-56. doi: 10.1016/j.stemcr.2016.01.013.

Ferrari, E., A. Cardinale, B. Picconi, and F. Gardoni. 2020. "From cell lines to pluripotent stem cells for modelling Parkinson's Disease." *J Neurosci Methods* 340:108741. doi: 10.1016/j.jneumeth.2020.108741.

Fiorenzano, A., E. Sozzi, M. Birtele, J. Kajtez, J. Giacomoni, F. Nilsson, A. Bruzelius, Y. Sharma, Y. Zhang, B. Mattsson, J. Emneus, D. R. Ottosson, P. Storm, and M. Parmar. 2022. "Author Correction: Single-cell transcriptomics captures features of human midbrain development and dopamine neuron diversity in brain organoids." *Nat Commun* 13 (1):3312. doi: 10.1038/s41467-022-31024-w.

Flones, I. H., E. Fernandez-Vizarra, M. Lykouri, B. Brakedal, G. O. Skeie, H. Miletic, P. K. Lilleng, G. Alves, O. B. Tysnes, K. Haugarvoll, C. Dolle, M. Zeviani, and C. Tzoulis. 2018. "Neuronal complex I deficiency occurs throughout the Parkinson's disease brain, but is not associated with neurodegeneration or mitochondrial DNA damage." *Acta Neuropathol* 135 (3):409-425. doi: 10.1007/s00401-017-1794-7.

Flores-Leon, M., and T. F. Outeiro. 2023. "More than meets the eye in Parkinson's disease and other synucleinopathies: from proteinopathy to lipidopathy." *Acta Neuropathol*. doi: 10.1007/s00401-023-02601-0.

Franks, P. W., C. Scheele, R. J. Loos, A. R. Nielsen, F. M. Finucane, C. Wahlestedt, B. K. Pedersen, N. J. Wareham, and J. A. Timmons. 2008. "Genomic variants at the PINK1 locus are associated with transcript abundance and plasma nonesterified fatty acid concentrations in European whites." *FASEB J* 22 (9):3135-45. doi: 10.1096/fj.08-107086.

Fusco, G., S. W. Chen, P. T. F. Williamson, R. Cascella, M. Perni, J. A. Jarvis, C. Cecchi, M. Vendruscolo, F. Chiti, N. Cremades, L. Ying, C. M. Dobson, and A. De Simone. 2017. "Structural basis of membrane disruption and cellular toxicity by alpha-synuclein oligomers." *Science* 358 (6369):1440-1443. doi: 10.1126/science.aan6160.

Gai, W. P., H. X. Yuan, X. Q. Li, J. T. Power, P. C. Blumbergs, and P. H. Jensen. 2000. "In situ and in vitro study of colocalization and segregation of alpha-synuclein, ubiquitin, and lipids in Lewy bodies." *Exp Neurol* 166 (2):324-33. doi: 10.1006/exnr.2000.7527.

Galaviz, K. I., K. M. V. Narayan, F. Lobelo, and M. B. Weber. 2018. "Lifestyle and the Prevention of Type 2 Diabetes: A Status Report." *Am J Lifestyle Med* 12 (1):4-20. doi: 10.1177/1559827615619159.

Galet, B., H. Cheval, and P. Ravassard. 2020. "Patient-Derived Midbrain Organoids to Explore the Molecular Basis of Parkinson's Disease." *Front Neurol* 11:1005. doi: 10.3389/fneur.2020.01005.

Galper, J., N. J. Dean, R. Pickford, S. J. G. Lewis, G. M. Halliday, W. S. Kim, and N. Dzamko. 2022. "Lipid pathway dysfunction is prevalent in patients with Parkinson's disease." *Brain* 145 (10):3472-3487. doi: 10.1093/brain/awac176.

Galvagnion, C., J. W. Brown, M. M. Ouberai, P. Flagmeier, M. Vendruscolo, A. K. Buell, E. Sparr, and C. M. Dobson. 2016. "Chemical properties of lipids strongly affect the kinetics of the membrane-induced aggregation of alpha-synuclein." *Proc Natl Acad Sci U S A* 113 (26):7065-70. doi: 10.1073/pnas.1601899113.

Gao, J., G. Perera, M. Bhadbhade, G. M. Halliday, and N. Dzamko. 2019. "Autophagy activation promotes clearance of alpha-synuclein inclusions in fibril-seeded human neural cells." *J Biol Chem* 294 (39):14241-14256. doi: 10.1074/jbc.RA119.008733.

Ge, P., V. L. Dawson, and T. M. Dawson. 2020. "PINK1 and Parkin mitochondrial quality control: a source of regional vulnerability in Parkinson's disease." *Mol Neurodegener* 15 (1):20. doi: 10.1186/s13024-020-00367-7.

Gegg, M. E., D. Burke, S. J. Heales, J. M. Cooper, J. Hardy, N. W. Wood, and A. H. Schapira. 2012. "Glucocerebrosidase deficiency in substantia nigra of parkinson disease brains." *Ann Neurol* 72 (3):455-63. doi: 10.1002/ana.23614.

Ghosh, N., N. Patel, K. Jiang, J. E. Watson, J. Cheng, C. E. Chalfant, and D. R. Cooper. 2007. "Ceramide-activated protein phosphatase involvement in insulin resistance via Akt, serine/arginine-rich protein 40, and ribonucleic acid splicing in L6 skeletal muscle cells." *Endocrinology* 148 (3):1359-66. doi: 10.1210/en.2006-0750.

Ginns, E. I., S. K. Mak, N. Ko, J. Karlgren, S. Akbarian, V. P. Chou, Y. Guo, A. Lim, S. Samuelsson, M. L. LaMarca, J. Vazquez-DeRose, and A. B. Manning-Bog. 2014. "Neuroinflammation and alpha-synuclein accumulation in response to glucocerebrosidase deficiency are accompanied by synaptic dysfunction." *Mol Genet Metab* 111 (2):152-62. doi: 10.1016/j.ymgme.2013.12.003.

Golikov, M. V., V. T. Valuev-Elliston, O. A. Smirnova, and A. V. Ivanov. 2022. "Physiological Media in Studies of Cell Metabolism." *Mol Biol* 56 (5):629-637. doi: 10.1134/S0026893322050077.

Gonzalez, P., P. Lozano, G. Ros, and F. Solano. 2023. "Hyperglycemia and Oxidative Stress: An Integral, Updated and Critical Overview of Their Metabolic Interconnections." *Int J Mol Sci* 24 (11). doi: 10.3390/ijms24119352.

Gray, S. M., and E. J. Barrett. 2018. "Insulin transport into the brain." *Am J Physiol Cell Physiol* 315 (2):C125-C136. doi: 10.1152/ajpcell.00240.2017.

Gray, S. M., R. I. Meijer, and E. J. Barrett. 2014. "Insulin regulates brain function, but how does it get there?" *Diabetes* 63 (12):3992-7. doi: 10.2337/db14-0340.

Grunblatt, E., S. Mandel, J. Jacob-Hirsch, S. Zeligson, N. Amariglo, G. Rechavi, J. Li, R. Ravid, W. Roggendorf, P. Riederer, and M. B. Youdim. 2004. "Gene expression profiling of parkinsonian substantia nigra pars compacta; alterations in ubiquitin-proteasome, heat shock protein, iron and oxidative stress regulated proteins, cell adhesion/cellular matrix and vesicle trafficking genes." *J Neural Transm (Vienna)* 111 (12):1543-73. doi: 10.1007/s00702-004-0212-1.

Grunewald, A., K. R. Kumar, and C. M. Sue. 2019. "New insights into the complex role of mitochondria in Parkinson's disease." *Prog Neurobiol* 177:73-93. doi: 10.1016/j.pneurobio.2018.09.003.

Gudmundsson, S., and I. Thiele. 2010. "Computationally efficient flux variability analysis." *BMC Bioinformatics* 11:489. doi: 10.1186/1471-2105-11-489.

Guo, C., L. Sun, X. Chen, and D. Zhang. 2013. "Oxidative stress, mitochondrial damage and neurodegenerative diseases." *Neural Regen Res* 8 (21):2003-14. doi: 10.3969/j.issn.1673-5374.2013.21.009.

Hallschmid, M., and B. Schultes. 2009. "Central nervous insulin resistance: a promising target in the treatment of metabolic and cognitive disorders?" *Diabetologia* 52 (11):2264-9. doi: 10.1007/s00125-009-1501-x.

Hamilton, J. A., C. J. Hillard, A. A. Spector, and P. A. Watkins. 2007. "Brain uptake and utilization of fatty acids, lipids and lipoproteins: application to neurological disorders." *J Mol Neurosci* 33 (1):2-11. doi: 10.1007/s12031-007-0060-1.

Hammerschmidt, P., and J. C. Bruning. 2022. "Contribution of specific ceramides to obesity-associated metabolic diseases." *Cell Mol Life Sci* 79 (8):395. doi: 10.1007/s00018-022-04401-3.

Han, K., B. Kim, S. H. Lee, and M. K. Kim. 2023. "A nationwide cohort study on diabetes severity and risk of Parkinson disease." *NPJ Parkinsons Dis* 9 (1):11. doi: 10.1038/s41531-023-00462-8.

Hartmann, A. 2004. "Postmortem studies in Parkinson's disease." *Dialogues Clin Neurosci* 6 (3):281-93. doi: 10.31887/DCNS.2004.6.3/ahartmann.

Hijaz, B. A., and L. A. Volpicelli-Daley. 2020. "Initiation and propagation of alpha-synuclein aggregation in the nervous system." *Mol Neurodegener* 15 (1):19. doi: 10.1186/s13024-020-00368-6.

Hogg, E., K. Athreya, C. Basile, E. E. Tan, J. Kaminski, and M. Tagliati. 2018. "High Prevalence of Undiagnosed Insulin Resistance in Non-Diabetic Subjects with Parkinson's Disease." *J Parkinsons Dis* 8 (2):259-265. doi: 10.3233/JPD-181305.

Hopkins, D. F., and G. Williams. 1997. "Insulin receptors are widely distributed in human brain and bind human and porcine insulin with equal affinity." *Diabet Med* 14 (12):1044-50. doi: 10.1002/(SICI)1096-9136(199712)14:12<1044::AID-DIA508>3.0.CO;2-F.

Hussain, G., J. Wang, A. Rasul, H. Anwar, A. Imran, M. Qasim, S. Zafar, S. K. S. Kamran, A. Razzaq, N. Aziz, W. Ahmad, A. Shabbir, J. Iqbal, S. M. Baig, and T. Sun. 2019. "Role of cholesterol and sphingolipids in brain development and neurological diseases." *Lipids Health Dis* 18 (1):26. doi: 10.1186/s12944-019-0965-z.

Hustad, E., and J. O. Aasly. 2020. "Clinical and Imaging Markers of Prodromal Parkinson's Disease." *Front Neurol* 11:395. doi: 10.3389/fneur.2020.00395.

Hwang, I. K., J. H. Choi, S. M. Nam, O. K. Park, D. Y. Yoo, W. Kim, S. S. Yi, M. H. Won, J. K. Seong, and Y. S. Yoon. 2014. "Activation of microglia and induction of pro-inflammatory cytokines in the hippocampus of type 2 diabetic rats." *Neurol Res* 36 (9):824-32. doi: 10.1179/1743132814Y.0000000330.

Isik, S., B. Yeman Kiyak, R. Akbayir, R. Seyhali, and T. Arpaci. 2023. "Microglia Mediated Neuroinflammation in Parkinson's Disease." *Cells* 12 (7). doi: 10.3390/cells12071012.

Jankovic, J., and E. K. Tan. 2020. "Parkinson's disease: etiopathogenesis and treatment." *J Neurol Neurosurg Psychiatry* 91 (8):795-808. doi: 10.1136/jnnp-2019-322338.

Jo, J., Y. Xiao, A. X. Sun, E. Cukuroglu, H. D. Tran, J. Goke, Z. Y. Tan, T. Y. Saw, C. P. Tan, H. Lokman, Y. Lee, D. Kim, H. S. Ko, S. O. Kim, J. H. Park, N. J. Cho, T. M. Hyde, J. E. Kleinman, J. H. Shin, D. R. Weinberger, E. K. Tan, H. S. Je, and H. H. Ng. 2016. "Midbrain-like Organoids from Human Pluripotent Stem Cells Contain Functional Dopaminergic and Neuromelanin-Producing Neurons." *Cell Stem Cell* 19 (2):248-257. doi: 10.1016/j.stem.2016.07.005.

Kalia, L. V., and A. E. Lang. 2016. "Parkinson disease in 2015: Evolving basic, pathological and clinical concepts in PD." *Nat Rev Neurol* 12 (2):65-6. doi: 10.1038/nrneurol.2015.249.

Kelley, D. E., J. He, E. V. Menshikova, and V. B. Ritov. 2002. "Dysfunction of mitochondria in human skeletal muscle in type 2 diabetes." *Diabetes* 51 (10):2944-50. doi: 10.2337/diabetes.51.10.2944.

Khan, R. M. M., Z. J. Y. Chua, J. C. Tan, Y. Yang, Z. Liao, and Y. Zhao. 2019. "From Pre-Diabetes to Diabetes: Diagnosis, Treatments and Translational Research." *Medicina (Kaunas)* 55 (9). doi: 10.3390/medicina55090546.

Kilpelainen, T., U. H. Julku, R. Svarcbahs, and T. T. Myohanen. 2019. "Behavioural and dopaminergic changes in double mutated human A30P*A53T alpha-synuclein transgenic mouse model of Parkinson s disease." *Sci Rep* 9 (1):17382. doi: 10.1038/s41598-019-54034-z.

Klein, C., and A. Westenberger. 2012. "Genetics of Parkinson's disease." *Cold Spring Harb Perspect Med* 2 (1):a008888. doi: 10.1101/cshperspect.a008888.

Koepsell, H. 2020. "Glucose transporters in brain in health and disease." *Pflugers Arch* 472 (9):1299-1343. doi: 10.1007/s00424-020-02441-x.

Konishi, M., M. Sakaguchi, S. M. Lockhart, W. Cai, M. E. Li, E. P. Homan, C. Rask-Madsen, and C. R. Kahn. 2017. "Endothelial insulin receptors differentially control insulin signaling kinetics in peripheral tissues and brain of mice." *Proc Natl Acad Sci U S A* 114 (40):E8478-E8487. doi: 10.1073/pnas.1710625114.

Konnova, E. A., and M. Swanberg. 2018. "Animal Models of Parkinson's Disease." In *Parkinson's Disease: Pathogenesis and Clinical Aspects*, edited by T. B. Stoker and J. C. Greenland. Brisbane (AU).

Kotagal, V., R. L. Albin, M. L. Muller, R. A. Koeppe, K. A. Frey, and N. I. Bohnen. 2013. "Diabetes is associated with postural instability and gait difficulty in Parkinson disease." *Parkinsonism Relat Disord* 19 (5):522-6. doi: 10.1016/j.parkreldis.2013.01.016.

Kotwas, A., B. Karakiewicz, P. Zabielska, S. Wieder-Huszla, and A. Jurczak. 2021. "Epidemiological factors for type 2 diabetes mellitus: evidence from the Global Burden of Disease." *Arch Public Health* 79 (1):110. doi: 10.1186/s13690-021-00632-1.

Kouli, A., K. M. Torsney, and W. L. Kuan. 2018. "Parkinson's Disease: Etiology, Neuropathology, and Pathogenesis." In *Parkinson's Disease: Pathogenesis and Clinical Aspects*, edited by T. B. Stoker and J. C. Greenland. Brisbane (AU).

Kumar, P., T. Raman, M. M. Swain, R. Mishra, and A. Pal. 2017. "Hyperglycemia-Induced Oxidative-Nitrosative Stress Induces Inflammation and Neurodegeneration via Augmented Tuberous Sclerosis Complex-2 (TSC-2) Activation in Neuronal Cells." *Mol Neurobiol* 54 (1):238-254. doi: 10.1007/s12035-015-9667-3.

Kwon, H. S., and S. H. Koh. 2020. "Neuroinflammation in neurodegenerative disorders: the roles of microglia and astrocytes." *Transl Neurodegener* 9 (1):42. doi: 10.1186/s40035-020-00221-2.

La Manno, G., D. Gyllborg, S. Codeluppi, K. Nishimura, C. Salto, A. Zeisel, L. E. Borm, S. R. W. Stott, E. M. Toledo, J. C. Villaescusa, P. Lonnerberg, J. Ryge, R. A. Barker, E. Arenas, and S. Linnarsson. 2016. "Molecular Diversity of Midbrain Development in Mouse, Human, and Stem Cells." *Cell* 167 (2):566-580 e19. doi: 10.1016/j.cell.2016.09.027.

Lancaster, M. A., M. Renner, C. A. Martin, D. Wenzel, L. S. Bicknell, M. E. Hurles, T. Homfray, J. M. Penninger, A. P. Jackson, and J. A. Knoblich. 2013. "Cerebral organoids model human brain development and microcephaly." *Nature* 501 (7467):373-9. doi: 10.1038/nature12517.

Lee, C. T., R. M. Bendriem, W. W. Wu, and R. F. Shen. 2017. "3D brain Organoids derived from pluripotent stem cells: promising experimental models for brain development and neurodegenerative disorders." *J Biomed Sci* 24 (1):59. doi: 10.1186/s12929-017-0362-8.

Leloup, C., M. Arluison, N. Kassis, N. Lepetit, N. Cartier, P. Ferre, and L. Penicaud. 1996. "Discrete brain areas express the insulin-responsive glucose transporter GLUT4." *Brain Res Mol Brain Res* 38 (1):45-53. doi: 10.1016/0169-328x(95)00306-d.

Liu, X., N. Yamada, W. Maruyama, and T. Osawa. 2008. "Formation of dopamine adducts derived from brain polyunsaturated fatty acids: mechanism for Parkinson disease." *J Biol Chem* 283 (50):34887-95. doi: 10.1074/jbc.M805682200.

Lo Sardo, V., W. Ferguson, G. A. Erikson, E. J. Topol, K. K. Baldwin, and A. Torkamani. 2017. "Influence of donor age on induced pluripotent stem cells." *Nat Biotechnol* 35 (1):69-74. doi: 10.1038/nbt.3749.

Loddo, G., G. Calandra-Buonaura, L. Sambati, G. Giannini, A. Cecere, P. Cortelli, and F. Provini. 2017. "The Treatment of Sleep Disorders in Parkinson's Disease: From Research to Clinical Practice." *Front Neurol* 8:42. doi: 10.3389/fneur.2017.00042.

Lopes, K. P., G. J. L. Snijders, J. Humphrey, A. Allan, M. A. M. Sneeboer, E. Navarro, B. M. Schilder, R. A. Vialle, M. Parks, R. Missall, W. van Zuiden, F. A. J. Gigase, R. Kubler, A. B. van Berlekom, E. M. Hicks, C. Böttcher, J. Priller, R. S. Kahn, L. D. de Witte, and T. Raj. 2022. "Genetic analysis of the human microglial transcriptome across brain regions, aging and disease pathologies." *Nat Genet* 54 (1):4-17. doi: 10.1038/s41588-021-00976-y.

Ma, C. X., X. N. Ma, C. H. Guan, Y. D. Li, D. Mauricio, and S. B. Fu. 2022. "Cardiovascular disease in type 2 diabetes mellitus: progress toward personalized management." *Cardiovasc Diabetol* 21 (1):74. doi: 10.1186/s12933-022-01516-6.

Mahul-Mellier, A. L., J. Burtscher, N. Maharjan, L. Weerens, M. Croisier, F. Kuttler, M. Leleu, G. W. Knott, and H. A. Lashuel. 2020. "The process of Lewy body formation, rather than simply alpha-synuclein fibrillization, is one of the major drivers of neurodegeneration." *Proc Natl Acad Sci U S A* 117 (9):4971-4982. doi: 10.1073/pnas.1913904117.

Marin de Mas, I., E. Aguilar, E. Zodda, C. Balcells, S. Marin, G. Dallmann, T. M. Thomson, B. Papp, and M. Cascante. 2018. "Model-driven discovery of long-chain fatty acid metabolic reprogramming in

heterogeneous prostate cancer cells." *PLoS Comput Biol* 14 (1):e1005914. doi: 10.1371/journal.pcbi.1005914.

Matikainen-Ankney, B. A., N. Kezunovic, R. E. Mesias, Y. Tian, F. M. Williams, G. W. Huntley, and D. L. Benson. 2016. "Altered Development of Synapse Structure and Function in Striatum Caused by Parkinson's Disease-Linked LRRK2-G2019S Mutation." *J Neurosci* 36 (27):7128-41. doi: 10.1523/JNEUROSCI.3314-15.2016.

McGarrity, S., O. Anuforo, H. Halldorsson, A. Bergmann, S. Halldorsson, S. Palsson, H. H. Henriksen, P. I. Johansson, and O. Rolfsson. 2018. "Metabolic systems analysis of LPS induced endothelial dysfunction applied to sepsis patient stratification." *Sci Rep* 8 (1):6811. doi: 10.1038/s41598-018-25015-5.

McGeer, P. L., S. Itagaki, B. E. Boyes, and E. G. McGeer. 1988. "Reactive microglia are positive for HLA-DR in the substantia nigra of Parkinson's and Alzheimer's disease brains." *Neurology* 38 (8):1285-91. doi: 10.1212/wnl.38.8.1285.

McNaught, K. S., R. Belizaire, O. Isacson, P. Jenner, and C. W. Olanow. 2003. "Altered proteasomal function in sporadic Parkinson's disease." *Exp Neurol* 179 (1):38-46. doi: 10.1006/exnr.2002.8050.

Menegas, W., J. F. Bergan, S. K. Ogawa, Y. Isogai, K. Umadevi Venkataraju, P. Osten, N. Uchida, and M. Watabe-Uchida. 2015. "Dopamine neurons projecting to the posterior striatum form an anatomically distinct subclass." *Elife* 4:e10032. doi: 10.7554/eLife.10032.

Meng, L., Y. Li, C. Liu, G. Zhang, J. Chen, M. Xiong, L. Pan, X. Zhang, G. Chen, J. Xiong, C. Liu, X. Xu, L. Bu, Z. Zhang, and Z. Zhang. 2023. "Islet amyloid polypeptide triggers alpha-synuclein pathology in Parkinson's disease." *Prog Neurobiol* 226:102462. doi: 10.1016/j.pneurobio.2023.102462.

Miller, J. D., Y. M. Ganat, S. Kishinevsky, R. L. Bowman, B. Liu, E. Y. Tu, P. K. Mandal, E. Vera, J. W. Shim, S. Kriks, T. Taldone, N. Fusaki, M. J. Tomishima, D. Krainc, T. A. Milner, D. J. Rossi, and L. Studer. 2013. "Human iPSC-based modeling of late-onset disease via progerin-induced aging." *Cell Stem Cell* 13 (6):691-705. doi: 10.1016/j.stem.2013.11.006.

Milosevic, J., S. C. Schwarz, V. Ogunlade, A. K. Meyer, A. Storch, and J. Schwarz. 2009. "Emerging role of LRRK2 in human neural progenitor cell cycle progression, survival and differentiation." *Mol Neurodegener* 4:25. doi: 10.1186/1750-1326-4-25.

Milstein, J. L., and H. A. Ferris. 2021. "The brain as an insulin-sensitive metabolic organ." *Mol Metab* 52:101234. doi: 10.1016/j.molmet.2021.101234.

Miranda, H. V., E. M. Szego, L. M. A. Oliveira, C. Breda, E. Darendelioglu, R. M. de Oliveira, D. G. Ferreira, M. A. Gomes, R. Rott, M. Oliveira, F. Munari, F. J. Enguita, T. Simoes, E. F. Rodrigues, M. Heinrich, I. C. Martins, I. Zamolo, O. Riess, C. Cordeiro, A. Ponces-Freire, H. A. Lashuel, N. C. Santos, L. V. Lopes, W. Xiang, T. M. Jovin, D. Penque, S. Engelender, M. Zweckstetter, J. Klucken, F. Giorgini, A. Quintas, and T. F. Outeiro. 2021. "Erratum to: Glycation potentiates alpha-synuclein-associated neurodegeneration in synucleinopathies." *Brain* 144 (6):e58. doi: 10.1093/brain/awab175.

Mita, Y., Y. Kataoka, Y. Saito, T. Kashi, K. Hayashi, A. Iwasaki, T. Imanishi, T. Miyasaka, and N. Noguchi. 2018. "Distribution of oxidized DJ-1 in Parkinson's disease-related sites in the brain and in the peripheral tissues: effects of aging and a neurotoxin." *Sci Rep* 8 (1):12056. doi: 10.1038/s41598-018-30561-z.

Monzel, A. S., K. Hemmer, T. Kaoma, L. M. Smits, S. Bolognin, P. Lucarelli, I. Rosety, A. Zagare, P. Antony, S. L. Nickels, R. Krueger, F. Azuaje, and J. C. Schwamborn. 2020. "Machine learning-assisted neurotoxicity prediction in human midbrain organoids." *Parkinsonism Relat Disord* 75:105-109. doi: 10.1016/j.parkreldis.2020.05.011.

Monzel, A. S., L. M. Smits, K. Hemmer, S. Hachi, E. L. Moreno, T. van Wuellen, J. Jarazo, J. Walter, I. Bruggemann, I. Boussaad, E. Berger, R. M. T. Fleming, S. Bolognin, and J. C. Schwamborn. 2017. "Derivation of Human Midbrain-Specific Organoids from Neuroepithelial Stem Cells." *Stem Cell Reports* 8 (5):1144-1154. doi: 10.1016/j.stemcr.2017.03.010.

Mucibabic, M., P. Steneberg, E. Lidh, J. Straseviciene, A. Ziolkowska, U. Dahl, E. Lindahl, and H. Edlund. 2020. "alpha-Synuclein promotes IAPP fibril formation in vitro and beta-cell amyloid formation in vivo in mice." *Sci Rep* 10 (1):20438. doi: 10.1038/s41598-020-77409-z.

Muguruma, K., A. Nishiyama, H. Kawakami, K. Hashimoto, and Y. Sasai. 2015. "Self-organization of polarized cerebellar tissue in 3D culture of human pluripotent stem cells." *Cell Rep* 10 (4):537-50. doi: 10.1016/j.celrep.2014.12.051.

Mukherjee, A., D. Morales-Scheihing, N. Salvadores, I. Moreno-Gonzalez, C. Gonzalez, K. Taylor-Presse, N. Mendez, M. Shahnawaz, A. O. Gaber, O. M. Sabek, D. W. Fraga, and C. Soto. 2017. "Induction of IAPP amyloid deposition and associated diabetic abnormalities by a prion-like mechanism." *J Exp Med* 214 (9):2591-2610. doi: 10.1084/jem.20161134.

Münch, G., Lüth, H. J., Wong, A., Arendt, T., Hirsch, E., Ravid, R., & Riederer, P. 2000. "Crosslinking of α-synuclein by advanced glycation endproducts — an early pathophysiological step in Lewy body formation? ." *Journal of Chemical Neuroanatomy* 20(3-4):253-257.

Muslimat Kehinde, Adebisi, Teddy Ehianeta, Salim Mzee Said Abdulraman, Liuyi, Mahmud Abdul Nazif, Kanton Aaron Gia, and Mustapha Abdullateef Taiye. 2019. "Obesity may Increase the Prevalence of Parkinson's Disease while Parkinson's may Reduce Obesity Index in Patients." *International Journal of Neurodegenerative Disorders* 2 (1). doi: 10.23937/2643-4539/1710012.

Mutskov, V., and G. Felsenfeld. 2009. "The human insulin gene is part of a large open chromatin domain specific for human islets." *Proc Natl Acad Sci U S A* 106 (41):17419-24. doi: 10.1073/pnas.0909288106.

Nagayach, A., N. Patro, and I. Patro. 2014. "Astrocytic and microglial response in experimentally induced diabetic rat brain." *Metab Brain Dis* 29 (3):747-61. doi: 10.1007/s11011-014-9562-z.

Nascimento, A. C., A. G. Erustes, P. Reckziegel, C. Bincoletto, R. P. Ureshino, G. J. S. Pereira, and S. S. Smaili. 2020. "alpha-Synuclein Overexpression Induces Lysosomal Dysfunction and Autophagy Impairment in Human Neuroblastoma SH-SY5Y." *Neurochem Res* 45 (11):2749-2761. doi: 10.1007/s11064-020-03126-8.

Navarro-Romero, A., I. Fernandez-Gonzalez, J. Riera, M. Montpeyo, M. Albert-Bayo, T. Lopez-Royo, P. Castillo-Sanchez, C. Carnicer-Caceres, J. A. Arranz-Amo, L. Castillo-Ribelles, E. Pradas, J. Casas, M. Vila, and M. Martinez-Vicente. 2022. "Lysosomal lipid alterations caused by glucocerebrosidase deficiency promote lysosomal dysfunction, chaperone-mediated-autophagy deficiency, and alpha-synuclein pathology." *NPJ Parkinsons Dis* 8 (1):126. doi: 10.1038/s41531-022-00397-6.

Navarro, E., E. Udine, K. de Paiva Lopes, M. Parks, G. Riboldi, B. M. Schilder, J. Humphrey, G. J. L. Snijders, R. A. Vialle, M. Zhuang, T. Sikder, C. Argyrou, A. Allan, M. J. Chao, K. Farrell, B. Henderson, S. Simon, D. Raymond, S. Elango, R. A. Ortega, V. Shanker, M. Swan, C. W. Zhu, R. Ramdhani, R. H. Walker, W. Tse, M. Sano, A. C. Pereira, T. Ahfeldt, A. M. Goate, S. Bressman, J. F. Crary, L. de Witte, S. Frucht, R. Saunders-Pullman, and T. Raj. 2021. "Dysregulation of mitochondrial and proteolysosomal genes in Parkinson's disease myeloid cells." *Nat Aging* 1 (9):850-863. doi: 10.1038/s43587-021-00110-x.

Ni, A., and C. Ernst. 2022. "Evidence That Substantia Nigra Pars Compacta Dopaminergic Neurons Are Selectively Vulnerable to Oxidative Stress Because They Are Highly Metabolically Active." *Front Cell Neurosci* 16:826193. doi: 10.3389/fncel.2022.826193.

Nickels, S. L., J. Modamio, B. Mendes-Pinheiro, A. S. Monzel, F. Betsou, and J. C. Schwamborn. 2020. "Reproducible generation of human midbrain organoids for in vitro modeling of Parkinson's disease." *Stem Cell Res* 46:101870. doi: 10.1016/j.scr.2020.101870.

Nonnekes, J., B. Post, J. W. Tetrud, J. W. Langston, and B. R. Bloem. 2018. "MPTP-induced parkinsonism: an historical case series." *Lancet Neurol* 17 (4):300-301. doi: 10.1016/S1474-4422(18)30072-3.

Oliveira, L. M., L. J. Falomir-Lockhart, M. G. Botelho, K. H. Lin, P. Wales, J. C. Koch, E. Gerhardt, H. Taschenberger, T. F. Outeiro, P. Lingor, B. Schule, D. J. Arndt-Jovin, and T. M. Jovin. 2015. "Elevated alpha-synuclein caused by SNCA gene triplication impairs neuronal differentiation and maturation in Parkinson's patient-derived induced pluripotent stem cells." *Cell Death Dis* 6 (11):e1994. doi: 10.1038/cddis.2015.318.

Oltra, J., C. Uribe, B. Segura, A. Campabadal, A. Inguanzo, G. C. Monte-Rubio, J. Pardo, M. J. Marti, Y. Compta, F. Valldeoriola, C. Junque, and A. Iranzo. 2022. "Brain atrophy pattern in de novo Parkinson's disease with probable RBD associated with cognitive impairment." *NPJ Parkinsons Dis* 8 (1):60. doi: 10.1038/s41531-022-00326-7.

Orenstein, S. J., S. H. Kuo, I. Tasset, E. Arias, H. Koga, I. Fernandez-Carasa, E. Cortes, L. S. Honig, W. Dauer, A. Consiglio, A. Raya, D. Sulzer, and A. M. Cuervo. 2013. "Interplay of LRRK2 with chaperone-mediated autophagy." *Nat Neurosci* 16 (4):394-406. doi: 10.1038/nn.3350.

Ou, Z., J. Pan, S. Tang, D. Duan, D. Yu, H. Nong, and Z. Wang. 2021. "Global Trends in the Incidence, Prevalence, and Years Lived With Disability of Parkinson's Disease in 204 Countries/Territories From 1990 to 2019." *Front Public Health* 9:776847. doi: 10.3389/fpubh.2021.776847.

Oun, A., A. M. Sabogal-Guaqueta, S. Galuh, A. Alexander, A. Kortholt, and A. M. Dolga. 2022. "The multifaceted role of LRRK2 in Parkinson's disease: From human iPSC to organoids." *Neurobiol Dis* 173:105837. doi: 10.1016/j.nbd.2022.105837.

Pagano, G., S. Polychronis, H. Wilson, B. Giordano, N. Ferrara, F. Niccolini, and M. Politis. 2018. "Diabetes mellitus and Parkinson disease." *Neurology* 90 (19):e1654-e1662. doi: 10.1212/WNL.0000000000005475.

Palomer, X., J. Pizarro-Delgado, E. Barroso, and M. Vazquez-Carrera. 2018. "Palmitic and Oleic Acid: The Yin and Yang of Fatty Acids in Type 2 Diabetes Mellitus." *Trends Endocrinol Metab* 29 (3):178-190. doi: 10.1016/j.tem.2017.11.009.

Park, J., S. Choi, and R. Kim. 2023. "Association between prediabetes and cognitive function in Parkinson's disease." *Brain Behav* 13 (1):e2838. doi: 10.1002/brb3.2838.

Park, K. Y., G. E. Nam, K. Han, H. K. Park, and H. S. Hwang. 2022. "Waist circumference and risk of Parkinson's disease." *NPJ Parkinsons Dis* 8 (1):89. doi: 10.1038/s41531-022-00353-4.

Parkinson, J. 2002. "An essay on the shaking palsy. 1817." *J Neuropsychiatry Clin Neurosci* 14 (2):223-36; discussion 222. doi: 10.1176/jnp.14.2.223.

Passi, A., J. D. Tibocha-Bonilla, M. Kumar, D. Tec-Campos, K. Zengler, and C. Zuniga. 2021. "Genome-Scale Metabolic Modeling Enables In-Depth Understanding of Big Data." *Metabolites* 12 (1). doi: 10.3390/metabo12010014.

Patikas, N., R. Ansari, and E. Metzakopian. 2023. "Single-cell transcriptomics identifies perturbed molecular pathways in midbrain organoids using alpha-synuclein triplication Parkinson's disease patient-derived iPSCs." *Neurosci Res* 195:13-28. doi: 10.1016/j.neures.2023.06.001.

Pembroke, W. G., C. L. Hartl, and D. H. Geschwind. 2021. "Evolutionary conservation and divergence of the human brain transcriptome." *Genome Biol* 22 (1):52. doi: 10.1186/s13059-020-02257-z.

Pezzoli, G., E. Cereda, P. Amami, S. Colosimo, M. Barichella, G. Sacilotto, A. Zecchinelli, M. Zini, V. Ferri, C. Bolliri, D. Calandrella, M. G. Bonelli, V. Cereda, E. Reali, S. Caronni, E. Cassani, M. Canesi, F. Del Sorbo, P. Soliveri, L. Zecca, C. Klersy, R. Cilia, and I. U. Isaias. 2023. "Onset and mortality of Parkinson's disease in relation to type II diabetes." *J Neurol* 270 (3):1564-1572. doi: 10.1007/s00415-022-11496-y.

Pissadaki, E. K., and J. P. Bolam. 2013. "The energy cost of action potential propagation in dopamine neurons: clues to susceptibility in Parkinson's disease." *Front Comput Neurosci* 7:13. doi: 10.3389/fncom.2013.00013.

Poewe, W., K. Seppi, C. M. Tanner, G. M. Halliday, P. Brundin, J. Volkmann, A. E. Schrag, and A. E. Lang. 2017. "Parkinson disease." *Nat Rev Dis Primers* 3:17013. doi: 10.1038/nrdp.2017.13.

Poitelon, Y., A. M. Kopec, and S. Belin. 2020. "Myelin Fat Facts: An Overview of Lipids and Fatty Acid Metabolism." *Cells* 9 (4). doi: 10.3390/cells9040812.

Potashkin, J. A., S. R. Blume, and N. K. Runkle. 2010. "Limitations of animal models of Parkinson's disease." *Parkinsons Dis* 2011:658083. doi: 10.4061/2011/658083.

Pouchieu, C., C. Piel, C. Carles, A. Gruber, C. Helmer, S. Tual, E. Marcotullio, P. Lebailly, and I. Baldi. 2018. "Pesticide use in agriculture and Parkinson's disease in the AGRICAN cohort study." *Int J Epidemiol* 47 (1):299-310. doi: 10.1093/ije/dyx225.

Prasad, C., K. E. Davis, V. Imrhan, S. Juma, and P. Vijayagopal. 2019. "Advanced Glycation End Products and Risks for Chronic Diseases: Intervening Through Lifestyle Modification." *Am J Lifestyle Med* 13 (4):384-404. doi: 10.1177/1559827617708991.

Prasuhn, J., R. L. Davis, and K. R. Kumar. 2020. "Targeting Mitochondrial Impairment in Parkinson's Disease: Challenges and Opportunities." *Front Cell Dev Biol* 8:615461. doi: 10.3389/fcell.2020.615461.

Preininger, M. K., and D. Kaufer. 2022. "Blood-Brain Barrier Dysfunction and Astrocyte Senescence as Reciprocal Drivers of Neuropathology in Aging." *Int J Mol Sci* 23 (11). doi: 10.3390/ijms23116217.

Pringsheim, T., N. Jette, A. Frolkis, and T. D. Steeves. 2014. "The prevalence of Parkinson's disease: a systematic review and meta-analysis." *Mov Disord* 29 (13):1583-90. doi: 10.1002/mds.25945.

Puri, D., and W. Wagner. 2023. "Epigenetic rejuvenation by partial reprogramming." *Bioessays* 45 (4):e2200208. doi: 10.1002/bies.202200208.

Qian, X., Y. Su, C. D. Adam, A. U. Deutschmann, S. R. Pather, E. M. Goldberg, K. Su, S. Li, L. Lu, F. Jacob, P. T. T. Nguyen, S. Huh, A. Hoke, S. E. Swinford-Jackson, Z. Wen, X. Gu, R. C. Pierce, H. Wu, L. A. Briand, H. I. Chen, J. A. Wolf, H. Song, and G. L. Ming. 2020. "Sliced Human Cortical Organoids for Modeling Distinct Cortical Layer Formation." *Cell Stem Cell* 26 (5):766-781 e9. doi: 10.1016/j.stem.2020.02.002.

Rahman, I., M. T. Athar, and M. Islam. 2020. "Type 2 Diabetes, Obesity, and Cancer Share Some Common and Critical Pathways." *Front Oncol* 10:600824. doi: 10.3389/fonc.2020.600824.

Raimundo, A. F., S. Ferreira, I. C. Martins, and R. Menezes. 2020. "Islet Amyloid Polypeptide: A Partner in Crime With Abeta in the Pathology of Alzheimer's Disease." *Front Mol Neurosci* 13:35. doi: 10.3389/fnmol.2020.00035.

Reinhardt, P., M. Glatza, K. Hemmer, Y. Tsytsyura, C. S. Thiel, S. Hoing, S. Moritz, J. A. Parga, L. Wagner, J. M. Bruder, G. Wu, B. Schmid, A. Ropke, J. Klingauf, J. C. Schwamborn, T. Gasser, H. R. Scholer, and J.

Sterneckert. 2013. "Derivation and expansion using only small molecules of human neural progenitors for neurodegenerative disease modeling." *PLoS One* 8 (3):e59252. doi: 10.1371/journal.pone.0059252.

Rhea, E. M., C. Rask-Madsen, and W. A. Banks. 2018. "Insulin transport across the blood-brain barrier can occur independently of the insulin receptor." *J Physiol* 596 (19):4753-4765. doi: 10.1113/JP276149.

Rhee, Y. H., M. Choi, H. S. Lee, C. H. Park, S. M. Kim, S. H. Yi, S. M. Oh, H. J. Cha, M. Y. Chang, and S. H. Lee. 2013. "Insulin concentration is critical in culturing human neural stem cells and neurons." *Cell Death Dis* 4 (8):e766. doi: 10.1038/cddis.2013.295.

Rocha, E. M., G. A. Smith, E. Park, H. Cao, E. Brown, P. Hallett, and O. Isacson. 2015. "Progressive decline of glucocerebrosidase in aging and Parkinson's disease." *Ann Clin Transl Neurol* 2 (4):433-8. doi: 10.1002/acn3.177.

Russo, T., and M. Riessland. 2022. "Age-Related Midbrain Inflammation and Senescence in Parkinson's Disease." *Front Aging Neurosci* 14:917797. doi: 10.3389/fnagi.2022.917797.

Ryan, A. S. 2000. "Insulin resistance with aging: effects of diet and exercise." *Sports Med* 30 (5):327-46. doi: 10.2165/00007256-200030050-00002.

Sabari, S. S., K. Balasubramani, M. Iyer, H. W. Sureshbabu, D. Venkatesan, A. V. Gopalakrishnan, A. Narayanaswamy, N. Senthil Kumar, and B. Vellingiri. 2023. "Type 2 Diabetes (T2DM) and Parkinson's Disease (PD): a Mechanistic Approach." *Mol Neurobiol*:1-27. doi: 10.1007/s12035-023-03359-y.

Sabate-Soler, S., S. L. Nickels, C. Saraiva, E. Berger, U. Dubonyte, K. Barmpa, Y. J. Lan, T. Kouno, J. Jarazo, G. Robertson, J. Sharif, H. Koseki, C. Thome, J. W. Shin, S. A. Cowley, and J. C. Schwamborn. 2022. "Microglia integration into human midbrain organoids leads to increased neuronal maturation and functionality." *Glia* 70 (7):1267-1288. doi: 10.1002/glia.24167.

Sakaguchi, H., T. Kadoshima, M. Soen, N. Narii, Y. Ishida, M. Ohgushi, J. Takahashi, M. Eiraku, and Y. Sasai. 2015. "Generation of functional hippocampal neurons from self-organizing human embryonic stem cell-derived dorsomedial telencephalic tissue." *Nat Commun* 6:8896. doi: 10.1038/ncomms9896.

Sanchez-Gomez, A., Y. Diaz, T. Duarte-Salles, Y. Compta, and M. J. Marti. 2021. "Prediabetes, type 2 diabetes mellitus and risk of Parkinson's disease: A population-based cohort study." *Parkinsonism Relat Disord* 89:22-27. doi: 10.1016/j.parkreldis.2021.06.002.

Satake, W., Y. Nakabayashi, I. Mizuta, Y. Hirota, C. Ito, M. Kubo, T. Kawaguchi, T. Tsunoda, M. Watanabe, A. Takeda, H. Tomiyama, K. Nakashima, K. Hasegawa, F. Obata, T. Yoshikawa, H. Kawakami, S. Sakoda, M. Yamamoto, N. Hattori, M. Murata, Y. Nakamura, and T. Toda. 2009. "Genome-wide association study identifies common variants at four loci as genetic risk factors for Parkinson's disease." *Nat Genet* 41 (12):1303-7. doi: 10.1038/ng.485.

Schapira, A. H., J. M. Cooper, D. Dexter, J. B. Clark, P. Jenner, and C. D. Marsden. 1990. "Mitochondrial complex I deficiency in Parkinson's disease." *J Neurochem* 54 (3):823-7. doi: 10.1111/j.1471-4159.1990.tb02325.x.

Schubert, K. M., M. P. Scheid, and V. Duronio. 2000. "Ceramide inhibits protein kinase B/Akt by promoting dephosphorylation of serine 473." *J Biol Chem* 275 (18):13330-5. doi: 10.1074/jbc.275.18.13330.

Schultz, N., S. Janelidze, E. Byman, L. Minthon, K. Nagga, O. Hansson, and M. Wennstrom. 2019. "Levels of islet amyloid polypeptide in cerebrospinal fluid and plasma from patients with Alzheimer's disease." *PLoS One* 14 (6):e0218561. doi: 10.1371/journal.pone.0218561.

Schwamborn, J. C. 2018. "Is Parkinson's Disease a Neurodevelopmental Disorder and Will Brain Organoids Help Us to Understand It?" *Stem Cells Dev* 27 (14):968-975. doi: 10.1089/scd.2017.0289.

Sergi, D., N. Naumovski, L. K. Heilbronn, M. Abeywardena, N. O'Callaghan, L. Lionetti, and N. Luscombe-Marsh. 2019. "Mitochondrial (Dys)function and Insulin Resistance: From Pathophysiological Molecular Mechanisms to the Impact of Diet." *Front Physiol* 10:532. doi: 10.3389/fphys.2019.00532.

Shahmoradian, S. H., A. J. Lewis, C. Genoud, J. Hench, T. E. Moors, P. P. Navarro, D. Castano-Diez, G. Schweighauser, A. Graff-Meyer, K. N. Goldie, R. Sutterlin, E. Huisman, A. Ingrassia, Y. Gier, A. J. M. Rozemuller, J. Wang, A. Paepe, J. Erny, A. Staempfli, J. Hoernschemeyer, F. Grosseruschkamp, D. Niedieker, S. F. El-Mashtoly, M. Quadri, IJcken W. F. J. Van, V. Bonifati, K. Gerwert, B. Bohrmann, S. Frank, M. Britschgi, H. Stahlberg, W. D. J. Van de Berg, and M. E. Lauer. 2019. "Lewy pathology in Parkinson's disease consists of crowded organelles and lipid membranes." *Nat Neurosci* 22 (7):1099-1109. doi: 10.1038/s41593-019-0423-2.

Sharma, M., and J. Burre. 2023. "alpha-Synuclein in synaptic function and dysfunction." *Trends Neurosci* 46 (2):153-166. doi: 10.1016/j.tins.2022.11.007.

Shepherd, C. E., H. Alvendia, and G. M. Halliday. 2019. "Brain Banking for Research into Neurodegenerative Disorders and Ageing." *Neurosci Bull* 35 (2):283-288. doi: 10.1007/s12264-018-0326-3.

Shetty, S. S., and S. Kumari. 2021. "Fatty acids and their role in type-2 diabetes (Review)." *Exp Ther Med* 22 (1):706. doi: 10.3892/etm.2021.10138.

Signaevsky, M., B. Marami, M. Prastawa, N. Tabish, M. A. Iida, X. F. Zhang, M. Sawyer, I. Duran, D. G. Koenigsberg, C. H. Bryce, L. M. Chahine, B. Mollenhauer, S. Mosovsky, L. Riley, K. D. Dave, J. Eberling, C. S. Coffey, C. H. Adler, G. E. Serrano, C. L. White, 3rd, J. Koll, G. Fernandez, J. Zeineh, C. Cordon-Cardo, T. G. Beach, and J. F. Crary. 2022. "Antemortem detection of Parkinson's disease pathology in peripheral biopsies using artificial intelligence." *Acta Neuropathol Commun* 10 (1):21. doi: 10.1186/s40478-022-01318-7.

Simon-Sanchez, J., C. Schulte, J. M. Bras, M. Sharma, J. R. Gibbs, D. Berg, C. Paisan-Ruiz, P. Lichtner, S. W. Scholz, D. G. Hernandez, R. Kruger, M. Federoff, C. Klein, A. Goate, J. Perlmutter, M. Bonin, M. A. Nalls, T. Illig, C. Gieger, H. Houlden, M. Steffens, M. S. Okun, B. A. Racette, M. R. Cookson, K. D. Foote, H. H. Fernandez, B. J. Traynor, S. Schreiber, S. Arepalli, R. Zonozi, K. Gwinn, M. van der Brug, G. Lopez, S. J. Chanock, A. Schatzkin, Y. Park, A. Hollenbeck, J. Gao, X. Huang, N. W. Wood, D. Lorenz, G. Deuschl, H. Chen, O. Riess, J. A. Hardy, A. B. Singleton, and T. Gasser. 2009. "Genome-wide association study reveals genetic risk underlying Parkinson's disease." *Nat Genet* 41 (12):1308-12. doi: 10.1038/ng.487.

Singh, J. N., G. Jain, and S. S. Sharma. 2013. "In vitro hyperglycemia enhances sodium currents in dorsal root ganglion neurons: an effect attenuated by carbamazepine." *Neuroscience* 232:64-73. doi: 10.1016/j.neuroscience.2012.12.011.

Sirangelo, I., and C. Iannuzzi. 2021. "Understanding the Role of Protein Glycation in the Amyloid Aggregation Process." *Int J Mol Sci* 22 (12). doi: 10.3390/ijms22126609.

Smith, L., and A. H. V. Schapira. 2022. "GBA Variants and Parkinson Disease: Mechanisms and Treatments." *Cells* 11 (8). doi: 10.3390/cells11081261.

Smits, Lisa M., Stefano Magni, Kaoru Kinugawa, Kamil Grzyb, Joachim Luginbühl, Sonia Sabate-Soler, Silvia Bolognin, Jay W. Shin, Eiichiro Mori, Alexander Skupin, and Jens C. Schwamborn. 2020. "Single-cell transcriptomics reveals multiple neuronal cell types in human midbrain-specific organoids." *Cell and Tissue Research* 382 (3):463-476. doi: 10.1007/s00441-020-03249-y.

Smits, Lisa M., Lydia Reinhardt, Peter Reinhardt, Michael Glatza, Anna S. Monzel, Nancy Stanslowsky, Marcelo D. Rosato-Siri, Alessandra Zanon, Paul M. Antony, Jessica Bellmann, Sarah M. Nicklas, Kathrin Hemmer, Xiaobing Qing, Emanuel Berger, Norman Kalmbach, Marc Ehrlich, Silvia Bolognin, Andrew A. Hicks, Florian Wegner, Jared L. Sterneckert, and Jens C. Schwamborn. 2019. "Modeling Parkinson's disease in midbrain-like organoids." *npj Parkinson's Disease* 5 (1):5. doi: 10.1038/s41531-019-0078-4.

Spillantini, M. G., R. A. Crowther, R. Jakes, M. Hasegawa, and M. Goedert. 1998. "alpha-Synuclein in filamentous inclusions of Lewy bodies from Parkinson's disease and dementia with lewy bodies." *Proc Natl Acad Sci U S A* 95 (11):6469-73. doi: 10.1073/pnas.95.11.6469.

Streubel-Gallasch, L., V. Giusti, M. Sandre, I. Tessari, N. Plotegher, E. Giusto, A. Masato, L. Iovino, I. Battisti, G. Arrigoni, D. Shimshek, E. Greggio, M. E. Tremblay, L. Bubacco, A. Erlandsson, and L. Civiero. 2021. "Parkinson's Disease-Associated LRRK2 Interferes with Astrocyte-Mediated Alpha-Synuclein Clearance." *Mol Neurobiol* 58 (7):3119-3140. doi: 10.1007/s12035-021-02327-8.

Subrahmanian, N., and M. J. LaVoie. 2021. "Is there a special relationship between complex I activity and nigral neuronal loss in Parkinson's disease? A critical reappraisal." *Brain Res* 1767:147434. doi: 10.1016/j.brainres.2021.147434.

Sulzer, D. 2007. "Multiple hit hypotheses for dopamine neuron loss in Parkinson's disease." *Trends Neurosci* 30 (5):244-50. doi: 10.1016/j.tins.2007.03.009.

Sun, H., P. Saeedi, S. Karuranga, M. Pinkepank, K. Ogurtsova, B. B. Duncan, C. Stein, A. Basit, J. C. N. Chan, J. C. Mbanya, M. E. Pavkov, A. Ramachandaran, S. H. Wild, S. James, W. H. Herman, P. Zhang, C. Bommer, S. Kuo, E. J. Boyko, and D. J. Magliano. 2022. "IDF Diabetes Atlas: Global, regional and country-level diabetes prevalence estimates for 2021 and projections for 2045." *Diabetes Res Clin Pract* 183:109119. doi: 10.1016/j.diabres.2021.109119.

Suzuki, R., K. Lee, E. Jing, S. B. Biddinger, J. G. McDonald, T. J. Montine, S. Craft, and C. R. Kahn. 2010. "Diabetes and insulin in regulation of brain cholesterol metabolism." *Cell Metab* 12 (6):567-79. doi: 10.1016/j.cmet.2010.11.006.

Suzzi, S., R. Ahrendt, S. Hans, S. A. Semenova, A. Chekuru, P. Wirsching, V. Kroehne, S. Bilican, S. Sayed, S. Winkler, S. Spiess, A. Machate, J. Kaslin, P. Panula, and M. Brand. 2021. "Deletion of lrrk2 causes early developmental abnormalities and age-dependent increase of monoamine catabolism in the zebrafish brain." *PLoS Genet* 17 (9):e1009794. doi: 10.1371/journal.pgen.1009794.

Sveinbjornsdottir, S. 2016. "The clinical symptoms of Parkinson's disease." *J Neurochem* 139 Suppl 1:318-324. doi: 10.1111/jnc.13691.

Taira, T., Y. Saito, T. Niki, S. M. Iguchi-Ariga, K. Takahashi, and H. Ariga. 2004. "DJ-1 has a role in antioxidative stress to prevent cell death." *EMBO Rep* 5 (2):213-8. doi: 10.1038/sj.embor.7400074.

Takahashi, K., and S. Yamanaka. 2006. "Induction of pluripotent stem cells from mouse embryonic and adult fibroblast cultures by defined factors." *Cell* 126 (4):663-76. doi: 10.1016/j.cell.2006.07.024.

Tang, Q., P. Gao, T. Arzberger, M. Hollerhage, J. Herms, G. Hoglinger, and T. Koeglsperger. 2021. "Alpha-Synuclein defects autophagy by impairing SNAP29-mediated autophagosome-lysosome fusion." *Cell Death Dis* 12 (10):854. doi: 10.1038/s41419-021-04138-0.

Tang, X., Y. Huang, J. Lei, H. Luo, and X. Zhu. 2019. "The single-cell sequencing: new developments and medical applications." *Cell Biosci* 9:53. doi: 10.1186/s13578-019-0314-y.

Thiruchelvam, M., E. K. Richfield, B. M. Goodman, R. B. Baggs, and D. A. Cory-Slechta. 2002. "Developmental exposure to the pesticides paraquat and maneb and the Parkinson's disease phenotype." *Neurotoxicology* 23 (4-5):621-33. doi: 10.1016/s0161-813x(02)00092-x.

Tracey, T. J., F. J. Steyn, E. J. Wolvetang, and S. T. Ngo. 2018. "Neuronal Lipid Metabolism: Multiple Pathways Driving Functional Outcomes in Health and Disease." *Front Mol Neurosci* 11:10. doi: 10.3389/fnmol.2018.00010.

Tremblay, C., S. Rahayel, A. Vo, F. Morys, G. Shafiei, N. Abbasi, R. D. Markello, Z. Gan-Or, B. Misic, and A. Dagher. 2021. "Brain atrophy progression in Parkinson's disease is shaped by connectivity and local vulnerability." *Brain Commun* 3 (4):fcab269. doi: 10.1093/braincomms/fcab269.

Twelves, D., K. S. Perkins, and C. Counsell. 2003. "Systematic review of incidence studies of Parkinson's disease." *Mov Disord* 18 (1):19-31. doi: 10.1002/mds.10305.

Um, J. W., E. Im, H. J. Lee, B. Min, L. Yoo, J. Yoo, H. Lubbert, C. Stichel-Gunkel, H. S. Cho, J. B. Yoon, and K. C. Chung. 2010. "Parkin directly modulates 26S proteasome activity." *J Neurosci* 30 (35):11805-14. doi: 10.1523/JNEUROSCI.2862-09.2010.

Van den Berge, K., H. Roux de Bezieux, K. Street, W. Saelens, R. Cannoodt, Y. Saeys, S. Dudoit, and L. Clement. 2020. "Trajectory-based differential expression analysis for single-cell sequencing data." *Nat Commun* 11 (1):1201. doi: 10.1038/s41467-020-14766-3.

Van Den Eeden, S. K., C. M. Tanner, A. L. Bernstein, R. D. Fross, A. Leimpeter, D. A. Bloch, and L. M. Nelson. 2003. "Incidence of Parkinson's disease: variation by age, gender, and race/ethnicity." *Am J Epidemiol* 157 (11):1015-22. doi: 10.1093/aje/kwg068.

Varadi, C. 2020. "Clinical Features of Parkinson's Disease: The Evolution of Critical Symptoms." *Biology (Basel)* 9 (5). doi: 10.3390/biology9050103.

Vecchio, L. M., Y. Meng, K. Xhima, N. Lipsman, C. Hamani, and I. Aubert. 2018. "The Neuroprotective Effects of Exercise: Maintaining a Healthy Brain Throughout Aging." *Brain Plast* 4 (1):17-52. doi: 10.3233/BPL-180069.

Vera, E., N. Bosco, and L. Studer. 2016. "Generating Late-Onset Human iPSC-Based Disease Models by Inducing Neuronal Age-Related Phenotypes through Telomerase Manipulation." *Cell Rep* 17 (4):1184-1192. doi: 10.1016/j.celrep.2016.09.062.

Vicente Miranda, H., O. M. El-Agnaf, and T. F. Outeiro. 2016. "Glycation in Parkinson's disease and Alzheimer's disease." *Mov Disord* 31 (6):782-90. doi: 10.1002/mds.26566.

Vincent, A. M., L. L. McLean, C. Backus, and E. L. Feldman. 2005. "Short-term hyperglycemia produces oxidative damage and apoptosis in neurons." *FASEB J* 19 (6):638-40. doi: 10.1096/fj.04-2513fje.

Volpicelli-Daley, L. A., K. C. Luk, T. P. Patel, S. A. Tanik, D. M. Riddle, A. Stieber, D. F. Meaney, J. Q. Trojanowski, and V. M. Lee. 2011. "Exogenous alpha-synuclein fibrils induce Lewy body pathology leading to synaptic dysfunction and neuron death." *Neuron* 72 (1):57-71. doi: 10.1016/j.neuron.2011.08.033.

Wallum, B. J., G. J. Taborsky, Jr., D. Porte, Jr., D. P. Figlewicz, L. Jacobson, J. C. Beard, W. K. Ward, and D. Dorsa. 1987. "Cerebrospinal fluid insulin levels increase during intravenous insulin infusions in man." *J Clin Endocrinol Metab* 64 (1):190-4. doi: 10.1210/jcem-64-1-190.

Walter, J., S. Bolognin, S. K. Poovathingal, S. Magni, D. Gerard, P. M. A. Antony, S. L. Nickels, L. Salamanca, E. Berger, L. M. Smits, K. Grzyb, R. Perfeito, F. Hoel, X. Qing, J. Ohnmacht, M. Bertacchi, J. Jarazo, T. Ignac, A. S. Monzel, L. Gonzalez-Cano, R. Kruger, T. Sauter, M. Studer, L. P. de Almeida, K. J.

Tronstad, L. Sinkkonen, A. Skupin, and J. C. Schwamborn. 2021. "The Parkinson's-disease-associated mutation LRRK2-G2019S alters dopaminergic differentiation dynamics via NR2F1." *Cell Rep* 37 (3):109864. doi: 10.1016/j.celrep.2021.109864.

Wang, L., U. Das, D. A. Scott, Y. Tang, P. J. McLean, and S. Roy. 2014. "alpha-synuclein multimers cluster synaptic vesicles and attenuate recycling." *Curr Biol* 24 (19):2319-26. doi: 10.1016/j.cub.2014.08.027.

Wang, S. Y., S. L. Wu, T. C. Chen, and C. S. Chuang. 2020. "Antidiabetic Agents for Treatment of Parkinson's Disease: A Meta-Analysis." *Int J Environ Res Public Health* 17 (13). doi: 10.3390/ijerph17134805.

Wauters, F., T. Cornelissen, D. Imberechts, S. Martin, B. Koentjoro, C. Sue, P. Vangheluwe, and W. Vandenberghe. 2020. "LRRK2 mutations impair depolarization-induced mitophagy through inhibition of mitochondrial accumulation of RAB10." *Autophagy* 16 (2):203-222. doi: 10.1080/15548627.2019.1603548.

Winner, B., R. Jappelli, S. K. Maji, P. A. Desplats, L. Boyer, S. Aigner, C. Hetzer, T. Loher, M. Vilar, S. Campioni, C. Tzitzilonis, A. Soragni, S. Jessberger, H. Mira, A. Consiglio, E. Pham, E. Masliah, F. H. Gage, and R. Riek. 2011. "In vivo demonstration that alpha-synuclein oligomers are toxic." *Proc Natl Acad Sci U S A* 108 (10):4194-9. doi: 10.1073/pnas.1100976108.

Wong, Y. C., and D. Krainc. 2016. "Lysosomal trafficking defects link Parkinson's disease with Gaucher's disease." *Mov Disord* 31 (11):1610-1618. doi: 10.1002/mds.26802.

Wu, J., X. Luo, N. Thangthaeng, N. Sumien, Z. Chen, M. A. Rutledge, S. Jing, M. J. Forster, and L. J. Yan. 2017. "Pancreatic mitochondrial complex I exhibits aberrant hyperactivity in diabetes." *Biochem Biophys Rep* 11:119-129. doi: 10.1016/j.bbrep.2017.07.007.

Xicoy, H., B. Wieringa, and G. J. Martens. 2017. "The SH-SY5Y cell line in Parkinson's disease research: a systematic review." *Mol Neurodegener* 12 (1):10. doi: 10.1186/s13024-017-0149-0.

Xie, J., M. Wang, Z. Long, H. Ning, J. Li, Y. Cao, Y. Liao, G. Liu, F. Wang, and A. Pan. 2022. "Global burden of type 2 diabetes in adolescents and young adults, 1990-2019: systematic analysis of the Global Burden of Disease Study 2019." *BMJ* 379:e072385. doi: 10.1136/bmj-2022-072385.

Xing, Y. Q., A. Li, Y. Yang, X. X. Li, L. N. Zhang, and H. C. Guo. 2018. "The regulation of FOXO1 and its role in disease progression." *Life Sci* 193:124-131. doi: 10.1016/j.lfs.2017.11.030.

Yanai, H., Y. Hirowatari, and H. Yoshida. 2019. "Diabetic dyslipidemia: evaluation and mechanism." *Glob Health Med* 1 (1):30-35. doi: 10.35772/ghm.2019.01007.

Yin, X., B. E. Mead, H. Safaee, R. Langer, J. M. Karp, and O. Levy. 2016. "Engineering Stem Cell Organoids." *Cell Stem Cell* 18 (1):25-38. doi: 10.1016/j.stem.2015.12.005.

Zagare, A., K. Barmpa, S. Smajic, L. M. Smits, K. Grzyb, A. Grunewald, A. Skupin, S. L. Nickels, and J. C. Schwamborn. 2022. "Midbrain organoids mimic early embryonic neurodevelopment and recapitulate LRRK2-p.Gly2019Ser-associated gene expression." *Am J Hum Genet* 109 (2):311-327. doi: 10.1016/j.ajhg.2021.12.009.

Zechel, S., A. Meinhardt, K. Unsicker, and O. von Bohlen Und Halbach. 2010. "Expression of leucine-rich-repeat-kinase 2 (LRRK2) during embryonic development." *Int J Dev Neurosci* 28 (5):391-9. doi: 10.1016/j.ijdevneu.2010.04.002.

Zeighami, Y., M. Ulla, Y. Iturria-Medina, M. Dadar, Y. Zhang, K. M. Larcher, V. Fonov, A. C. Evans, D. L. Collins, and A. Dagher. 2015. "Network structure of brain atrophy in de novo Parkinson's disease." *Elife* 4. doi: 10.7554/eLife.08440.

Zhang, X., Y. Fan, Y. Luo, L. Jin, and S. Li. 2020. "Lipid Metabolism is the common pathologic mechanism between Type 2 Diabetes Mellitus and Parkinson's disease." *Int J Med Sci* 17 (12):1723-1732. doi: 10.7150/ijms.46456.

Zhao, Y., A. Ray, L. Portengen, R. Vermeulen, and S. Peters. 2023. "Metal Exposure and Risk of Parkinson Disease: A Systematic Review and Meta-Analysis." *Am J Epidemiol* 192 (7):1207-1223. doi: 10.1093/aje/kwad082.